Studies on Controlled Growth and Optoelectronic Properties of ZnO Nanowires, Nanorods and its Heterostructures for Efficient UV Photodetection

A Dissertation Submitted to
Indian Institute of Technology Guwahati
For the Degree of

Doctor of Philosophy

By

Soumen Dhara

Department of Physics
Indian Institute of Technology Guwahati
Guwahati-781039, India

February 2012

Dedicated To

…..My Beloved Parents

ACKNOWLEDGEMENT

The research reported in this thesis is the culmination of years of hard work, and would not have been possible without the help of a number of people. I want to take this opportunity to thank them for their help and support.

First, I would like to acknowledge my thesis supervisor, Dr. P. K. Giri. I am thankful to him for his excellent supervision, kindness and encouragement. I am always gratitude to him for giving me complete freedom in my work to achieve the goal. I would like to thank the Doctoral committee members, Dr. Saurabh Basu (chairman), Dr. Deepak K. Goswami and Dr. G. Krishnomoorthy for regular review of my work and their constructive criticism and valuable suggestions. Their suggestions enriched me to think deeply on the interpretation of results for a quality research work.

I am also thankful to our Head of the Department and other faculty members of Physics, members of the Central Instruments Facilities and Centre for nanotechnology for providing me a research friendly atmosphere with up–to–date research facilities. I am grateful to Indian Institute of Technology Guwahati for providing the fellowship and such a good accommodation in this beautiful campus. A special thanks to the scientific officers, Dr. Sidananda Sarma Indrajit Talukdar, Kaustubh Acharya, Kula K. Senapati, Chandan Borgohain and Madhurjya Borah for their help and cooperation to complete my work. I am also thankful to Central Workshop, Department of Mechanical Engineering for the fabrication of essential components used in my experimental setup.

I would like to express my appreciation and thanks to my seniors, friends and labmates for their helps and a good company. I should mention one of my close friends, Arindam for the fun–filled enjoyable company since my university days. He is always helpful for any kind of work or any discussion in Physics. Talking to him has helped me to overcome my frustrations. A special thanks to Barun-

da, who help me lot and with his company I did not felt lonely during my early days at IITG campus.

I must thank my parents, Mr. Swades Ranjan Dhara and Mrs. Kajal Dhara for their love, blessing and constant encouragement to pursue higher studies. I especially thank my father for inspiring me for hard work and to be honest. His hard work and dedication to help me to pursue higher studies is the strongest source of inspiration for me. My lovely brother Anup Dhara and sister Pratima Maity are always a source of love, support and affection in all walks of life.

Finally, I should acknowledge the supports received from my school teachers and well–wishers. They supported me in all possible ways during my early days of study by means of motivation, academic books, free tuitions and financial help. I must mention the name of my secondary school teachers, Timir babu and Subash babu for their strong advice to pursue higher studies in science.

CONTENTS

SYNOPSIS

One–dimensional nanostructures, including nanowires (NWs), nanorods (NRs) are the most studied nanomaterials for their important physical properties and application prospects. ZnO is a direct wide bandgap materials having bandgap ~3.37 eV and high excitonic binding energy, 60 meV at room temperature. One–dimentional ZnO nanostructures are extensively studied for their applications in various electronic and optoelectronic devices, e.g., field effect transistors, UV photodetectors, piezoelectric nanogenerators, nanolasers, UV light emitting diodes, solar cells, biosensores etc.. ZnO NWs could be grown by thermal vapor deposition, chemical vapor deposition and hydrothermal/solvothermal methods. Various types of one–dimensional ZnO nanostructures have been grown by several groups worldwide and they studied the effect of growth conditions on the morphology of the ZnO NWs. However, any direct correlations of the source material, growth temperature and ZnO vapor pressure on the desired shape, size and orientation of the ZnO NWs and NRs are not well understood. For device applications, large–scale and highly oriented NWs array structures are preferable for direct conduction path of the carriers as well as simplification of device fabrication. However it is very difficult to grow highly oriented NWs arrays over large surface area with very high aspect ratio. Therefore, control and tunability on shape, size and orientation of NWs is the key to the success of any method of synthesizing NWs and assembling them in different nanoscale devices ranging from nanoelectronics to biological and chemical sensors. Depending upon the growth method, the as–grown one–dimensional ZnO nanostructures invariably contain several surface defects which have a detrimental effect on the band edge UV emission and related applications. Hence, obtaining highly efficient UV emission from the ZnO nanostructures is one of most important issues for optoelectronic applications of ZnO.

The electronic conductivity of the ZnO NWs/NRs is extremely sensitive to ultraviolet light exposure. The light–induced change in conductivity allows us to use it as optoelectronic switch or UV photodetector. Since the first report on UV photodetection from single ZnO nanowires by Kind *et al.*, many efforts have been made on one–dimentional ZnO nanostructures, including NWs to improve the photodetection and photoresponse behaviours. However, photosensitivity and photoresponce time of the

ZnO NWs based photodetectors will require significant improvements in order to meet future demands in variety of fields. From the reported results, it is found that the single ZnO NW based devices have comparatively faster response. However, due to low photosensitivity it does not find applications in the real world. Fabrication of photodetectors by using large numbers of ZnO NWs array could be an alternative; however, integration and collective electrical contacts to a large number of NWs is a crucial issue. Note that, the photodetection and photoresponse of the ZnO NWs depends on the surface condition, structural quality, method of synthesis and rate of oxygen adsorption and photodesorption. Therefore, it is expected that arrays of NWs, surface modification or structural improvement, heterostructures can enhance the photosensitivity as well as photoresponse. In the steps towards this goal, very recently, a few groups have reported enhanced photodetection behaviours from the ZnO NWs heterostructures. Although the heterostructures are superior for modulation of the properties, however selection of right external material, control on the external layer and formation of high quality interface between the external material and NW are the challenging issues.

This thesis focuses on the growth of vertically aligned high quality ZnO NWs and NRs arrays over large area and fabrication of ZnO NWs based heterostructures for efficient UV photodetection. We have grown and characterized varieties of ZnO NWs and NRs, and systematically studied the effect of growth parameters to achieve control over the shape, size and orientations. ZnO NWs and NRs are grown by vapor transport method using a home–built thermal vapor deposition (TVD) system and by an aqueous chemical method using an autoclave. Morphology and microstructures of the NWs and NRs are studied in detail by using several scientific tools, e.g., field emission scanning electron microscope (FESEM), transmission electron microscope (TEM), X–ray diffractometer, micro–Raman spectrometer. The optical absorption and photoluminescence (PL) measurements are also performed to explore the suitability of these nanostructures for the use in laser or LED as well as to identify several radiative surface defects present on the as–grown ZnO NWs and NRs. The photdetection properties of the ZnO NWs are also carried out by measuring the photoresponse and wavelength dependent PC for the use in UV photodetectors. From these studies, several new and significant results have been obtained. A new growth strategy has been shown for the growth of vertically well–aligned ZnO NWs and NRs arrays. In the study of effects of growth conditions and

source materials, we observed nanostructure shape evolution and a detail investigation was performed to find out the origin of this shape evolution. The origin of the visible emission in the PL spectra is directly correlated with the several surface defects present on the as–grown NWs/NRs. To improve the structural quality as well as the UV emission efficiency, a simple and effective post–growth processing technique has been employed for the as–grown one–dimensional ZnO nanostructures. For the first time, we report on the very high photosensitivity and improved photoresponse from the post–growth processed ZnO NWs without making any complex structure. For the fabrication of the highly sensitive and ultrafast UV photodetectors, we prepared different novel types of ZnO NW heterostructures with different materials and characterized for the applications in UV photodetection. These heterostructures show very high improvement in the photosensitivity and photoresponse time, which are the essential requirement for the efficient photodetection. The origin of this improvement from these heterostructures is studied systematically and explained in details.

The thesis work is presented in **seven chapters**. The first one is devoted to the introduction, present status of the ZnO NWs and NRs research and motivation for the present work. The next chapter, chapter 2 describes the details of the several in–house developed and commercial experimental techniques used for the growth and characterization of the ZnO NWs and NRs. In chapter 3, several approaches of the strategic growth methods of well aligned ZnO NWs and NRs and their micro–structural characterization are discussed. Chapter 4 and 5 present the results on the optical absorption, PL and photodetection properties of the ZnO NWs and NRs. And a strategy for the improvement in UV PL and the photodetection behavior is also presented. Chapter 6 deals with the fabrication, characterization, photoluminescence and photodetection behaviours of the several novel types of ZnO NWs based heterostructures. The last chapter highlights the new findings and important conclusions of the present work.

Chapter 1 presents the glimpse of the important features of the ZnO NWs, NRs and their potential use in different nanodevices ranging from the nanoelectronics to biological and chemical sensors. The present status of the ZnO NWs and NRs based photodetectors and the motivation for the present work is presented at the end of this chapter.

Chapter 2 provides brief information about the experimental techniques used for the present work and their working principle. The design and in–house development of the thermal vapor deposition and photoresponse properties measurement systems are presented in details. The methodology adopted to analyze the data of the NWs/NRs is also described in details.

In **chapter 3**, some new approaches for the strategic growth of the well aligned ZnO NWs and NRs and their micro–structural characterization have been described. We studied the effects of growth parameters for the growth of well–aligned ZnO NWs and NRs over large area by using TVD method as well as low temperature aqueous chemical method. A major emphasize is given to the control on the growth orientation and alignment of the NWs and NRs. We have shown that the independent use of ZnO seed layer or Au catalyst layer does not lead to the growth of well aligned ZnO NWs and NRs. The combined effect of ZnO seed layer and Au catalyst are found to favor the growth of well–aligned ZnO NWs and NRs arrays. High quality well–aligned ZnO NWs and NRs arrays have been grown over large area with diameter 50–200 nm using ZnO seed layer coated with the Au catalyst layer. In this case, ZnO seed layer and Au layer together act as a nucleation site and guide the NWs growth. Au layer transfer the same orientation of the ZnO seed layer to the ZnO NWs/NRs leading to the well–aligned growth. Therefore, structural quality and orientation of the ZnO seed layer are the key factors for the well–aligned growth of the NWs/NRs. To study the effect of doping on the optoelectronic and optical properties, Al doped ZnO NWs with different concentration of Al is synthesized by ball milling of the source material followed by TVD process of growth.

We have shown that ZnO nanostructures exhibit shape evolution as a function of growth temperature for ZnO nanopowder as source material. With the increase in growth temperature, the nanostructure changes from NWs to nanoribbons and then to NRs at higher growth temperature. On the other hand, in case of ZnO bulk powder as a source material, only nanowires are produced at these temperatures. Systematic studies on the observed shape evolution reveal that zinc vapor pressure, supersaturation rate, growth temperature and ultrathin catalyst layer are the key factors in determining the morphology of the ZnO nanostructures.

In **chapter 4**, optical absorption and room temperature PL properties of the as–grown and processed NWs/NRs are presented. The PL spectroscopy is extensively used to study the band–edge related UV emission as well as to identify the origin of the broad visible emission. The origin of the visible emission in the PL spectra is correlated with the surface defects present on the as–grown samples. It is found that, different growth method introduce different types of radiative surface defect states. The ZnO nanostructures grown by TVD method in general introduces two types of defects giving rise to the PL bands, one centered at 500 nm and other at 545 nm. The first one corresponds to the oxygen vacancy related defect emission and second one corresponds to the interstitial oxygen related defects. In contrast, ZnO NWs grown by aqueous chemical method show two new types of defects. It is also observed that intensity of the band–edge related UV PL emission is very low in the NWs due to the presence of native surface defects. In order to improve the UV emission efficiency, a simple post–growth processing technique, rapid thermal annealing (RTA) has been employed and it is demonstrated to be very effective. The as–grown ZnO NWs and NRs are RTA treated at 700°C and 800°C for 120 s. The UV emission intensity could be enhanced by three–five times, while the green emission band completely disappears after RTA. It is shown that the RTA processing improves the structural quality as well as the UV PL emission efficiency of the ZnO NWs and NRs by releasing built–in stress and removing the structural and surface defects. The PL decay process of the visible emission is also systematically studied to see the changes in the defect states after RTA processing. The results show a gradual reduction of the defect state density with increase in RTA processing temperature.

Chapter 5 presents the UV photocurrent and photoresponse of the as–grown and RTA processed NWs array. We report on the major improvement in photodetection behaviors of the RTA processed ZnO NWs array and the origin of enhancement is investigated. We obtained a very high photosensitivity (~25000) and an improved photoresponse from the RTA processed ZnO NWs without making any complex heterostructure. By studying the dark current–voltage (I–V) characteristic, we have shown that the presence of defect/trap centres on the surface of the NWs could be recognized from the linear fit to the log–log (I–V) plot. From the analysis of the dark I–V data, we further confirmed a significant reduction of the surface defect states in the RTA processed ZnO NWs. The photocurrent growth and decay behaviours under the UV excitation and dark conditions are also

studied in detail to understand the mechanism of conductivity enhancement under the excitation of UV light. The photoresponse mechanism of the ZnO NWs is also explained through energy band diagram. The photoresponse of the ZnO NWs consists of two parts: a rapid process of photogeneration and recombination of electron–hole pairs, and a slow process of surface adsorption and photodesorption. After RTA processing, a five–fold enhancement in the UV photosensitivity and two–fold faster photoresponse are obtained. Although, the photosensitivity value of the RTA processed NWs is enough for real time application, the photoresponse and reset times are however slow.

Chapter 6 discusses about several new types of ZnO NWs heterostructures and their photoluminescence and photodetection properties for the fabrication of the high sensitive and ultrafast UV photodetectors. Two types of heterostructures were fabricated; one with decorating the surface of the NWs with ultra small metal (Au and Ti) nanoparticles (NPs) and other one is inorganic/organic type heterostructures with anthracene and copper phthalocyanine (CuPc). Using the heterostructure approach we are able to achieve very high UV PL intensity, higher PC and faster photoresponse. The origin of this improvement from these heterostructures is studied systematically and explained in details on the basis of interfacial interaction and transfer of electrons in the NW heterostructures. The absorption and PL properties of these heterostructures are also studied to correlate the effect of external heterostructure materials on the improved photoresponse properties.

ZnO/Au NW and ZnO/Ti NW heterostructures were fabricated by directly depositing small sizes Au and Ti NPs on the surface of the NWs with different sizes by sputter deposition process in a controlled way. In the metal NPs decorated heterostructures, metal NPs and ZnO NWs interface strongly influence the photodetection process. ZnO/Au NWs heterostructure shows nearly linear dark I–V characteristic with reduced dark current. On the contrary, ZnO/Ti NW heterostructures show a linear I–V behavior with very high dark current. A large enhancement (seven–ten times) in photocurrent and UV PL intensity is obtained from ZnO/Au NW and ZnO/Ti NW heterostructures, and much faster photoresponse is obtained from both the systems. For the ZnO/Au NW heterostructures, the photocurrent increases with increase of Au coverage up to a certain thickness and then decreases. In contrast, the photocurrent in ZnO/Ti NW heterostructures increases with the increase of the Ti coverage. The mechanism of

enhancement in ZnO/Ti NWs is explained on the basis of electron transfer from Ti to ZnO through an Ohmic contact. On the other hand, in the ZnO/Au NW heterostructures it is explained by surface plasmon resonance assisted electrons transfer to the conduction band of ZnO. Therefore, nature of contacts formed between metal NPs and ZnO NWs plays an important role on the enhancement of photocurrent and faster photoresponse.

Next we studied the inorganic/organic type NW heterostructures using two different organic semiconductors, anthracene and copper phthalocyanine (CuPc). In ZnO/anthracene heterostructure, the dark current is increased after the covering of anthracene layer with thickness about ~15 nm. A significant improvement in the photosensitivity is obtained from the heterostructure. The wavelength dependence of photodetection shows a kind of visible blindness, which is highly beneficial for UV photodetection. Compared to the as–grown NWs, the ZnO/anthracene NWs system exhibits six–fold enhancement in the photosensitivity and much faster photoresponse with response and reset times below one second. The room temperature PL spectra show three–fold enhancement in the UV emission with high enhancement in the ratio of UV to green emission intensities. It is argued that the transfer of photoexcited electrons from the LUMO in anthracene to the conduction band of ZnO results in the enhancement of UV PL intensity and the photocurrent in the ZnO/anthracene NW heterostructure.

Studies on ZnO/CuPc heterostructure results in very high photocurrent with two–fold enhancement in the photosensitivity. The room temperature PL spectra show significant improvement in the UV PL intensity with an enhancement factor of one order of magnitude. The CuPc molecule has high absorption in the UV region (~330 nm) which is above the absorption edge of ZnO (~367 nm). This high absorption by ZnO/CuPc NW heterostructures generates more numbers of electron–hole pairs and transfer of electrons from CuPc to ZnO resulting in high UV photoluminescence and photocurrent.

Note that, the above described heterostructures are able to give very high photosensitivity. However it fails to show ultrafast photoresponse, which is one of the essential requirements for the real times applications of ZnO NWs based UV photodetectors. Here we have shown an effective new approach to improve the photoresponse and reset times as well as the photosensitivity of ZnO NWs. Improved ultrafast photoresponse and reset time, and enhanced photosensitivity were obtained by combined effects of Al doping and Au NPs decoration on the surface of the ZnO NWs

network. The obtained photoresponse and reset times are 0.10 and 0.11 s, respectively, which are much faster than those of undoped bare ZnO NWs. With further decoration of the ultra small Au NPs, the photoresponse and reset times are further reduced to several ms. At the same time, PC is significantly enhanced. In contrast, only Al doping results in very fast response and reset times but low photosensitivity. The absorption spectra show slight widening of the band gap due to the incorporation of Al atoms inside the Zn lattice.

Chapter 7 presents the summary and important conclusions of this work to highlight the new findings on the studies on controlled growth of ZnO NWs and NRs arrays and their UV photodetection properties. In the present work, I have studied the effect of several growth parameters for the growth of vertically aligned high quality ZnO NWs and NRs arrays over large area and fabricated several new types of ZnO NWs based heterostructures for efficient UV photodetection. A new approach has been shown for the growth of vertically aligned ZnO NWs and NRs arrays. The origin of the observed visible emission in the PL spectra is studied in details and directly correlated with the surface defects. We have demonstrated that the post–growth RTA processing is an effective and simple way to achieve higher photosensitivity and faster photoresponse as well as enhanced UV PL intensity and significant reduction in defect related visible emission. Our studies establish that the ZnO NWs heterostructures are indeed excellent candidates for UV photodetectors with very high sensitivity and fast response for real time photosensing applications. The mechanisms of improved photodetection behaviours from different systems are also explained. These understanding will help to design and fabricate ZnO NWs heterostructure based efficient UV photodetectors. Our approaches show comparable/significant improvement over other approaches that are relatively complex reported in the literature for the ZnO NWs based photodetectors. The results demonstrate that Au NPs decorated Al doped ZnO NWs and ZnO/anthracene NW heterostructures are highly suitable for the real time photosensing applications.

The new findings from this work are published in several international journals and presented in various international conferences, as listed next.

List of Publications

In Book Chapter:

1. **Soumen Dhara** and P. K. Giri, ""Chapter–1: ZnO nanorods arrays and heterostructures for the high UV photodetection", ***Nanorods***, Ed. Orhan Yalcin, InTech publisher, ISBN 979–953–307–356–8, pp. 1-32 (**2012**).

In Peer–Reviewed Journals:

1. P. K. Giri, **Soumen Dhara** and Ritun Chakraborty, "Effect of ZnO seed layer on the catalytic growth of vertically aligned ZnO nanorods arrays", ***Mat. Chem. Phys.***122, 18–22 (**2010**).

*2. **Soumen Dhara** and P. K. Giri, "Self–catalytic growth of horizontally aligned straight Si nanowires on Si substrates using a sputter deposition technique", ***Solid State Comm.*** 150, 1923–27 (**2010**).

*3. **Soumen Dhara** and P. K. Giri, "Effect of growth temperature on the catalyst free growth of long silicon nanowires using radio frequency magnetron sputtering", ***Int. J. Nanosci.*** 10, 13–17 (**2011**).

*4. **Soumen Dhara** and P. K. Giri, "Size–depedent visible absorption and fast photoluminescence decay dynamics from strained silicon nanocrystals", ***Nanoscale Res. Lett.*** 6, 320 (**2011**).

*5. R. Chakraborty, **Soumen Dhara** and P. K. Giri, "Effect of rapid thermal annealing on microstructure and optical properties of ZnO nanorods"**,** ***Int. J. Nanosci.*** 10, 65–68 (**2011**).

6. **Soumen Dhara** and P. K. Giri, "Shape evolution in one–dimensional ZnO nanostructure grown from ZnO nanopowder source: vapour–liquid–solid vs. vapour–solid growth mechanisms", ***Int. J. Nanosci.*** 10, 75–79 (**2011**).

7. **Soumen Dhara** and P. K. Giri, "Rapid thermal annealing induced enhanced band–edge emission from ZnO nanowires, nanoribbons and nanorods", ***Funct. Mater. Lett.*** 4, 25–29 (**2011**).

8. **Soumen Dhara** and P. K. Giri, "Enhanced UV photosensitivity from rapid thermal annealed vertically aligned ZnO nanowires", ***Nanoscale. Res. Lett.*** 6, 504 (**2011**).

9. **Soumen Dhara** and P. K. Giri, "Effect of ZnO nanopowder source and growth temperature on the shape evolution of one–dimensional ZnO nanostructures", ***Int. J. Nanosci.*** 10, 833–837 (**2011**).

*10. **Soumen Dhara** and P. K. Giri, "Quick single–step mechanosynthesis of ZnO nanorods and their optical characterization: milling time dependence", ***Appl. NanoSci.*** 1, 165–171 (**2011**).

*11. **Soumen Dhara** and P. K. Giri, "Size–dependent anisotropic strain and optical properties of strained silicon nanocrystals", ***J. Nanosci. Nanotechnol.*** 11, 9215–9221 (**2011**).

12. **Soumen Dhara** and P. K. Giri, "On the origin of enhanced photoconduction and photoluminescence from metal nanoparticles decorated ZnO nanowire heterostructures", ***J. Appl. Phys.*** 110, 124317 (**2011**).

---

*This work is not included in this dissertation.

*13. P. K. Giri and **Soumen Dhara**, "Freestanding Ge/GeO_2 core–shell nanocrystals with varying sizes and shell thickness: microstructure and photoluminescence studies", ***J. NanoMater.*** 2012, 905178 (**2012**).

*14. **Soumen Dhara** and P. K. Giri, "Stable p–type conduction and enhanced photoconductivity from nitrogen–doped ZnO thin films", ***Thin Solid Films*** 520, 5000–5006 (**2012**).

15. **Soumen Dhara** and P. K. Giri, "ZnO/anthracene based inorganic/organic nanowires heterostructure: photoluminescence and photoconductivity studies", ***J. Appl. Phys.*** 111, 044320 (**2012**).

16. **Soumen Dhara** and P. K. Giri, "Improved fast photoresponse from Al doped ZnO nanowires network decorated with Au nanoparticles", Chem. Phys. Lett. 541, 39–43 (**2012**).

17. **Soumen Dhara** and P. K. Giri, "Organic CuPc coating induced improved photoluminescence and photoconductivity of ZnO nanowires array", ***Funct. Mater. Lett.*** (**2012**)**,** DOI: 10.1142/S179360471250021X.

18. **Soumen Dhara** and P. K. Giri, "Ti nanoparticles decorated ZnO nanowires heterostructure: photocurrent and photoluminescence properties", ***J. Exp. NanSci.*** (**2012**), DOI: 10.1080/17458080.2012.682284.

Conference Presentations:

1. **Soumen Dhara** and P. K. Giri, "Effect of growth temperature on the catalyst free growth of long silicon nanowires using radio frequency magnetron sputtering", *International Conference on Advanced Nanomaterials and Nanotechnology* (**ICANN–2009**), December 9–11, 2009, IIT Guwahati, India.
2. **Soumen Dhara** and P. K. Giri, "Temperature dependence of shape evolution in one–dimensional ZnO nanostructure grown from ZnO nanopowder source: vapour–liquid–solid vs. vapour–solid growth mechanisms", *International Conference on Advanced Nanomaterials and Nanotechnology* (**ICANN–2009**), December 9–11, 2009, IIT Guwahati, India.
3. R. Chakraborty, **Soumen Dhara** and P. K. Giri, "Effect of rapid thermal annealing on microstructure and optical properties of ZnO nanorods", *International Conference on Advanced Nanomaterials and Nanotechnology* (**ICANN–2009**), December 9–11, 2009, IIT Guwahati, India.
4. **Soumen Dhara** and P. K. Giri, "Effect of ZnO nanopowder source and growth temperature on shape evolution of one–dimensional ZnO nanostructure", *International Conference on Nanoscience and Technology* (**ICONSAT–2010**), February 17–20, 2010, IIT Bombay, India.
5. **Soumen Dhara** and P. K. Giri, "Microstructure and optical properties of freestanding Si nanocrystals", *3rd International Conference on Nanostructures SElf–Assembly* (**NanoSEA–2010**), June 28– July 2, 2010, Cassis, France.
6. **Soumen Dhara** and P. K. Giri, "Self–catalytic growth of straight Si nanowires with high aspect ratio on Si(100) substrate by simple sputter deposition", *8th International*

Nanotechnology Symposium – New Ideas for Industry (**NanoFair 2010**), July 6–7, 2010, Dresden, Germany.

7. **Soumen Dhara** and P. K. Giri, "Studies on photocarrier transport mechanism in ZnO nanowires grown by vapor–liquid–solid method*",* *International Symposium on Advances in Nanomaterials* (**ANM 2010**), December 6–7, 2010, CGCRI Kolkata, India.
8. Bappaditya Pal, **Soumen Dhara,** Pankaj Mishra and P. K. Giri, ″Studies on structure, magnetic and optical properties of Co–doped ZnO Nanowires″, *International Symposium on Advances in Nanomaterials* (**ANM 2010**), December 6–7, 2010, CGCRI Kolkata, India.
9. **Soumen Dhara** and P. K. Giri, ″Rapid thermal annealing induced enhanced near band–edge emission from ZnO nanowires, nanorods and nanoribbons″, *International Conference on Fundamental and Applications of Nanoscience and Technology* (**ICFANT 2010**), December 9–11, 2010, Jadavpur University. Kolkata, India.
10. **Soumen Dhara** and P. K. Giri, ″Enhanced ultraviolet photocurrent response from rapid thermal annealed ZnO nanowires″, *International Conference on Materials for Advanced Technologies* (**ICMAT 2011**), June 26–July 1, 2011, Suntec, Singapore.
11. **Soumen Dhara** and P. K. Giri, "On the origin of enhanced photoconduction and photoluminescence from metal nanoparticles decorated ZnO nanowire heterostructures", *International Conference on Advanced Nanomaterials and Nanotechnology* (**ICANN-2011**), December 8-10, 2011, IIT Guwahati, India.
12. **Soumen Dhara** and P. K. Giri, "ZnO/anthracene based nanowires photodetector: photoresponse and photoluminescence studies", *International Conference on Advanced Nanomaterials and Nanotechnology* (**ICANN-2011**), December 8-10, 2011, IIT Guwahati, India.
13. **Soumen Dhara** and P. K. Giri, "Ultrafast photoresponse and reset times from ZnO nanowires network by Al doping and Au nanoparticles decoration", *5th International Conference on Nanoscience and Technology* (**ICONSAT-2012**), January 20-23, 2012, Hyderabad, India.
14. **Soumen Dhara** and P. K. Giri, "Inorganic/organic and inorganic/metal based ZnO nanowire heterostructures for highly efficient UV photodetection", *4th International Conference on Nanostructures SElf-Assembly* (**NanoSEA-2012**), June 25-29, 2012, Cagliari, Italy.

List of Abbreviations

Abbreviation	Description
NWs	Nanowires
NRs	Nanorods
Al:ZnO	Al doped ZnO
NPs	Nanoparticles
TVD	Thermal Vapor Deposition
VLS	Vapor–Liquid–Solid
VS	Vapor–Solid
RTA	Rapid Thermal Annealing
PC	Photocurrent
SEM	Scanning Electron Microscopy
FESEM	Field Emission Scanning Electron Microscopy
EDX	Energy Dispersive X–ray Spectroscopy
TEM	Transmission Electron Microscopy
HRTEM	High Resolution Transmission Electron Microscopy
SAED	Selected Area Electron Diffraction
XRD	X–ray Diffraction
FWHM	Full With at Half Maximum
UV–Vis	Ultraviolet–Visible
PL	Photoluminescence
TRPL	Time Resolved Photoluminescence
NBE	Near Band edge Emission
FTIR	Fourier Transformed Infrared Spectroscopy

Chapter 1
Introduction

In the past years, varieties of nanostructures of metal and semiconductor are synthesized by top–down as well as by bottom–up approaches and extensively studied. The synthesized nanostructures include thin films, nanowires (NWs), nanorods (NRs), nanobelts, nanotubes, nanocrystals, quantum dot etc..The research community witnessed the several unusual properties of these nanostructures which is completely different from their bulk counterpart. The reduction in size of crystalline structures ultimately mean that physical principles important to atoms, but normally negligible in bulk, which begin to increase in importance.[1] High surface–to–volume ratio and quantum confinement effect are the two unique effects of nanostructure materials that modify the properties.[2,3] Depending upon the properties, several nanoscale devices have been made and find applications in the chemical industry,[4] medical diagnostics,[5] food technology,[6] ultraviolet radiation monitoring,[7] national defense,[8] and our daily life.[9] In this chapter a brief introduction to the important features of the ZnO NWs, NRs and their potential use in different nanoelectronic devices are presented. The present status of the ZnO NWs and NRs research and motivation for the present work is also presented in this chapter. The organization of this thesis is described at the end of this chapter.

1.1. Nanowires and Nanorods

NWs and NRs are one–dimensional structure with diameter ranging from few nm to 200 nm and length up to several microns. With respect to other nanostructures, they present several advantages, like a larger surface–to–volume ratio, a direct carrier conduction path, a large variety of potential novel properties available through the control of size and structure and a high compatibility with standard industrial device fabrication technologies. Such structures are of particular interest for device

applications, as they exhibit quantum confinement in two dimensions while the third is relatively unrestricted.[10] They also have potential to act as interconnects between functional nanoscale components; such components can even be fabricated sequentially within the same wire. Several books and review articles are dedicated to the basics of NWs and NRs growth, shape control and their applications in to a diverse filed.[11-15] Rao *et al.*[13] presented an intense review of the controlled growth of large numbers of inorganic NWs. The key parameters for the radial and axial heterostructures growth and their potential uses in the electronic industry are well summarized by Lu *et al.*.[14] Whereas, Voon *et al.*[15] summarized the theoretical prediction on the electronic properties of the NWs and compared with the available experimental results.

1.1.1. ZnO Nanowires and Nanorods

Significant amounts of intense research have been devoted to the semiconducting NWs and NRs for the fascinating properties of semiconductors and existence of billion dollar electronic industry made with semiconducting materials. Si, GaN, TiO_2, ZnO, Ge are the most studied semiconducting nanostructures. However, ZnO find some edge over the others due the comparatively easy synthesis, unusual electronic properties and huge application prospects in diverse area of electronic and optoelectronic industry. Typical images of the ZnO NWs and NRs are shown in Fig. **1.1**. Although NWs and NRs have similar shape and structure, however they are divided according to their shape of the facet and aspect ratio. In case of ZnO, circular facet and comparatively larger aspect ratio is considered as NWs whereas, hexagonal facet and comparatively lower aspect ratio is consider as NRs.

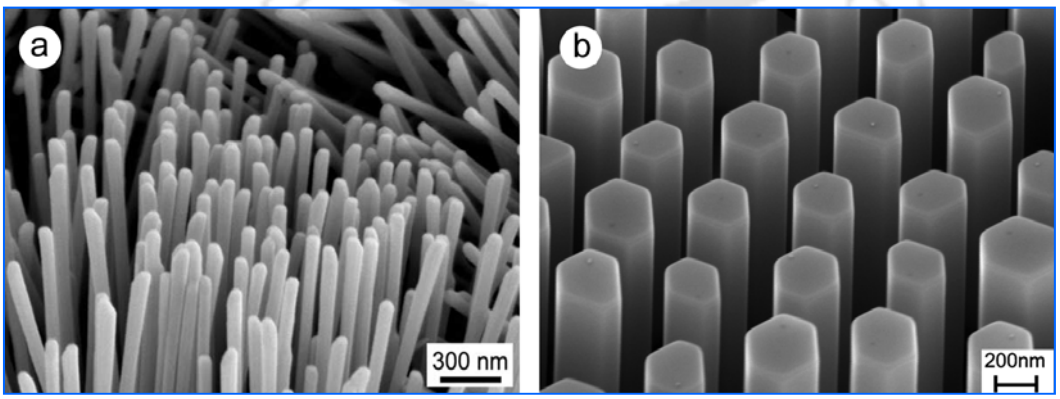

Figure 1.1: Electron microscopy images of the vertically aligned ZnO (a) nanowires and (b) nanorods. Adapted from Ref. [**16,17**].

ZnO is a II–VI group, direct wide bandgap semiconductor having bandgap of ~3.37 eV and high excitonic binding energy, 60 meV at room temperature. The energy band diagram of ZnO is shown in Fig. **1.2**. One–dimentional ZnO nanostructures are extensively studied for their applications in various electronic and optoelectronic devices, e.g., field effect transistors[18,19], UV photodetectors[20,21], piezoelectric nanogenerators,[22,23] nanolasers,[24,25] light emitting diodes,[26,27] solar cells,[28,29] biosensores[30,31] etc..

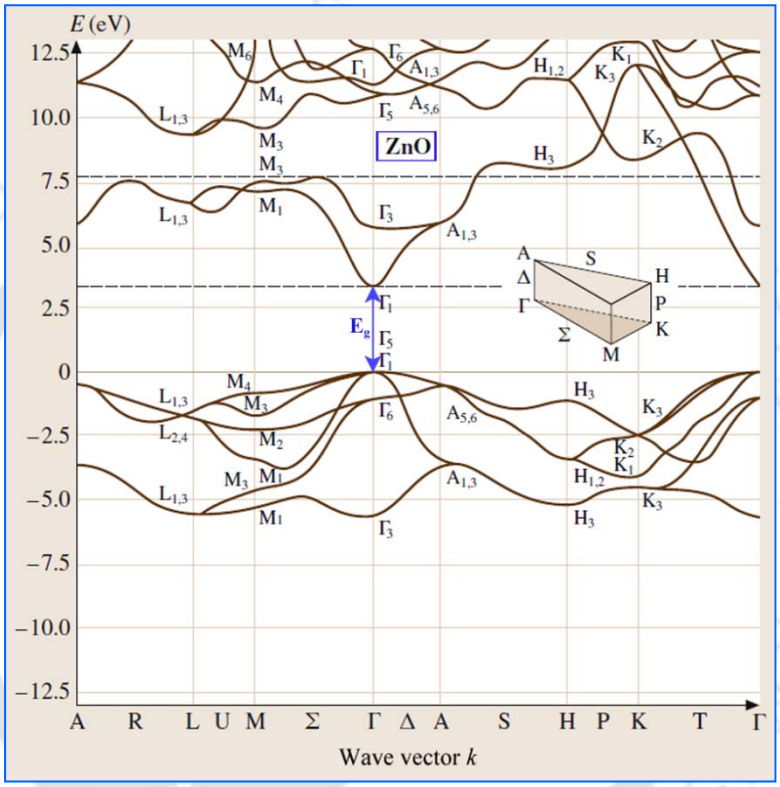

Figure 1.2: Energy band diagram of the ZnO, the arrow shows the energy gap between the conduction band and valence band at Γ point. Adapted from Ref. [**32**].

1.2. Growth of ZnO Nanowires and Nanorods

ZnO is a compound semiconductor whose ionic nature is in between covalent and ionic semiconductor. Although the crystal structures shared by ZnO are wurtzite, zinc blende, and rocksalt, however at ambient conditions, only wurtzite phase is thermodynamically stable. The wurtzite structure has a hexagonal unit cell with two lattice parameters, *a* and *c*, in a ratio of *c*/*a*=1.633 and belongs to the space group of C_{6v}^4or $P6_3mc$. The hexagonal lattice of ZnO is characterized by two interconnecting sublattices of Zn^{2+} and O^{2-}, such that each Zn ion is surrounded by a tetrahedral of O ions, and vice–versa, which is shown in Fig. **1.3**. The tetrahedral coordination in ZnO results in noncentral symmetric

structure. Another important characteristic of ZnO is the polar surfaces. The most common polar surface is the basal plane. The oppositely charged ions produce positively charged Zn-(0001) and negatively charged O-$(000\bar{1})$ polar surfaces, resulting in a normal dipole moment and spontaneous polarization along the *c*-axis. The O terminated polar (0001) plane is the primary growth direction due to the lower surface energy of this plane, as calculated by Fujimura *et al.*.[33]

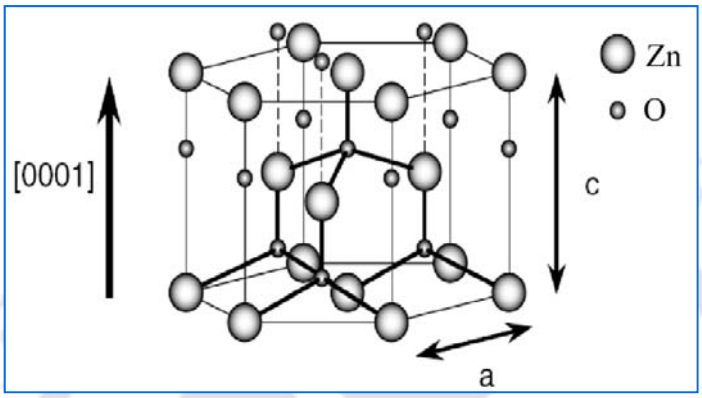

Figure 1.3: The wurtzite crystal structure model of ZnO having lattice constants *a* in the basal plane and *c* in the basal direction.

Various types of one–dimensional ZnO nanostructures have been grown by several groups worldwide[24,26,34-40] and they studied the effect of growth conditions on the morphology. An in–depth review has been presented by Fortuna *et al.*[41] on the control of growth direction of metal–catalyst assisted growth of semiconductor NWs. However, any direct correlations of the source material, growth temperature and ZnO vapor pressure on the desired shape, size and orientation of the ZnO NWs and NRs are not well understood. For device applications, large–scale and highly oriented NWs array structures are preferable for direct conduction path of the carriers as well as simplification of device fabrication. However, it is very difficult to grow highly oriented NWs arrays over large surface area with very high aspect ratio. In reality, ZnO NWs/NRs grown by different techniques give rise to various kinds of point defects (vacancy and interstitial defects) and lattice strain. Therefore, control and tunability on shape, size and orientation of defect free NWs is the key to the success of any method of synthesizing NWs and assembling them in different nanoscale devices ranging from nanoelectronics to biological and chemical sensors.

ZnO NWs and NRs with controlled shape and order could be grown by thermal vapor deposition (TVD),[40,42,43] metal–organic chemical vapor deposition,[44-46] molecular beam

epitaxy,[47] hydrothermal/solvothermal methods[26,48-52] and top down approach by eatching.[53] Among those techniques, TVD and hydrothermal methods are the widely used techniques for their versatility about controllability, repeatability, quality and mass production. MOCVD and MBE can give high quality ZnO NWs/NRs arrays, but use of these techniques are limited, due to the poor sample uniformity, low product yield, choices of proper substrate, and also the high experimental cost. The ZnO NWs and NRs studied in this thesis were grown by using a bottom–up approach by TVD and aqueous chemical growth by hydrothermal process. In the vapor deposition method, the growth process follows either vapor–liquid–solid (VLS) or vapor–solid (VS) mechanisms, depending on the growth conditions. On the other hand, the NWs are grown by chemical reaction in the hydrothermal/solvothermal methods with the assistance of cationic surfactant. For the growth of one–dimensional ZnO nanostructures, in general metal catalyst or ZnO seed layer are used to promote the one dimensional and vertical growth. In this section, some regularly used synthesis methods for the NWs/NRs and its heterostructures are discussed.

1.2.1. Vapor Transport Growth

Among all vapor–based synthesis methods, the VLS growth seems to be the most successful in generating large quantities of NWs and NRs with single crystalline structures. Wagner & Ellis[54] first reported this growth mechanism in the 1960s to produce micrometer–sized wires, later justified thermodynamically and kinetically by Givargizov in 1975.[55] In the early twenty–first century, this mechanism is extensively explored by several research groups worldwide to prepare NWs and NRs from a rich variety of inorganic materials.[56-65] The VLS growth mechanism is practically demonstrated by Yang group[58] with the help of in–situ transmission electron microscopy (TEM) techniques by monitoring the VLS growth mechanism in real time. Their finding first confirmed the association of VLS process in the growth of the NWs.

The VLS growth mechanism is shown schematically in Fig. **1.4**. This process consists primarily of three steps: (1) formation of the liquid alloy droplet, (2) crystal nucleation upon gas adsorption and supersaturation, and (3) axial growth from the crystalline seeds to form NWs.[58,66] In a typical VLS growth, the growth species (precursor) is evaporated/decomposed first, and then diffuses and dissolves into a liquid droplet (catalyst particle). It is also found that the metal cluster remains in solid form up to

melting point of this metal, if there is no vapor condensation on the liquid droplet. The formation temperature of the liquid alloy droplet is governed by the phase diagram of the metal with the growth species. The surface of the liquid alloy has a large accommodation coefficient, and is therefore a preferred site for deposition. Saturated growth species in the liquid droplet will diffuse to and precipitate at the interface between the substrate and the liquid. The precipitation will first follow nucleation and then crystal growth. Continued precipitation or growth will separate the substrate and the liquid droplet, resulting in the growth of NWs/NRs. Preferential one–dimensional growth continues in the presence of reactant as long as the catalyst nanocluster remains in the liquid droplet state. The wire diameter is determined by the diameter of the alloy liquid droplet which in turn is determined by the size of the metal particle and the temperature. The wire length is determined by the growth rate and time.[67]

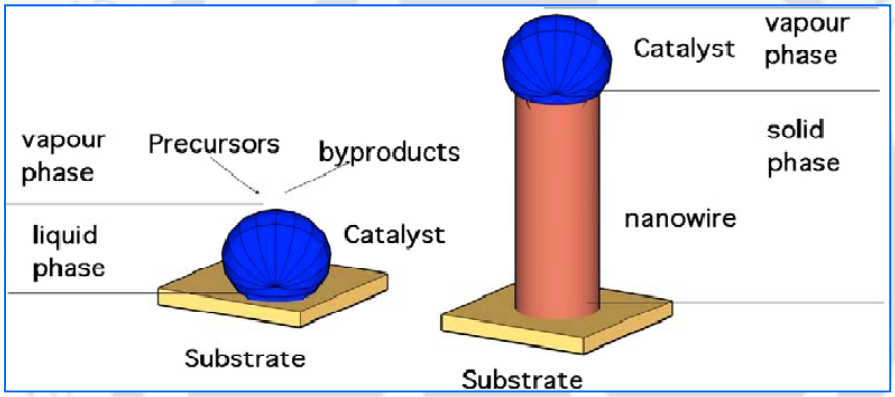

Figure 1.4: Schematic representation of vapor–liquid–solid growth of the NWs/NRs. The catalyst is in the liquid phase and precursors can adsorb and condense on the surface of the catalyst to form the NWs. Adapted from Ref. [**4**].

Single–crystalline ZnO NWs grown with the thermal vapor deposition method was first reported in 2001 by Kong *et al.*,[68] with an average diameter of about 60 nm. In 2002, Yao *et al.* reported the mass production of ZnO NWs, nanoribbons and needle–like NRs by thermal evaporation of ZnO.[43] Banerjee *et al.* succeeded in producing grams of ZnO NWs via thermal evaporation of ZnO powder in a tube furnace at high temperatures.[69] However, thermal evaporation of only ZnO powder needs very high temperature. To facilitate the production of ZnO NWs at a lower temperature, pre–growth reduction is utilized to decompose the high–melting–point ZnO (~1,975°C) into low–melting–point Zn or Zn suboxide (~420°C). The Zn vapor is then transported and it reacts with the metal catalyst to form liquid alloy droplets preferred for a VLS growth. Several reduction approaches are employed to produce Zn or Zn suboxide vapor:

1. Carbothermal Reduction

In this approach, graphite powder is added to pure ZnO powders.[42,70] At a high source temperature (~900–1100°C), Zn or Zn suboxides are produced by the following reactions:

$ZnO + C \rightarrow Zn + CO_2$

$ZnO + CO \rightarrow ZnO_x + CO_2$ $(0 \leq x < 1)$

2. Hydrogen Reduction

A wet oxidation condition (10% O_2, 5% H_2, 85% Ar) is advantageous because of the much lower bonding energy of the H–O bond as compared to the O–O bond to produce atomic oxygen and form ZnO.[68] Simple gas reaction with water vapor is also found favorable for the lower temperature growth of ZnO NRs.[71]

3. Reduction of Zinc Salts

Reduction and further oxidation of ZnS powder has been explored to grow tubular ZnO whiskers.[72,73] At a high temperature (~750°C), ZnS reduction follows: ZnS (solid) → Zn (gas) + S (gas). Then oxidization of Zn vapor results one–dimensional structures under certain growth condition.

There are several processing parameters such as temperature, pressure, carrier gas (including gas species and its flow rate), substrate and evaporation period, which can be controlled and need to be selected properly before and/or during the thermal vaporization.[37] The source temperature selection mainly depends on the volatility of the source material. Usually, it is slightly lower than the melting point of the source material. The pressure is determined according to the evaporation rate or vapor pressure of the source material. The local temperature determines the type of product that will be obtained. It is also noted that the thermal evaporation process is very sensitive to the concentration of oxygen in the growth system. Oxygen influences not only the volatility of the source material and the stoichiometry of the vapor phase, but also the formation of the product. Selection of metal catalyst species depends on the formation of a eutectic phase at the deposition temperature according to the phase diagram, as well as vapor/liquid/ solid interfacial energies and chemical stability in the reaction product.

1.2.1.1. Self–Catalytic Seed Layer Assisted Growth

For VLS growth of the NWs, metal catalyst nanocluster is essential. However, undesired metal contamination is generally seen for the NWs/NRs grown at relatively lower temperature. For the binary compound, it is possible for one of these elements or the binary compound itself to serve as the VLS catalyst. The nanostructures grown by this process is named as self catalytic growth. The major advantage of a self–catalytic process is that it avoids undesired contamination from foreign metal atoms typically used as VLS catalyst. Different groups have reported the ZnO seed layer assisted catalyst free growth of ZnO NWs and NRs and studied its morphology and crystallinity by different methods.[46,74-76] Li *et al.*[74] synthesized vertically aligned ZnO NRs with uniform length and diameter on silicon substrate by vapor–phase transport method and studied the structure, temperature dependent photoluminescence (PL) and field emission behaviours. In this case ZnO seed layer was prepared by pulsed laser deposition technique. Kim *et al.*[46] obtained ZnO NRs by metal–organic chemical vapour deposition method with enhanced aspect ratio at a relatively low temperature (300 °C) by supplying additional Ar carrier gas at a high flow rate. In another work by Feng *et al.*,[77] well–crystalline with excellent optical properties, flower–like ZnO NRs have been synthesized on Si(111) substrate coated with Zn film as "self–catalyst" by the simple thermal evaporation oxidation of the metallic zinc powder. The crystalline quality and orientation of the ZnO seed layer strongly control the structural quality and growth orientation of the NWs/NRs. In most of the cases, synthesized NWs/NRs were not aligned, hence have limited applications in nanosize electronic and optoelectronic devices. The precise control over the NRs/NWs lengths and diameters using a self–catalytic VLS technique is very difficult. Recently, there have been some experimental efforts to control the texture of ZnO films by changing the deposition conditions such as bias voltage, ambient pressure,[78] Laser pulse power[79] or the application of ion beam irradiation during the deposition.[80]

1.2.1.2. Metal Catalyst Assisted Growth

For the metal catalyst assisted growth of ZnO NWs and NRs, Au catalyst has got major popularity and extensively used due to its comparatively lower eutectic temperature (temperature require to form liquid droplet alloy of Au with the ZnO) and good solvent capability of forming liquid alloy with ZnO. The Au nanoparticles may be produced by

evaporation and annealing of thin films, colloid reduction techniques, and lithography. Huang *et al.*[42] first reported on the synthesis of highly crystalline ZnO NWs via VLS growth mechanism using mono–dispersed Au colloid as catalyst. Diameter control of the NWs was achieved by varying the Au layer thickness. They were also able to synthesize patterned NWs network by patterning the Au catalyst on the substrate. Hejazi *et al.*[81] prepared Au–catalyzed ZnO NRs and studied the growth rate on lateral size of NRs, concentration and supersaturation of Zn atoms in the liquid droplet by a theoretical kinetic model, which is in good agreement with the experimental results. A general expression for the NW/NR growth rate was obtained by materials' balance in the liquid droplet and growth front. Based on the derived formula, growth rate is inversely proportional to NR radius. A new understanding of the VLS process of Au catalyzed ZnO NWs was presented by Kirkham *et al.*[82] by studying orientation relationships between the substrates, NWs and Au particles using x–ray texture analysis. From the analysis, they claimed that the Au catalyst particles were solid during growth, and that growth proceeded by a surface diffusion process, rather than a bulk diffusion process. ZnO NWs/NRs are also grown successfully on the Si (100) or Al_2O_3 substrates by using Cu, Co, NiO and Sn as catalyst.[16,63,83-86]

1.2.2. Hydrothermal (Chemical) Growth

Aqueous chemical (hydrothermal) growth method is attractive for several reasons: low cost, less hazardous, and capable of easy scaling up; growth occurs at a relatively low temperature, compatible with flexible organic substrates; there is no need for the use of metal catalysts; in addition, there are a variety of parameters that can tuned to effectively control the morphologies and properties of the final products.[87-89] The growth process ensures that a majority of the NWs/NRs in the array are in direct contact with the substrate and provide a continuous pathway for carrier transport, an important feature for future electronic devices based on these materials. Aqueous chemical method has been demonstrated as a very powerful technique for the growth of ZnO NWs and NRs via selective capping mechanisms. It is believed that molecular capping agents play a significant role in the kinetic control of the nanocrystal growth by preferentially adsorbing to specific crystal faces, thus inhibiting growth of that surface. Probably the most commonly used chemical agents in the existing literature for the hydrothermal synthesis of ZnO NWs/NRs are $Zn(NO_3)_2$ and hexamethylenetetramine (HMT).[50,52,90,91]

In this case, $Zn(NO_3)_2$ provides Zn^{2+} ions required for building up ZnO NWs/NRs. Using HMT as a structural director, Greene *et al.*[92] produced dense arrays of ZnO NWs in aqueous solution having controllable diameters of 30–100 nm and lengths of 2–5 μm. With addition of polyethylenimine (PEI) in the hydrothermal method, Qiu *et al.*[93] able to synthesized well–aligned ZnO NWs arrays with a long length of more than 40 μm. However, without the additive PEI, the length of the NWs was not more than 5 μm. Guo *et al.*[89] studied the factors influencing the size, morphology and orientation of the ZnO NRs on the solution using hydrothermal method and discussed about tuning of the size and morphology. Commercially available microwave could be used for the hydrothermal growth of ZnO NWs/NRs.[94] Using microwave heating; rapid synthesis of aligned ZnO NWs within minute could be possible.

The role of HMT in aqueous chemical method is still not clearly understood. HMT is a nonionic cyclic tertiary amine that can act as a Lewis base to metal ions and has been shown to be a bidentate ligand capable of bridging two zinc(II) ions in solution. In this case, HMT acts as a pH buffer by slowly decomposing to provide a gradual and controlled supply of ammonia, which can form ammonium hydroxide as well as complex zinc(II) to form $Zn(NH_3)_4^{2+}$.[92] Because dehydration of the zinc hydroxide intermediates controls the growth of ZnO, the slow release of hydroxide may have a profound effect on the kinetics of the reaction. Additionally, ligands such as HMT and ammonia can kinetically control species in solution by coordinating to zinc(II) and keeping the free zinc ion concentration low. HMT and ammonia can also coordinate to the ZnO crystal, hindering the growth of certain surfaces.

1.2.3. ZnO Nanowires/Nanorods Arrays

Assembly and integration of highly ordered NWs arrays in large scale is essential for multifunctional devices and systems.[95] Significant efforts have been made to assemble large quantity of NWs through parallel processes, which can be grouped into two categories: grow–and–place (GAP) and grow–in–place (GIP). The GAP approach includes but is not limited to alignment induced by electrostatic,[96] molecular forces,[97] and methods utilizing magnetic fields.[98] Although the GAP technique can be used to fabricate a finite number of devices, it is rather challenging to assemble the as–synthesized NWs into desired configurations in large scale. In GIP technique, nanostructures grow in situ at the patterned catalyst/seed sites created through electron

beam lithography (EBL),[99] nanoimprint lithography (NIL),[100] and using ordered nanosphere pre layer.[17] Control over the growth substrate can guide the size, placement, and orientation of the grown NWs. He *et al.*[70], using AFM nanomachining technique together with catalytically activated vapor phase transport and the condensation deposition process, have grown a variety of patterned and featured ZnO NRs arrays. The growth pattern and feature are designed by the dotted catalyst prepared by using AFM tip indentation with controlled location, density, and geometrical shape. The vertical orientation of the NRs is achieved by the epitaxial growth on a single–crystal substrate. This technique allows a control over the location, shape, orientation, and density of the grown NRs arrays. However, none of the above approaches provides a reliable, high–throughput, and low–cost solution for large scale fabrication of patterned ZnO NW arrays at a level required for industrial applications.

Recently, there are reports on the growth of high yield NWs/NRs arrays by Zhou *et al.*[17] and Wei *et al.*.[34] Ordered arrays of *n*–type ZnO single crystal NRs have been grown perpendicularly on the *p*-GaN/Al_2O_3 substrates by Zhou *et al.*[17] For the substrate preparation, mask transfer technique is applied. First, a self–organized polystyrene nanospheres layer mask was prepared on glass and then it is dipped in to water. The floated mask was then transferred onto cleaned *p*-GaN substrates. A 15 nm In thin film was then evaporated onto the substrate followed by removal of the polystyrene nanospheres by dissolving them in CH_2Cl_2. This process leaves the patterned In nanoparticle array on *p*-GaN substrates which results in perfectly oriented ZnO NRs array. Whereas, Wei *et al.*[34] demonstrated an effective approach for controllable wafer–scale fabrication of ZnO NWs arrays by combining Laser interference lithographic patterning and hydrothermal growth. Laser interference patterning is employed to control the position, size, and orientation of synthesized ZnO NWs, while a hydrothermal chemical method is used to control the morphology and material properties of NWs. More importantly, combinations of both the laser interference patterning and the hydrothermal method allow more available access to large–scale uniformly patterned nanostructures at a high–throughput.

1.2.4. ZnO Nanowire Heterostructures

It is consider that heterostructures are superior for the modulation of selective properties of that material. Using suitable external materials for the heterostructures, one can

modify the properties of that material according to their requirements. In NWs heterostructures, two types of heterostructures could be fabricated either axial or radial with suitable materials, which are shown in Fig. **1.5**. Fabrication of planar semiconductor heterostructures for thin films is common, whereas the synthesis of one–dimensional heterostructures is difficult. Axial heterostructures along the length of the NWs axis, have been reported for a few systems, such as InAs/InP, GaAs/GaP and Si/SiGe NWs.[101-103] The first attempt for the fabrication of axial heterostructure in ZnO NWs was based on spatially controlled doping of single NW during the growth. Selective doping of single ZnO NW was carried out for creation of nano–junctions by introducing the dopant in vertically grown single–crystalline ZnO NWs. A section of the NWs was doped with aluminum as donor during crystal nucleation, resulting in n–n^+ junction.[104] Recently there are reports on radial heterostructures of ZnO NWs/NRs using several organic/inorganic materials.[29,36,105-110] ZnO–Al_2O_3 and ZnO–TiO_2 core–shell NWs have been synthesized using a two–step process.[29] First, ZnO NWs were grown in aqueous solution using a seeded growth process. Then atomic layer deposition was applied to cover each NW with a thin layer of amorphous Al_2O_3 or TiO_2. These core–shell NWs based dye–sensitized solar cell show comparatively higher energy conversion efficiency. Organic polymer (poly(vinyl alcohol)) as well as monomer (lysine) is also utilized for the fabrication of the ZnO NWs heterostructure.[105,106] These polymer or monomer based heterostructures show improvement in PL and photocurrent (PC) properties. Although the heterostructures are superior for modulation of the properties, however control on the external layer and formation of high quality interface between the external material and NW are challenging issues.

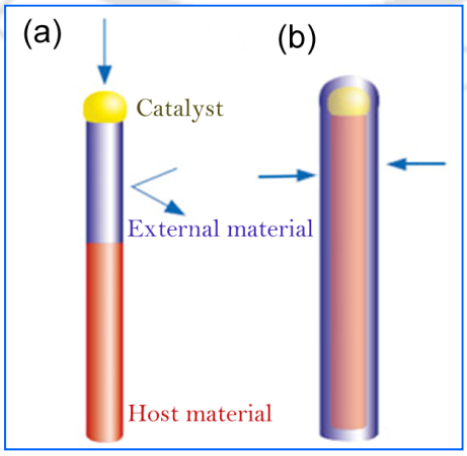

Figure 1.5: Schematic of nanowire heterostructures: (a) axial heterostructure (b) radial heterostructure. Adapted from Ref. [**14**].

ZnO NWs/NRs covered with dense and uniform ultra small metal nanoparticles (NPs) is another form of NW heterostructures. Using suitable noble metal or low work function metal NPs one could be able to achieve very high intense UV PL with significant reduction in visible emission, which is one of the most important requirements for the application in UV LED or laser. However, decoration of different metal NPs results in an anomalous behaviours in PL and PC properties. Earlier, Lin *et al.*[111] and later Cheng *et al.*[112] reported on the significant enhancement of UV PL intensity and subsequent reduction in the defect related visible emission from the ZnO NWs covered with ultra small Au NPs. It is also observed that, after certain size of the Au NPs, the UV PL intensity start decreasing. They proposed that the obtained enhancement is due to the defect loss along with the localized surface plasmon assisted recombination. On the otherhand, when the NRs surface is covered with Ag NPs, a significant improvement in the yellow–green light emission is obtained.[113] Whereas, for Ti NPs decoration both the UV PL and green emission intensity increases with increase in Ti coverage.[114] Interestingly, it is also observed that NWs covered with some metal gives rise to the decrement of the PL intensity.[115] Although a significant changes are obtained from the metal NPs covered NWs/NRs, however a general understanding on the mechanism for all types of metal covering is yet to emerge.

1.2.5. Intrinsic Defects in ZnO Nanowire and Nanorods

Depending upon the growth method, the as–grown ZnO NWs/NRs invariably contain several intrinsic structural defects which have a detrimental effect on the band edge UV emission.[116] These intrinsic defects have strong spectroscopic signature in the PL spectrum. The commonly observed radiative defects are tabulated in Table–**1.1**. Lin *et al.*[117] and Djurisic *et al.*[118] identified several oxygen and zinc related intrinsic defects and also some complex defect states which were probed by PL spectroscopy. Liu *et al.*[119] demonstrated that PL of the ZnO NWs can be tuned from UV to green by controlling the native defects, either by the gas flow during growth process or post–growth annealing in O_2. Some reports show that the most commonly observed green emission is caused by the presence of Zn vacancy.[120,121] On the contrary, other groups reported that it is not caused by Zn vacancy, however oxygen vacancy is responsible.[117,122] Therefore, a systematic generalized correlation of the defects and the corresponding emission need to be done for the improvement of UV PL intensity. Hence, obtaining highly efficient UV

emission from the ZnO nanostructures is one of most important issues for optoelectronic applications of ZnO.

Table 1.1: Summary of the commonly observed defects related PL peaks reported in the literature.

Sl. No.	Peak Position (nm)	Origin	Reference
1	398	singly ionized Zn vacancy	Janotty *et al.* 2006[123]
2	452	doubly ionized Zn vacancy	
3	470	interstitial oxygen	Liu *et al.* 2009[119]
4	500	oxygen vacancy	
5	520	antisite oxygen	
6	576	attachment of hydroxil group on the surface of the NWs	Djuriˇsi´c *et al.* 2007[118]
7	650	excess oxygen, possibly involving Zn vacancy complexes	
8	446	neutral oxygen vacancy	Liao *et al.* 2008[124]
9	500	singly ionized oxygen vacancy	
10	620	doubly ionized oxygen vacancy	
11	405	Zn vacancy	Lin *et al.*2001[117]
12	428	interstitial Zn	
13	545	deep interstitial oxygen	
14	600	excess oxygen	Greene *et al.* 2003[125]

The first–principle calculation on ZnO nanostructures shows the possible formation of six types of native point defects in ZnO: oxygen and zinc vacancies (V_O and V_{Zn}), interstitials (O_i and Zn_i), and antisites O_{Zn} and Zn_O). The calculation shows that there is also a possibility of formation of three types of oxygen vacancy defects according to their charge states namely, neutral (V_O^0), singly ionized (V_O^+) and doubly ionized (V_O^{++}). The atomic configuration of these point defects in the ZnO crystal is shown in Fig. **1.6**. The calculation shows that oxygen vacancies are deep donors and have high formation energies. Zinc vacancies are deep acceptors and have low formation energies under *n*-type conditions; they can therefore occur as compensating defects in *n*-type ZnO. It is suggested that zinc vacancies are a possible source of the often–observed green

luminescence in ZnO. Zinc interstitials are shallow donors, but have high formation energies under *n*-type conditions; moreover, they are fast diffusers and hence unlikely to be stable as isolated point defects. Zinc antisites are also shallow donors, but they have higher formation energies. Oxygen antisites have the highest formation energies among the acceptor–type native point defects. They are deep acceptors and also show large off–site displacements, in which the oxygen atom bonds chemically to only one of the oxygen nearest neighbors. Oxygen antisites have the highest formation energies among the acceptor–type native point defects. They are deep acceptors and also show large off–site displacements, in which the oxygen atom bonds chemically to only one of the oxygen nearest neighbors. Oxygen interstitials have high formation energies and are not expected to exist in significant concentrations.

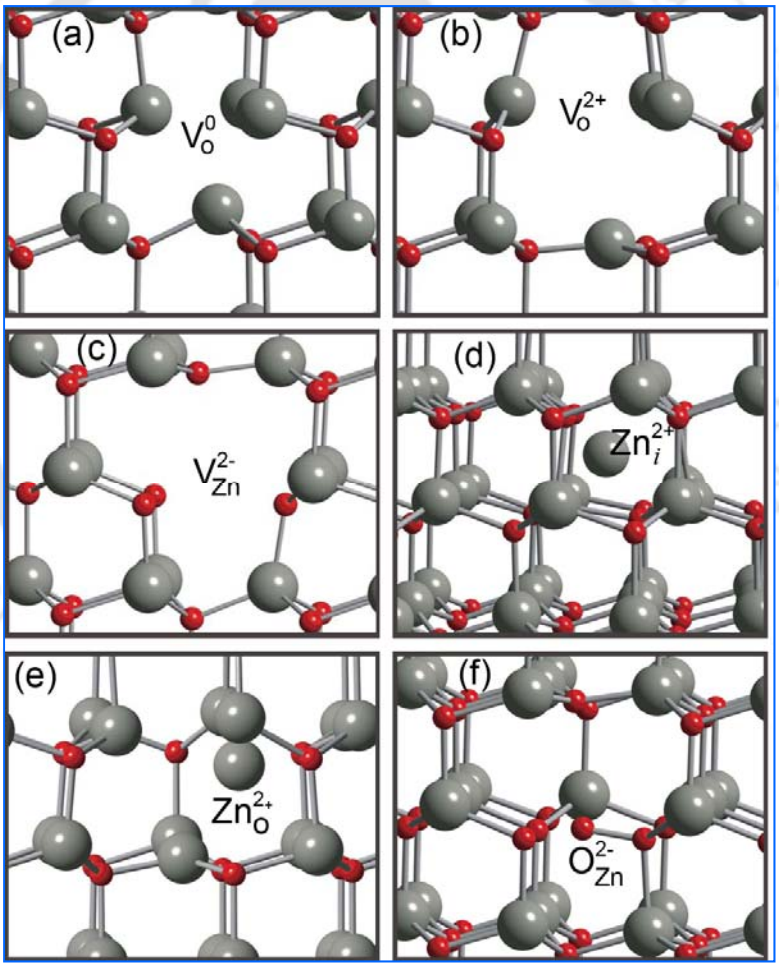

Figure 1.6: The side view along the *c*–axis of atomic configuration of the ZnO crystal with several point defects, obtained from first–principle calculation. Adapted from Ref. [**121**].

In a theoretical study of the diffusion mechanism of the oxygen vacancy and interstitial in ZnO, Huang *et al.*[126] shown that oxygen interstitial can be present in two forms, non–

symmetric octahedral interstitial oxygen (O_i^{2-}(oct)) and split interstitial (O_i^0(split)). The formation of above two oxygen interstitials in the ZnO lattice is shown in atomic geometry in Fig **1.7**. Their calculation shown that the most stable configuration is the oxygen octahedral interstitial (O_i^{2-}(oct)). Therefore obtained PL in the yellow–green region, which is generally attributed to interstitial oxygen, is due to the formation of above mentioned non–symmetric octahedral interstitial oxygen.

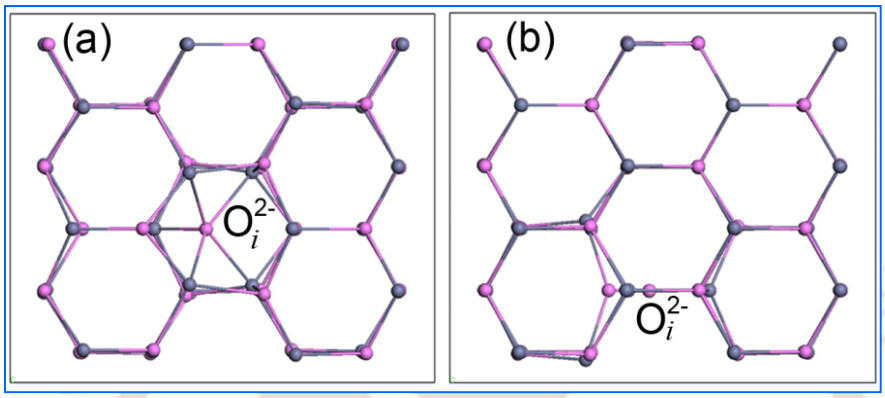

Figure 1.7: The top view along the *c* axis of atomic geometry of ZnO with (a) octahedral interstitial oxygen (O_i^{2-}(oct)) and (b) split interstitial (O_i^0(split)). Adapted from Ref. [**126**].

Along with the radiative point defects, several nonradiative structural defects are also observed in the ZnO NWs/NRs from high resolution TEM images. Ding *et al.*[127] shown various kinds of planar defects in ZnO NWs/NRs and nanobelts, such as stacking faults, twins, inversion domain walls, resulting in a weak crystallinity.

1.3. Doping in ZnO Nanowires/Nanorods

It is well known that nominally undoped ZnO reveals *n*–type conduction with a typical carrier concentration of $\leq 10^{17}$ cm^{-3}.[128] This value is however inadequate for practical electronic applications, where a carrier concentration of ~10^{18}–10^{20} cm^{-3} is required. Therefore, the doping of ZnO NWs or NRs to increase the carrier concentration or to decrease the resistivity is essential to realize nanoscale devices. The group III elements (i.e., Al, Ga, and In) have been the major candidates for *n*–type dopants in ZnO.[129-131] Dopant addition is basically carried out by modifying the composition of the precursor in the evaporation–condensation process, despite the limited capability to manage the amount of dopant eventually introduced in the NWs. The significant difference between the elemental ratio in the precursor material and the composition obtained for the NWs marks a critical issue of the evaporation–condensation approach, as discussed by Nguyen

et al..[132] However, doping in the ZnO NWs/NRs in a controllable manner seems to be not easy. Most of the relevant works on the *n*–type doped ZnO NWs or NRs have the problems in controlling the morphology, structure and the composition of the nanostructures. For example, for doping of ZnO NWs/NRs with In by TVD method, a mixture of ZnO and In_2O_3 powder is always used as the starting source material. Besides the unavoidable presence of the secondary phase of In_2O_3,[131,133] changes in the morphology into various shapes such as nanobelts[133] and hierarchical structures[134] were observed. On the other hand, solvothermal and hydrothermal methods are promising for controlled stoichiometry and precise doping of the NWs.[129,135] However, finding of compatible precursor chemicals for doping is another crucial issue.

1.4. Important Applications of ZnO Nanowires/Nanorods

To date, no production–scale NW applications have reached the marketplace, but many simple device structures have been demonstrated, illustrating the possibilities that may be available in the future. Some of these are discussed below.

1.4.1. Field Effect Transistors

Electronic applications have dominated to date, driven by the need for new technology to accommodate rapid downscaling. ZnO NW field–effect transistors (FETs) with highest mobilities (μ_e=13 ± 5 $cm^2.V^{-1}.s^{-1}$) were fabricated and studied in vacuum and ambient gases from 5 to 300 K.[136] Using lithographic patterning technique, top gate electrode based ZnO NW FET (or MOSFET) was demonstrated by Heo *et al.*[137], which is shown in Fig. **1.8**. The drain current–drain voltage (I_D–V_{DS}) characteristics show typical I–V behaviour of FET. There is also report on fabrication of ZnO NW based FET in vertical geometry.[138] These devices look promising for transparent transistor based flat panel display applications. Hybrid FET based on the organic polymer, poly(3-hexylthiophene) (P3HT) and inorganic doped ZnO NW; ZnO/a–C core shell NW were fabricated successfully and investigated the charge transport behaviour.[139,140] Yet there remains a significant overall influence of the surface chemistry and physical nature of the gate voltage shielding on the transport properties of these devices, and it needs further study.

1.4.2. Light Emitting Diodes

ZnO NW based LEDs have been widely investigated. Due to the lack of *p*–type doping,

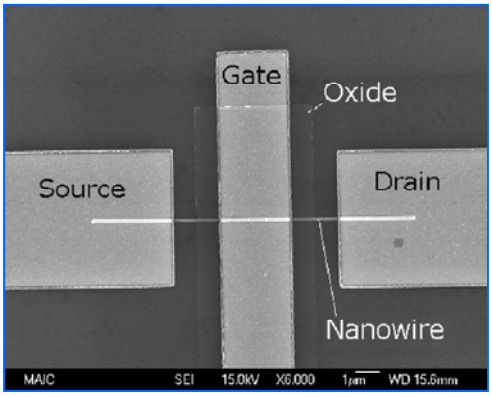

Figure 1.8: SEM image of a ZnO single NW based FET. Adapted from ref. [**137**].

there are few reports on ZnO NW homojunction based LEDs,[141,142] most of the investigations are based on hybrid structures using a polymer as the *p*–conducting material.[26,27,143-145] Strong UV electroluminescence was observed from the ZnO homo *p*–*n* junction fabricated by controlled arsenic doping process. However, obtaining of stable *p*–type conductivity in ZnO is a major issue.

On the other hand, hybrid structures offer several unique advantages: the polymers, usually applied in a liquid form, can penetrate the dense arrays of NWs and, thus, can form the junction on almost the entire NW surface. The structure also offers wavelength tunability that can be achieved by using different polymers. In addition, this technique is suitable for scaling up at low cost. Bao *et al.*[144] demonstrated a new method for achieving reliable electrical injection into single semiconductor NWs and fabricated the first ZnO single NW hybrid LED. The device structure is shown schematically in Fig. **1.9**. The *n*–type ZnO NWs is placed between a heavily doped *p*–type silicon (p-Si) wafer and a metallic thin film, serving as hole– and electron–injecting contacts, respectively. The cross–linked poly(methyl methacrylate) (PMMA) on the sides of the

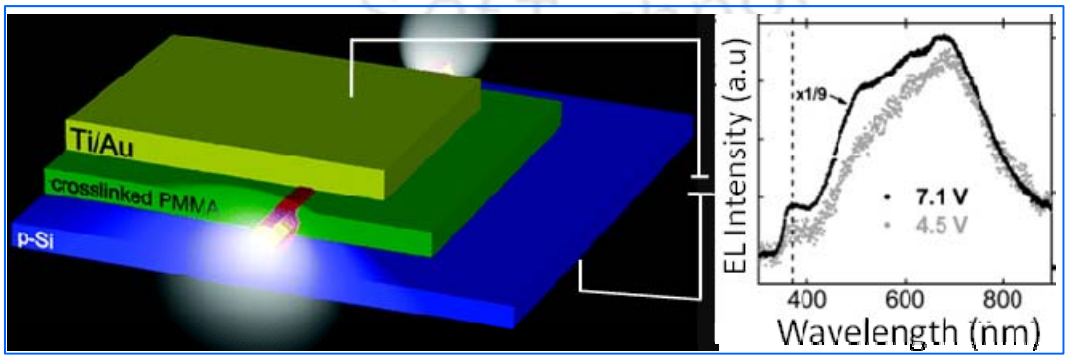

Figure 1.9: Schematic geometry of the single ZnO NW hybrid LED and corresponding electroluminescence spectra. Adapted from Ref. [**144**].

nanowire functions as an insulating layer between the two contacts, thus allowing planarization and uniform electrical injection along the NW. This device exhibits broad sub–bandgap emission at room temperature. Liu *et al.*[27] demonstrated the fabrication of hybrid LED using flexible sheets of mass produced ZnO NWs. A ZnO NW/polymer heterojunction diode based LED was presented by Shaer *et al.*.[145] The device consists of a dense array of ZnO NWs covered with hole–conducting polymer. They obtained strong broad electroluminescence almost covering the visible spectrum, with peak centre in the red region. However, the device shows negligible UV emission in EL. However, strong UV emission from a similar device was observed by Könenkamp *et al.*[146] only when the NWs were annealed prior to the device fabrication.

1.4.3. Lasers

ZnO NWs array show lasing action based on exciton recombination at room temperature due to the high exciton binding energy (60 meV), much greater than the thermal energy at room temperature (26 meV). Outer flat end face and wafer/other face contact of ZnO arrays both serve as good laser cavity mirrors. Optically pumped ZnO NW laser arrays as well as single ZnO NW lasers have been demonstrated successfully.[25,147-149] Schematic of excitation and laser output from the ZnO NWs array is shown in Fig. **1.10**. The ZnO NW array was grown on an Au–patterned a–sapphire substrate via a VLS growth mechanism. By properly controlling the growth conditions, ZnO NWs array with a high area density of 10^{10} cm^{-2} are achieved. The NWs are directly pumped by the fourth harmonic of an Nd:YAG laser at room temperature and the light emission was collected along the *c*-axis of the NWs. Figure **1.10(c)** is the emission spectra from ZnO NWs array below and above the lasing threshold. Whereas, the single NW lasing behavior is further proved by using near–field scanning optical microscopy (NSOM).[148] The emission spectrum shows that the single NW serves as an active Fabry–Perot optical cavity. The intense signal collected near the ends of the NW demonstrates the wave guided and confinement of the NW lasing emission to a cone–shaped region near the end faces. In another work Yang *et al.*[24] demonstrated high–temperature UV random laser action in ZnO nanoneedles up to 600°K. It is also reported that the changing of temperature allows "tuning" of the lasing peak energy of ZnO nanoneedles from UV to the blue spectral region. In addition, by creating *p–n* junctions in these individual NWs, one should be able to test the possibility of making electron ejection UV/blue lasers out of individual

NWs. Such miniaturized NW nanolasers will find applications in nano–photonics and microanalysis.

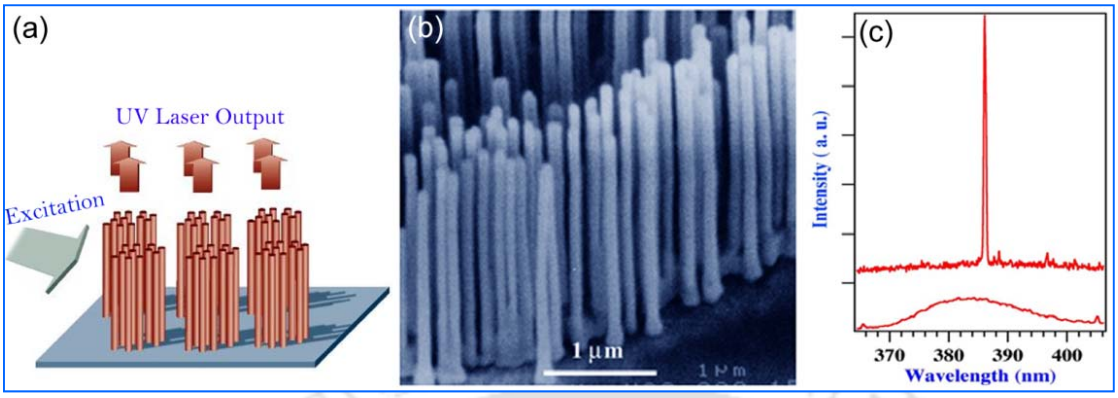

Figure 1.10: Schematic illustration of the excitation and detection configuration for stimulated emission. (a) An SEM image of aligned ZnO nanowire arrays grown on sapphire substrate coated with a 3 nm thick layer of Au. (b) Emission spectra from nanowire arrays at pump powers of 20 and 100 kW cm^{-2}. Adapted from Ref [**25**].

1.4.4. Dye Sensitized Solar Cells

One classic example of a photovoltaic device is the dye–sensitized solar cell (DSSC). DSSC follows the sequence of physical processes: (i) a light–absorbing dye generates an electron–hole pair, (ii) the electron and hole separate quickly into two different phases, and (iii) the carriers are transported in these respective phases to opposing electrodes. ZnO NWs based Dye Sensitized solar cells (DSSC) show faster operation and higher energy conversion efficiency compared to existing nanoparticles based DSSC.[28] The main advantage of single–crystalline NW is the fast electron transport across the wires and rapid collection by the anode. One further advantage is the possibility of precisely tailoring of the electronic properties of the NWs /NRs for tuning the absorption spectrum of the hybrid system of dye/NWs with the solar emission spectrum. So in DSSC nanoparticles can be replaced by vertical NWs/NRs for better efficiency.

Innovative geometries and structures are being continuously developed, such as fully–inorganic cell composed by ZnO NWs sensitized with CdSe quantum dots acting as light absorbers.[150] The schematic diagram of the quantum dots sensitized solar cell and the corresponding performance characteristics are shown in Fig. **1.11**. This cell consists of an array of ZnO NWs coupled with CdSe quantum dot. An array of ZnO NWs, grown vertically from an F–doped SnO_2/glass substrate and decorated with CdSe quantum dots, serves as the photoanode. A second F–doped SnO_2/glass substrate, coated with Pt, is the

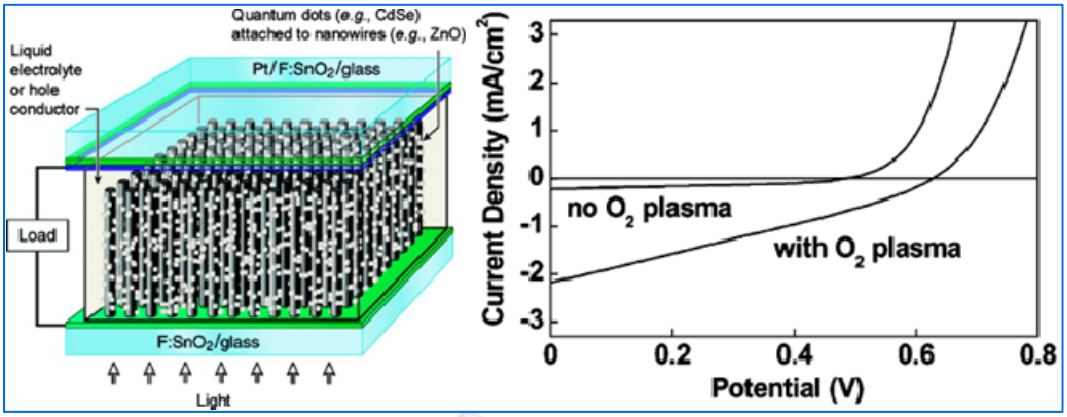

Figure 1.11: Schematic of the quantum–dot–sensitized solar cell and corresponding current–voltage performance characteristic. Here an array of ZnO NWs decorated with CdSe quantum dots is used as core materials for the current generation. Adapted from Ref. [**150**].

photocathode. The space between the two electrodes is filled with a liquid electrolyte, and the cell is illuminated from the bottom. During radiation of sunlight the current is generated in between the electrodes. This cell results in conversion efficiency of 0.4% at 100 mW/cm^{-2} light power, however it can improve be further.

Core–shell heterostructures have been utilized for DSSC. ZnO–Al_2O_3 and ZnO–TiO_2 core–shell NW based DSSC have shown an overall conversion efficiency of 2.25% under 100 mW cm^{-2} at AM 1.5 simulated sunlight.[29] ZnO–MgO core–shell NWs have shown for an almost five–fold improvement compared to pristine NW device with overall conversion efficiency of 0.33%.[151] Better electron transport in such structures is a product of their single crystalline assembly and of the presence of a radial electric field within each NW. This field assists carrier collection by repelling the photoinjected electrons from the surrounding electrolyte.

1.4.5. Photodetectors

The electronic conductivity of the ZnO NWs/NRs is extremely sensitive to ultraviolet light exposure. The light–induced change in conductivity allows us to use it as optoelectronic switch or UV photodetector. Yang group[20] first reported and patented the ZnO NW photodetectors in 2002. The single ZnO NW was first dispersed on the nonconducting substrate. After that, electron beam lithography was used to fabricate gold electrodes on top of the ZnO NW. A SEM image shown in inset of Fig. **1.12**(**a**) shows the structure of the single NW photodetector. Figure **1.12**(**a**) shows the I–V curves of the device measured in dark and upon UV light exposure, respectively. From these curves, it can be seen that the NW is highly insulating in the dark with a resistivity above 3.5

MΩcm, while the resistivity decreased by typically 4 to 6 orders of magnitude when it was exposed to UV light with wavelengths below 380 nm, resulting in a photosensitivity (defined as photocurrent–to–dark current ratio) value of 10^4. The dramatic change of conductance between dark and UV exposure suggest that the ZnO NW photodetectors are good candidates for optoelectronic switches, with the dark state as "OFF" and the UV exposed state as "ON" and the result is shown in Fig. **1.12**(**b**). It is evident that the NW photodetectors can be reversibly switched between the low and the high conductivity

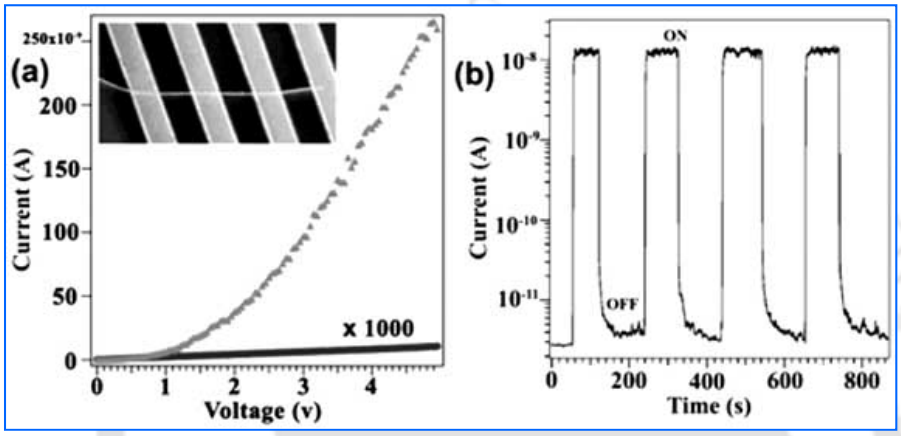

Figure 1.12: (a) I–V curves show dark current and photocurrent of a single ZnO NW under 365 nm, 0.3 $mWcm^{-2}$ UV light illumination. The inset reveals an FESEM image of a ZnO NW bridging four Au electrodes. (b) Reversible switching of a ZnO nanowire between low and high conductivity states when the UV lamp was turned on and off. Adapted from Ref. [**20**].

state. Inspired by this work, many kinds of photodetectors have been fabricated by using different one–dimensional ZnO nanostructures, which are tabulated in Table–**1.2**. The researchers also investigated about the underlying mechanism of the photoconduction behavior of the ZnO NWs.[21,152-154] The photoresponse of the ZnO NWs consists of two parts: a rapid process of photogeneration and recombination of electron–hole pairs, and a slow process of surface adsorption and photodesorption of oxygen molecules. The oxygen molecules play a key role on the conductivity enhancement. It is also found that the surrounding medium has a strong effect on the photoresponse time of the ZnO NWs.[153,155] During UV illumination, it was found that the current decreases gradually under high humidity, whereas the current increases under low humidity. In the recovery phase, a change of two to three orders of magnitude in the decay time is observed by varying the humidity. Whereas, the PC did not reached the saturation value after long time when it was measured in vacuum.[155]

Table **1.2:** The performance characteristics of one–dimensional ZnO nanostructures based photodetectors reported in the literature.

Morphology	Device Type	Detection waveleng--th (nm)	Bias (V)	Photosens itivity	Rise time (s)	Decay time (s)	Reference
Nanowire	Resistor	365	5	10^4–10^6	~1	~1	Kind *et al.* 2002[20]
Nanorods	Resistor	325	2	19	3.7	63.6	Ahn *et al.* 2004[35]
Nanowire	Resistor	254	–	66	66	115	Li *et al.*, 2004[156]
Nanowires film	Resistor	254	5	17.7	12	13	Li *et al.* 2005[152]
Nanorod	FET	254	0.2	1000	–	1800	Park *et al.*, 2005[157]
Nanowires array	Resistor	365	5	150	–	–	Hsu *et al.*, 2005[158]
Nanowires array	Resistor	370	5	1.4	.0004	–	Law *et al.*, 2006[159]
Nanowire	Resistor	300–425	10	7	–	–	Fan *et al.*, 2006[160]
Nanowire	Resistor	390	5	10^4	–	–	Soci *et al.*, 2007[21]
Nanowires array	Resistor	330	3	2000–3000	~4.1	~2.7	Bera *et al.*, 2008[154]
Nanowires	Resistor	340	1	–	170	300	Prades *et al.*, 2008[161]
Microtube	Resistor	365	5	90	5.9	638	Cheng *et al.*, 2008[162]
Nanoneedle array	Resistor	365	–	4	–	–	Park *et al.*, 2008[163]
Co doped nanobelt	Resistor	370	–	85	–	–	Peng *et al.*, 2008[164]
Nanowires	Resistor	350	5		0.7	1.4	Li *et al.*, 2009[165]
Nanowires inerdigitated	Resistor	365	5	10^4	–	–	Li *et al.*, 2009[153]
Nanowire	Resistor	365	2	8	45	55	Lin *et al.*, 2009[166]
Nanotube	Resistor	325	1	50	150	250	Chantarat *et al.*, 2009[167]
Nanorods	Resistor	360	10	80	–	–	Manekkathodi *et al.*, 2010[168]
Nanowires nanobridge	Resistor	254	3	400–1000	1.2	4.4	Huang *et al.*, 2010[169]

1.4.6. Gas Sensors

ZnO NWs gas sensors are based on the fact that conductance changes with the reversible chemisorption process of reactive gases on the surface of ZnO. ZnO NWs are considered as one of the most potential candidates for testing reductive gases due to their high sensitivity. Once adsorbed on the surface of ZnO nanostructures, the reductive gas molecules such as H_2, CO, CO_2, H_2S, NH_3 and CH_4 will react with the adsorbed O^- or O^{2-} ions and release the electrons back to the ZnO nanostructures. Because of the large specific surface area and high electron mobility, the ZnO nanostructures will adsorb a large quantity of gas molecules after exposing to the gas, resulting in a large change of conductivity. The sensor signal could be the change of resistance, current, conductivity or voltage.

Figure **1.13**(**a**) shows the schematic of reductive gas sensing process of ZnO NWs based gas sensors. The ZnO NW based CO sensor has been fabricated by Ra *et al.*[170] by using nanoscale spacer lithographic technique. The sensitivity of the above CO sensor shows much higher sensitivity than the ZnO thin film based gas sensor. The voltage change of the sensor device has been used as the sensor signal to test NH_3 gas by Li *et al.*[171] (demonstrated in Fig. **1.13**(**b**)) and H_2S gas by Zhang *et al.*.[172] The ZnO NWs based gas sensors are also successfully used for the detection of several oxidative gases, e.g. NO_2, NO, O_3 and O_2, and chemical gases, e.g. methanol, ethanol, acetone, butane, dimethylamine, triethylamine, chlorobenzene and LPG.[5]

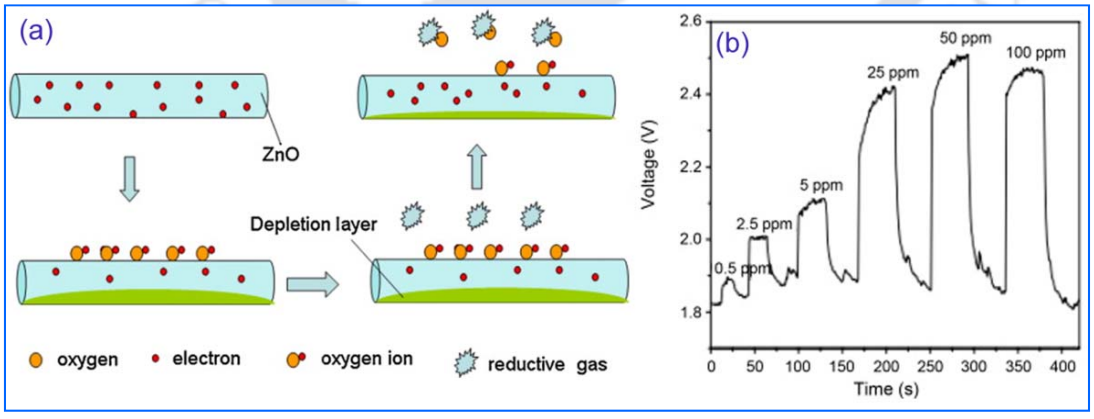

Figure 1.13: (a) The schematic image of the reductive gas sensing process of ZnO NWs based sensors. (b) Signals of the ZnO nanostructures based gas sensor to NH_3 gas. Adapted from Ref. [**5**].

Due to the biocompatibility, stability, and high isoelectric point, ZnO nanostructures have been used widely in the biological detection, such as in the detection of urea,[173]

DNA sequence,[31] and glucose.[30] The enzyme or DNA segments used as the detecting elements are immobilized on the surfaces of ZnO which serve as the nanoscale platforms and then the testing signal can be transformed into surface plasmon resonance, fluorescence, electrochemical or the field emitter signal.[5]

1.4.7. Nano Generator

The lack of a centre of symmetry in wurtzite structure, combined with large electromechanical coupling, results in strong piezoelectric and pyroelectric properties and the consequent use of ZnO as a piezoelectric nano generator. The tetrahedral coordination in ZnO results in noncentral symmetric structure and consequently piezoelectricity, when it was deflected by an atomic force microscopy tip.[23]

Wireless devices may allow in–situ, real–time biomedical monitoring and detection, but such devices still requires a power source. Ideally, such devices should be self–powered rather use a battery. The body provides numerous potential power sources–mechanical energy, vibrational energy, and chemical energy (glucose), but the challenge is their efficient conversion into electric energy. If accomplished on the nanoscale such power sources could have greatly reduced the size of the integrated nanosystems for optoelectronics, biosensors, resonators and more.[174-176] Wang group has demonstrated an approach of converting mechanical energy into electric power using aligned ZnO NWs.[22] The device geometry and corresponding output voltage is shown in Fig. **1.14**. Due to the insufficient power production by a single NW they used vertical and lateral integration of ZnO NWs arrays that are capable of producing sufficient power to operate real devices.

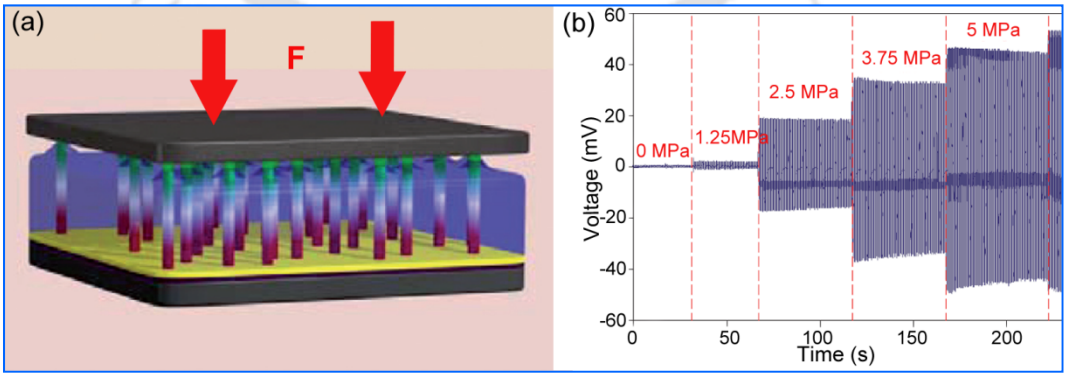

Figure 1.14: (a) Schematic image of vertical NWs array integrated nanogenerator and (b) magnitude of the output voltage as a function of the magnitude of the compressive stress at a frequency of 2 Hz. As the applied stress is gradually increase from 0 to 1.25, 2.5, 3.75, and then 5 MPa, the output voltage increases almost linearly. Adapted from Ref. [**177**].

When a uniaxial stress is applied at the top electrode, the NWs are readily compressed, the straining of the crystallographically aligned NWs generating a macroscopic piezoelectric potential along the *c*–axis of the NWs. A vertical integration of three layers of ZnO NWs arrays produces a peak power density of 240 mV. Whereas, a lateral integration of 700 rows of ZnO NWs produces a peak voltage of 1.26 V at a low strain of 0.19%, which is potentially sufficient to recharge an AA battery. Later this group got major success towards the fabrication of self–power devices by integrating this nano generator to a nanoscale gas sensor devices.[177]

1.5. Challenges in ZnO Nanowire based Photodetectors

High photosensitivity and selectivity, faster response and reset times, and reproducible characteristics are the basic requirements for an efficient photodetector.[178,179] Since the first report on UV photodetection from single ZnO NWs by Kind *et al.*[20], many efforts have been made on one–dimentional ZnO nanostructures, including NWs to improve the photodetection and photoresponse behaviours.[35,152,180-184] However, there are still a lot to be done to address the challenges that remain. The photosensitivity and photoresponce time of the ZnO NWs based photodetectors will require significant improvements in order to meet future demands in variety of fields. From the studies, it is found that the single ZnO NW based devices have comparatively faster response. However, due to low PC it does not find applications in the real world. Fabrication of photodetectors by using large numbers of ZnO NWs could be an alternative; however, integration and collective electrical contacts to a large number of NWs is a crucial issue.[169,185] As the photodetection and photoresponse of the ZnO NWs depends on the surface condition, structural quality and rate of oxygen adsorption and photodesorption.[152-154,186] Therefore, it is expected that surface modification or structural improvement, heterostructures can enhance the photosensitivity as well as photoresponse. The assembling of one–dimensional nanostructures via a simple and effective method for real device applications is another important issue.[7,179]

In the steps towards this goal, very recently few groups have reported enhanced photodetection behaviours from the ZnO NWs heterostructures, which are summarized in Table **1.3**.[36,106,187,188] Several types of approaches have been reported e.g. structural improvement, efficient doping, and heterostructures formation with suitable external materials. Zhou et al.[182] used nonsymmetrical Schottky–type contact devices and

obtained higher sensitivity and faster reset time. Pt microelectrode arrays were first fabricated on a SiO_2 /Si substrate by UV lithography to make Schottky–type contact on one end of the NWs and a focused–ion–beam (FIB) deposited Pt–Ga electrode on other end of the ZnO NW for a good Ohmic contact. He and coauthors[18] utilized FIB technique to deposit Pt metal on ZnO NWs to effectively reduce the contact resistance, and thus achieved high photoconductive gain as high as 10^8. Chang *et al.*[36] reported the synthesis of a ZnO NR/graphene heterostructure by a facile *in situ* solution growth method. By combining the attributes of photosensitive ZnO NRs and highly conductive graphene, they are able to fabricate a highly sensitive visible–blind ultra UV sensor. Recently, Park and coauthors obtained enhanced photoresponse from isopropyl alcohol treated ZnO NW devices by introducing surface roughness induced traps.[180] They propose that obtained enhancement is attributed to an increase in adsorbed oxygen on roughening induced surface traps. We have shown that a five–fold enhancement of photosensitivity in the UV region and faster photoresponse could be obtained from the ZnO NWs by structural improvement using RTA processing.[189] Radial NW heterostructures with external inorganic or organic materials, e.g. lysine,[106] poly(vinyl alcohol),[105] anthracene,[190] polyacrylonitrile[191] and polystyrene sulfate[192] have also been utilized to improve the photodetection behaviours of the ZnO NWs based photodetectors. These heterostructures based photodetectors show higher photosensitivity and comparatively faster photoresponse.

However, the selection of right material for the fabrication of ZnO NWs heterostructures and understanding the origin of improvement in the photodetection behaviours are the big challenges to the researchers. It should be mentioned that, till now, the lack of well–established fabrication method and standard characterization procedures make it difficult to compare the experimental results between different devices.

1.6. Focus of the Present Thesis

This thesis focuses on the growth of vertically aligned high quality ZnO NWs and NRs arrays over large area and fabrication of ZnO NWs based heterostructures for efficient UV photodetection. We have grown and characterized varieties of ZnO NWs and NRs, and systematically studied the effect of growth parameters to achieve control over the shape, size and orientation. ZnO NWs and NRs are grown by vapor transport method using a home–built thermal vapor deposition system and by an aqueous chemical method

Table **1.3:** The photosensitivity improvement factors of the ZnO NRs/NWs based efficient photodetectors reported in the literature and in this thesis.

Morphology	Device Type	Detection wavelen--gth (nm)	Bias (V)	Maximum Photosensitivity	Photosensitivity enhancement factor from unmodified photodetector	Reference
Nanowire	*p–n* homojunction	325	3	32000	–	Li *et al.*, 2009[193]
Nanowires array	Resistor	325	3	18000	~2.6	Bera *et al.*, 2009[105]
Nanowires array	Resistor	360	3	10^4	~2.8	Bera *et al.*, 2009[155]
Nanowire	Resistor	365	1	1500	~4	Zhou *et al.*, 2009[182]
Nanowire	Resistor	254	4	1800	~9.4	Lin *et al.*, 2009[194]
Nanowires array	Resistor	370	3	3367	`~5.2	Bera *et al.*, 2010[107]
Nanowires film	Resistor	365	8	–	~4.7	Liu *et al.*, 2010[106]
Nanowire (strained)	Resistor	372	-5	18000	~2	Yang *et al.*, 2010[187]
Nanowires array	Resistor	369	2.5	24200	~5.4	Present work Dhara *et al.*, 2011[189]
Nanorod	Resistor	370	20	–	~3.0	Chang *et al.*, 2011[36]
Nanowires	*n-i-n* junction	365	-5	1345	–	Kim *et al.*, 2011[183]
Nanowires array	Resistor	360	5	7600	~2.2	Bera *et al.*, 2011[181]
Nanowire	FET	365	0.4	10^6	~1.8	Park *et al.*, 2011[180]
NWs network	Resistor	254	5	52	~3	Kim *et al.*, 2011[184]
Nanowires array	Resistor	365	3	2937	~7	Present work Dhara *et al.*, 2011[114]
Nanowires array	Resistor	360	3	4000	~6	Present work Dhara *et al.*, 2012[190]
Al doped Nanowires network	Resistor	365	3	300	~6.4	Present work Dhara *et al.*, 2012[195]

using an autoclave. Morphology and microstructures of the NWs and NRs are studied in detail by using several scientific tools, e.g., FESEM, TEM, X–ray diffractometer, micro–Raman spectrometer. The optical absorption and PL measurements are also performed to explore the suitability of these nanostructures for the use in laser or LED as well as to identify several radiative surface defects present on the as–grown ZnO NWs and NRs. The photodetection properties of the ZnO NWs are also carried out by measuring the photoresponse and wavelength dependent photocurrent for the use in UV photodetectors. From these studies, several new results have been obtained. A new growth strategy has been shown for the growth of vertically well–aligned ZnO NWs and NRs arrays. In the study of effects of growth conditions and source materials, we observed nanostructures shape evolution for the first time and a detail investigation was done to find out the origin of this shape evolution. The origin of the visible emission in the PL spectra is directly correlated with the several surface defects present on the as–grown NWs/NRs. To improve the structural quality as well as the UV emission efficiency, a simple and effective, post–growth rapid thermal processing technique has been employed to the as–grown one–dimensional ZnO nanostructures.

For the first time, we report on the very high photosensitivity and improved photoresponse from the post–growth processed ZnO NWs without making any complex structure. For the fabrication of the high sensitive and ultrafast UV photodetectors, we prepared different new types of ZnO NWs heterostructures with different materials and characterized for the applications in UV photodetection. These heterostructures show very large improvement in the photosensitivity and photoresponse time, which are the essential requirements for the efficient photodetectors. The origin of this improvement from these heterostructures is studied systematically and explained in details.

1.7. Organization of the Thesis

The thesis work is presented in seven chapters. This chapter has given an introduction to the studies on the growth and important applications of ZnO NWs and NRs and the motivation of the present work. The next chapter describes the details of the several in–house developed and commercial experimental techniques used for the growth and characterization of the ZnO NWs and NRs. In the chapter 3, several approaches of the strategic growth methods of well–aligned ZnO NWs and NRs and their micro–structural characterization are discussed. Chapter 4 and 5 present the significant results on the

optical absorption, PL and photodetection properties of the ZnO NWs and NRs. And an improvement strategy for the UV PL and the photodetection behavior is also presented. Chapter 6 deals with the fabrication, characterization and photodetection behaviours of the several new types of ZnO NWs based heterostructures. The last chapter, Chapter 7 summarizes the new findings and important conclusions of the present study followed by the scopes for further works on this topic.

Chapter 2
Experimental Techniques and Data Analysis

In this chapter, brief information about the experimental techniques developed/used for the present work is discussed. The design and in–house development of the thermal vapor deposition system and photoresponse measurement system are presented in detail. The growth methodology of ZnO NWs and NRs used in this study is discussed in details. For the characterization of the NWs and NRs, several standard analytical and spectroscopic techniques are used, which are presented in this chapter. The methodology adopted to analyze the data of the NWs/NRs is also described in details.

2.1. Growth Techniques of ZnO Nanowires and Nanorods

For the growth of the ZnO NWs and NRs, we used so called *bottom–up* approaches. The ZnO NWs and NRs are grown by two different techniques: (i) vapor phase method using thermal vapor deposition (TVD) system, and (ii) aqueous chemical method using an autoclave. For the vapor phase growth, we designed and developed the TVD system in our laboratory. For the chemical growth, commercially available Teflon coated stainless steel autoclave (Heidolph, Germany) is used. ZnO powder is used as the source of ZnO in vapor phase growth, while zinc nitrate is used as precursor in chemical growth process. We varied several growth parameters during the growth of the NWs/NRs and studied the morphology and orientation of the NWs/NRs, which are described in details in Chapter 3.

2.1.1. Design and Development of Thermal Vapor Deposition System

Vapor phase growth by using TVD system is a widely used technique for the growth of

one–dimensional ZnO nanostructures. For our present study we designed and developed a TVD system in our laboratory. Photograph and schematic diagram of this system is shown in Fig. **2.1**. It consists of a horizontal muffle furnace, a closed cylindrical quartz/alumina tube with vacuum accessories and gas flow option through a mass flow controller. One side (inlet) of the quartz/alumina tube is connected to the Ar gas cylinder through a mass flow controller (MFC) and other side (outlet) is connected to the rotary pump as exhaust side. The whole system is placed inside the split type horizontal muffle furnace. The chamber pressure is monitored using a pirani gauge connected to the tube at the exhaust side. We achieved a chamber base pressure of 16×10^{-3} mbar without any flow of Ar gas. During the flow of Ar gas, i.e. during the deposition the chamber pressure is fixed to a desired value using a gate valve connected at the mouth of the rotary pump.

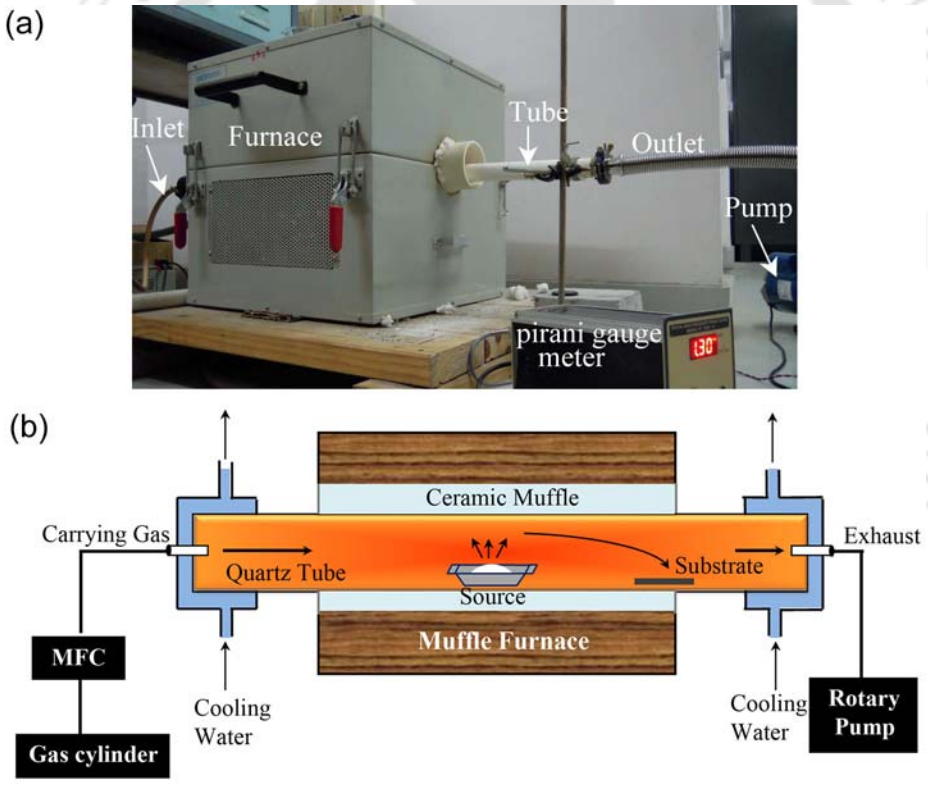

Figure 2.1: (a and b) Photograph and schematic diagram of the in–housed developed thermal vapor deposition setup, respectively.

The temperature profile of the furnace measured from the centre position of the furnace is shown in Fig. **2.2**. The temperature gradient shows a Boltzmann type profile. Here the source material is placed in a quartz boat and this boat is placed inside the chamber where temperature is maximum. The substrates are placed in downstream direction at

the elevated temperature regions which is a few cm apart from the centre positions. The temperature ramping rate of the furnace was maintained at a fixed value of 15°C/min. When the temperature of the furnace is reached the maximum set value, the ZnO powder vaporizes and it is carried by the carrier gas (Ar) to the substrate positions. The flow of the carrier gas is controlled precisely by using a mass flow controller (Sevenstar, China). During the process, the Zn/ZnO vapor is sufficiently reacted with the substrate and condensed, which results in the growth of ZnO NWs/NRs.

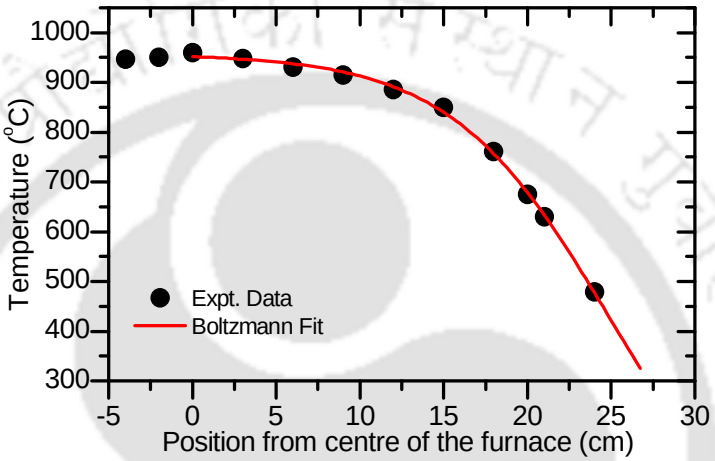

Figure 2.2: Temperature profile of the high–temperature furnace used in thermal vapor deposition setup. Temperature is monitored inside the chamber using a *K*–type thermocouple.

2.1.2. DC and RF Magnetron Sputtering

Magnetron sputtering deposition is a useful technique for the preparation of good quality crystalline thin films. We used this technique for the preparation of good quality ZnO seed layer and Au layer on the Si substrate. The photograph of the magnetron sputtering system is shown in Fig. **2.3**. The magnetron sputtering system consists of a high vacuum chamber, magnetron head (Angstrom Science, USA) along with the holder of the target material, 13.56 MHz radio frequency (RF) source (Comdel, USA)/high voltage DC source (Aplab, India) and a substrate heater assembly (Hindhivac, India). The magnetron sputtering is the process of ejection of atoms by ionic bombardment under the magnetic field and RF/DC source. Here crossed electric and magnetic field lines are created by alternate arrangement of permanent magnet pole assembly and DC/RF source. Magnetic field lines form a closed path on the target (material to be deposited) surface which confines more and more electrons on the surface causing ionization. Due to mobility differences between electrons and ions target surface have negative potential. Then ions

are accelerated towards the target and ejecting surface atoms from the target. Then these atoms move towards the substrate by electric field and then condensed on the substrate surface resulting in a thin film. In the DC magnetron sputtering, the target material is connected to the negative terminal of the DC source and operates in the range 300–1000 V. Whereas in case of RF magnetron sputtering, the target is connected to the RF source and operates in the range of 50–200 W.

Figure 2.3: Photograph of the magnetron sputtering system (Hindhivac, India) used for the preparation of high quality ZnO seed layer.

2.1.3. Growth of Nanowires and Nanorods by Vapor Deposition

In this section, we will present the detailed description of the growth of ZnO NWs and NRs which were grown by vapor deposition process over a range of temperature. We have attempted to grow vertically aligned ZnO NWs and NRs by this method. To get well–aligned vertical orientation of the NWs/NRs, we studied the effects of several growth parameters on the morphology of the as–grown products. The growth of NWs/NRs by vapor deposition process includes substrate cleaning, substrate preparation and vapor deposition processes.

A. Substrate Cleaning: The substrate used for the growth of the NWs/NRs throughout the present work is commercially available nominally *n*–type doped Si (100) wafer (University wafers, USA). Si wafer was first cleaned in acetone and then trichloroethylene under ultrasonic bath for 15 mins each to remove impurities and organic grease. The native oxide layer was etched out with 10% hydrofluoric acid

solution for 60 sec. After each step, substrate was rinsed with de–ionized water several times and finally dried with N_2 gas blow.

B. Substrate Preparation: For self–catalytic as well as for metal catalytic growth of NWs/NRs, we used very thin layer of ZnO for self–catalytic and Au for metal catalytic growth. ZnO seed layer was deposited on the pre–cleaned Si(100) substrates by using the RF magnetron sputtering system. Sputtering was carried out at incident RF power of 100 W for different time duration at substrate temperature of 300°C. A mixture of argon and very low concentrated oxygen were used as reacting gases during sputtering. Prior to deposition, the chamber was evacuated to high vacuum at a base pressure of 4×10^{-6} mbar. During deposition, the chamber pressure was maintained at a fixed value of 0.008 mbar. For self–catalytic growth of ZnO NWs about 200 nm thick ZnO seed layer was used. The thickness of the deposited layer was estimated from the deposition rate and further confirmed from surface height profile measurement (Dektak 150, Veeco, USA). A very thick layer of 35 μm ZnO seed layer was used for the growth of ZnO NRs with comparatively larger diameter. On the other hand, for the preparation of the ultrathin Au layer a mini sputtering system (SC7620, Polaron, UK) with fixed bias of 1kV was used. The Au sputtering was carried out in vacuum at a current of 5 mA for 60 sec. In this process, about 2 nm thick Au layer was deposited on the cleaned Si substrates.

C. Vapor Deposition: For the growth of ZnO NWs and NRs by vapor deposition method, we used ZnO bulk powder (Sigma–Aldrich, USA, purity 99.999%) as the source material for vapor. ZnO nano powder (Sigma–Aldrich, USA, purity 99.999%, average size 50–70 nm) source is also used to study the effect of source powder on the morphology of the final products. As the melting point of ZnO is very high (1975°C), we used high quality graphite powder (Fluka, USA, purity 99.99%,) as the reducing agent. Therefore, mixture of ZnO and graphite powder is loaded at the centre positions of the furnace inside the TVD chamber. During heating, a carbothermal reaction takes place which produces zinc and zinc suboxide vapor in the temperature range 900–1000°C. This vapor is transported by carrier gas, Ar to the elevated temperature regions. Then the vapor mixture was deposited on the substrate. The chamber pressure was maintained at 1.3 mbar during the growth. In this case, at high temperature the molten Au catalyst or ZnO seed layer absorbs the incoming vapor and after condensation growth of NWs/NRs

has been started. Prolonged condensation results in the growth of vertically aligned ZnO NWs/NRs.

D. Rapid Thermal Annealing: To improve the structural quality of the as–grown ZnO nanostructures thermal annealing is one of the routes. Conventional furnace annealing (CFA) and rapid thermal annealing (RTA) are often used for improving the material properties. But RTA provides certain advantages over CFA.[196] Relatively long thermal cycles of CFA may cause certain impurities to activate and they may be diffused into the material under study which is undesirable. Whereas, in RTA this possibility is much reduced because of its lower thermal cycles, which is of the order of minutes rather than hours of furnace annealing. Therefore, we performed RTA to improve the structural properties by using a mini lamp annealer (Mila 3000P, ULVAC, Japan) and study the influence of RTA treatment on the structural and optical properties of ZnO nanostructures. Figure **2.4** shows the photograph of the compact table top mini lamp annealer. This system is build around a gold reflector infrared lamp furnace and contains a high precision programmable temperature controller. This system can perform up to a maximum heating rate of 50°C/sec. This system also has option for annealing in vacuum and gas feeding. We performed the RTA in argon gas medium in the temperature region 700–800°C. The heating and cooling rate was fixed at a value of 30°C/sec.

Figure 2.4: (a) Photograph of the table top RTA setup, and (b) magnified view of the sample holder.

2.1.4. Low Temperature Chemical Growth of Nanowires

For the low temperature growth of the ZnO NWs, we utilized the aqueous chemical growth technique. In this case, chemical reactions take place in a reversible equilibrium condition, and the driving force is the minimization of the free energy of the entire

reaction system.[197] When a ZnO nucleus is newly formed, owing to the high energy of the polar surfaces [±(0001)], the incoming precursor molecules tend to favorably adsorb on the polar surfaces. However, after adsorption of one layer of precursor molecules, the polar surface transforms into another polar surface with inverted polarity.[198] For instance, a Zn^{2+}–terminated surface changes into an O^{2-}–terminated surface, or vice versa. Such a process is repeated over time, leading to a fast growth along the ± <0001> directions. This is essentially how the NWs are formed. We used zinc nitrate [$Zn(NO_3)_2$] as precursor and hexamethylenetetramine (HMT) to control the reaction and anisotropic growth. The chemical reaction is carried out in presence of water using a stainless steel autoclave with teflon lining in the reaction flask. The photograph of the autoclave used in this study is shown in Fig. **2.5**. HMT plays two essential roles: first, it produces a basic environment that is necessary for the formation of $Zn(OH)_2$; second, it coordinates with Zn^{2+} and thus stabilizes the aqueous Zn^{2+}. Then $Zn(OH)_2$ dehydrates into ZnO when heated in an oven. In the present case, the reaction was carried out at a fixed temperature of 90°C for one hour. During the hydrolysis of zinc nitrate and HMT, following reactions take place.

$Zn(NO_3)_2 \leftrightarrow Zn^{2+} + 2NO_3^-$

$HMT + 6H_2O \leftrightarrow 4NH_3 + 6HCHO$

$NH3 + H_2O \leftrightarrow NH4^+ + OH^-$

$Zn^{2+} + 4NH_3 \leftrightarrow [Zn(NH_3)_4]^{2+}$

$Zn^{2+} + 2OH^- \leftrightarrow Zn(OH)_2$

$Zn(OH)_2 \leftrightarrow ZnO + H_2O$

Figure 2.5: Photograph of the stainless steel autoclave with hot plate heater.

2.2. Characterization Techniques

After the growth of the NWs and NRs, several scientific tools have been utilized to characterize the samples. For analytical characterization, field emission scanning electron microscopy (FESEM), transmission electron microscopy (TEM) and x–ray diffraction (XRD) techniques are used to know the morphology, orientation, structure and crystal phase of the ZnO NWs and NRs. For spectroscopic study, we used micro–Raman spectroscopy, UV–Vis spectroscopy, photoluminescence (PL) spectroscopy, Time–resolved PL spectroscopy (TRPL) and Fourier Transform Infrared Spectroscopy (FTIR).

2.2.1. Analytical Techniques

In this section we will present the brief description of the tools used for the analytical characterization of the NWs and NRs. Sample preparation for imaging as well as for specific measurements are also discussed in detail.

A. Field–Emission Scanning Electron Microscopy (FESEM): The FESEM is a very useful tool for high resolution surface imaging in the fields of nanomaterials science. The FESEM use a field of electrons to probe objects on a very fine scale. The use of electrons has two main advantages over optical microscopes: much larger magnifications are possible since electron wavelengths are much smaller than photon wavelengths and the depth of field is much higher. The electron wavelength λ_e depends on the electron velocity v or the accelerating voltage V as

$$\lambda_e = \frac{h}{mv} = \frac{h}{\sqrt{2qmv}} = \frac{1.22}{\sqrt{V}} \text{ nm} \qquad \text{.....(2.1)}$$

The photograph of the FESEM (Sigma, Zeiss, Germany) used in the present study is shown in Fig. **2.6**. In the FESEM, field emission gun is used which utilizes field–emission effect. Field emission is the emission of electrons from the surface of a conductor caused by a strong electric field. An extremely thin and sharp tungsten needle (tip diameter 10–100 nm) works as a cathode. The FE source reasonably combines with conventional scanning electron microscope (SEM). The acceleration voltage between cathode and anode is commonly in the order of magnitude of 0.5 to 30 kV, and the apparatus requires an extreme vacuum (~10^{-9} torr) in the column of the microscope. After the emission, the electrons are then accelerated off of the source by two anodes.

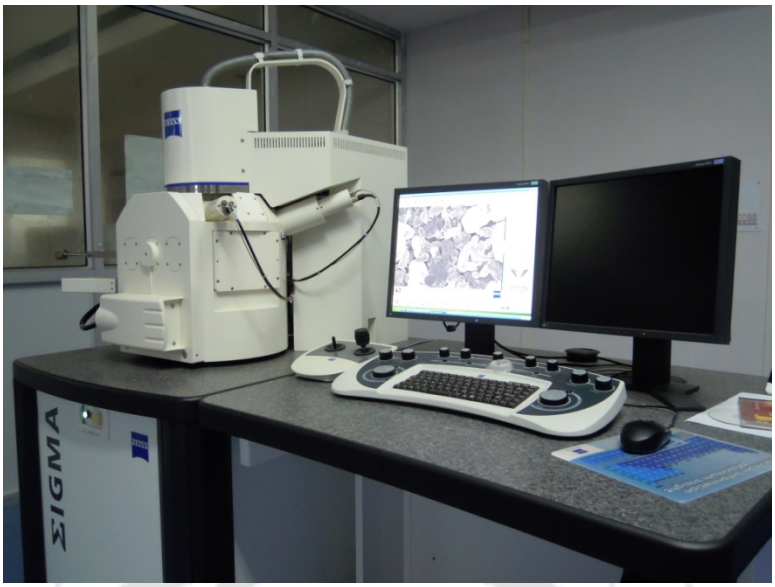

Figure 2.6: Photograph of the field emission scanning electron microscope (Sigma, Zeiss, Germany) used for the morphological characterization of the NWs.

Because of the microscopic size of the electron source, the beam produced by this emitter is about 1000 times smaller than that in a standard SEM, which markedly improves the image. That beam is collimated by electromagnetic condenser lenses, focused by an objective lens, and scanned across the surface of the sample by electromagnetic deflection coils. The primary imaging method is by collecting emitted secondary electrons that are released by the sample. A secondary electron detector is placed near to the specimen. By correlating the sample scan position with the resulting signal, an image is formed on the screen that is strikingly similar to what would be seen through an optical microscope. The FESEM is equipped with a special objective or focusing lens that projects the magnetic field below the lens. Very high resolution is obtained by shortening the specimen–lens distance and using a specially designed in–lens. The distance is shorten by placing the specimen in the lens magnetic field. In this case, secondary electron detector is placed above the objective in–lens (called as in–lens detector), which makes different in the image compared to the conventional image of the secondary electron detector. Very high resolution and contrast can be obtained by using in–lens detector.

For the sample preparation of the FESEM imaging, Si substrate containing NWs was directly mounted on the FESEM stub using a carbon coated tape. Here the carbon tape is used as adhesive and also provides an electrical conduction to the sample.

B. Transmission Electron Microscopy (TEM): TEM is one of the best characterization techniques of nanophase materials with resolution close to atomic level. By combining TEM with selected area electron diffraction (SAED) pattern, a wealth of information, such as NWs growth direction, defect or dislocation, crystallinity, and lattice constants can be studied. A schematic diagram of a TEM is shown in Fig. **2.7**. It works on the principle of optical projection; when an object is placed in front of a light source, its image is enlarged and shadow is created on the screen placed far distance behind this object. Electrons emitted from an electron gun are accelerated to high voltages (typically 100 to 400 kV) and focused on the sample by the numbers of condenser lenses.[199] We used a lanthanum hexaboride (LaB_6) crystal for thermionic electrons emission. The emitted electrons pass through a series of lenses to be focused and scanned across the sample. The sample is placed on a small copper grid a few mm (~ 3mm) in diameter. The static beam has a diameter of a few microns. The sample must be sufficiently thin (a few tens to a few hundred nm) to be transparent to electrons. The transmitted and forward scattered electrons form a diffraction pattern in the back focal plane and a magnified image in the image plane. With additional lenses, either the image

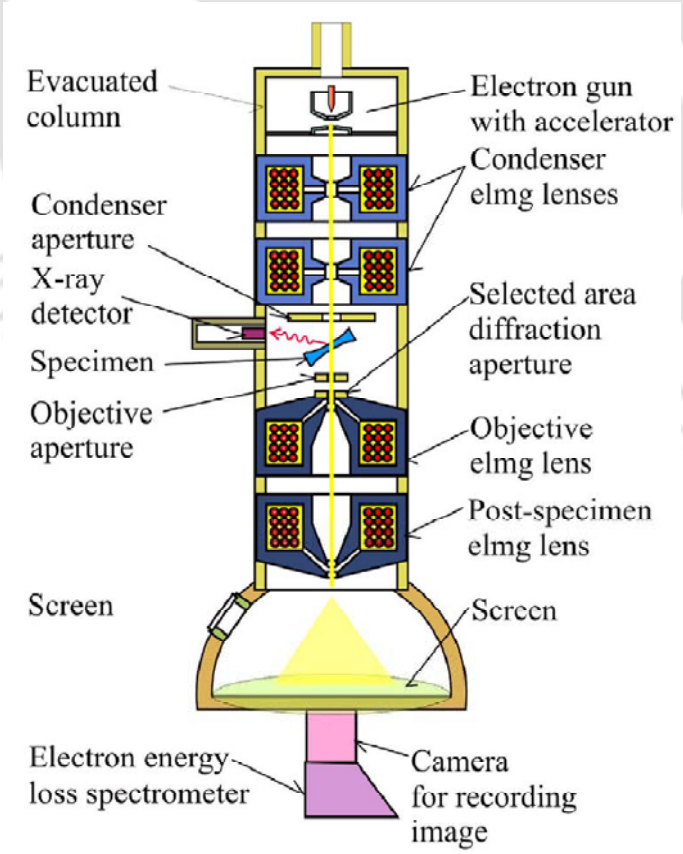

Figure 2.7: Schematic diagram of the transmission electron microscopy used for the structural characterization of the NWs.

or the diffraction pattern is projected onto a fluorescent screen for viewing or photographic recording. High resolution TEM (HRTEM) gives structural information on the atomic size level, is known as *lattice imaging,* and has become very important to know the NWs growth direction, lattice parameters and presence of any defects/dislocations.

In the present study, a 200kV TEM (JEM2100, JEOL, Japan) with high resolution CCD camera (Gatan, USA) is used for the normal TEM and HRTEM imaging. Sample for the TEM imaging was prepared by transferring the NWs in to a methanol solution. A transparent dispersion of NWs was made by sonication and then drop casted on the carbon coated copper grid containing few hundreds of square shaped hollow meshes with dimension of 1μm. After normal dry for prolong time this grid is used for TEM imaging. Improved resolution of the lattice image is obtained after processing of fast Fourier transformation (FFT) using '*Digital Micrograph* (Gatan, USA)' image analysis software. In addition, we used SAED to get information about crystallinity and growth direction of the ZnO NWs.

C. X–ray Diffraction (XRD): XRD is the most widely used non–destructive technique for general crystalline material characterization. The XRD patterns provide information on crystal phase, lattice parameter, strain and preferred growth direction of the NWs. In XRD a collimated beam of x–rays, with wavelength λ=0.5–2.0Å**,** is incident on a specimen and is diffracted by the crystalline phases in the specimen according to 'Bragg's law',

$$2d\sin\theta = n\lambda \qquad \text{.....(2.2)}$$

where d is the spacing between atomic planes in the crystalline phase, θ is the angle of incidence of the x–ray beam with the atomic plane, n represents the order of diffraction (we consider only the first order diffraction, n =1). The intensity of the diffracted x–rays is measured as a function of the diffraction angle 2θ and the specimen's orientation. In the present study, the Seemann–Bohlin geometry is used,[200] where the incident x–rays impinge on a fixed specimen at a small angle 1–5° and the diffracted x–rays are recorded by a detector that moves along the focusing circle. This method provides good sensitivity for thin films, due to parafocusing and the large diffracting volume. Owing to the huge data bank available from JCPDS Powder Diffraction Files[201] covering practically every phase of every known material, crystal phase of the sample is identified from the peak

positions of the diffractogram. Homogeneous or uniform elastic strain in the (hkl) direction can also be calculated from the shift in the diffraction peak positions, and the d_{hkl} spacing of the unstrained crystal.

X–ray diffraction patters of the NWs were obtained using a commercial XRD (Seifert 3003 T/T, GE, USA) using a Cu$K\alpha_1$ (λ=1.5406 Å) radiation or Mo X–ray radiation (λ=0.7093Å) with nickel filter. A photograph of the XRD machine is shown in Fig. **2.8**. All the data are taken at room temperature in thin film mode at a grazing angle of 3°. All

Figure 2.8: Photograph of the x–ray diffractometer (Seifert 3003 T/T, GE, USA) used for the structural characterization of the NWs.

measurements were carried out at an accelerated voltage of 40 kV and tube current of 30 mA. The scanning step size and sampling time were 0.05 and two second, respectively. The exact peak position and FWHM of the XRD peak is obtained from the Lorentzian fitting to the experimental peak position, using following expression

$$y = y_0 + \frac{2A}{\pi}\frac{w}{4(x-x_c)^2+x^2} \quad \text{.....(2.3)}$$

Where y_0 is the offset constant, x_c, w and A are the peak position, FWHM and area, respectively. FWHM gives the crystallite size and lattice strain is calculted from the shift in x_c from the x_c in unstrained sample.

2.2.2. Spectroscopic Techniques

In this section we will present a brief description of the tools used for the spectroscopic characterization of the NWs and NRs. The spectroscopic data analysis techniques used in the present study is also discussed.

A. Micro–Raman Spectroscopy: Micro–Raman spectroscopy is a vibrational spectroscopic technique use to characterize many properties (such as crystallinity, strain, and oxygen vacancy) of ZnO bulk and nanostructures. It is based on the Raman scattering process that corresponds to the interaction between incident photons and the optical phonons. During Raman spectroscopy measurement, an intense laser beam is incident on the sample through a commercial microscope with spot size about few microns. The weak back–scattered light or signal from the sample is passed through a double monochromator to reject the Raleigh scattered light and the Raman–shifted wavelengths are detected by a photodetector or CCD detector. The lines become very broad for amorphous semiconductors, allowing a distinction to be made between single crystal, polycrystalline, and amorphous materials. Raman spectral profile contains information about structure, crystallinity, strain and phonon confinement effects in NWs. The frequency of the Raman signal is also shifted by stress and strain in NWs. Both compressive and tensile stress can be determined with compressive stress giving an upward and tensile stress a downward shift compared to the peak position of the unstrained crystal.

We used a high resolution micro–Raman ((LabRAM HR–800, Jobin Yvon, USA) with liquid nitrogen cooled CCD detector. The photograph of the micro–Raman setup used in the present study is shown in Fig. **2.9**. All the measurements are carried out at room temperature using a 488 nm Ar^{+} laser at a resolution of 0.3 cm^{-1}. The laser power at the sample side was fixed at approximately 0.9 mW.

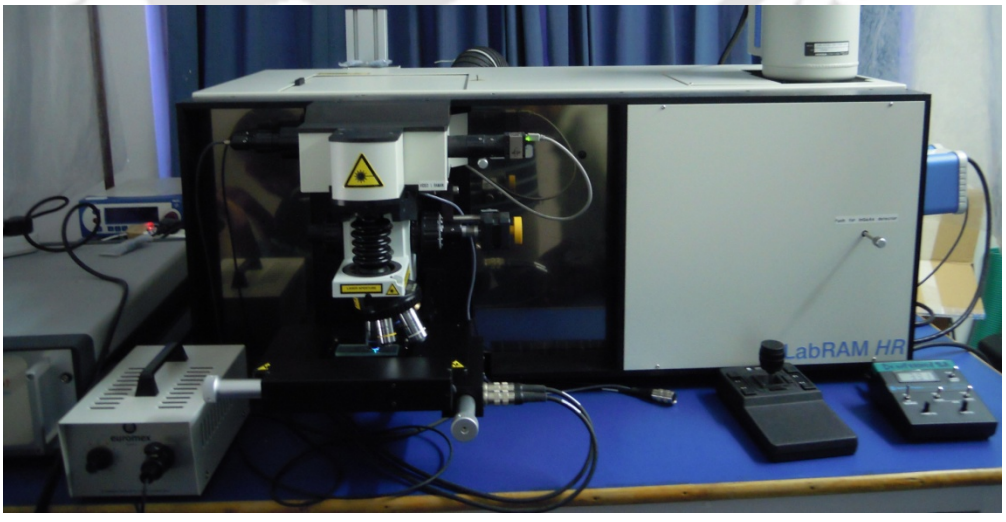

Figure 2.9: Photograph of the micro–Raman spectrometer (LabRAM HR–800, Jobin Yvon, USA).

ZnO in hexagonal wurtzite structure belongs to the space group $P6_3mc$ which has two formula units in the primitive cell. For a single crystalline ZnO, at Γ point of the Brillouin zone, it has eight sets of optical phonon modes,[202] which is shown in phonon dispersion curve of pure hexagonal ZnO in Fig. **2. 10**. They are $A_1 + E_1 + 2E_2$ modes

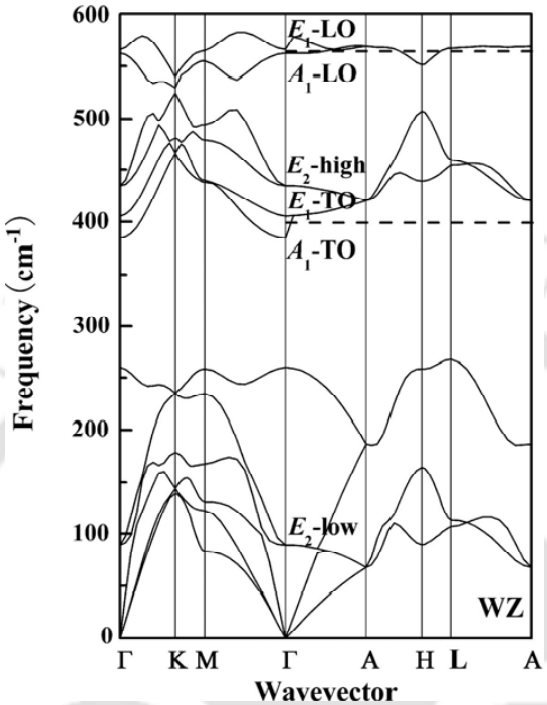

Figure 2.10: First–principles calculated phonon dispersion curve of hexagonal wurtzite (WZ) structured ZnO crystal. Adapted from Ref. [**202**].

which are Raman active, $2B_1$ modes which are Raman silent and $A_1 + E_1$ modes which are infrared active. The polar modes of A_1 and E_1 are splitted into tranverse (TO) and longitudinal optical (LO) phonon, while the nonpolar modes of E_2 have two frequencies identified as E_2^{high} and E_2^{low} associated with oxygen atoms and Zn sublattice, respectively.[203] E_1^{LO} mode is caused by the defects such as oxygen vacancy, zinc interstitial or their complex, which enables to identify the defects present in the ZnO nanostructures. Compared to bulk ZnO, the decreased dimensions of ZnO NWs lead to spatially confined phonons, giving rise to the phonon quantum confinement effect. Characteristics of phonon confinement could be:[204] (1) frequency downshift and Raman line shape broadening, whereas structure defects and residual stress could also contribute to the phonon linewidth broadening; and (2) generation of new features absent in the corresponding bulk spectrum. Raman spectrum typically shows Lorentzian line shape. Experimental data is analyzed by fitting multiple peaks with Lorentzian peak shape profile to extract the peak parameters.

B. UV–Vis Spectroscopy: This technique is used to study either reflection or absorption or transmission properties because the electronic band structure of semiconductors and metals are determined by their optical properties. The optical reflection or absorption is a result of interaction between the material and light. In the present case we have grown the ZnO NWs on the Si substrate. As the Si is an opaque substrate in the UV–Vis region, there is a limitation in optics for the direct measurement of the absorption of the ZnO NWs. Therefore, we measured the specular reflectance at an angle of 45°. In the measurement of specular reflectance, the detector collects only those reflected signals having angle of reflectance is equal to the angle of incidence. Then we used this data to calculate the absorption coefficient of the ZnO NWs in the UV–Vis region. The absorption coefficient, α is calculated for each wavelength in this region according the method proposed by Rusli *et al.*.[205]

We consider the case of NWs film on Si substrate. The length of the NWs or film thickness is *d* and refractive index $\mathbf{n}= n–ik$. The refractive index of the Si substrate is denoted by $\mathbf{n_s}=n_s–ik_s$ and the substrate thickness is much larger than that of the NWs film. The normal incidence reflectance **r** can be written as

$$\mathbf{r} = \frac{\mathbf{r}_{01}+\mathbf{r}_{12}\exp(-i2\delta)}{1+\mathbf{r}_{01}\mathbf{r}_{12}\exp(-i2\delta)}, \quad \text{..... (2.4)}$$

$$\delta = \frac{2\pi d\mathbf{n}}{\lambda} \quad \text{..... (2.5)}$$

Here, *n* and *k* are the real and imaginary parts of a refractive index, respectively, and λ is the wavelength of light. $\mathbf{r}_{01}$ and $\mathbf{r}_{12}$ are the Fresnel reflection coefficients at the air–NWs and NWs–substrate interfaces, respectively.

$$\mathbf{r}_{01} = \frac{1-\mathbf{n}}{1+\mathbf{n}} \quad \text{..... (2.6)}$$

$$\mathbf{r}_{01} = \frac{\mathbf{n}-\mathbf{n_s}}{\mathbf{n}+\mathbf{n_s}} \quad \text{..... (2.7)}$$

To reduce the complexity in the mathematics, only the normal incidence of light is considered for the calculation of absorption coefficient. However, the spectral features are not changed even when it is averaged over all oblique angles of incidence from 0 to π/2. Now the expression of absorption coefficient can be obtain from the expression of magnitude of reflectance, $R=rr^*$. With the following assumptions,

$n^2 >> k^2$, $n_s^2 >> k_s^2$, and $n < n_s$,

the magnitude of the constructive (R_c) and destructive (R_d) interference fringes at the envelope can be expressed as

$$R_c = \frac{Fx^2 + Gx + E}{Ix^2 + Gx + H}, \quad \text{..... (2.8)}$$

$$R_d = \frac{Fx^2 - Gx + E}{Ix^2 - Gx + H}, \quad \text{..... (2.9)}$$

where, $x = \exp(-\alpha d)$, $\alpha = \frac{4\pi k}{\lambda}$ and *E, F, G, H, I* are the functions of n and n_s only. In the weak and medium absorption regions, expression of x can be obtained from the solution of eqs. 2.8 and 2.9

$$x = \frac{(n^2-1)(1-R_c) - 4n^2\sqrt{R_c}}{(n-1)^2 R_c - (n+1)^2} \frac{n_s+n}{n_s-n} \quad \text{..... (2.10)}$$

$$x = \frac{-(n^2-1)(1-R_d) \pm 4n^2\sqrt{R_d}}{(n-1)^2 R_d - (n+1)^2} \frac{n_s+n}{n_s-n} \quad \text{..... (2.11)}$$

Simplification of above two equations gives

$$C_1 y^4 + C_2 y^3 + C_3 y^2 + C_4 y + C_5 = 0, \quad \text{..... (2.12)}$$

where, $y = \frac{1-n}{1+n}$, C_1, C_2, C_3, C_4, C_5 are the functions of R_c and R_d only.

As $-1 < y < 0$ and $x \geq 0$, therefore n is positive. Solving of eqs. (2.12) gives only one positive roots for a set of R_c and R_d at a particular wavelength. Having set of n and corresponding wavelength, one can estimate the d by using following equation

$$d = \frac{\lambda_i \lambda_j}{2(\lambda_i n_j - \lambda_j n_j)} \quad \text{..... (2.13)}$$

where λ_i and λ_j are the wavelengths at two adjacent maxima (or minima) and n_i, n_j are the real parts of the corresponding refractive indices. In a similar way as that proposed by Swanepoel,[206] we take an average value of the d and use it together with n to determine the order numbers m of the interference fringes by using the following equation

$$2nd = \begin{cases} m\lambda, & \text{constructive} \\ \left(m + \frac{1}{2}\right), & \text{destructive} \end{cases} \quad \text{..... (2.14)}$$

Where, m is a positive integer. Then we recalculated the *d* and then *n* using eqs. (2.14) to minimize the errors involved in the *d* and *n*. Having values of *n* and *k* in the transparent, weak, and medium regions, we used the dispersion equations [$n(\lambda)=A/\lambda^2+B/\lambda+C$] to fit *n* and therefore extrapolate their values in the strong absorption region. Using the obtained set of values of *n*, R_c, and n_s, we can calculate *x* using eqs. 2.10 or 2.11 in the range 200–900 nm. The values of n_s in the range 200–900 nm are obtained from the reference book by Palik.[207] Then absorption coefficient in the above mentioned range is calculated by using the obtained set of *x* values in the following equation

$$\alpha(\lambda) = -\frac{\ln x(\lambda)}{d} \qquad \text{..... (2.15)}$$

C. Photoluminescence (PL) Spectroscopy: In PL spectroscopy, one measure physical properties of the material by shining photons to excite electrons to higher energy levels and analyzing the optical emission as these states relax. The spectral distributions of the emission are related to electronic transition probabilities within the sample. Photoexcitation causes electrons–holes generation within the material and that electrons move into permissible excited states. When these electrons return to their equilibrium states, the excess energy is released and electron and a hole can either recombine non–radiavely by emitting phonons (or transferring energy to other particles) or radiatively by emitting photons. The energy of the emitted light (PL) relates to the difference in energy levels between the two electronic states involved in the transition between the excited state and the equilibrium state. The PL spectroscopy measures the count of emitted photons in a spectral range. The PL spectroscopy provides quantitative information like exciton transition, exciton binding energy, trap states, impurities states etc. From PL spectrum information of the radiative defects present on the samples could be obtained. An excellent review of photoluminescence spectroscopy of crystalline semiconductors has been given by G.D. Gilliland.[208]

We used a high sensitive steady–state fluorimeter (FS920P, Edinburgh Inst. UK) in the present study. The photograph of this instrument is shown in Fig. **2.11**. A He–Cd continuous laser (Kimmon Koha, Japan) of wavelength 325 nm is used to excite the samples. The emitted photons are captured using standard single photon counting detector tube. It has two grating monochromator, one at the excitation side and other one at the emission side. The monochromators have computer controlled slits and the spectrometer software displays the band with settings in nm units, taking automatically

into account the opto–mechanical properties of the grating. The steady state PL peaks are usually Gaussian in lineshape expressed by

$$y = y_0 + A\, exp[-(\frac{(x-x_c)^2}{2w^2}] \qquad \text{.....(2.16)}$$

Where y_0 is the offset constant, x_c, w and A are the peak position, width and peak amplitude, respectively. w multiplied by $\sqrt{2ln\,2}$ gives the exact value of FWHM of the Gaussian profile. The measured spectral profile of the PL spectrum is analysed by fitting with Gaussian lineshape function or combination of number of this function using PeakFit software.

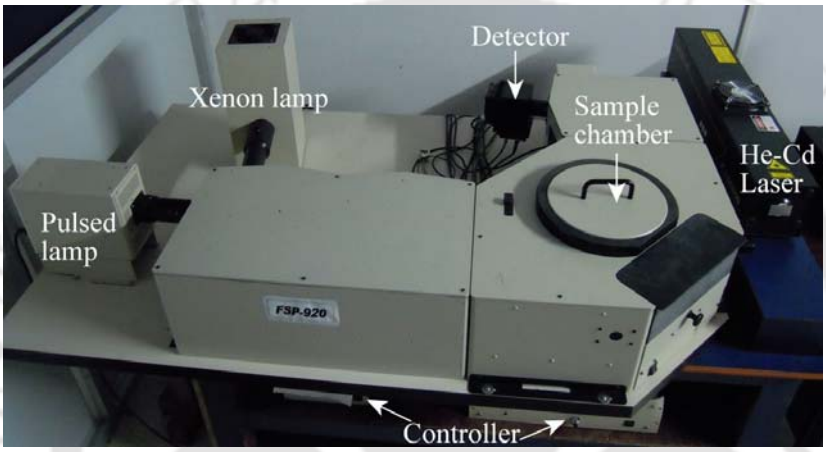

Figure 2.11: Photograph of the steady–state photoluminescence spectrometer (FS920P, Edinburgh Inst., UK).

D. Time–resolved Photoluminescence Spectroscopy: TRPL spectroscopy is used to study exciton dynamics in semiconductors. In TRPL spectroscopy, photons from a short laser pulse are used to excite electrons and holes in one instant, which then form excitons. As an electron and a hole recombine, TRPL spectroscopy allows one to measure the lifetime of the exciton, i.e. the time since it was created until it is annihilated. Knowledge of life time of the emitted photons is essential to understand the origin of this PL from the NWs. It is basically counts the number of photons of fixed wavelength with time. The emitted photon is analyzed by a spectrometer and detected by a micro–channel–plate photomultiplier tube (MCP–PMT) detector. A Multi Channel Analyzer (MCA) board in the computer bins output the pulse voltages into various channels, which correspond to different times. In this way, the MCA can record each photon arriving at the MCP–PMT at a particular time. The number of output pulses from the MCP–PMT is directly proportional to the number of incident photons. Averaging

over millions of photons, the measurement creates a histogram which shows how long excitons "live" after being created by the laser pulse.

Figure **2.12** shows the photograph of the TRPL spectroscope (LifeSpec II, Edinburgh Inst., UK) used in this study. We used adjustable nanosecond pulsed pump laser (EPL series, Edinburgh Inst., UK) of wavelength 375 nm to measure the PL decay of the defects related green emission in the ZnO NWs. This instrument has a time resolution of ~50 ps. The TRPL data usually follow an exponential decay behaviour or combination of such function depending upon the number of decay channels available in the sample. The PL decay equation is expressed as

$$I(t) = I_1 exp(-t/\tau_1) + I_2 exp(-t/\tau_2) + I_3 exp(-t/\tau_3) \ldots\ldots\ldots\ldots + I_0 \quad \ldots\ldots\ldots (2.17)$$

Where *I(t)* is the PL count, I_1, I_2, I_3 are decay channel amplitude and τ_1, τ_2, τ_3 are the decay time constants and I_0 accounts for the background noise.

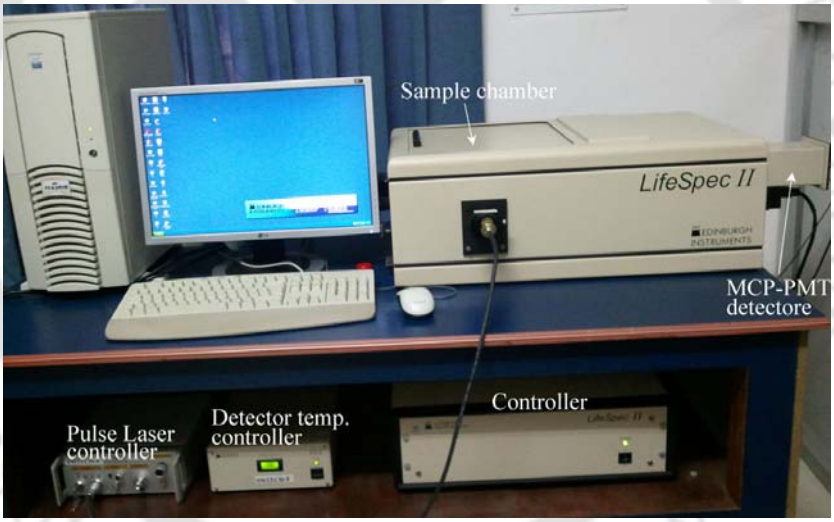

Figure 2.12: Photograph of the time–resolved photoluminescence spectrometer (LifeSpec II, Edinburgh Inst., UK).

E. FTIR Spectroscopy: Fourier Transform Infrared Spectroscopy (FTIR) is one of the powerful spectroscopic tool used to determine the structural bonding information, impurities and chemical functional groups in the sample. The FTIR is based on the phenomena *Michelson interference* combined with Fourier transformation of the source spectrum.[209] FTIR interferogram consists of spectral information of the source along with the reflectance characteristic of the sample. Here we used FTIR reflectance spectroscopy to confirm the attachment of organic molecules on the surface of the inorganic/organic type ZnO NWs heterostructures with anthracene and copper

phthalocyanine. A FTIR spectrometer of Perkin Elmer (Spectrum BX) is used in this study. The infrared reflection spectrum of ZnO NWs is taken at room temperature in the range of 400–4000 cm^{-1} at a resolution of 2 cm^{-1}.

2.3. Design and Development of Photocurrent and Photoresponse Measurements Setup

For the studies on the photodetection behaviour of the ZnO NWs, We have designed and developed a photocurrent and photoresponse measurement setup. The photograph of this instrument is shown in Fig. **2.13** and the schematic diagram of this setup is shown in Fig. **2.14**. It consists of a light source, electrical contacts through two microprobes and a source meter with computer interfacing. A monochromated UV–Vis light from a 150W xenon lamp is used for excitation. Before the monochromator, there is a slit to completely block or pass the light coming out from the xenon lamp source. The light coming out from the monochromator is tightly focused in to a small area on the sample through a convex lens and a concave mirror. The sample is placed horizontally on the bench of a probe station (EPS 500, Ecopia, South Korea). The electrical connections to the bundle of NWs are made using two tungsten made microprobes of diameter ~1.5 μm. The electrical connection to the NWs is shown schematically as inset with arrow mark. For making contacts with NWs, two circular Al contacts were made on the top of the NWs array by thermal evaporation process using shadow mask. To estimate the thickness of the Al contact, we simultaneously deposited Al on a cleaned Si substrate and thickness is measured by using a surface profilometer (Dektak 150, Veeco, USA). Figure

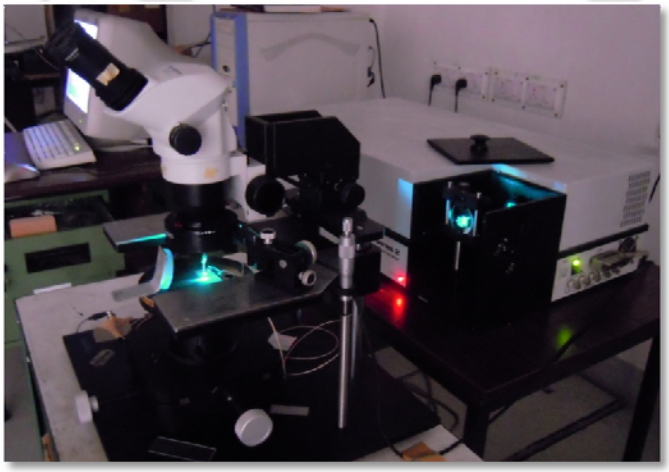

Figure 2.13: Photograph of the in–house developed photocurrent and photoresponse measurements setup.

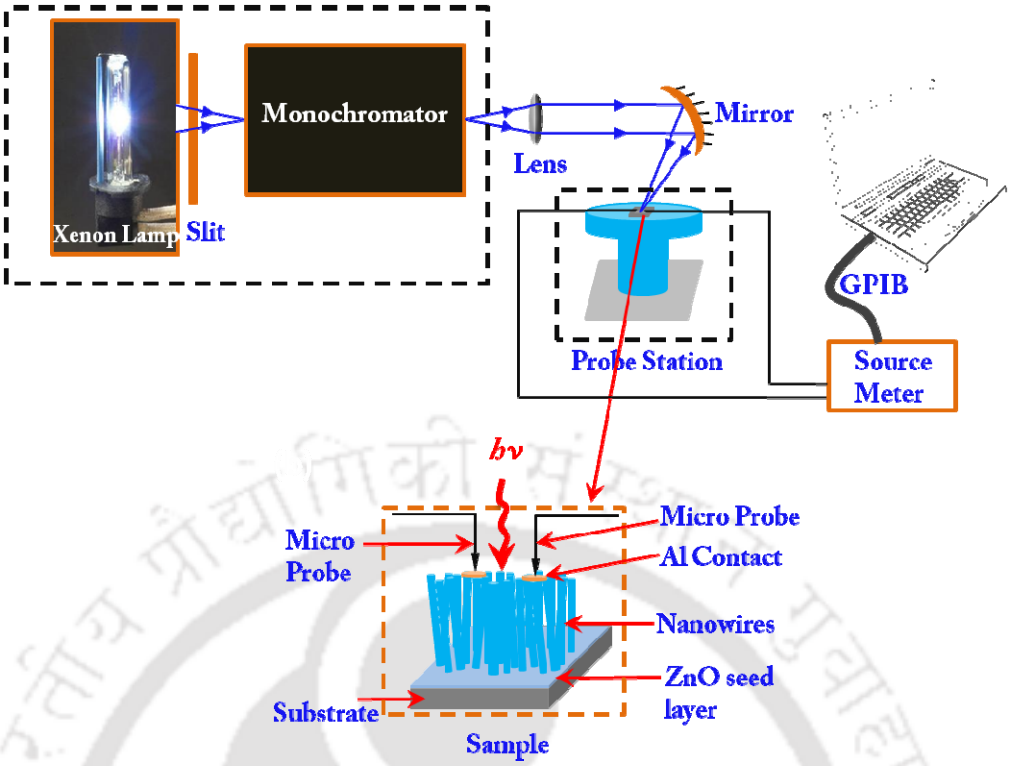

Figure 2.14: Schematic diagram of the in–house developed photocurrent and photoresponse measurements setup. Magnified schematic view of the ZnO NWs array with micro probe contacts is shown as inset with arrow mark.

2.15 shows the surface height profile of the Al contacts made on the cleaned Si wafer. The diameter of the circular contact is ~350 μm with thickness ~100 nm. The separation of the two contacts is about 2.5 mm. For all the samples, these parameters are kept fixed. The electrical properties of the samples are measured using a source meter through GPIB interfacing with the computer. The light falls on the top surface of the NWs and illuminates only the area in between the two metal contacts. The wavelength dependent

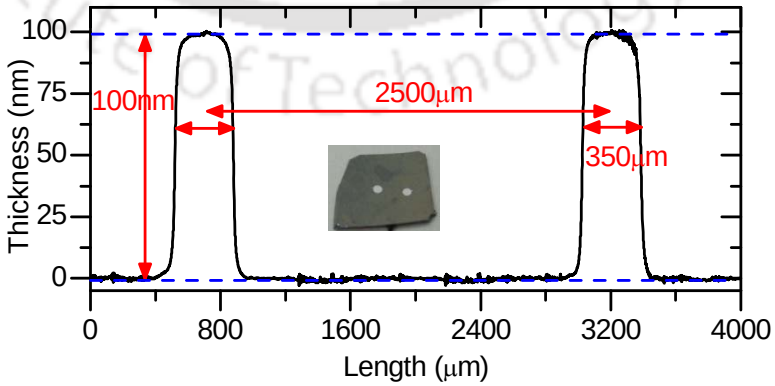

Figure 2.15: The surface height profile of the circular Al contacts made by thermal evaporation. Inset shows the photograph of the sample with Al contacts (white spot).

PC is measured at a fixed bias and by changing the wavelength of the incoming light through monochromator. The PC is monitored by using a picoammeter (Model 6487, Keithley Inst., USA) and the same instrument supply the necessary bias voltage. The photoresponse was measured under the illumination of monochromated UV light (wavelength 365 nm) at a light intensity of ~0.5 mW/cm^2 in ON and OFF conditions. All the measurements were carried out at room temperature and atmospheric pressure.

Chapter 3

Controlled Growth of ZnO Nanowires and Nanorods

ZnO nanowires (NWs) and nanorods (NRs) arrays over large area are grown by using thermal vapor deposition (TVD) technique as well as low temperature aqueous chemical method. An intense emphasize is given to the control on the growth orientation and alignment of the NWs and NRs. A systematic study is performed on the effects of several growth parameters to achieve a control over the shape, size and orientation of the NWs and NRs. A new growth strategy has been adopted for the growth of vertically well–aligned ZnO NWs and NRs arrays. To study the effect of doping on the optoelectronic and optical properties, Al doped ZnO NWs with different concentration of Al is synthesized. Al doped ZnO powder is used as a source for the Al doped ZnO NWs.

We have shown that ZnO nanostructures exhibit shape evolution as a function of growth temperature with the ZnO nano powder as a source. A systematic study is performed to understand the observed shape evolution and it is explained on the basis of vapor–liquid–solid (VLS) and vapor–solid (VS) growth mechanisms.

Microstructural characterization is made on the above as–grown NWs and NRs to understand the quality, structure, defects, strain etc. by using transmission electron microscopy, x–ray diffraction and micro–Raman spectroscopy techniques. To improve the structural quality of the as–grown ZnO nanostructure, rapid thermal annealing (RTA) is performed at different temperatures and characterized.

3.1. Growth of ZnO Nanowires and Nanorods

In this section, we present the growth methodology of the ZnO NWs and NRs. Two different techniques have been used to grow NWs and NRs, namely vapor phase growth

by using TVD system and aqueous chemical growth by using autoclave. ZnO NWs and NRs were grown on the nominally *n*–type doped Si(100) substrates. The NWs/NRs were grown vertically or horizontally to the substrate plane depending upon the growth conditions. We also synthesized high quality Al doped ZnO NWs with different concentrations.

3.1.1. Vapor Phase Growth of Vertically Aligned ZnO Nanowires

This section describes only the vapor phase growth of ZnO NWs and NRs. We also present the effects of several growth parameters in TVD method on the morphology of the as–grown nanostructures.

3.1.1.1. Self–Catalytic Seed Layer Assisted Growth

To grow well–aligned ZnO NWs, first we synthesize NWs by self catalytic growth process. We have synthesized vertically grown ZnO NWs by self catalytic growth process using ZnO seed layer. First, high quality thin ZnO seed layer of thickness of 200 nm was deposited on the pre–cleaned, HF etched Si wafer by RF–magnetron sputtering, which is shown schematically in Fig. **3.1(a)**. A mixture of high purity ZnO powder and high purity graphite powder at a weight ratio of 1:1 was used as a source. ZnO vapor was produced inside the chamber at 900°C, which was placed inside the muffle furnace. The ZnO vapor was deposited on the seed layer coated Si substrate in downstream direction at 800°C. The vapor deposition was carried out under the Argon gas flow of 70 sccm (standard cubic centimeter mass) for 30 mins. After deposition the entire system was cooled down to room temperature and the synthesized product was characterized by standard tools.

Figure **3.1(b)** shows the ZnO seed layer assisted self–catalytically grown ZnO NWs, which were found to grown vertically on the Si substrate. The diameter of the NWs varies in the range of 100–200 nm with a length up to 1μm. Although the ZnO NWs are grown vertically, however the growth orientation is random. From the FESEM image, it is revealed that ZnO seed droplet is present on the top of the NWs. ZnO NWs are grown by a self–catalytic VLS method. It is reported that the quality and diameters of the ZnO NWs depended on the crystallinity and particle size of the seed layer.[52,210,211] In this case, the grown NWs are non–uniform in diameter and length also not well–aligned due to the non–uniform distribution of ZnO seed layer. As a result, these ZnO NWs are not suitable

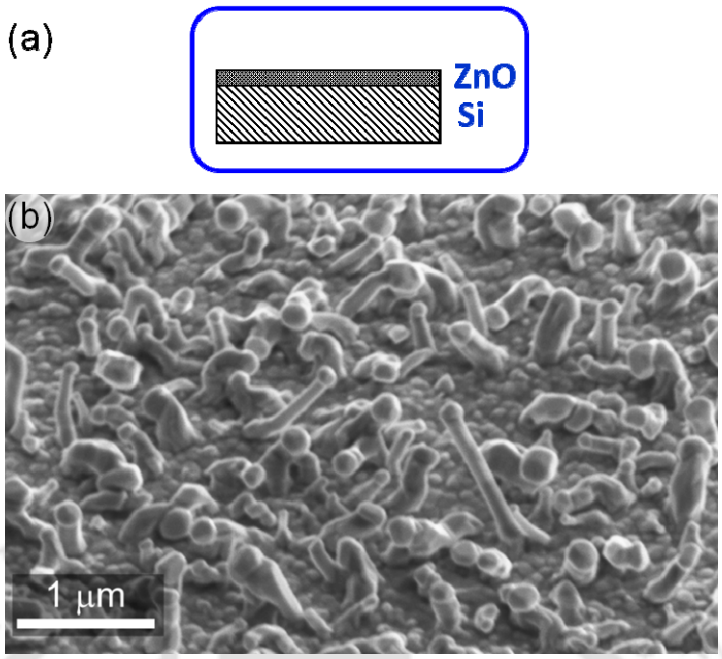

Figure 3.1: (a) Schematic diagram of the ZnO layer of Si substrate. (b) 45° tilted FESEM image of the seed layer assisted self catalytically grown ZnO nanowires.

for further use in nanodevices. Then we used metal catalyst to grow well–aligned ZnO NWs, which is discussed in the next section.

3.1.1.2. Gold Catalyst Assisted Growth

Here we used about 2 nm thick Au layer on Si substrate as metal catalyst. The ZnO vapor was formed at 950°C and was deposited on the Au coated Si substrate. The NWs were grown at substrate temperatures of 750° and 800°C for 30 mins of deposition. Figure **3.2** shows the SEM image of the randomly oriented vertically grown ZnO NWs. Fig. **3.2(a)** shows the NWs grown at 750°C with diameter of 30–70 nm at the top edge and 110–160 nm at the bottom side of the NWs. The length of the NWs varies in the

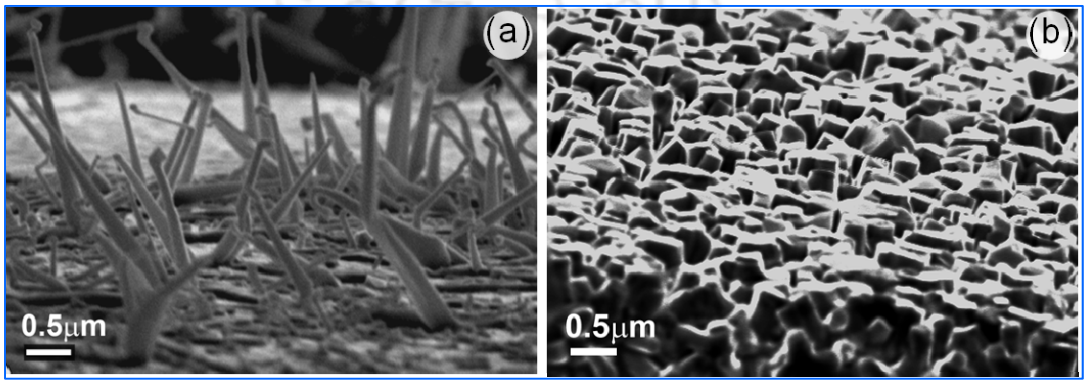

Figure 3.2: SEM images (tilted view) of the Au catalyst assisted vertically grown ZnO nanowires, grown at a substrate temperature of (a) 750 and (b) 800°C, respectively.

range of 2–5 μm. The diameters of the NWs grown at 800°C (Fig. **3.2(b)**) show a variation from 100 nm to few hundreds of nm with length about few microns. This is a large estimation of diameter of the nanowires due to non–uniformity of the NWs. It is observed that the NWs grown at higher temperature has larger diameter. Although these NWs have vertical orientation, these are not so well–aligned. It is believed that lattice mismatch between Si and ZnO is responsible for the non–uniform orientation. Therefore, ZnO seed layer as well as the Au catalyst both independently failed to produce well–aligned ZnO NWs by vapor transport method.

3.1.1.3. Combined Seed Layer and Gold Catalyst Assisted Growth

Then we used a new approach by combining effects of both the ZnO and Au layer.[114] The schematic diagram of this growth approach is shown in Fig. **3.3(a)**. First, ZnO seed layer was deposited by RF–magnetron sputtering on the cleaned Si substrate followed by deposition of ultrathin Au layer by DC sputtering. In this process about 200 nm seed layer and 2 nm Au layer was deposited. Then ZnO NWs were grown at 750° and 800°C by vapor transport method.

Figure **3.3(b–c)** shows the FESEM images of the as–grown ZnO NWs, clearly showing the formation of vertically aligned ZnO NWs arrays on the ZnO coated Si substrate. The NWs grown at 750°C have the diameters in the range of 50–80 nm and length about a few microns. It is observed that a few of the NWs have tapered structure, i.e., slightly lower diameter at the tip compared to the bottom end. Whereas, the NWs grown at 800°C show the diameters in the range of 100–220 nm and length about a few microns. Due to the combined effect of ZnO seed layer and Au catalyst, here we obtained a perfect vertical orientation of the NWs. Therefore, we have successfully grown good quality well–aligned ZnO NWs arrays over large surface area. ZnO seed layer has a strong effect on the aligned growth of ZnO nanorods array. In this case, ZnO seed layer and Au layer together act as a nucleation site and guide the NWs growth, resulting a high alignment. The Si/ZnO/Au substrate offer very negligible lattice mismatch or almost mismatch free interface between seed layer and NWs, which results in the high quality vertically aligned growth of ZnO NWs arrays.

3.1.2. Low Temperature Chemical Growth of ZnO Nanowires

For the low temperature growth of ZnO NWs we used an aqueous chemical growth

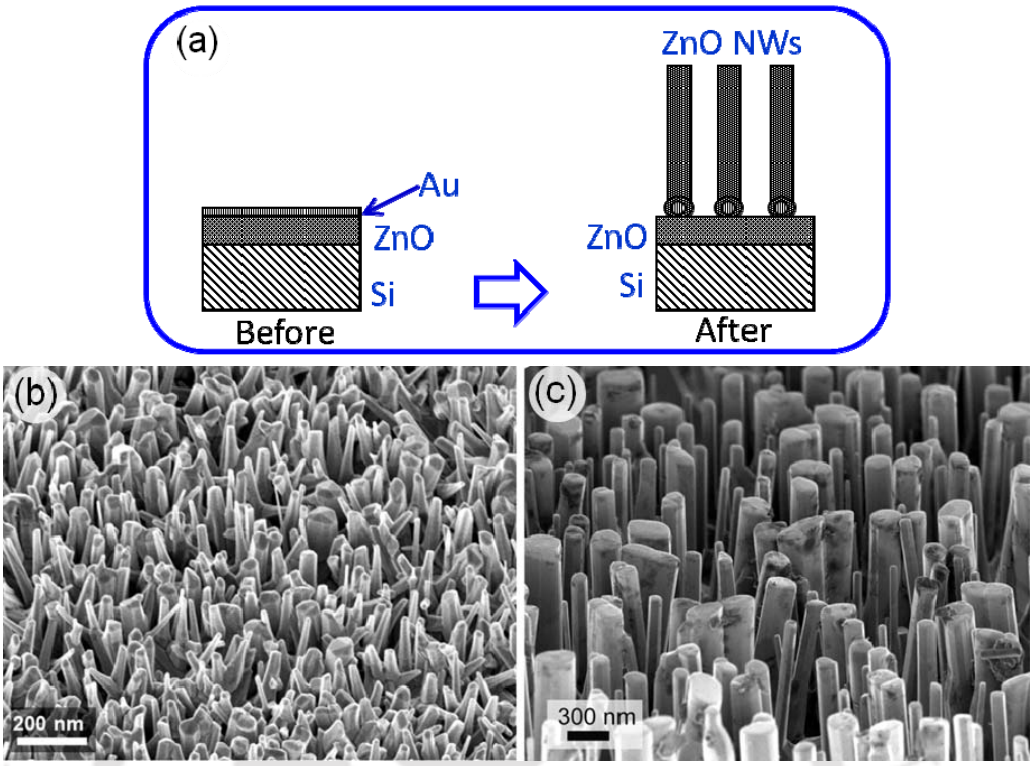

Figure 3.3: (a) Schematic diagram of various layers grown on the Si substrate, before the growth and after the growth with the ZnO NWs. FESEM images (tilted view) of the the combined seeded layer and Au catalyst assisted grown vertically aligned ZnO nanowires arrays, at (b) 750 and (c) 800°C, respectively.

method using an autoclave with teflon coated reaction flask. For this method, a uniform distribution of ZnO nanocrystals seeds ware prepared on the Si substrate by thermal decomposition of a zinc acetate precursor. First, 20mM zinc acetate [$(CH_3COO)_2Zn$] solution in ethanol was uniformly coated on the Si substrate. Then the coated substrate was heated at 350°C for 30 mins to get ZnO seed layer. The well–aligned ZnO NWs were synthesized by hydrolysis of zinc nitrate [$Zn(NO_3)_2$] in water in the presence of hexamethylenetetramine (HMT) on that substrate. In this case, $Zn(NO_3)_2$ provides Zn^{2+} ions required for building up ZnO NWs and HMT guide the growth direction. The O^{2-} ions are coming from the hydrolysis of DI–water. The above prepared substrate is dipped in to a mixture of equimolar (25 mM) concentration of zinc nitrate and HMT in DI–water. The chemical reaction was carried out at 90°C for one hour. The substrate was then removed from the solution, rinsed in DI–water and dried in air.

Figure **3.4** shows the well–aligned growth of ZnO NWs by aqueous chemical method with the help of ZnO seed layer.[212] As seen from the images, a dense ZnO NWs grew vertically on the substrate over a large area and formed an array like structure. The diameters of the NWs are very small, which ranges from 30 to 40 nm and the length are

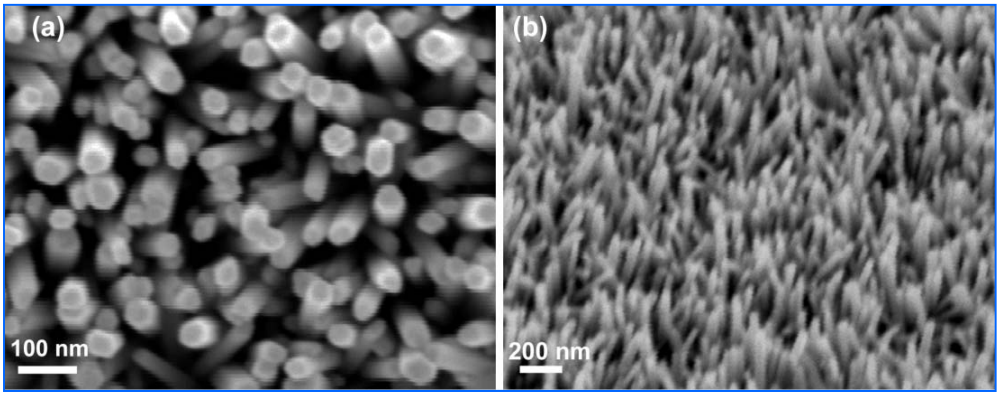

Figure 3.4: FESEM images of the chemically grown vertically aligned ZnO nanowires grown on ZnO/Si substrate: (a) top view and (b) 45° tilted view.

about few microns. During the chemical growth process, ZnO NWs preferentially nucleate from the tip near the grain boundaries between two adjacent grains in the ZnO seed film.[213] The diameter of the as–grown NWs usually depends on the grain size of the ZnO seeds. The degree of alignment in the as–grown ZnO NWs is strongly controlled by the orientation of the ZnO seed layer.

3.1.3. Vapor Phase Growth of ZnO Nanorods

We have successfully grown ZnO NRs using vapor deposition method by changing the growth parameters.[214] We used a thick layer of ZnO seed as well as Au catalyst layer and the vapor was deposited at higher temperature. Approximately 35 μm thick ZnO seed layer was deposited on Si(100) substrate by sputtering process. In the next step, a thin (~5 nm) layer of Au was deposited on that substrate. The well–aligned ZnO NRs arrays were grown in the temperature range 700–900°C.

Figure **3.5** shows typical SEM morphology of ZnO NRs grown on Si/ZnO/Au substrate at various growth temperatures. The NRs grow vertically on the substrate plane, as seen from the images. The sizes of the NRs are in the range of few hundred nanometers and non–uniform diameters are due to the variation in the local thickness of ZnO seed layer. It is found that the NRs grown at 900° and 850°C have larger diameter and highly aligned as compared to the NRs grown at 700°C. At high growth temperature, as the growth rate is high and ZnO seed layer allows epitaxial growth process. Size control of these NRs can be accomplished by lowering the growth temperature and depositing a thinner ZnO seed layer.[40,52]

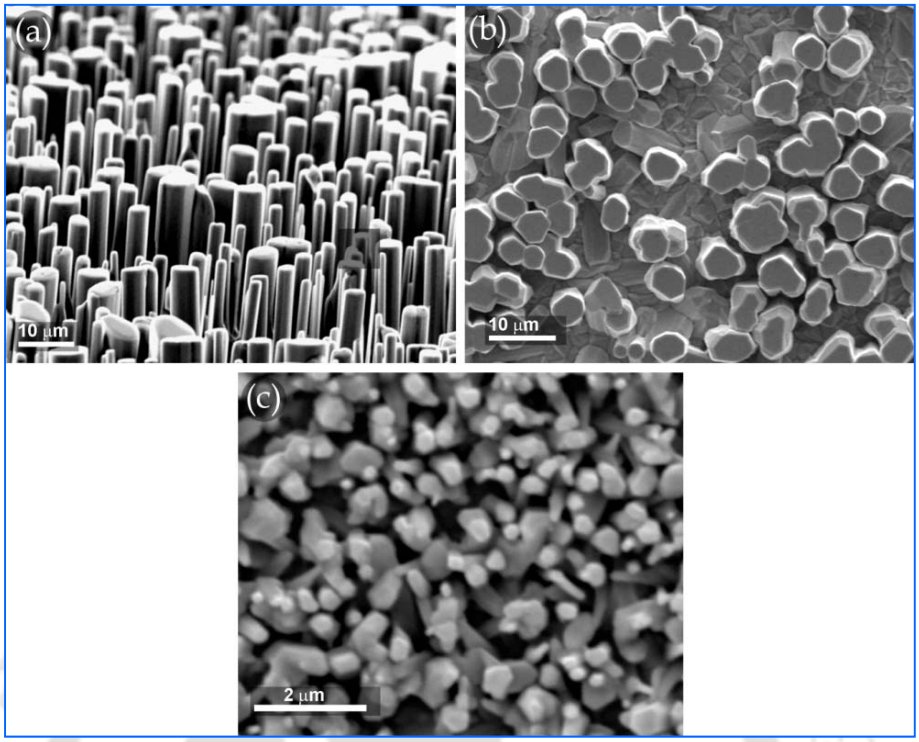

Figure 3.5: SEM images of the combined seeded layer and Au catalyst assisted grown aligned ZnO nanorods grown at substrate temperatures: (a) 900°, (b) 850°, (c) 700°C, respectively.

3.1.4. Shape Evolution of ZnO Nanostructures

In the study of effects of several growth parameters, we used ZnO nano powder as a source material, instead of bulk ZnO powder. We observed shape evolution of the nanostructures as a function of growth temperature.[215] With the increase in growth temperature, the nanostructure changes from NWs to nanoribbons and then to NRs at higher temperature. On the other hand, in case of ZnO bulk powder as a source material, only NWs are produced at all temperatures. Earlier, Ye *et al.*[37] have studied morphology derivation of ZnO nanostructures from nanoplatelets to NWs using ZnO bulk powder as the source material and changing the growth parameters. They also investigated the underlying mechanism responsible for the observed morphology derivation. Effect of zinc sources on the morphology of ZnO nanostructures has been investigated by Yu *et al.*.[216] The zinc sources involved pure zinc, ZnO, and $ZnCO_3$ bulk powders, respectively. It is found that the zinc sources have a strong effect on the morphology of the ZnO nanostructures. For the pure zinc and ZnO sources, uniform ZnO nanowires and tetrapods are obtained, respectively. However, in the case of the $ZnCO_3$ source, the products are nanowire–tetrapod combined nanostructures. So far, the underlying mechanism for the evolution of the nanostructures has not been elucidated in depth.

In our work, commercial ZnO nano powder (grain size 50–70nm) was mixed with high purity graphite powder and was used as the source material and the vapor mixture was created at 950°C inside the quartz chamber. Then the vapor mixture was transported by Ar gas and deposited on the 2 nm Au coated Si(100) substrate pieces placed at elevated temperature zones (650°–870°C) of the furnace inside the quartz chamber. The deposition was carried out for 30 mins.

Figure **3.6** shows various nanostructures grown from the ZnO nano powder source. The shape of the nanostructures vary from NWs to nanoribbons and then to NRs as the distance between source and substrate decreases. Vertically aligned dense NWs were grown at 650° and 750°C (Fig. **3.6(a-b)**). These NWs have diameter 50–80 nm and length about few microns. Figure **3.6(c)** shows the growth of dense and long nanoribbons at 850°C, which is closer to the source material than the previous case. The nanoribbons have length of more than 10 μm and width 300–500 nm. The nanoribbons are tapered shaped with smallest tip size about 40 nm. At 870°C, which is nearer to the source material, we observed the formation of dense NRs with hexagonal facet (Fig. **3.6(d)**).

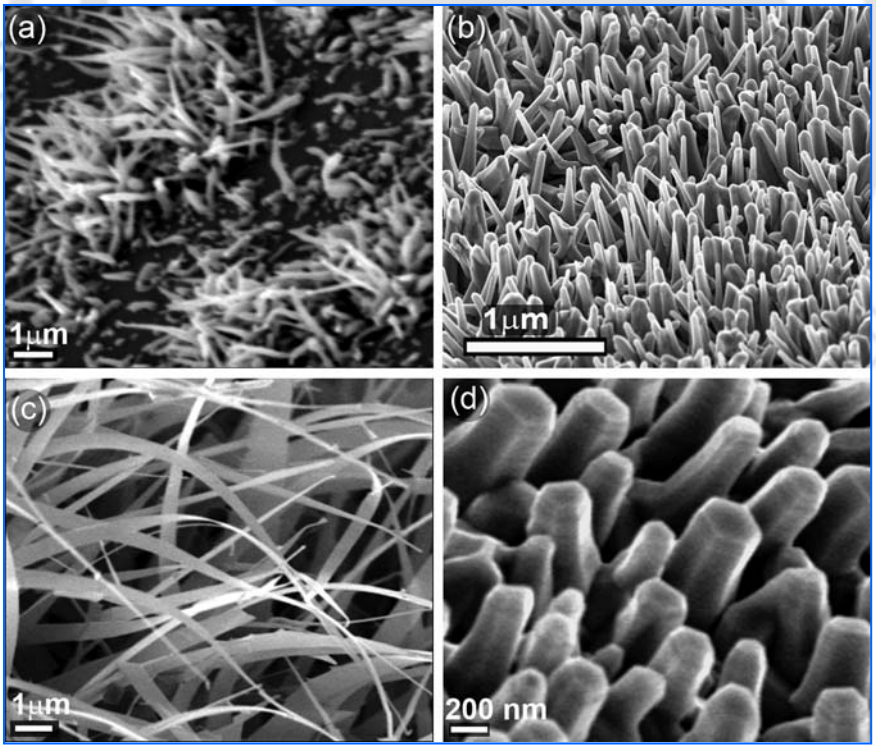

Figure 3.6: SEM images (tilted view) of vertically grown ZnO nanostructures: (a) nanowires grown at 650°C, (b) nanowires grown at 750°C, (c) nanoribbons grown at 850°C and (d) nanorods grown at 870°C using ZnO nano powder as the source material. Here ZnO nanostructures undergo a shape evolution from nanowires to nanoribbons and then to nanorods.

The NRs are found to be vertically aligned. The diameter of the nanorods varies from 200–300 nm and length of several microns. As described earlier, in case of ZnO bulk powder as a source material for Au catalytic growth, we observed only NWs with different diameter depending upon the growth temperatures. Therefore, we observed temperature dependent shape evolution of ZnO nanowires only when ZnO nano powder is used as the source material. At lower temperature and lower zinc vapor pressure, NWs were formed and then transformed towards nanoribbons and then to NRs at high temperature region and higher vapor pressure.

It is accepted that in catalyst mediated growth, ZnO NWs and NRs are grown by vapor–liquid–solid (VLS) mechanism[42] and nanoribbons are grown by vapor–solid (VS) mechanism.[62] Formation of varieties of ZnO nanostructures mainly controlled by growth temperature, surface energy of the growth plane and source material and zinc vapor pressure.[37] In general, it is observed that temperature below 800°C is suitable for the growth of ZnO NWs and above 800°C is suitable for the growth of ZnO nanorods. In the present case, final shape of the as–grown nanostructures is controlled by growth temperature as well as the Zn/ZnO_x vapor pressure. Growth mechanism of the ZnO NWs, nanoribbons and NRs by single deposition is explained schematically in Fig. **3.7**. Since the high temperature region is nearer to the ZnO source, there is a large variation of zinc vapor pressure and ZnO_x concentration in different temperature regions. Due to ultrafine size of the ZnO nano powder, during thermal evaporation the yield of vapor mixture (Zn, ZnO_x and CO) is too high. From the classical nucleation theory for Whiskers growth,[217,218] it is calculated that the supersaturation rate is dependent on the carries gas flow rate and the position of the substrate from the source. For a low flow rate of carries gas, the supersaturation rate initially increase and then start decreasing with increase in distance from the source position. At high temperature region, which is nearer to the source material the supersaturation rate is low.[37] That low supersaturation rate and high vapor pressure results in the growth of the NRs rather than NWs. In the present case depending upon the carrier gas flow rate and growth temperature, vapor mixture concentration and also supersaturation is maximum at ~850°C. Then, in this temperature vapor is deposited on the substrate in a fast rate and does not have sufficient time to react with the catalyst particles. The molecules have a good chance to diffuse to the front and the side surfaces. This deposition results in the growth of long nanoribbons by VS process. In the lower temperature region, which is away from the source material, the

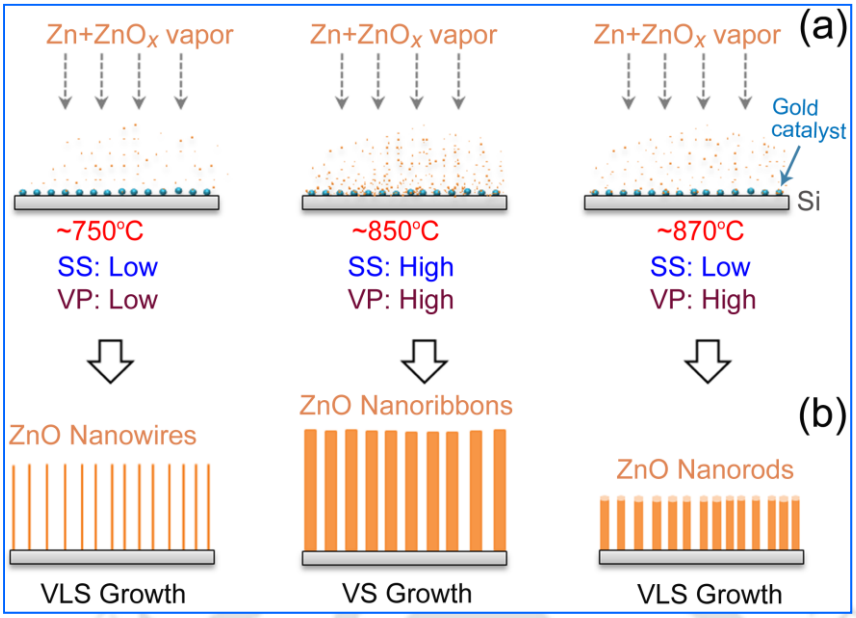

Figure 3.7: Schematic diagram showing the growth of ZnO nanowires, nanoribbons and nanorods at different growth conditions by vapor deposition process. (a) Liquid droplet of gold formed on the Si substrate and the Zn/ZnO_x vapor cloud is coming after the evaporation of the source material for deposition. (b) Depending upon the growth temperature, vapor pressure and supersaturation rate, ZnO nanowires, nanoribbons and nanorods are formed on the Si substrate by VLS and VS growth process. SS and VP means supersaturation rate and vapor pressure, respectively.

supersaturation rate and vapor concentration both are low. The Zn (ZnO_x) vapor sufficiently reacted with the catalyst particles during deposition. This deposition results in the growth of NWs by VLS process.

3.1.5. Al doped ZnO Nanowires by Vapor Phase Growth

To study the effect of doping on the optoelectronic and optical properties of the ZnO NWs, we synthesized Al doped ZnO NWs with different concentration of Al. The Al doped ZnO (Al:ZnO) NWs network of two different concentration of Al (3% and 6%) were grown on the oxidized Si substrate by VLS process. Al doped ZnO powder as the source and Au coated (~2 nm thick) oxidized Si as the substrate were used during the growth of the NWs. 3% and 6% Al doped ZnO powder was prepared by using mechanical ball milling process. Commercial high purity ZnO powder and Al powder were used as starting materials. At first 3% Al powder was mixed properly with ZnO powder and ball milling was performed at 300 rpm for duration of 5 h in a zirconium vial (PM100, Retsch, Germany) using small zirconium balls at a weight ratio of 1:10 for powder mixture. The 6% Al doped powder was prepared by similar process. The uniform

doping of Al in the as–prepared ZnO powder was confirmed by x–ray diffraction and EDX scanning. The XRD patterns do not shows any segregation of Al in the doped powder. For the growth of Al:ZnO NWs, as–prepared doped powder and graphite powder (Fluka, USA) mixture was used as ZnO vapor source material and placed inside a horizontal muffle furnace. The ZnO vapor was formed at 950°C and was deposited on the Au coated oxidized Si substrate at 700°C for 30 mins.

Figure **3.8(a)** shows the FESEM image of the 6% Al:ZnO NWs grown on the Si substrate. The NWs grew horizontally to substrate plane and form a network like structure where each one is connected with the other nearest neighbour NWs. Image at the top right corner of Fig. **3.8** shows the magnified view of the NWs. These NWs are ultra small with diameter ranging from 10 to 16 nm and length in the range of 0.6–1.0 µm. The EDX spectrum, shown in Fig. **3.8(b)** confirms the presence of Al in the Al:ZnO NWs sample. An average of 4.8 at.% of Al is obtained from the 6% Al:ZnO NWs. The 3% Al:ZnO NWs shows similar morphology with average diameter of 12 nm. The Al:ZnO NWs were expected to grow with vertical orientation. However, in this case we obtained a horizontal alignment or planar growth. This is probably due to the side effect of doping. Earlier, it was reported that doping in the NWs by TVD method could significantly change the morphology into various shapes such as nanobelts[133] and hierarchical structures.[134] It is believed that, the presence of dopants may introduce a distortion of the lattice and guide the growth of the NWs to a specific crystallographic direction, which is different for the case of undoped one.

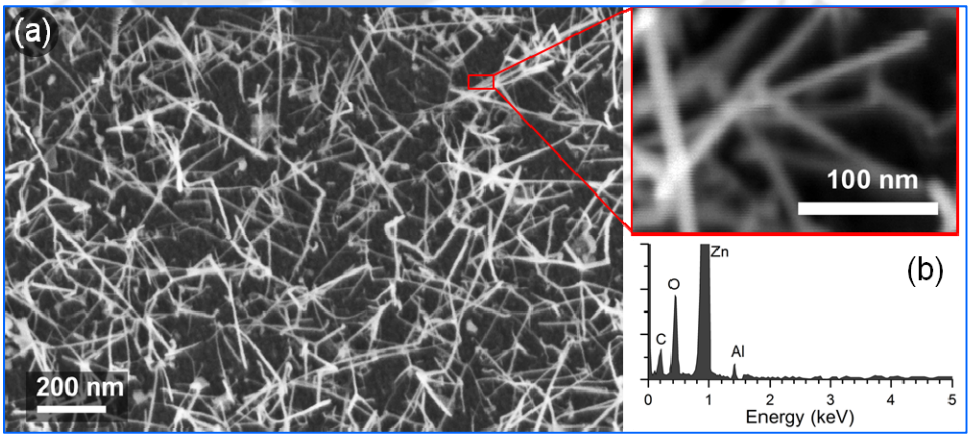

Figure 3.8: (a) FESEM image of the horizontally grown Al doped (6%) ZnO nanowires network with diameter 10–16 nm. Inset at the top right corner shows the NWs at higher magnification. (b) EDX spectra of the above nanowires, showing the presence of Al content in the nanowires.

3.2. Structural Characterization

After the synthesis of nanostructures, it is essential to characterize the as–grown sample to know the structure and related properties. Low–dimensional nanostructures, with possible quantum–confinement effects and large surface area, show distinct mechanical, electronic and optical properties, compared to the bulk materials counterpart. In this section, we will summarise the structural characteristics of the ZnO NWs and NRs by x–ray diffraction (XRD), TEM imaging and micro–Raman spectroscopy.

3.2.1. X–Ray Diffraction Studies

XRD is an ideal probe to characterize structure and orientation of the NWs/NR with respect to the substrate. The XRD measurement is performed with Cu Kα radiation at 3° grazing angle and with higher integration time. The structural characterization of the ZnO NWs and NRs done by XRD shows characteristic peaks of pure hexagonal wurtzite phase of ZnO. Figure **3.9** shows the XRD patterns of the Au catalytically and combines Au and seed assisted grown ZnO NWs. XRD pattern of the ZnO nanoribbons is shown at Fig. **3.9 (d)** as inset. All the patterns show one intense peak corresponding to the (002) plane and a weak peak corresponding to the (103) plane of hexagonal structure. Strong (002) peak and smaller full width at half maximum (FWHM) value indicates the c–axis orientation of the single crystalline ZnO NWs and the growth direction is perpendicular to the base surface. From Fig. **3.9 (a–d)**, comparatively higher values of peak intensity ratio of (002) peak to (103) peak is observed from Fig. **3.9 (b and c)**. This indicates well–aligned vertical growth of the NWs, which were grown by using combined seed layer and Au catalyst. The XRD results are in agreement with the SEM/FESEM results.

The lattice parameters for hexagonal ZnO NWs are estimated from the (002) plane using the equation:

$$\frac{1}{d_{hkl}^2} = \frac{4}{3}\left(\frac{h^2+hk+k^2}{a^2}\right) + \frac{l^2}{c^2} \qquad \text{..... (3.1)}$$

Where, a and c are the lattice parameters and h, k, and l are the Miller indices and d_{hkl} is the inter–planar spacing for the plane (hkl). This interplanar spacing can be calculated from the Bragg angle θ using the relation,

$$2d_{hkl}\sin\theta = n\lambda \qquad \text{..... (3.2)}$$

Where λ is the wavelength of x–ray (1.5406 Å), θ is diffraction angle, and n is the order of diffraction (n=1). The calculated lattice parameters are a= 3.250Å, c= 5.208Å and a=

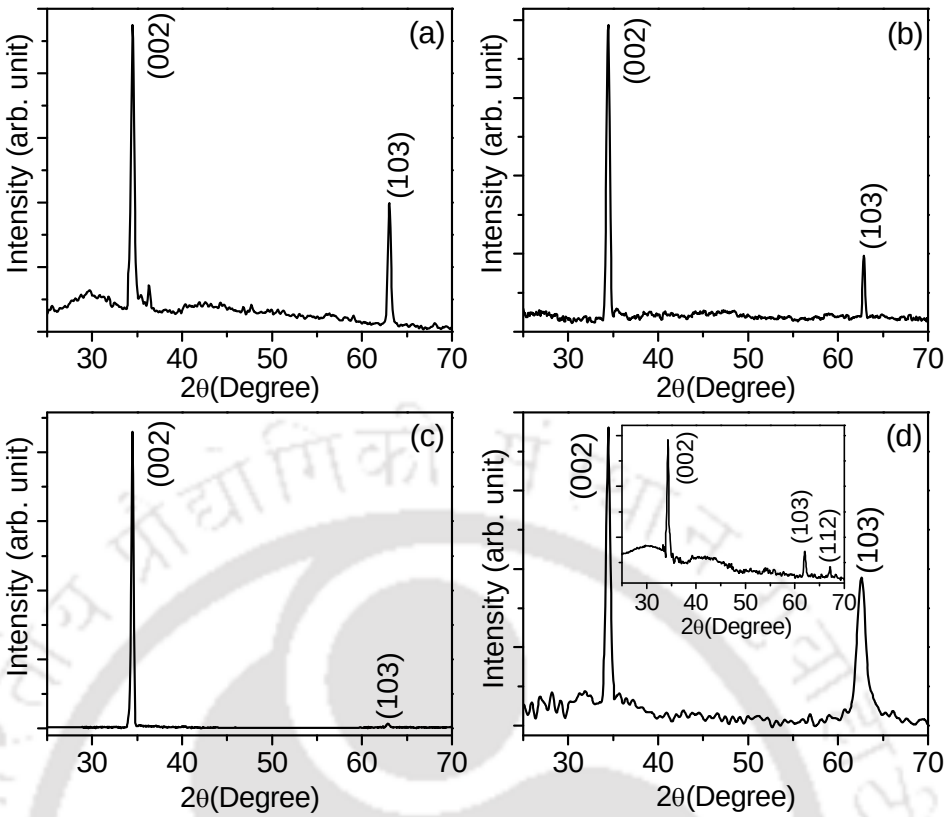

Figure 3.9: XRD patterns of the ZnO nanowires grown by: (a) Au catalyst assisted, (b and c) combined seed layer and Au catalyst assisted at substrate temperature of 750° and 850°c, respectively. Above mentioned nanowires are grown by using ZnO bulk powder as the source material. (d) XRD pattern of the Au catalyst assisted grown ZnO nanowires by using ZnO nano powder as the source. Inset shows the XRD pattern of the ZnO nanoribbons.

3.249Å, c= 5.207Å for the Au catalyst assisted grown NWs by using bulk and nano powder, respectively. On the other hand, the lattice parameters for the combined seed and Au assisted grown NWs are a= 3.250Å, c= 5.206Å and a= 3.251Å, c= 5.208Å for the NWs grown at 750° and 800°C, respectively. Therefore, as compared to the lattice parameters of bulk ZnO (a=3.249, c=5.206, JCPDS Data, PDF#790206), the obtained lattice constants of the as–grown NWs are found to be larger. This indicates that the as–grown ZnO NWs are weakly strained and the nature of strain is tensile. The calculated strain varies in the range 0.02–0.04% of the above samples.

The XRD result of the chemically grown ZnO NWs is shown in Fig. **3.10**, which shows a strong peak at 34.45° corresponding to (002) planes of hexagonal ZnO. The observed strong peak indicates highly crystalline nature of the as–grown NWs with growth orientation along the *c*–axis of hexagonal structure of ZnO.

XRD pattern of the ZnO seed layer is shown in Fig. **3.11(a)**, which reveals (002) oriented growth of the ZnO film. Figure **3.11(b-d)** shows the XRD patterns of the ZnO

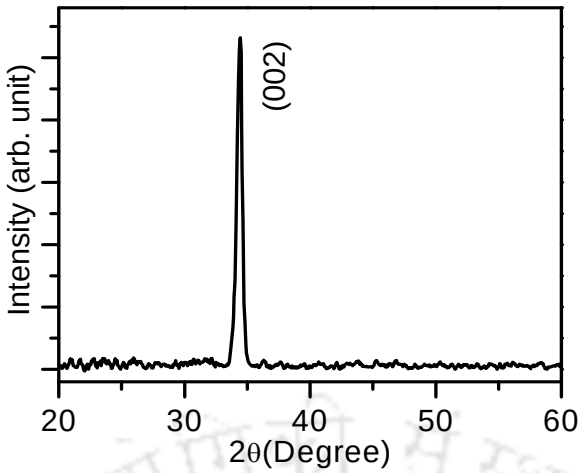

Figure 3.10: XRD pattern of the chemically grown vertically aligned ZnO nanowires.

NRs grown at 900°, 850° and 700°C, respectively. In this case, we observed a strong (002) peak of hexagonal ZnO, indicating the *c*–axis orientation. These patterns also indicate a well–aligned orientation and the growth direction is perpendicular to the basal plane. Identical growth orientations of the seed layer and the as–grown NRs suggest that

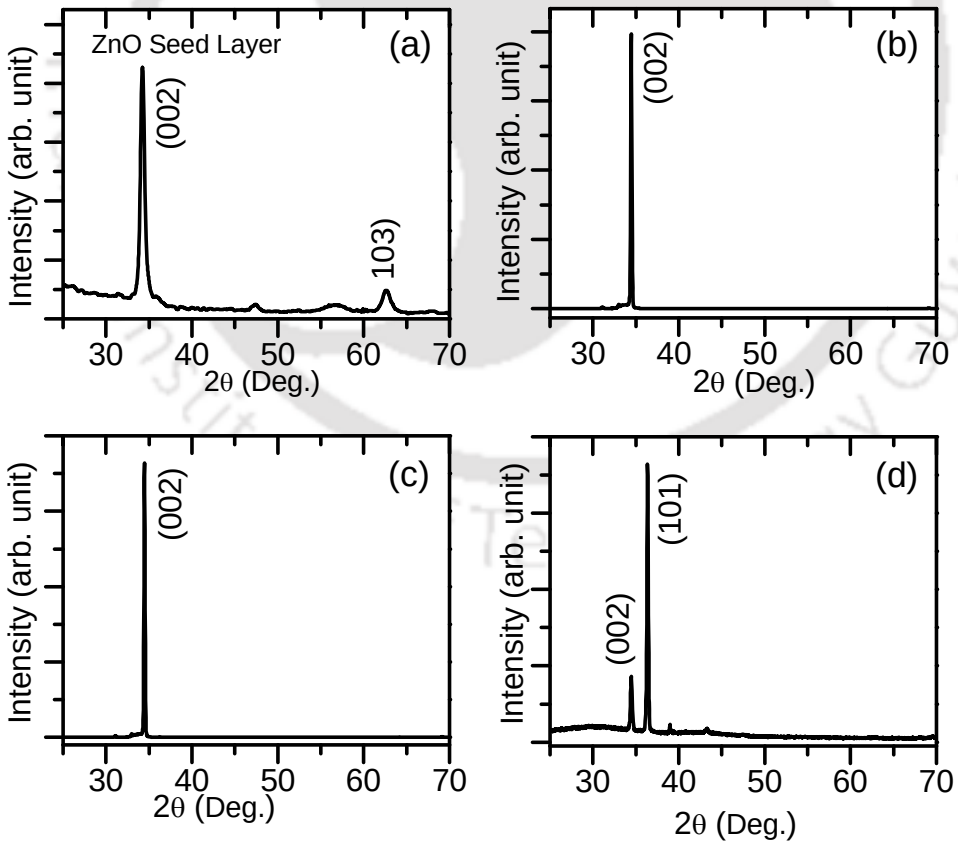

Figure 3.11: XRD patterns of ZnO seed layer and nanorods arrays: (a) sputter deposited ZnO seed layer on Si substrate; (b–d) vertically aligned ZnO nanorods grown at substrate temperature 900°, 850° and 700°C, respectively

Au layer transfer the same orientation of the ZnO seed layer to the ZnO NRs leading to the well–aligned growth. Therefore, structural quality and orientation of the ZnO seed layer are the key factors for the well–aligned growth of the NWs/NRs. Relative intensities of the XRD peaks show that NRs grown at higher temperature have higher value of peak intensity, which implies higher crystallinity. Because, highly crystalline sample contains larger number of perfect Bragg planes than the weakly crystalline sample, even if both the samples have same crystal volume. The as–grown NRs at 900°C show very small FWHM (0.0305°) and highest intensity peak in XRD, which is ~1.6 times higher than that of the NRs grown at 850°C. And the NRs grown at 700°C (Fig. **3.11(d)**) show large FWHM (0.0987°) and weak (002) peak intensity, which is ~46 times smaller than the NRs grown at 900°C. As the nanorods contains (101) planes at the connecting face between top (002) and side (100) surface of the nanorods, it may possible that comparatively larger number of (101) planes take part in the scattering event than the (002) plane. This results in a weak (002) peak.

The structural characterization of the Al:ZnO NWs also performed and presented in Fig. **3.12**. The XRD patterns of the 3% and 6% doped Al:ZnO NWs show characteristics peaks of crystalline hexagonal phase of ZnO with strong (002) planes related peak. No other peaks related to the Al or aluminium oxide are detected. Exact position of the (002) peak is calculated from the Lorentzian fitting to the experimental data. It is found that the peak position is slightly shifted towards higher 2θ. This up shift indicates that Al:ZnO NWs are weakly strained and the nature of strain is compressive, It is also noticed that the compressive strain increases with increase in Al concentration. In case of Al doping in ZnO, it is known that the Al atoms occupy the Zn lattice site due to

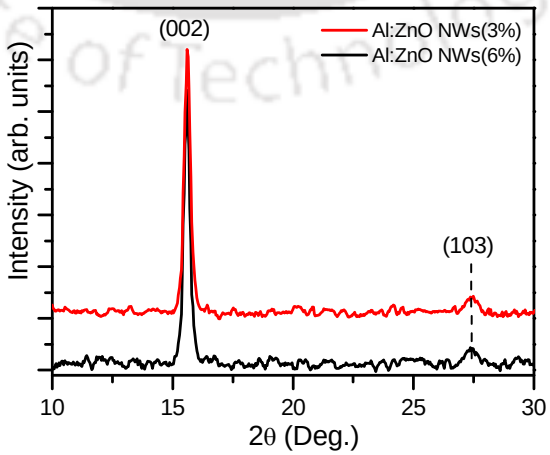

Figure 3.12: XRD patterns of the Al doped ZnO NWs, where Mo (λ=0.7093Å) x-ray gun was used.

almost identical covalent radius of Al atom (121 pm)[219] and the Zn atom (122 pm). Formation of interstitial Al atoms is also possible, however the chances are lower compared to the possibility of substitutional doping. Therefore, incorporation of Al into ZnO leads to slight decrease of lattice constants in ZnO, resulting in the compressive strain in the Al:ZnO NWs. It is known that, strain has a strong affect on the optical properties, as it directly influences the band gap of the material. Compressive strain usually leads to increase in band gap and the tensile strain leads to decrease in band gap. [220,221] Therefore, a change in optical properties with band gap widening is expected from the Al:ZnO NWs and this is discussed in the next chapter.

3.2.2. TEM Imaging

The ZnO nanostructures are further investigated by employing TEM imaging and SAED pattern. Figure **3.13(a-c)** shows the typical TEM images of NWs, nanoribbons and NRs, respectively synthesized by using ZnO nano powder. The diameters of the NWs, nanoribbons and NRs are found to be 50, 402 and 240 nm, respectively. The diameters

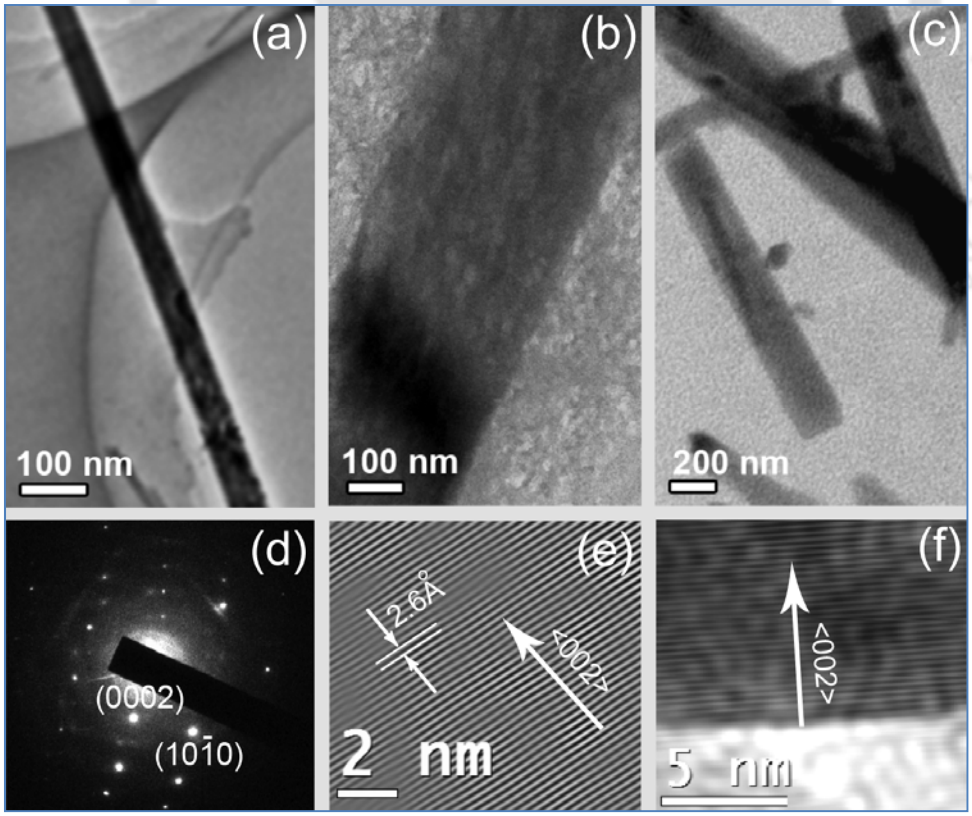

Figure 3.13: (a) TEM images of ZnO: (a) nanowire, (b) nanoribbon and (c) NRs grown at different temperatures; (d) SAED pattern of the corresponding nanowire; (e) and (f) HRTEM images of the corresponding nanowire and nanorod, respectively. These one–dimensional nanostructures are grown along <002> direction, which is the *c*–axis of hexagonal structure.

closely match with the sizes obtained from the SEM/FESEM images of these nanostructures. The SAED pattern of the NW is shown in Fig. **3.13(d)**, which can be indexed to (002) zone axis of the wurtzite ZnO. The SAED data for nanoribbons and NRs shows similar pattern. The SAED pattern confirms single crystalline growth along <002> direction. HRTEM images (Fig. **3.13(e and f)**) of the NW and NR does not show any extended defects in the crystal structure. To calculate the inter–planar spacing, an average value of inter–planar distance over a number of lattice fringes is considered. The inter planar spacing is found to be ~2.60 Å, equivalent to the spacing of (002) planes in wurtzite ZnO crystal indicating growth along <002> direction. Therefore, the HRTEM and SAED results are consistent with the XRD results discussed in earlier section.

Figure **3.14(a)** shows the TEM image of the 6% Al:ZnO NWs. The measured diameter of the NWs is in the range of 11–16 nm, which is in close agreement with the diameter obtained from the FESEM image. Figure **3.14(b)** shows the SAED pattern of the corresponding single NW, which clearly shows the intense diffraction spot of (002) planes. Figure **3.14(c)** shows the high–resolution lattice image taken from one end of single NWs (shown by dotted rectangle). The arrow shows the growth direction of the NW. The measured lattice spacing is 2.58 Å, which corresponds to the (002) plane. Therefore, the SAED pattern and lattice image confirm the one–dimensional single–crystalline structure of the Al:ZnO NWs. Compared to the d_{002} spacing (2.61Å) of the bulk ZnO, a smaller d_{002} spacing is obtained in the present case. Therefore, the Al:ZnO

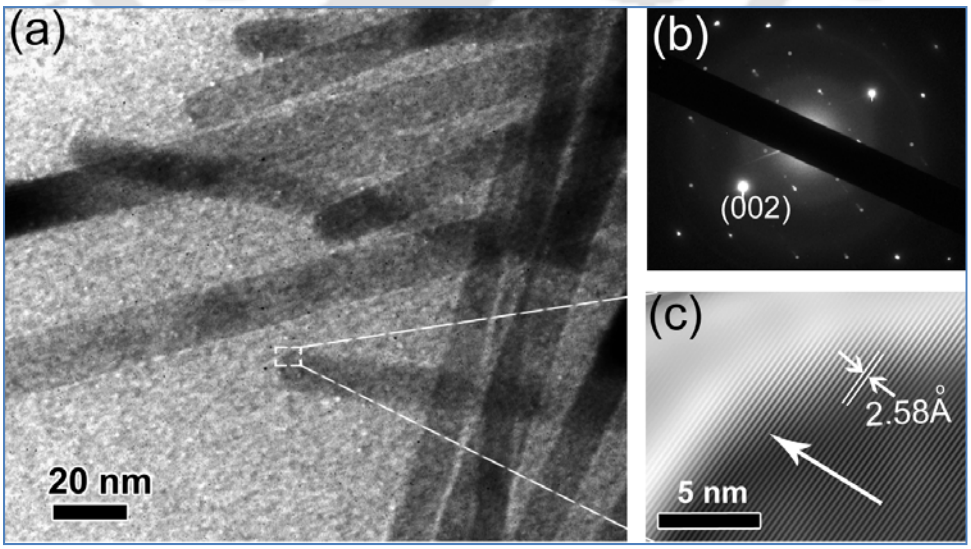

Figure 3.14: (a–b) TEM image of the Al doped (6%) ZnO nanowires and corresponding SAED pattern of one of the single nanowire. (c) High resolution lattice image of the nanowire taken from one end of the nanowire.

NWs are found to be strained and the nature of strain is compressive, which is fully consistent with the XRD results discussed in previous section.

3.2.3. Raman Scattering Studies

The ZnO NWs, nanoribbons and NRs are further studied by micro–Raman scattering measurements, which are shown in Fig. **3.15**. The Raman spectra of the ZnO NWs, nanoribbons and NRs show characteristic phonon modes of the good quality crystalline hexagonal wurtzite phase. The summary of the observed peak positions and corresponding intensities are presented in Table–**3.1**. The observed strong Raman mode at ~436.5 cm^{-1} corresponds to E_2^{high} phonon mode of wurtzite ZnO.[203] The occurrence of this peak is due to the vibration of oxygen atoms in ZnO lattice. Along with the strong E_2^{high} mode five other Raman modes of wurtzite ZnO phase are observed. These modes are located at ~330, ~379, ~408, ~540 and ~579 cm^{-1} corresponding to the $2E_2$, A_1^{TO}, E_1^{TO},

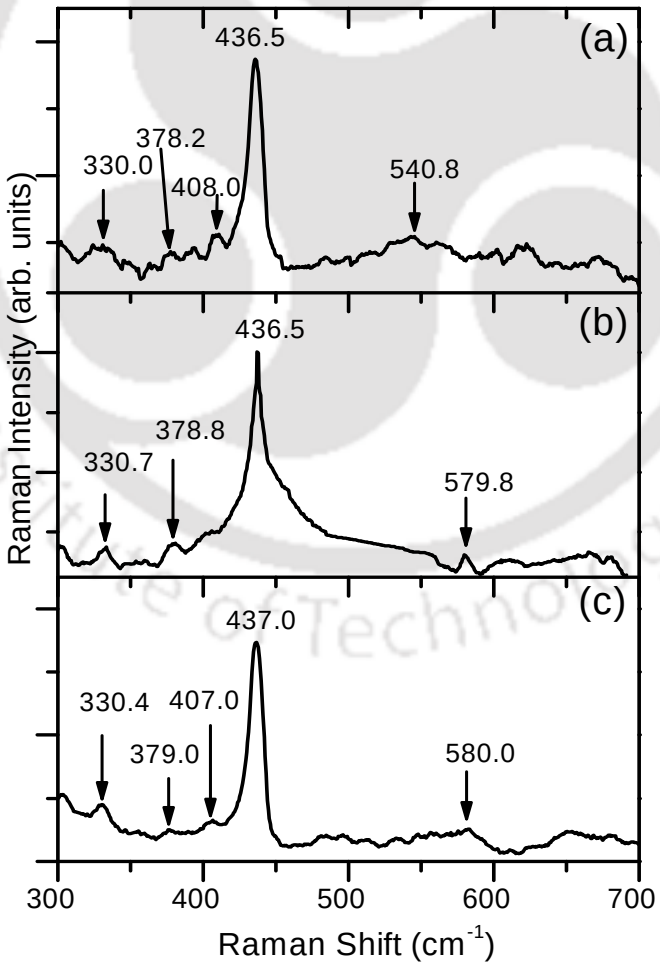

Figure 3.15: (a) The micro–Raman spectra of ZnO nanostructures: (a) nanowires, (b) nanoribbons and (c) nanorods grown by using ZnO nano powder.

$2LA$ and A_1^{LO} phonon modes of wurtzite ZnO, respectively. Compared to the Raman modes of strain free wurtzite ZnO (E_2^{high} mode at 438.0 cm^{-1}), the observed Raman peaks are found to be red shifted. This peak shift is due to the presence of a tensile strain in the as–grown ZnO nanostructures.[222] Besides the local heating effect on the Raman shift, a major contribution to the red shift comes from the tensile strain present in the as–grown ZnO nanostructures. In the present case, the quantum confinement effect is unlikely to affect the Raman modes due to the large size of the nanostructures as compared to exciton–Bohr radius of ZnO. Therefore, the Raman results of the as–grown ZnO nanostructures are in agreement with the XRD analysis.

Table 3.1: Summary of the observed peak positions and corresponding intensities (inside bracket) of the Raman modes of ZnO NWs, nanoribbons and NRs.

Sample	**Position of the Raman peaks in cm^{-1} (Intensity in arb. units)**					
	Peak I	Peak II	Peak III	Peak IV	Peak V	Peak VI
Nanowires	330.0 (186)	378.2 (169)	408.0 (223)	436.5 (764)	540.8 (206)	–
Nanoribbons	330.7 (144)	378.8 (161)	–	436.5 (750)	–	579.8 (284)
Nanorods	330.4 (158)	379.0 (76)	407.0 (106)	437.0 (692)	–	580.0 (116)
Peak Identity	$\boldsymbol{2E_2}$	$\boldsymbol{A_1^{TO}}$	$\boldsymbol{E_1^{TO}}$	$\boldsymbol{E_2^{high}}$	$\boldsymbol{2LA}$	$\boldsymbol{A_1^{LO}}$

Similar to the earlier mentioned Raman modes for the NWs, the Raman spectra of the combined seeded layer and Au catalyst assisted grown NWs show highly crystalline nature with very strong E_2^{high} mode, which is shown in Fig. **3.16**. Other Raman modes associated with the hexagonal phase are also observed with relatively weak intensities. It is found that the relative intensity of the E_2^{high} mode in the NWs grown at 800°C is much stronger than the case of NWs grown at 750°C, which indicates higher crystallinity. Very low value of FWHM (~7.3 cm^{-1}) of E_2^{high} mode further indicates highly aligned structure due to small area of scattering cross–section.

The structural quality of the Al:ZnO NWs is similarly checked by micro–Raman analysis. Figure **3.17** shows the Raman spectra of the 3% and 6% Al:ZnO NWs. The Raman spectra show characteristic Raman modes of hexagonal ZnO, which are summarized in Table–**3.2**. The Raman peaks at ~332, ~381 and ~438 cm^{-1} correspond to

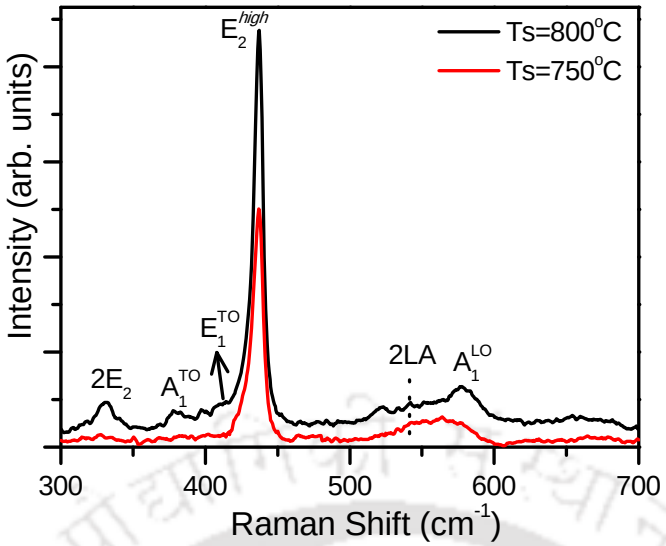

Figure 3.16: The micro–Raman spectra of the the combined seeded layer and Au catalyst assisted grown vertically aligned ZnO nanowires arrays, at substrate temperature (T_s) (a) 750° and 800°C, respectively.

$2E_2$, A_1^{TO} and E_2^{high} modes of hexagonal ZnO, respectively.[203] The strong E_2^{high} mode indicates the highly crystalline structure of the as–grown Al:ZnO NWs. It is also observed that with increase in Al doping concentration, the intensity of the E_2^{high} mode decreases. The observed intensity reduction indicates the deterioration of crystal quality. Along with the hexagonal modes, two additional modes are observed from both the samples, one at 620 $cm^{-1}$and other at 680 cm^{-1}. The intensity of the above two peaks are increases with the increase in Al concentration. In general, it has been observed that doping caused structural disorder in the host lattice. Therefore, above two peaks can be

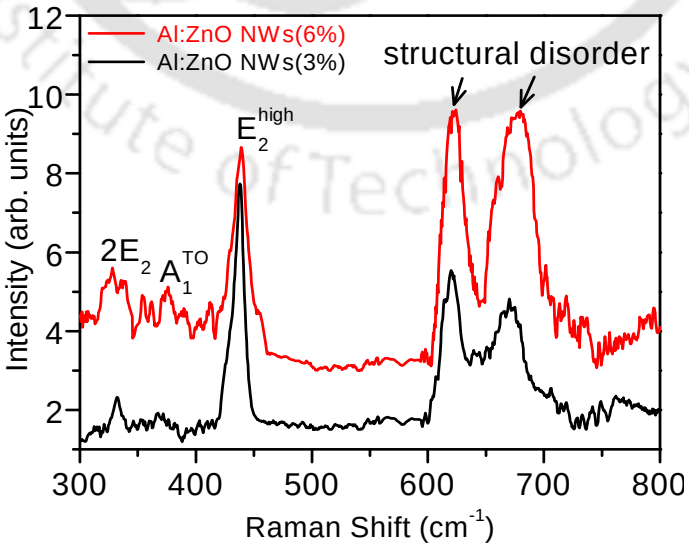

Figure 3.17: The micro–Raman spectra of the 3% and 6% Al doped ZnO nanowires, respectively.

attributed to the structural disorder induced modes, as both the peaks are not associated with the Raman modes of Al. Here, as the doping concentration is increased, the substitution of dopants into the Zn lattice can cause strain and the lattice oxygen can be shared by both Zn and Al. This will lead to neighboring disorder and local geometric disorientation, as a result increase in intensity of the disorder related peak. The strain–free ZnO bulk crystal shows E_2^{high} mode at 438 cm^{-1}. In the Fig. **3.17**, frequency of the E_2^{high} mode for 3% and 6% Al:ZnO NWs are at 438.1 cm^{-1} and 438.7 cm^{-1}, respectively. From previous studies, it has been seen that E_2^{high} mode is very sensitive to strain/stress state of ZnO crystal.[223,224] Therefore, high frequency shift of E_2^{high} mode is the result of increment of compressive biaxial strain. Earlier, similar compressive strain is detected from the Al doped ZnO thin films.[225]

Table 3.2: Summary of the observed peak positions and corresponding intensities (inside bracket) of the Raman modes of Al:ZnO NWs.

Sample	**Position of the Raman peaks in cm^{-1} (Intensity in arb. units)**				
	Peak I	Peak II	Peak III	Peak IV	Peak V
3% Al:ZnO Nanowires	332.0 (231)	382.0 (200)	438.1 (772)	620.0 (550)	680.0 (450)
6% Al:ZnO Nanowires	332.9 (229)	381.8 (201)	438.7 (551)	620.5 (665)	680.5 (640)
Peak Identity	$2E_2$	A_1^{TO}	E_2^{high}	***Structural Disorder***	

3.3. Structural Improvement by Rapid Thermal Annealing

ZnO nanostructures prepared by TVD technique are found to possess structural or morphological defects such as strain. So, it becomes necessary to adopt some mechanism to improve structural quality by removing such defects. One such effective route is RTA. To increase the structural quality, the as–grown ZnO NWs, nanoribbons and NRs were subjected to RTA at 700° and 800°C for 2 mins in argon gas medium. During RTA process, the heating and cooling rate was kept at a very high value of 30°C/s.

Figure **3.18** shows the XRD pattern of the as–grown and RTA treated (at 700°C) ZnO NWs grown by using ZnO nano powder. After the RTA process, no significant change in morphology is observed, while the sizes of the ZnO NWs, NRs and nanoribbons are slightly increased. With the increase in RTA process temperature, the position of the

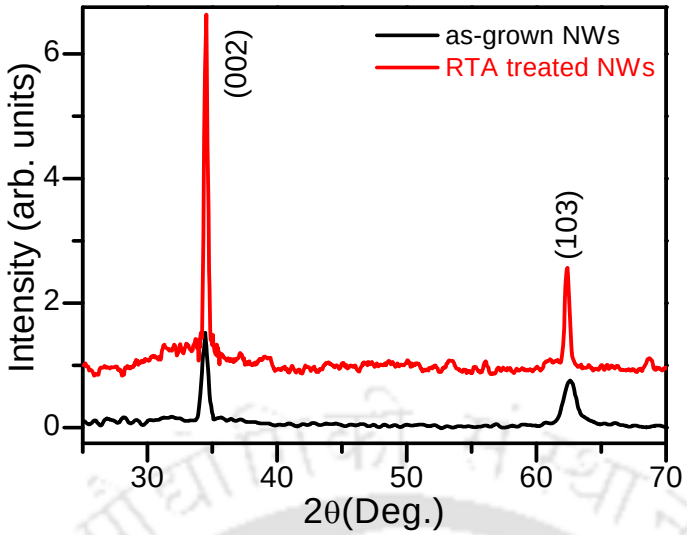

Figure 3.18: XRD pattern of the as–grown and RTA treated ZnO NWs processed at 700°C. These NWs were grown by using ZnO nano powder source.

diffraction peaks of ZnO NRs remain same, while the intensity of the (002) peak increases with the temperature, which indicates an improvement of crystalline quality of the nanostructures. We also observed a decrease in FWHM of (002) peak with increase in RTA temperature. The results imply that the NWs recrystallize during RTA processing; as a result crystallinity improved and strain is reduced in the RTA processed samples. RTA processed ZnO nanoribbons and NRs show similar structural changes.

The Raman spectra of the RTA processed ZnO NWs, nanoribbons and NRs are shown in Fig. **3.19**. It is evident from the spectra that RTA treated ZnO nanostructures show gradual enhancement in intensity of the E_2^{high} mode due to improved crystallinity. In case of NWs after RTA at 700°C, E_2^{high} mode intensity increases by a factor of 1.8, while that of the nanoribbons and NRs are 1.1 and 1.24, respectively. However, after the RTA treatment at 700°C, the FWHM of E_2^{high}mode is nearly doubled for the NWs and nanoribbons, while it is slightly reduced for the NRs. In case of NWs and nanoribbons, higher FWHM is primarily due to wider size distribution after RTA treatment. Similar trends in changes in the Raman spectra are observed for the nanostructures RTA treated at 800°C. Compare to the peak positions of the as–grown nanostructures, we observed a gradual blue shift with increase in temperature of RTA. Note that the RTA processed NWs clearly show an increase in Raman frequency. After RTA at 700°C, we observed a blue shift of 1.0 cm^{-1} for the E_2^{high} mode from that of the as–grown nanostructures. This blue shift confirms that tensile strain is reduced after RTA. And 800°C RTA processed

samples shows almost no strain.

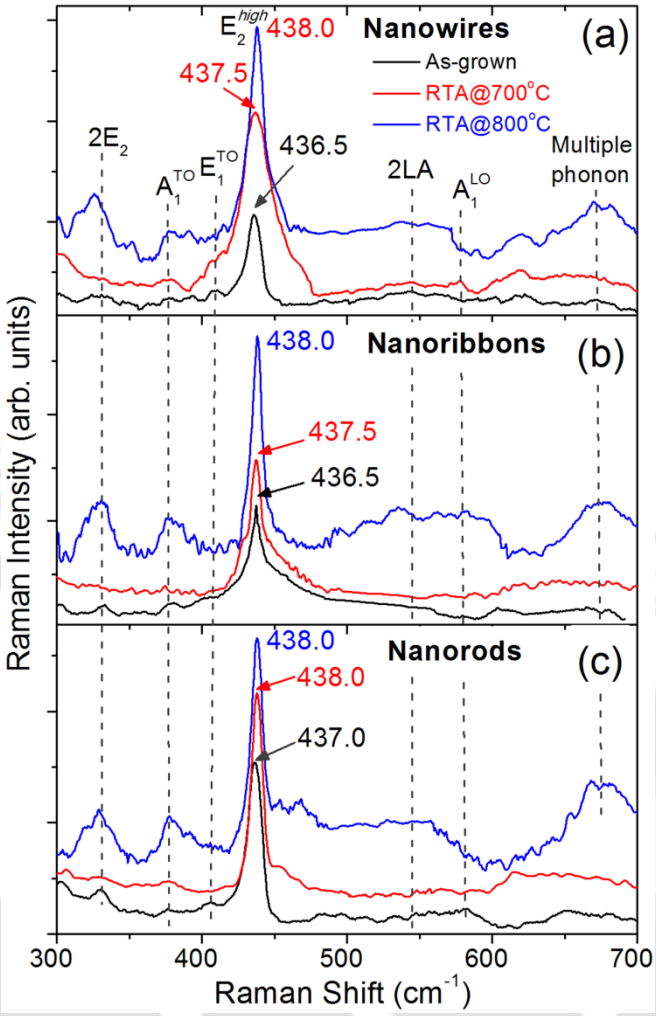

Figure 3.19: micro–Raman spectra of as–grown and RTA treated ZnO: (a) nanowires at 750°C, (b) nanoribbons and (c) nanorods. Along with the strong E_2^{high} mode, other Raman modes of wurtzite ZnO phase are observed from all the samples. These nanostructures are RTA treated at 700° and 800°C. A significant gradual blue shift in E_2^{high} mode is observed from all the samples.

Table 3.3: Summary of the peak positions and corresponding intensity of the E_2^{high} mode of as–grown and RTA processed ZnO nanostructures.

Sample	Position of the E_2^{high} mode in cm^{-1} (Intensity in arb. units)		
	As-grown	RTA at 700°C	RTA at 800°C
Nanowires	436.5 (764)	437.5 (1358)	438.0 (1617)
Nanoribbons	436.5 (750)	437.5 (814)	438.0 (1614)
Nanorods	437.0 (692)	438.0 (854)	438.0 (1096)

3.4. Summary

In this chapter we present a new growth strategy for the highly aligned vertical growth of ZnO NWs and NRs arrays and systematically studied the effects of several growth parameters on the morphology and alignment of the ZnO nanostructures. Al doped ZnO NWs is also successfully fabricated to study the effect of doping on the optoelectronic properties. The ZnO NWs and NRs are grown by two different methods, namely thermal vapor deposition and aqueous chemical method. The microstructure and quality of the as–grown and RTA treated NWs and NRs are characterized by using transmission electron microscopy, x–ray diffraction and micro–Raman spectroscopy techniques and explained. The important findings of this chapter are summarized below.

1. Effects of several critical growth parameters for the well–aligned and large surface area growth of ZnO NWs and NRs have been studied.
2. We demonstrated that the combined effects of ZnO seed layer and Au catalyst layer are favorable for the growth of well–aligned ZnO NWs and NRs arrays. ZnO seed layer and Au layer together act as a nucleation site and guide the NWs growth.
3. It is found that growth temperature and thickness of the seed layer primarily control the diameter of the NWs and NRs.
4. Shape evolution of ZnO nanostructures is observed and explained.
5. Zn vapor pressure, supersaturation rate, growth temperature and ultrathin catalyst layer are the key factors controlling the shape evolution.
6. Al doped ZnO NWs network of diameter 10–16 nm with different Al concentrations were synthesized by TVD method and characterized.
7. RTA is shown to improve the structural quality of the NWs and NRs by releasing the built–in stress and removing the defects partially.

Chapter 4
Optical Absorption and Photoluminescence Studies

In this chapter, the optical absorption and photoluminescence (PL) properties of the as–grown and processed ZnO NWs and NRs are presented. The PL spectroscopy is extensively used to study the band–edge related UV emission as well as to identify the origin of the broad visible emission. The origin of the visible emission in the PL spectra is directly correlated with the surface defects present on the as–grown samples. The ZnO NWs, nanoribbons and NRs grown by thermal vapor deposition (TVD) method using ZnO nano powder source, chemically grown ZnO NWs and Al doped ZnO NWs are used for the optical absorption and PL studies.

To improve the UV PL efficiency, a simple post–growth processing technique, rapid thermal annealing (RTA) has been employed and the resulting optical absorption and PL properties are studied. The PL decay process of the visible emission is also systematically studied by time–resolved PL (TRPL) spectroscopy to monitor the changes in the defect states after RTA processing.

4.1. As–grown ZnO Nanowires, Nanorods and Nanoribbons grown by TVD method

In this section, we present the absorption and PL properties of ZnO NWs, nanoribbons and NRs which were grown by TVD method using the nano powder source. For the UV–Vis absorption studies, the specular reflectance spectra of the samples were measured at an incident angle 45° in the range 200–900 nm. Thereafter the absorption coefficient for each wavelength is calculated according to the method proposed by Rusli *et al.*[205] as described in the Chapter–2. The room temperature PL spectra of the ZnO NWs,

nanoribbons and NRs were measured under the excitation at 325 nm from a steady–state He–Cd laser.

4.1.1. Specular Reflection Studies

Figure **4.1** shows the UV–Vis specular reflectance spectra of the as–grown ZnO NWs (grown at 750°C), nanoribbons and NRs, respectively. When the incident photon energy is larger than the direct band gap energy of ZnO (λ<367 nm), the reflectance is related with band–gap absorption, leading to a flat and very low reflectance. When the incident photon energy is below the band–gap energy of ZnO (λ>367 nm), observed reflectance characteristics can be correlated with the structural properties instead of band–gap absorption. All the samples exhibits significantly low reflectance over a wide range of wavelengths. In addition, the reflectance spectra reveal interference oscillations. The observed oscillation is due to multiple internal reflections between air–NWs and NWs–substrate interface.[226] The periodicity of the reflectance oscillation is inversely proportional to the wavelength of the incident light. The as–grown NWs shows a maximum reflectance of ~16% in the range 200–900 nm. While for the nanoribbons and NRs, the maximum reflectance is 23% and 28%, respectively.

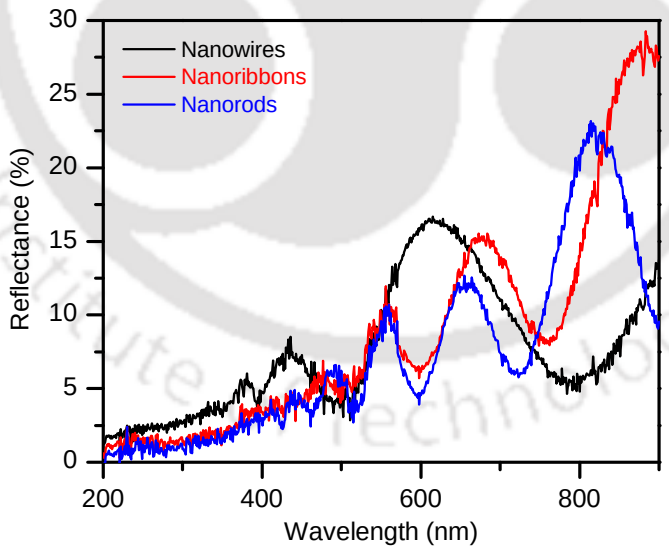

Figure 4.1: UV–Vis specular reflectance spectra of the as–grown ZnO nanowires, nanoribbons and nanorods synthesized from ZnO nano powder source.

4.1.2. Optical Absorption Studies

The variation in absorption coefficient of the ZnO nanostructures calculated from their corresponding reflectance spectrum is shown in Fig. **4.2**. The UV–Vis absorption spectra

of the ZnO nanostructures show a high absorption in the UV region with a sharp peak at 367 nm. This absorption peak is due to the corresponding band–to–band transition in ZnO. The weak absorption in the visible region of 400–550 nm is due to the absorption by the surface defects present on the as–grown ZnO nanostructure. The NWs shows comparatively higher band edge absorption and very low absorption in the visible region. Whereas, lower band edge absorption and comparatively higher visible absorption found in the nanoribbons and NRs indicate presence of high density of surface defect states.

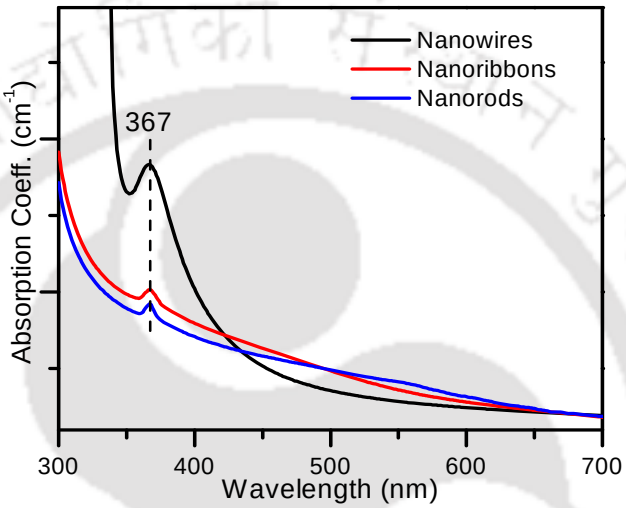

Figure 4.2: UV–Vis absorption spectra of the as–grown ZnO nanowires, nanoribbons and nanorods, calculated from corresponding reflectance spectra.

4.1.3. Photoluminescence Studies

The room temperature PL spectra of the ZnO NWs (grown at 750°C), nanoribbons and NRs are shown in Fig. **4.3**, which are measured under identical conditions. ZnO NWs exhibit strong near band edge (NBE) UV emission at 380 nm and a broad green emission peak [Fig. **4.3(a)**]. On the other hand, nanoribbons and NRs show relatively weak UV emission peak with nearly equal intensities at ~380 nm and an intense broad green emission band at ~527 nm [Fig. **4.3(b–c)**]. The PL spectra of the ZnO nanostructures are fully consistent with their corresponding absorption spectra. The exact positions and other parameters of the constitute PL peaks are obtained from the Gaussian multi–peak fitting to the experimental data points, and these are tabulated in Table **4.1**. The Gaussian fitting reveals that the broad green emission band constitutes of two Gaussian peaks, one at ~500 nm and other at ~545 nm, as shown by the fitted line. The NBE emission is due to the free excitonic recombination and green emission at ~500 nm is attributed to the recombination of photo–generated holes with the electrons belonging to oxygen vacancy

states on the surface.[122] And the other green emission band at ~545 nm is due to presence of deep interstitial oxygen inside the nanostructure.[117] With increase in growth temperature, intensity of the 1st green emission is increased by 3.12 times for the nanoribbons and 4.08 times for the NRs, as compared to the peak intensity of the NWs. Whereas, intensity of ~545 nm peak is increased by 3.44 times for the nanoribbons and then decreased to 2.17 times for the NRs. The intensity ratio of 1st to 2nd green emissions is calculated to be 0.89, 0.82 and 2.29 for the NWs, nanoribbons and NRs, respectively. Since the ZnO NRs and nanoribbons are grown at relatively higher temperatures where oxygen vapor pressure is relatively low compared to the low temperature growth region this results in the formation of large number of oxygen vacancy related defect states. As a result, stronger green emission is observed from the NRs/nanoribbons. The PL results

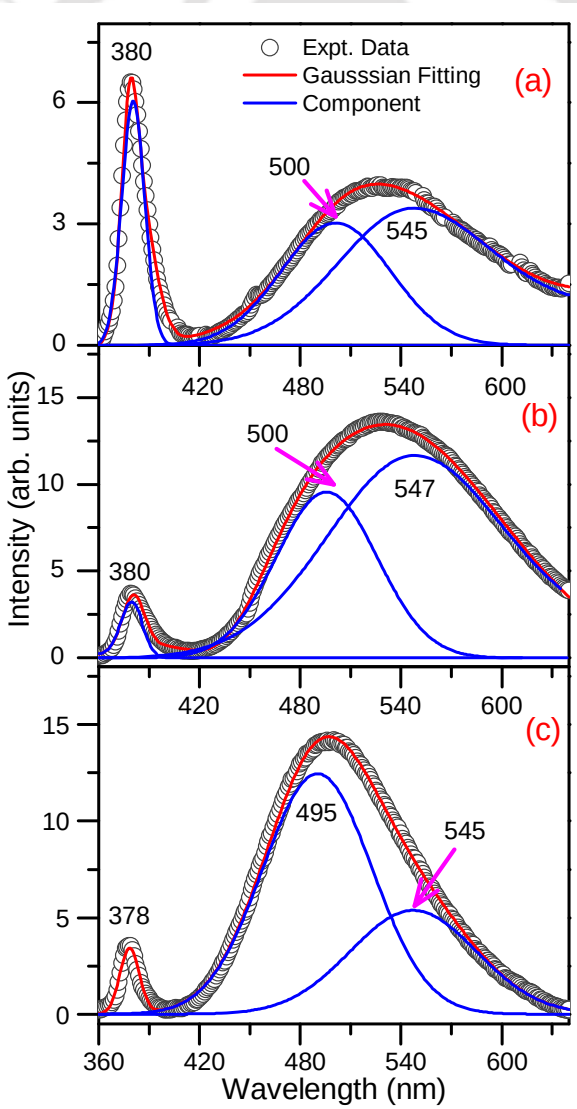

Figure 4.3: Room temperature PL spectra of the as–grown ZnO: (a) nanowires, (b) nanoribbons and (c) nanorods synthesized from ZnO nano powder source. Solid lines are the fitted line with Gaussian function to the experimental data.

on the ZnO NWs, NRs and nanoribbons are consistent with the earlier reports,[112,227,228] which show relatively weak UV emission in the nanostructures grown at relatively higher temperature. FWHM of the above mentioned PL peaks are marginally constant for the NWs, nanoribbons and NRs.

Table 4.1: Summary of the Gaussian fitted parameters for the PL spectra of the ZnO nanowires, nanoribbons and nanorods.

Sample	Peak I			Peak II			Peak III		
	Centre (nm)	Ampl. (count)	FWHM (nm)	Centre (nm)	Ampl. (count)	FWHM (nm)	Centre (nm)	Ampl. (count)	FWHM (nm)
Nanowires	380	6.1	13.6	500	3.1	76.8	545	3.4	103.9
Nanoribbons	380	3.2	15.4	500	9.5	70.5	547	11.7	128.2
Nanorods	378	3.4	13.0	495	12.3	78.0	545	5.4	116.5
Peak identity	**Free exciton**			**Oxygen vacancy defects**			**Deep interstitial oxygen defects**		

4.1.4. Time–resolved Photoluminescence Studies

The steady–state PL spectra indicate the presence of defects in the as–grown ZnO nanostructures, which are essentially radiative trap centre and these affect the intrinsic PL decay behavior. In order to study the PL decay dynamics of the green emission from the ZnO nanostructures, we measured TRPL decay at 500 nm using a pulsed 375 nm

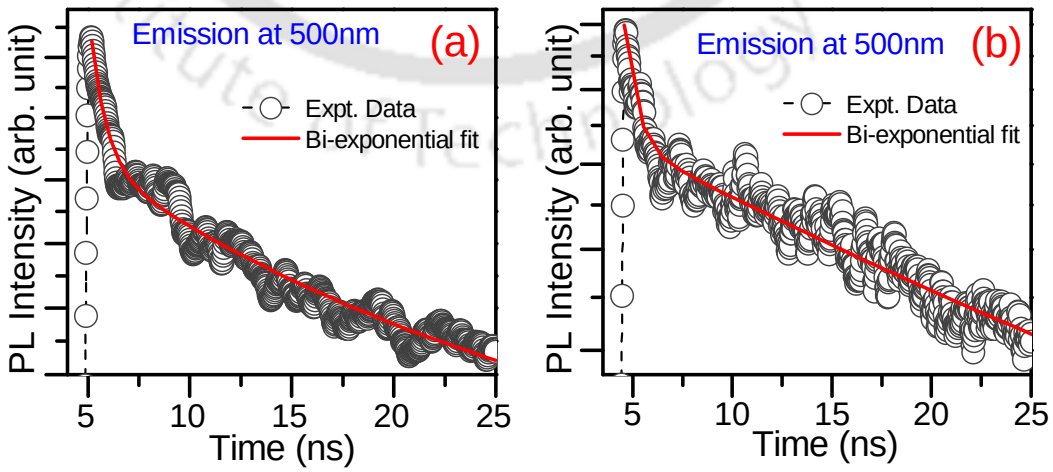

Figure 4.4: PL decay profile of the as–grown ZnO: (a) nanowires and (b) nanorods. The PL decay was measured at emission wavelength of 500 nm.

laser excitation and the results are shown in Fig. **4.4**. The as–grown ZnO NWs (grown at 750°C) and NRs show a bi–exponential decay in the TRPL data. The observed decay can be fitted with a bi–exponential decay equation

$$I = I_0 + A_1 e^{-t/\tau_1} + A_2 e^{-t/\tau_2} \quad \text{..... (4.1)}$$

where τ_1 and τ_2 are the decay time constants. The fitted parameters are tabulated in Table **4.2**. The NWs show τ_1=0.75 ns and τ_2=23.8 ns, while the NRs shows τ_1=0.58 ns and τ_2=38.2 ns. Two different time constants are associated with the two different defects states having different radiative decay channels and this is consistent with the steady state PL spectra described in the previous subsection. The relative amplitude ratios of the decay time constants are found to be 322 and 809 for the ZnO NWs and NRs, respectively. From the ratio of their relative amplitude, τ_1 can be attributed to decay time constant of 1st green emission (~500 nm) and τ_2 can be attributed to decay time constant of 2nd green emission (~545 nm). Our results are consistent with previous reports on green emission from ZnO NPs, thin films and doped NWs with decay time constants in µs range.[229-231] However, in the present case due to the presence of high density of trap centers, it is in the range of ns.

Table 4.2: Summary of the bi–exponential fitting parameters for the PL decay in ZnO nanowires and nanorods.

Sample	PL decay time constants at emission wavelength 500 nm (ns)		Amplitude Ratio (A_1/A_2)
	τ_1	τ_2	
Nanowires	0.75±0.08	23.8±0.37	322
Nanorods	0.58±0.08	38.2±0.32	809

4.2. Effect of Rapid Thermal Annealing

In the previous chapter, we have seen that the RTA processed ZnO nanostructures show improvement in the structural quality. Therefore, one would expect improvement in the UV PL emission as well as the subsequent reduction in the defects from the RTA processed ZnO NWs, nanoribbons and NRs. In this section, results of the absorption and PL studies of the RTA processed ZnO NWs, nanoribbons and NRs are presented.

4.2.1. Specular Reflection Studies

Figure 4.5 shows the UV–Vis specular reflection spectra of the as–grown and RTA treated ZnO NWs processed at 700° and 800°C. The as–grown NWs shows a maximum reflectance of ~16% in the 200–900 nm range, whereas after RTA, it increases to 40% in the transparent region of ZnO. This increase of the reflectance can be explained on the basis of modification in the structural characteristics (diameter of the NWs, surface roughness, defects etc) during RTA treatment. Huang *et al.*[232] reported similar reflection spectra of the hydrothermally grown ZnO NWs with highest reflection of 18%. Note that after RTA processing, the reflectance magnitude is reduced below the band–gap wavelength of ZnO (~367nm) and enhanced above the band–gap wavelength, which indicates an enhancement in absorption intensity below the band–gap wavelength and a reduction in absorption intensity above this wavelength. This reduced absorption in the visible region clearly indicates the reduction of oxygen vacancy states after RTA processing. Note that the magnitude of reflectance in the UV region (200–400 nm) is quite low (average value ~2.7%), which indicates a very high absorption in this region. The high UV absorption of the ZnO NWs demonstrates its suitability for the use in UV photodetctors.

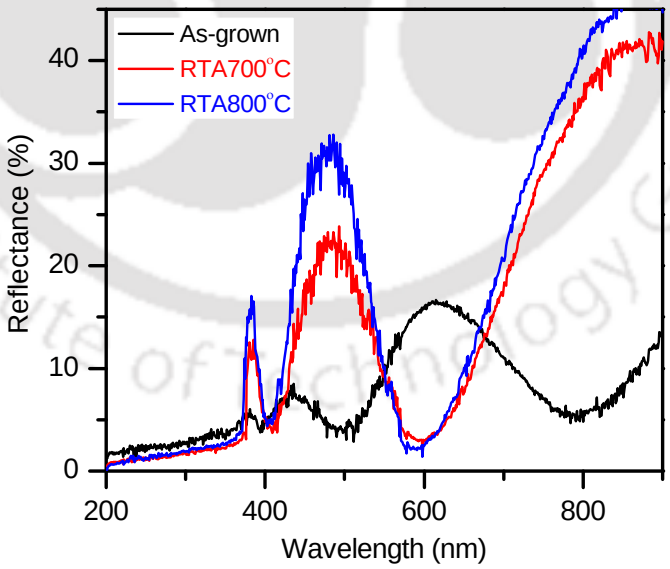

Figure 4.5: UV–Vis specular reflectance spectra of the as–grown and RTA treated ZnO nanowires processed at 700° and 800°C.

4.2.2. Optical Absorption Studies

The UV–Vis absorption spectra of the as–grown and RTA treated ZnO NWs processed

at 700° and 800°C [Fig. **4.6**] show a high absorption in the UV region with a sharp peak at 367 nm corresponding to the band–to–band absorption. After RTA treatment, the intensity of the UV–absorption peak is enhanced by a factor of ~1.4, compared to the as–grown case. Note that visible absorption is considerably reduced in 800°C RTA treated ZnO NWs, implying significant reduction of the defect density as a result of RTA processing. The RTA treated ZnO nanoribbons and NRs show similar changes in the absorption spectra. Therefore, it is expected that the RTA treated ZnO NWs, nanoribbons and NRs will results in enhanced UV PL as well as photocurrent in the UV region.

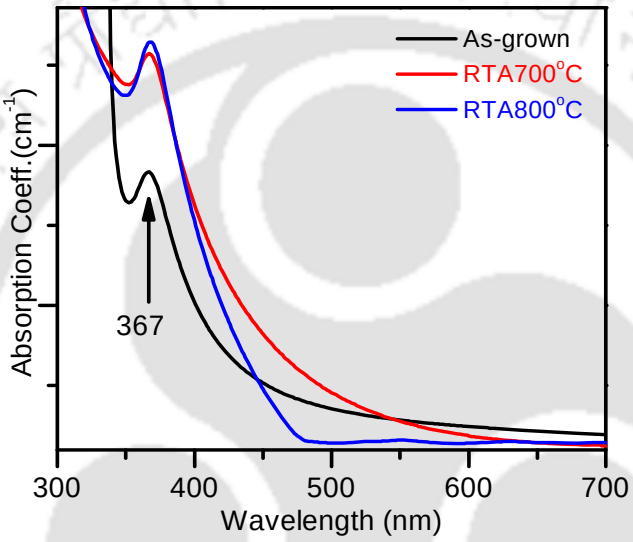

Figure 4.6: UV–Vis absorption spectra of the as–grown and RTA treated ZnO nanowires processed at 700° and 800°C, calculated from corresponding reflectance spectrum.

4.2.3. Photoluminescence Studies

The PL spectra of the RTA treated ZnO nanostructures processed at 700° and 800°C are shown in Fig. **4.7**. It is observed that the UV emission peak intensity of the RTA treated ZnO nanostructures are enhanced by three–five folds as compared to the as–grown nanostructures.[233] After the RTA, no significant shift in the UV emission peak is observed. The peak parameters obtained from the Gaussian fitting are summarized in Table **4.3**. Note that after the RTA, the intensity of the green emission band is considerably reduced for the nanoribbons and NRs, while the peak at 545 nm is fully suppressed from all the samples. This implies that the interstitial oxygen defect states are substantially reduced in the RTA treated ZnO nanostructures. However, a new emission band is observed at ~390 nm after RTA, which may be due to the recombination at band tail states.[234]

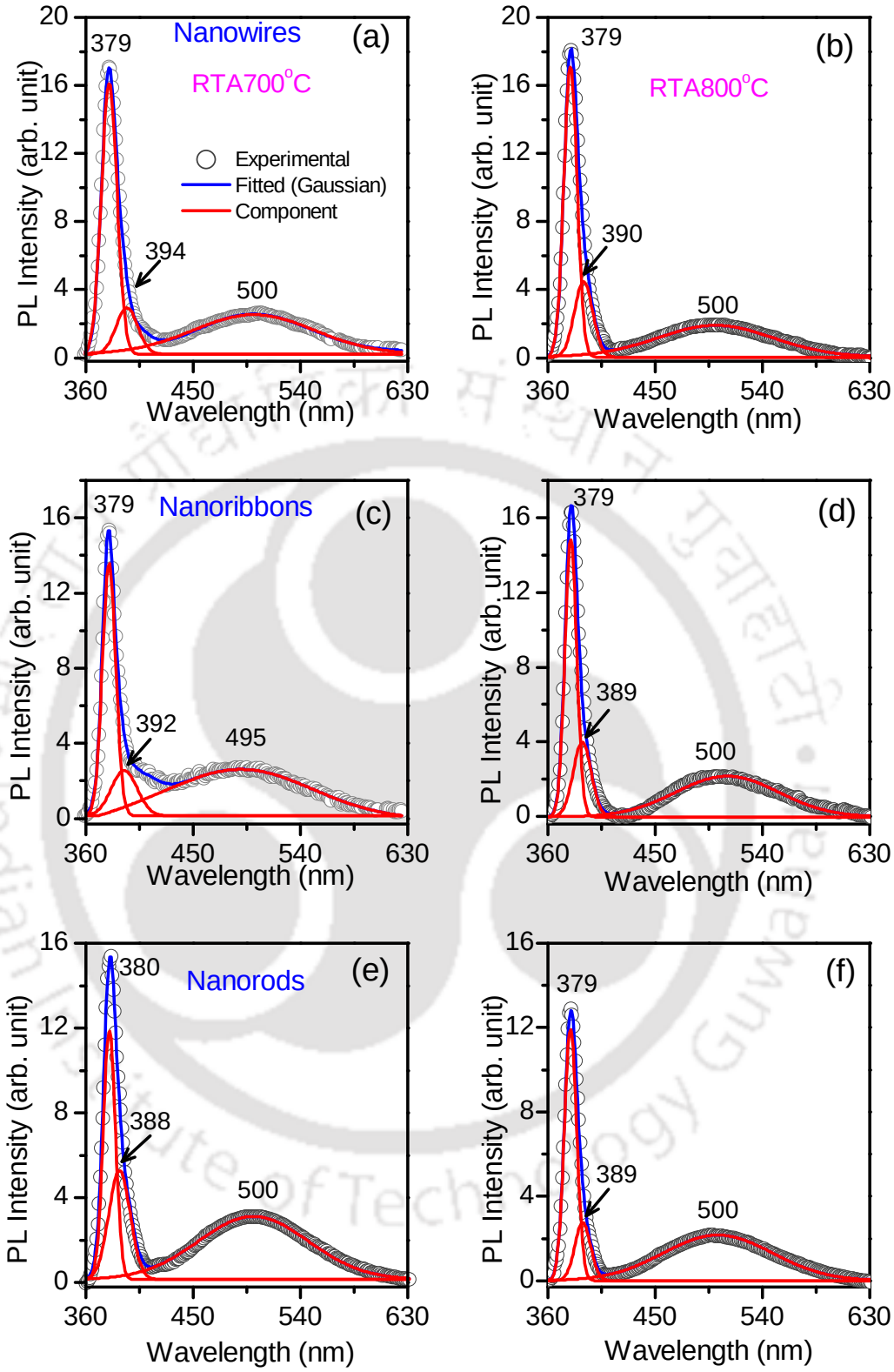

Figure 4.7: Room temperature PL spectra of the ZnO: (a–b) RTA treated nanowires at 700° and 800°C; (c–d) nanoribbons at 700° and 800°C; (e–f) nanorods at 700° and 800°C, respectively. The ZnO nanowires, nanoribbons and nanorods were grown at 750°C, 850°C and 870°C, respectively. Solid lines are the fitted curve with Gaussian function to the experimental data.

Table 4.3: Summary of the PL peak parameters for the ZnO nanowires, nanoribbons and nanorods. Peak centre and FWHM are expressed in nm unit.

Sample		RTA 700°C			RTA 800°C		
		Peak I	Peak II	Peak III	Peak I	Peak II	Peak III
Nanowires	Centre	379	394	500	379	390	500
	Ampl.	16.1	2.9	2.5	18.0	4.3	1.8
	FWHM	15.4	21.2	119.6	12.4	19.4	113.4
Nanoribbons	Centre	379	392	495	379	389	500
	Ampl.	13.6	2.6	2.6	14.8	4.0	2.1
	FWHM	13.2	25.5	171.7	11.7	17.7	101.7
Nanorods	Centre	380	388	500	379	389	500
	Ampl.	11.9	5.3	3.1	11.9	2.7	2.1
	FWHM	12.0	21.1	108.0	12.2	15.5	107.7

Figure **4.8** shows the variation in intensity of various PL peaks with the growth temperatures for the as–grown and RTA treated ZnO NWs, nanoribbons and NRs. The intensity ratio of 380 nm to 500 nm peak [Fig. **4.8(a)**] slowly decreases with the increase in growth temperature, which indicates the formation of large number of trapping centres at higher growth temperatures. After RTA at 700°C, this intensity ratio is nearly doubled for the NWs, while this enhancement is one order of magnitude for the nanoribbons and NRs. The nanostructures RTA treated at 800°C shows the similar changes in the peak intensity ratio with higher value of enhancement factors. The relative change in intensity before and after RTA for the 380 nm and 500 nm peaks are shown in Fig. **4.8(b–c)**. The

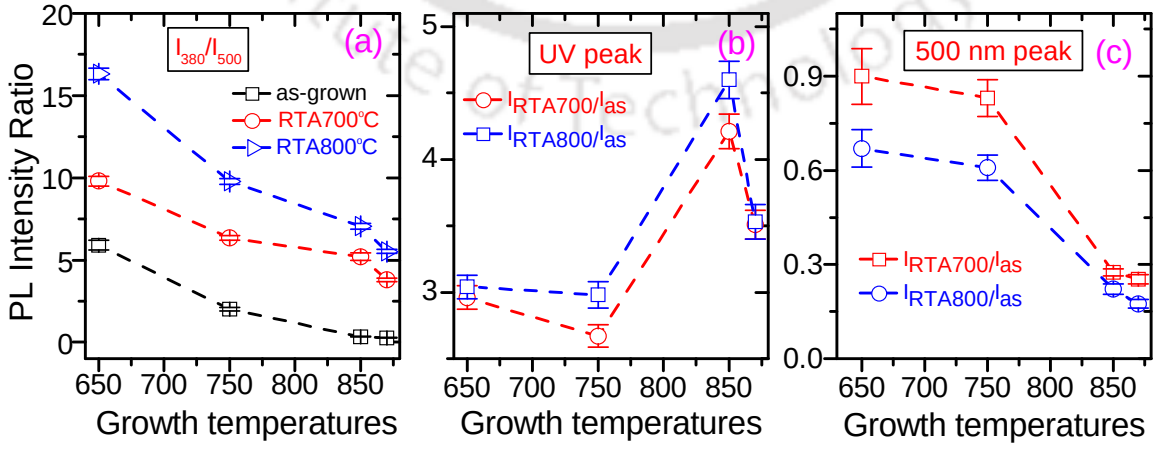

Figure 4.8: Variation in intensity ratio of different PL emission bands as a function of growth temperatures. These nanostructures are RTA treated at 700° and 800°C.

380 nm band shows a gradual increase in intensity with increase in growth temperature, while the 500 nm band intensity correspondingly decreases. The enhancement factor of the UV emission is increased while the enhancement factor for the green emission is decreased with RTA annealing at higher temperature. After RTA treatment, the FWHM of 380 nm peak is marginally reduced while the FWHM of the 500 nm peak is nearly doubled.

4.2.4. Time–resolved Photoluminescence Studies

As the RTA processing reduces the defect states, it is expected that it will affect the PL decay dynamics for the defect related green emission. To study the changes in defect states with RTA, we measured TRPL decay of green emission at 500 nm. Figure **4.9** shows the PL decay profile of the ZnO NWs and NRs after RTA treatment. The data fit well to a single exponential decay pattern indicating only one decay channel after the RTA processing. The observed decay channel is associated with the 500 nm component in the PL and it confirms the suppression of 545 nm component after RTA, consistent with the steady state PL spectra. After RTA processing at 700°C, the measured decay time constants are 0.93 ns and 2.0 ns for the NWs and NRs, respectively. Note that, the time constant of 500 nm peak is increased from 0.75 to 0.93 ns for the NWs and 0.58 to 2.0 ns for the NRs, respectively. With further annealing at higher temperature, the time

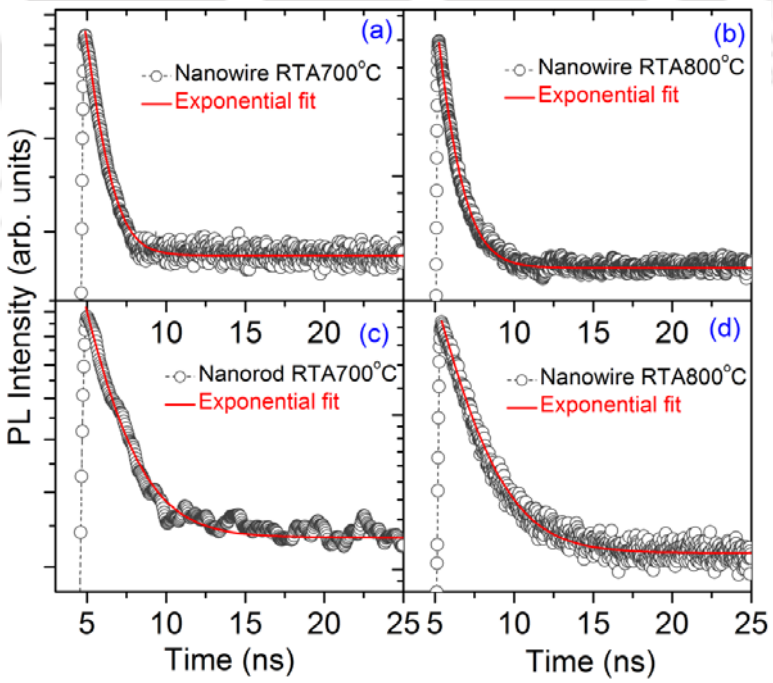

Figure 4.9: PL decay profile of the RTA treated ZnO: (a) nanowires and (c) nanorods, processed at 700° and 800°C, respectively.

constants increase. Therefore, the RTA processing slows down the decay rate of green emission band. This is due to the reduction in the density of surface defect states, as τ is inversely proportional to trap density N_t. This result is consistent with the steady state PL data of the RTA treated ZnO nanostructures, where reduction in green emission intensity was evident.

4.3. Photoluminescence of Chemically Grown ZnO Nanowires

The room temperature PL spectrum of the chemically grown ZnO NWs is shown in Fig. **4.10**. As–grown NWs exhibits NBE UV emission at 379 nm and a broad visible emission band in the blue–green region. Gaussian multi–peak fitting shows the existence of two emission bands, one at blue region and another at green region. The first one is centred at ~436 nm and second one is at 520 nm. The observed NBE emission is due to free excitonic recombination while the blue emission and green emission are due to the presence of interstitial zinc (Zn_i)[117] and single ionised oxygen vacancy (V_o^+)[122], respectively. The strong blue peak indicates the formation of dense interstitial zinc states in the as–grown ZnO NWs. It is known that in aqueous chemical method the zinc nitrate provides Zn^{2+} ions whereas the H_2O supply the OH^- ions required for the oxidation of Zn^{+2} ions. Due to the comparatively faster rate of hydrolysis of zinc nitrate than the H_2O, the formation of high density of interstitial zinc in the as–grown NWs is quite expected.

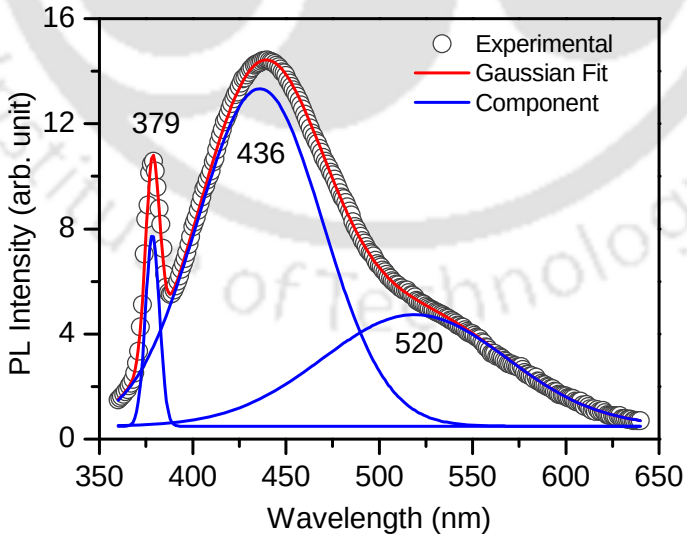

Figure 4.10: Room temperature PL spectrum of the chemically grown ZnO nanowires.

4.4. Effect of Al Doping on the ZnO Nanowires

In this section, we present the effect of Al doping on the optical absorption and PL

properties of the Al:ZnO NWs. In the previous chapter, we have seen from the structural characterization that the Al:ZnO NWs contains compressive strain. Therefore, in this case a band gap widening is expected. To study this, we utilized the absorption and PL spectroscopy and the results are discussed below.

4.4.1. Absorption Studies

The absorption spectra of the Al:ZnO NWs are calculated from their corresponding reflectance spectrum according to the method as described in the Chapter–2. The UV–Vis absorption spectra of the Al:ZnO NWs is shown in Fig. **4.11**. Absorption spectra show a sharp UV absorption edge. Compared to the absorption edge of undoped ZnO NWs (367 nm),[189] we observed a systematic blue shift in absorption edge as a function of Al doping concentration. The 3% Al:ZnO NWs shows absorption edge at 364 nm and with further doping it is shifted towards lower wavelength. The observed blue shift indicates a band gap widening in the Al:ZnO NWs due to the Al incorporation in the ZnO lattice. This is consistence with the XRD results presented in the previous chapter. The band gap widening is possibly due to the presence of compressive strain in the Al:ZnO lattice. It is also known that, there is a possibility of band gap widening in doped semiconductors due to Burstein–Moss (BM) effect.[235,236] The Burstein–Moss effect is seen in semiconductors as a shift in band gap with increasing doping. The shift arises because the Fermi energy (E_F) lies in the conduction band for heavy *n*–type doping (or in the valence band for *p*–type doping). The filled states therefore block thermal or optical excitation. Consequently the measured band gap determined from the onset of interband

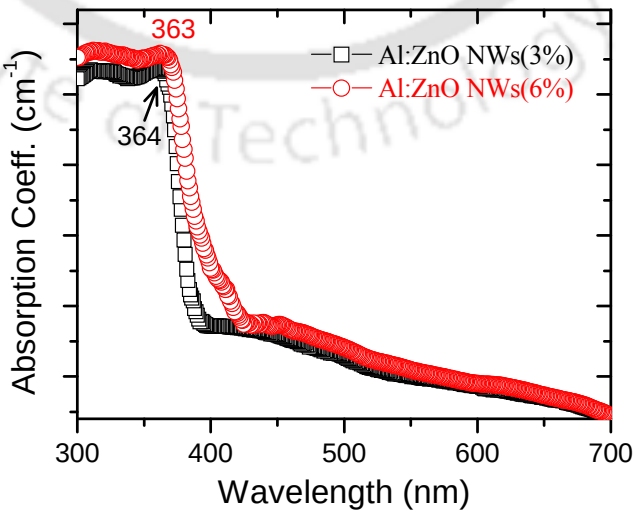

Figure 4.11: UV–Vis absorption spectra of the 3% and 6% Al doped ZnO nanowires.

absorption moves to higher energy (i.e. suffers "a blue shift"). Therefore, the observed band gap widening is attributed to the combined effects of compressive strain and BM effect. The Al:ZnO NWs also show absorption in the blue–green region, which is attributed to the surface defects related absorption.

4.4.2. Photoluminescence Studies

The room temperature PL spectra of the Al:ZnO NWs are shown in Fig. **4.12**. The Al:ZnO NWs exhibit NBE UV emission at ~378 nm and a broad green emission band. Constitute two green emissions in the broad emission are obtained from the Gaussian multi–peak fitting. 1st green emission is centred at 494 nm and the 2nd green emission is at 545 nm. It is found that the intensities of the UV PL as well as the green emission gradually increase with increase in Al concentration. The PL spectra are consistent with the absorption spectra, which show enhancement in the peak intensities in the UV as well as visible region. Compared to the peak position of the UV PL in undoped ZnO NWs (at 380 nm), here we observed a blue shift in the UV PL peak from both the samples.

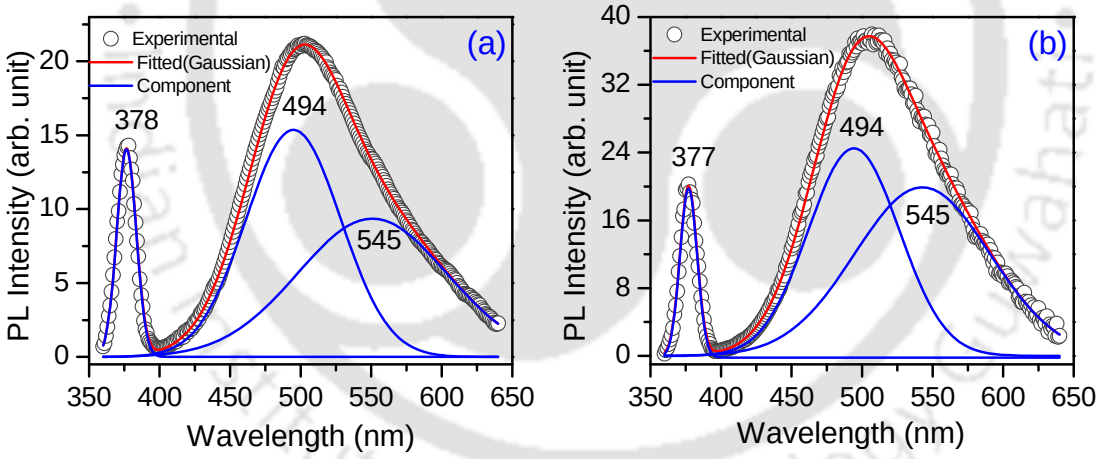

Figure 4.12: Room temperature PL spectra of the: (a) 3% and (b) 6% Al doped ZnO nanowires.

4.5. Summary

In this chapter, we studied the optical absorption and PL properties for the as–grown and RTA processed ZnO NWs, nanoribbons and NRs. The PL properties are studied in details and the emissions which are not associated with the ZnO band–to–band transition are directly correlated with the surface defects present on the samples. The observed changes in the absorption and PL properties after the RTA processing of ZnO NWs,

nanoribbons and NRs are studied systematically and explained. The important findings of this chapter are summarized below.

1. Structural quality of the as–grown ZnO NWs, nanoribbons and NRs are assessed from optical absorption and photoluminescence studies. Presence of several kinds of surface defects have been confirmed and identified from the studies.
2. In the as–grown NWs/NRs, the band–edge emission intensity is very low due to the presence of surface defects.
3. We have shown that the RTA processing is an important and effective tool to improve the structural quality as well as the UV PL emission efficiency of the ZnO NWs, nanoribbons and NRs.
4. With RTA processing, the band–edge emission intensity is enhanced by 3–5 times, while the green emission is significantly reduced.
5. The Al doping in the ZnO NWs causes band gap widening. The PL spectra shows increment of surface defect related peak intensity with increase in Al concentration due to the deterioration of the structural quality.

भारतीय प्रौद्योगिकी संस्थान गुवाहाटी
Indian Institute of Technology Guwahati

Chapter 5
UV Photodetection in ZnO Nanowires

Since the conductivity of the ZnO NWs increases under the illumination of UV light, we studied the photodetection behaviour of the ZnO NWs for the use in UV photodetectors. In this chapter, the UV photocurrent and photoresponse of the as–grown and RTA processed NWs array are presented. We report on the major improvement in photodetection behavior of the RTA processed ZnO NWs array and the origin of enhancement is investigated. The photocurrent growth and decay behaviours under the UV excitation and dark conditions are studied in detail to understand the mechanism of conductivity enhancement under the excitation of UV light. The photoresponse mechanism of the ZnO NWs is explained through an appropriate model. The effect of Al doping on the photoresponse behaviour of the ZnO NWs is also studied.

5.1. Photodetection Studies of as–grown ZnO Nanowires

The ZnO NWs grown at 750°C by TVD method using ZnO nano powder source is used for the photodetection studies. The collective photocurrent (PC) passing through the bundle of vertically aligned NWs array was measured under the excitation of monochromatic light at different wavelengths in the range of 300–700 nm. The PC growth and decay behaviours (photoresponse) are also studied at an excitation wavelength of 360 nm, where the PC is high. The mechanism of the photoresponse behaviour is explained through photogeneration, recombination, surface adsorption and photodesorption processes.

5.1.1. Dark Current–Voltage Characteristic

The dark current–voltage (I–V) characteristic of the as–grown ZnO NWs shown in Fig. **5.1** shows a linear behavior up to a certain bias voltage, after that there is a rapid change in current with voltage. The transition from linearity in the I–V characteristic is probably due to presence of defect states which release electrons at higher bias voltage and contributes to the current conduction process.

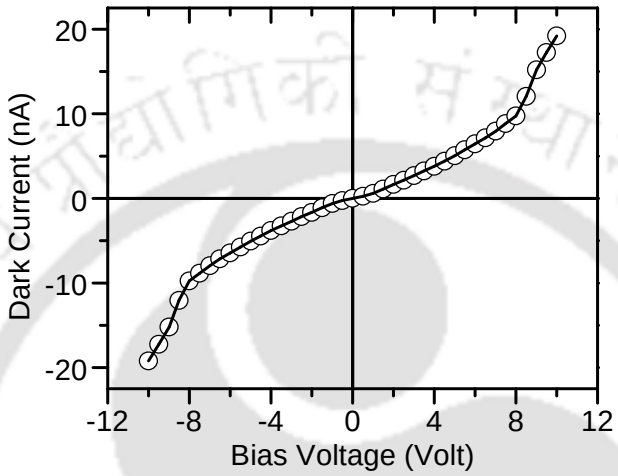

Figure 5.1: The dark current–voltage (I–V) characteristics of as–grown ZnO Nanowires.

5.1.2. Spectral Dependence of Photocurrent

Figure **5.2(a)** shows the PC spectra of the as–grown ZnO NWs, measured at a bias of 2.5 V, which shows a strong PC peak at 369 nm and two other relatively weak peaks in the visible region. The observed strong peak is due to the band–edge absorption followed by generation of photocarriers (electron–hole pair). The maximum PC obtained at 369 nm is 9.6μA. Therefore in this case, the UV photosensitivity (photo–to–dark current ratio) is ~4.5×10^3. The other small peaks in the visible region in the PC spectra are fitted with two Gaussian peaks and obtained peak positions are at 496 nm and 620 nm. The observed peaks in the visible region are possibly due to the generation of carriers from different defect states. The observed PC spectra are consistence with the PL spectra of the as–grown NWs, which show similar spectra with strong peak in the UV region and two relatively weak peaks in the visible region. ZnO nucleation layer (Fig. **5.2(b)**) shows similar features with three peaks located at 369, 408 and 495 nm. Note that, here the ZnO NWs grown on the Si substrate; therefore observed improvement in the UV PC is the full contribution of ZnO NWs only. In this case, the obtained photosensitivity is quite low for

practical applications. Since the as–grown ZnO nanostructures contains surface defects which are basically trap centres for carriers resulting in a low PC. It is expected that by structural improvement or heterostructure formation with suitable materials, a visible–blind ZnO NWs based photodetectors with high sensitivity could be made.

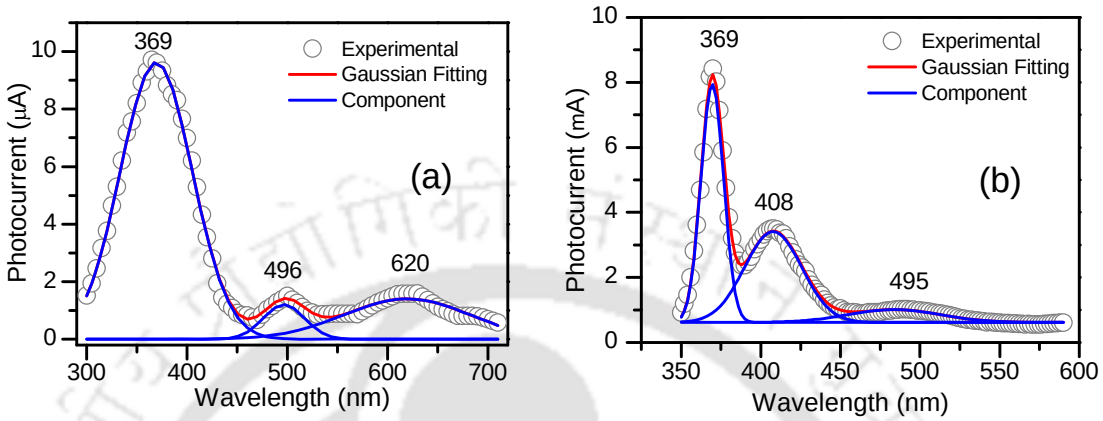

Figure 5.2: The photocurrent spectrum of the ZnO: (a) nanowires and (b) nucleation layer, measured at 2.5 V bias.

5.1.3. Photoresponse

The photoresponse behaviour of the ZnO NWs measured at air under the excitation of 360 nm UV light is shown in Fig. **5.3**. It is seen that PC initially grows very fast and then slowly increases with time and finally saturates. During decay, i.e. when the UV light is turned off, the PC initially decreases rapidly and then slowly reach the initial dark current value after long time. The PC takes more than 20 mins to reach the maximum value and falls to 90% of its maximum value within 11 mins. As expected, the as–grown NWs shows slow photoresponse due to the presence of intrinsic defects/trap centres.

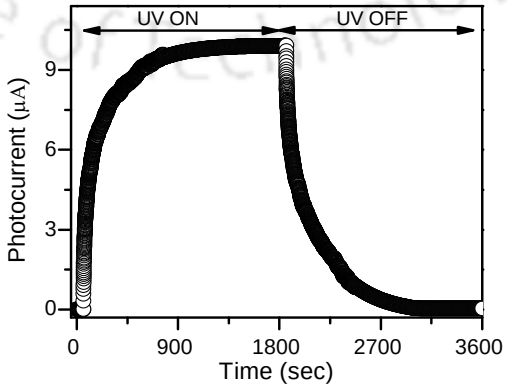

Figure 5.3: The photocurrent growth and decay behaviors (photoresponse) of the as–grown ZnO nanowires measured at 2.5V bias.

5.1.4. Mechanism of Photoresponse in ZnO Nanowires

The photoresponse of the ZnO NWs consists of two parts: a rapid process of photogeneration and recombination of electron–hole pairs, and a slow process of surface adsorption and photodesorption of oxygen molecules. The oxygen plays a crucial role in the photoresponse of ZnO. In dark condition, oxygen molecules from the air are easily stuck on the surface of the NWs by adsorption process and trapped electrons [$O_2(g)+e^- \rightarrow O_2^-$] available on the surface near the Zn lattice and decreased the conductivity,[20] which is shown schematically in Fig. **5.4(a)**. This process leads to the formation of depletion layer near the surface resulting in the upward band bending of the conduction band (C.B) and the valence band (V.B). The formation of this depletion layer has a prominent effect on the current conduction process when the diameter of the NWs is comparable to the thickness of the depletion layer. Formation of large number of ionized oxygen on the NWs surface enhances the band bending, resulting in a very low conductivity. During the UV illumination with energy greater than the band gap energy of ZnO, electron–hole pairs are generated [$h\nu \rightarrow e^- + h^+$] by light absorption. Now these electrons/holes easily cross the depletion layers and contribute to the photoconduction process. At the same time, holes take part in the oxidization of ionized oxygen [$O_2^- + h^+ \rightarrow O_2(g)$, photodesorption process] and release one oxygen gas molecule by electron–hole recombination process [Fig. **5.4(b)**]. Then few of the released oxygen molecules are re–adsorbed on the surface and decrease the free electron carriers. The energy band diagram during UV illumination is shown in Fig. **5.4(c)**. After a certain time electron–hole

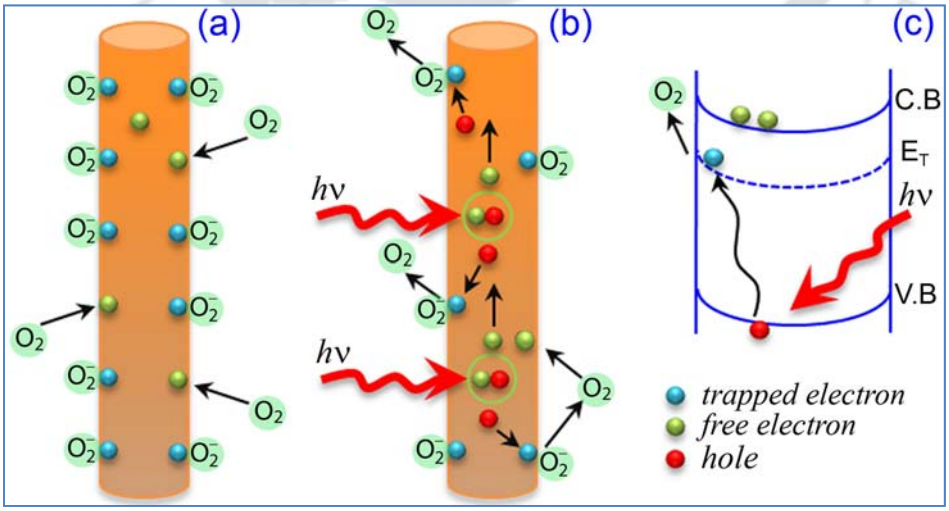

Figure 5.4: A schematic of photoresponse mechanism in ZnO nanowires: (a) at dark condition and (b) during UV illumination. (c) Schematic energy band diagram of photoresponse process during UV illumination.

generation rate and oxygen re–adsorption rate become constant resulting in a steady photocurrent. It is known that adsorption process is slower than the photodesorption process. Therefore, during UV illumination, not all the holes recombine with the electrons present in the ionized oxygen. As a result, excess holes are available for recombination with the exciton related free electrons. During photocurrent decay, the exciton related electron–hole recombination dominates, which corresponds to the faster decay component, so the photocurrent initially decreases very rapidly. With the surface re–adsorption of oxygen, the photocurrent comes to the initial dark current value very slowly.

5.2. Effect of Rapid Thermal Annealing

In the previous chapter, we seen that defect related trap centres on the ZnO NWs surface can be considerably removed by employing the RTA processing and an enhanced band–edge PL could be obtained. As a consequence, it is expected that RTA treated ZnO NWs can show enhanced UV photosensitivity. Therefore, we studied the effect of RTA on the photoconduction and photoresponse behaviours of these RTA treated vertically aligned ZnO NWs and the results are presented below.

5.2.1. Dark Current–Voltage Characteristics

Figure **5.5(a)** shows the dark current–voltage characteristics of the as–grown and RTA treated ZnO NWs. The RTA processed NWs show a linear I–V characteristics. Selected region of the I–V characteristics plots at logarithmic scale is shown in Fig. **5.5(b)**. For the as–grown NWs, it shows an Ohmic behavior ($I \sim V^{1.0}$) up to a bias voltage of ±8 V with current in the range of nA, beyond which dark current is proportional to $V^{3.0}$. In this case obtained trap filled limit voltage (V_T) is 8 V. The observed transition in the power dependence of current in the I–V curve is likely to arise from charge carriers trapped in the surface defect states that contribute to the high current at higher bias voltage. The high current at higher bias voltage can be well explained by the space charge limited current (SCLC) mechanism. Although, power dependence of 2.0 is considered as SCLC, higher power dependence on voltage can be observed depending on the energy distribution of trap centres.[237] As the PL spectra of the NWs (discussed in the previous chapter) reveal the presence of trap centres with different energies, the higher power

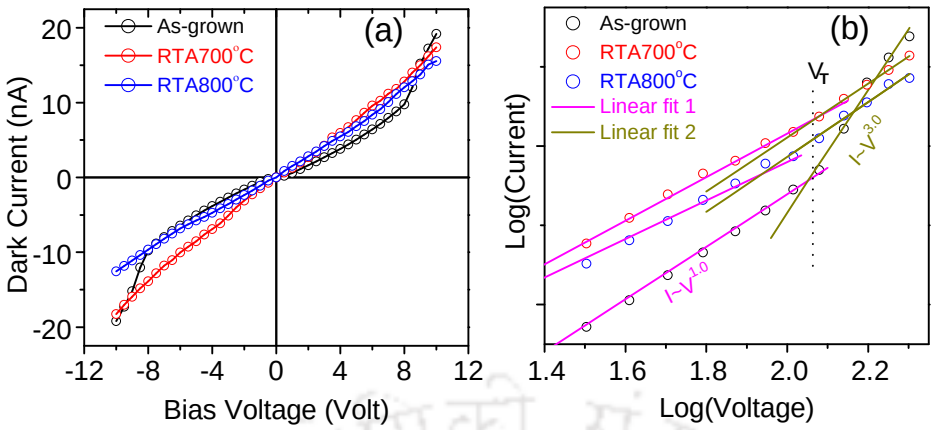

Figure 5.5: (a) The dark current–voltage characteristics of as–grown and RTA treated ZnO nanowires processed at 700° and 800°C. (b) Plot of this I–V characteristics of selected region in log–log scale.

dependence of current on voltage is expected. This behavior is consistent with previous reports on doped metal oxide thin film based resistive switching devices[238,239] and it is explained on the basis of presence of oxygen vacancy related traps within the bandgap of the material. Under a negative bias voltage, oxygen vacancies with positive charges migrate away from the interface between contact and the ZnO, which widens the depletion layer, resulting in high resistivity. On the other hand, with positive bias voltage, the oxygen vacancies start moving toward the interface, resulting in higher current. Therefore, the presences of native surface defects (oxygen vacancies) could be identified from the dark I–V characteristic. In case of RTA treated NWs, a nearly linear dark I–V characteristic with slightly high current is observed. Therefore, the analysis of the dark I–V characteristics of the ZnO NWs clearly indicates the presence of high density of trap centres on the surface of the as–grown ZnO NWs, while the trap density is significantly reduced in RTA processed ZnO NWs.[189]

5.2.2. Photocurrent Spectra

Figure **5.6(a)** shows the PC spectra of the RTA treated ZnO NWs processed at 700°C, measured at a bias of 2.5V. After RTA at 700°C, the PC at 369 nm reaches a maximum value of 82.1 μA from that of 9.6 μA for the as–grown NWs and full width at half maxima (FWHM) is reduced compared to the case of as–grown NWs. As a consequence, the photosensitivity is increased to ~24.2×10^3, leading to an enhancement of a factor of five. With RTA at 800°C, a similar high PC is obtained (~ 84.1 μA) with photosensitivity of ~24.2×10^3 [Fig. **5.6(b)**]. Note that the enhancement in

photosensitivity is significant in this case and is similar to the earlier reports, as shown in Table **1.3** in Chapter–1, where more complex structures were fabricated by surface passivation of the ZnO NWs with different inorganic/organic materials. In our case, observed enhancement factor is quite high compared to the previously reported value for the conventional furnace annealed ZnO NWs.[155] Here we obtained a high photosensitivity by employing a simple RTA process, which shows the effectiveness of this process. In the PL spectra of the RTA processed NWs, we observed a reduction in oxygen related defect states after RTA treatment. Therefore, RTA induced reduction in defect density is primarily responsible for the enhanced photoconduction, because very

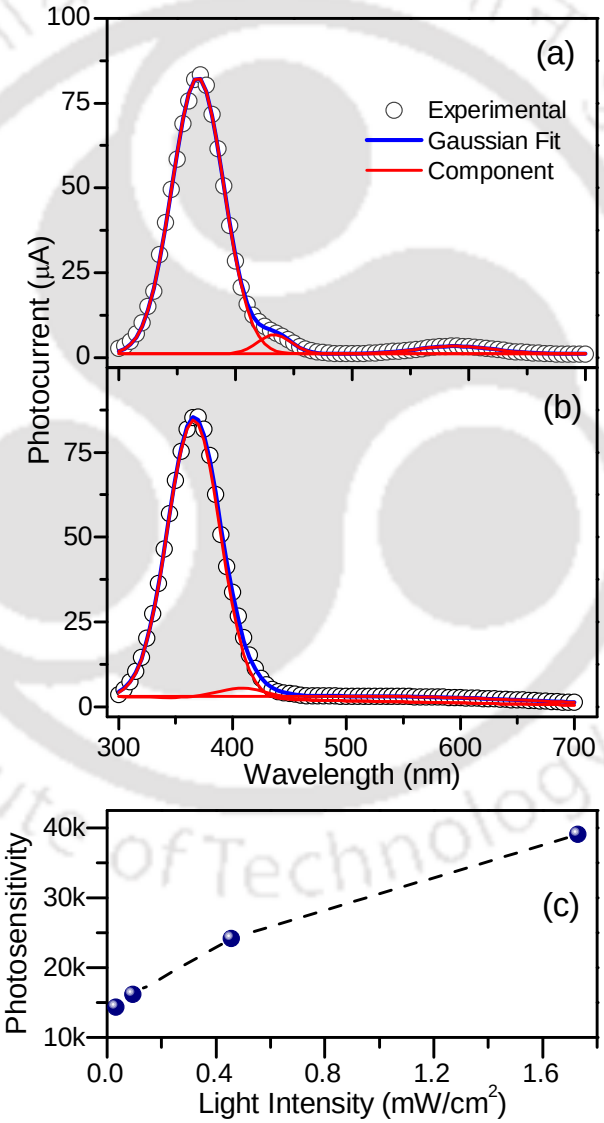

Figure 5.6: The photocurrent spectra of the RTA treated ZnO nanowires processed at: (a) 700°C, and (b) 800°C, respectively at 2.5 V bias. (c) The variation of photosensitivity at different intensity of UV light (wavelength 369 nm) for the ZnO nanowires RTA treated at 800°C.

few photogenerated carriers can be trapped inside the defect states and most of the excess carriers contribute to the PC. It is observed that the trap centres related PC peaks in the visible region are considerably reduced for the RTA treated NWs. Figure **5.6(c)** shows the UV light (wavelength 369 nm) intensity dependence of photosensitivity of the ZnO NWs, RTA treated at 800°C. The photosensitivity plot shows a sub–linear behavior with the UV light intensity. The observed sub–linear behavior is because of the complex interplay of electron–hole generation, carrier trapping, and recombination within the semiconductor NWs. The high photosensitivity even in low light intensity is an indication of very low value of detection limit. Therefore, we obtained a high value of photosensitivity without making any complex structures, which is advantageous for the fabrication of UV photodetectors.

5.2.3. Photoresponse

To study further the effect of RTA on the PC time response, we performed the photoresponse measurement of the RTA treated NWs under similar conditions. The obtained results of the RTA treated NWs are shown in Fig. **5.7**. The photoresponse of the ZnO NWs shows a bi–exponential growth and bi–exponential decay behaviors. The growth and decay time constants are calculated from the bi–exponential fitting to the experimental data and the obtained parameters are summarized in Table **5.1**. The time dependent growth behavior of the photoresponse curve is fitted with the equation,

$$I_{ph}(t) = I_1 + A_1\left(1 - e^{-t/\tau_1}\right) - A_2 e^{-t/\tau_2} \quad \text{..... (5.1)}$$

where I_1, A_1 and A_2 are positive constants. The first exponential term corresponds to the electron–hole generation process and the last exponential term represents the oxygen adsorption process. Calculated time constants from fittings are τ_1 =24.7s and τ_2 =295.0s for the as–grown NWs indicating a very rapid photocurrent growth initially followed by a very slow decay process. For the RTA treated NWs, the photocurrent growth and decay time constants are 11.4s and 261.8s, respectively for 700°C annealing and 12.3s and 107.0, respectively for 800°C annealing. In this process, the electron–hole generation is the only source for current carriers and all other processes decrease the carriers. Similarly, when the UV light is turned off, the photocurrent show a rapid decay followed by a slow decay. The time dependent decay behavior can be fitted with a bi–exponential decay equation,

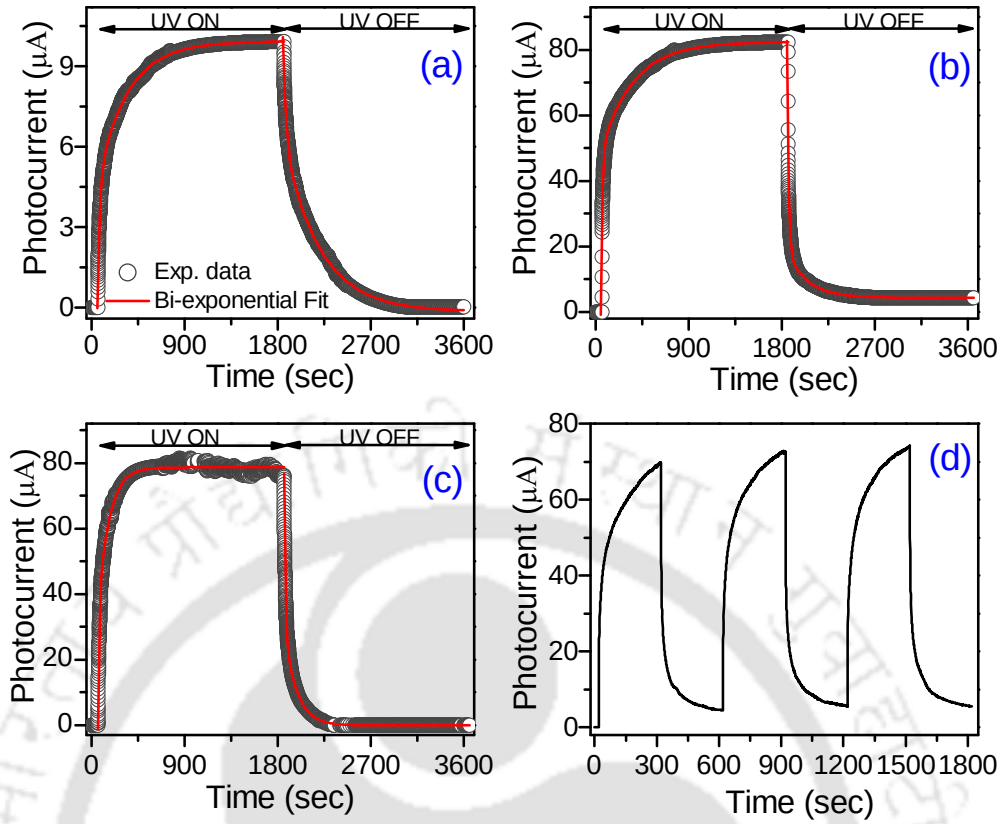

Figure 5.7: The photocurrent growth and decay behaviors of the ZnO nanowires: (a) as–grown, (b) RTA processed at700°C, (c) RTA processed at 800°C, respectively. Photocurrent growth and decay are measured under the illumination of 360 nm UV light. (d) Photocurrent growth and decay of the RTA treated ZnO nanowires (700°C) under the pulsed (300 s) UV light illumination at a bias voltage of 2.5 V.

$$I_{ph}(t) = I_{ph}(\infty) + A_3 e^{-t/\tau_3} - A_4 e^{-t/\tau_4} \quad \text{..... (5.2)}$$

where A_3 and A_4 are positive constants and $I_{ph}(\infty)$ refers to the photocurrent after infinitely long time of the decay experiment, which essentially is the dark current. The first exponential term in eqs. 5.2 corresponds to the electron–hole recombination process

Table 5.1: Summary of the growth and decay time constants of the ZnO nanowires, obtained from the bi–exponential fitting to the experimental data points.

ZnO NWs	PC Growth time constants (s)		PC Decay time constants (s)	
	τ_1	τ_2	τ_3	τ_4
As–grown	24.7±0.4	295.0±0.8	25.7±0.5	347.9±1.1
RTA700°C	11.4±0.3	261.8±1.1	12.3±0.3	298.5±1.1
RTA800°C	12.3±0.5	107.0±1.1	13.6±0.3	118.4±0.5

and the last exponential term represents the oxygen adsorption process. The decay time constants are calculated to be 25.7s and 347.9s for the as–grown NWs, 12.3s and 298.5s for the RTA treated at 700°C, 13.6s and 118.4s for the RTA treated at 800°C, respectively. Therefore, the PC growth as well as decay becomes faster after the RTA treatment. The calculations of individual time constants show that electron–hole recombination as well as generation rates become double after RTA at 700°C and do not change significantly with higher temperature annealing. On the other hand, oxygen adsorption rates during the photocurrent growth as well as decay are systematically decreased. Similar bi–exponential decay behavior with time constants of several seconds has been reported by several groups for the ZnO nanobelts, NWs and thin film.[18,106,186,191,240] Figure **5.7(d)** shows the photoresponse of the RTA treated NWs under periodic UV illumination. It is observed that the maximum photocurrent in the next cycle is slightly increased compared to the previous cycle because of the incomplete growth and decay of the PC during the measurement cycle. Second and third cycle of photocurrent growth and decay show exactly the replica of first cycle, indicating a reproducible PC response of the RTA treated ZnO NWs, which is important for the real time application in photodetectors.

As the RTA processing significantly reduces the surface defect related trap centres and modified the surface of the ZnO NWs, the band bending is less here compared to the as–grown NWs case resulting in a comparatively higher conductivity, as revealed in the dark I–V characteristics. As a consequence, the photocurrent reached the saturation value very fast. Therefore, the structural improvement caused faster photocurrent growth and decay from the RTA treated ZnO NWs. This is consistent with the PL results discussed earlier.

5.3. Photoresponse Behaviour of Al doped ZnO Nanowires

In this section, we present the PC and photoresponse behaviour of the Al doped ZnO (Al:ZnO) NWs network. The effect of Al doping on the photoresponse properties of the ZnO NWs are studied in detail and the results are compared with the undoped NWs. 3% and 6% doped Al:ZnO NWs network are used for this study.

5.3.1. Dark Current–Voltage Characteristics

Figure **5.8** shows the dark current–voltage (I–V) characteristics of the 3% and 6% doped

Al:ZnO NWs network. As each of the NWs is connected with the nearest neighbour, current carriers can easily flow from one NW to the other by tunnelling process through the junction between the NWs. The I–V characteristics show nearly linear behaviour with comparatively higher dark current than the undoped NWs. Earlier we found that the dark current of the undoped ZnO NWs varies in the range 2–10 nA. However in the present case, the obtained dark current is one order of magnitude higher and it increases with the increase in doping concentration. The dark current increases from 110 to 180 nA at a bias of 3V with increase in Al concentration from 3% to 6%. The higher dark current could be attributed to the substitutional doping of Al atoms at the Zn site of the ZnO lattice. Here trivalent Al^{+3} ions contribute to the enhanced current conduction process by increasing the free electron density in the doped NWs.

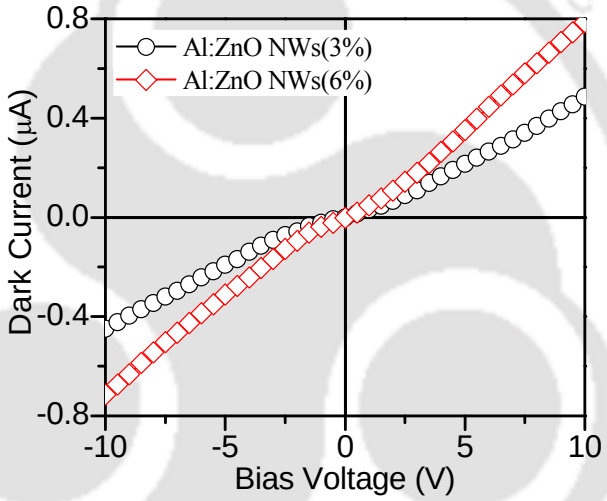

Figure 5.8: The dark current–voltage characteristics of the 3% and 6% Al doped ZnO nanowires.

5.3.2. Photoresponse

The photoresponse of the Al:ZnO NWs measured under the excitation of 365 nm UV light is shown in Fig. **5.9**. The obtained PC and photoresponse parameters are tabulated in Table **5.2**. The response and reset times are <1s, which is far lower than the response time of the undoped ZnO NWs (several seconds). For the 3% and 6% doped Al:ZnO NWs, the maximum PC is about 5.2–5.6 μA. Although these NWs show a high increment in the PC under the UV excitation, the photosensitivity values are very low due to the higher dark current. This behaviour is consistent with the previous studies on Al:ZnO NWs.[184,241,242] Such a low photosensitivity from the Al:ZnO NWs hinders the fabrication and development of highly efficient UV photodetectors. However in the

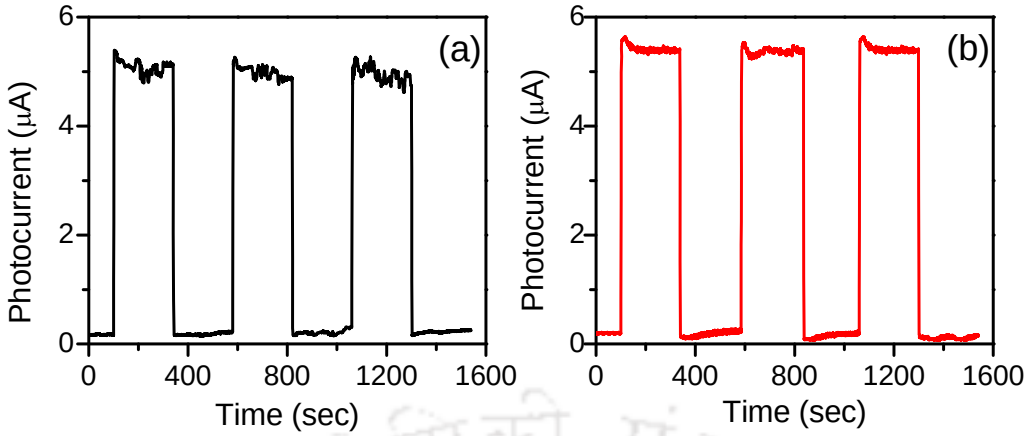

Figure 5.9: Reproducible photoresponse behaviors (at 365 nm) of the: (a) 3% and (b) 6% Al doped ZnO nanowires, measured at 3 V bias.

present case, the photoresponse and reset times are very fast, compared to the as–grown undoped ZnO NWs. The photoresponse and reset times of the Al:ZnO NWs show a dependence on Al concentration. At low doping level of Al, the photoresponse and reset times (defined as the time required to reach 1–1/*e* (63%) and recovery to 1/*e* (37%) of maximum PC) are significantly reduced. The 3% doped Al:ZnO NWs shows photoresponse and reset times of 0.9 and 1.1s, respectively. Additional doping shows a marginal reduction in the photoresponse and reset times. Therefore, the presence of Al accelerates the photocurrent saturation rate, which indicates that the oxygen re–adsorption rate reached equilibrium instantly. Earlier, similar improvements in the photoresponse and reset times are obtained by Ag doping in the ZnO NWs.[194] Therefore, the Al:ZnO NWs show a fast response and comparatively low photosensitivity. The low photosensitivity could be considerably improved by making metal/semiconductor heterostructures with the NWs, which is discussed in the next chapter.

Table 5.2: Photocurrent and photoresponse parameters of the 3% and 6% Al doped ZnO nanowires.

Sample Name	Dark current (nA)	Photocurrent (μA)	Photosensitivity	Response time (s)	Reset time (s)
3%Al:ZnO	110	5.2	47	0.9	1.1
6%Al:ZnO	180	5.6	31	0.8	1.0

The obtained ultrafast photoresponse from the Al:ZnO NWs can be explained as follows. It is known that the photoresponse of ZnO depends on electron–hole generation, surface

adsorption and photodesorption processes. It is also known that fast or slow response strongly depends on the time taken to reach the equilibrium rate of oxygen desorption and re–adsorption process. In the present case of Al:ZnO NWs, Al doping possibly change the equilibrium defect concentration. Due to this, surface defects in the Al:ZnO NWs gradually increases with the increase in Al concentration. This is supported by the optical absorption and PL results as explained in the previous chapter. The optical absorption and PL data show gradual increment in the surface defects related absorption and emission in the green region. For this reason, the rates of oxygen desorption and re–adsorption processes are significantly improved and it instantly reach the equilibrium rate. This process results in a much faster photoresponse in the Al:ZnO NWs.

5.4. Summary

The photodetection properties of the ZnO NWs are studied by measuring wavelength dependent PC and photoresponse. The RTA treated ZnO NWs shows major improvement in the photodetection behavior, as a result of structural improvement. The RTA processing substantially removes the surface defect–related trap centers and modified the surface of the ZnO NWs, resulting in enhanced PC and faster photoresponse. The important studies and findings of this chapter are summarized below.

1. Photosensitivity and photoresponse characteristics of the ZnO NWs are studied and shown to be very important for making UV photodetectors.
2. Mechanism of photoresponse is explained through photogeneration, recombination, surface adsorption and photodesorption processes.
3. Due to the presence of several surface defects, the photosensitivity and photoresponse time of the as–grown ZnO NWs are quite low.
4. By employing RTA, very high value (~25k) of photosensitivity and comparatively faster photoresponse could be obtained. However, the response time is still quite slow for the fabrication of ZnO NWs based fast photodetectors.
5. The Al:ZnO NWs shows very fast response (~ 1s), however the photosensitivity value is below the required level for practical applications.

भारतीय प्रौद्योगिकी संस्थान गुवाहाटी
Indian Institute of Technology Guwahati

Chapter 6

ZnO Nanowire Heterostructures: Photoresponse and Photoluminescence

For the fabrication of the highly sensitive and ultrafast UV photodetectors, several novel ZnO NW heterostructures with different materials have been fabricated and the results are presented in this chapter. Two types of heterostructures were fabricated; one with decorating the surface of the NWs with ultra small metal (Au and Ti) nanoparticles (NPs) i.e. semiconductor/metal and other one is inorganic/organic type semiconductor/semiconductor heterostructures with anthracene and copper phthalocyanine (CuPc). Using the heterostructure approach we are able to achieve very high photosensitivity and a faster photoresponse from ZnO NWs. The origin of this improvement from these heterostructures is studied systematically and explained in details on the basis of interfacial interaction of electrons in the NW heterostructures. The absorption and PL properties of these heterostructures are also studied to correlates the effect of heterostructure materials to the improvement in the photoresponse properties.

6.1. Metal nanoparticles decorated ZnO Nanowire Heterostructures

We investigated the photoinduced charge transport mechanism in metal (Au and Ti) NPs decorated vertically aligned ZnO NWs heterostructures. For the fabrication of heterostructures, two types of metals were chosen, one with low work–function (Ti, 4.26 eV)[243] and other with high work–function (Au, 5.47 eV)[243] with respect to the work–function of ZnO (4.65 eV).[244] ZnO/Au NWs and ZnO/Ti NWs heterostructures were fabricated by directly depositing small sizes Au and Ti NPs on the surface of the NWs by sputter deposition process in a controlled way. For the systematic studies, surface of the NWs were covered with NPs with different sizes/thicknesses.

6.1.1. ZnO/Au Nanowire Heterostructure

In this section, we present the method of fabrication and characterization of ZnO/Au heterostructures. Fabrication of ZnO/Au heterostructures were confirmed by FESEM and TEM imaging and the photoresponse and PL properties were subsequently studied.

6.1.1.1. Fabrication of the Heterostructure

The ZnO NWs grown at 800°C by using combined ZnO seed and Au catalyst layer, was used for the fabrication of ZnO/Au heterostructures. The heterostructures were fabricated by directly depositing a ultra thin layer of Au NPs on the surface of the vertically aligned ZnO NWs by DC sputter deposition process. Au was deposited for different time durations and the samples are named according to the deposition time. The details of the sputtering parameters and approximate thicknesses of the metal layers are mentioned in the Table **6.1**. For the as–grown and Au deposited for 30, 60, 90 and 145 sec samples are named as Au_0s, Au_30s, Au_60s, Au_90s, and Au_145s, respectively. The approximate thicknesses calculated from Au deposition rate are 1, 2, 3 and 5 nm for Au_30s, Au_60s, Au_90s, and Au_145s, respectively. The exact thickness of the metal NPs layer in each case cannot be estimated properly as the metal deposition may take place at an oblique angle for some NWs depending on the orientation of the NWs. Size of the NPs are actually larger than the metal layer thickness and the size of the NPs over the NWs surfaces strongly influences the optoelectronic properties of the NW heterostructures. A schematic diagram of the ZnO/Au heterostructure is shown in Fig. **6.1**.

Table 6.1: The sputter deposition parameters of Au NPs layer for the fabrication of ZnO/Au heterostructures.

Sample Name	DC Bias (kV)	DC Current (mA)	Deposition Time (s)	Approx. Thickness (nm)
Au_30s	1	5	30	1
Au_60s	1	5	60	2
Au_90s	1	5	90	3
Au_145s	1	5	145	5

6.1.1.2. Morphology and Structural Characterization

Figure **6.2(a)** shows the FESEM image of the as–grown single ZnO NW, which was

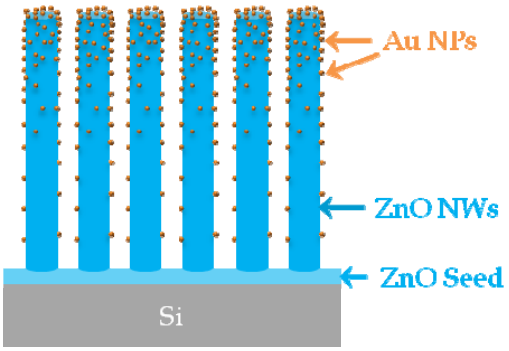

Figure 6.1: Schematic diagram of the Au nanoparticles decorated ZnO heterostructures.

grown at 800°C. Smooth side surface of this NW can be easily seen. Figure **6.2(b and c)** show the side view and top view of the NW after deposition of Au NPs layer for 60 sec. A closer look on these images reveals that Au NPs are distributed on the top as well as the side surface of the NWs. It is also found that Au NPs density is more at the top of the NWs as compared to the side surface, as expected.

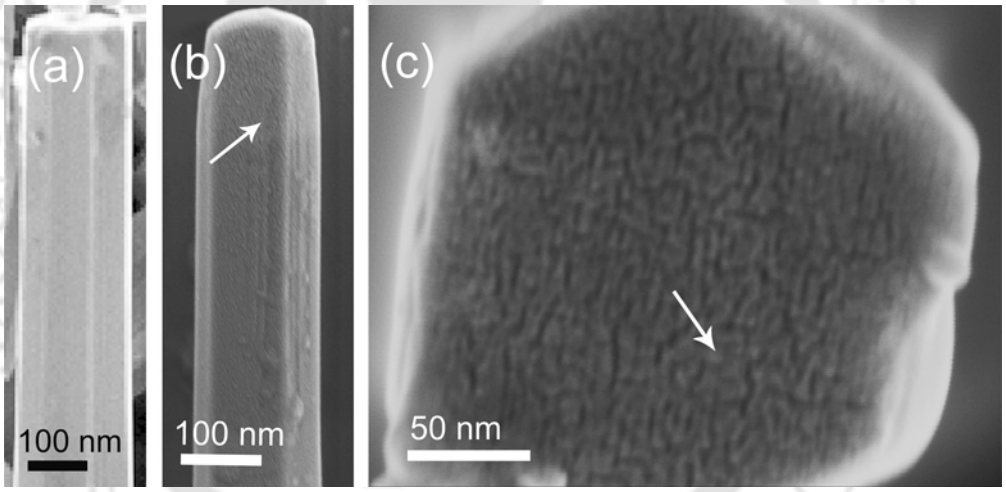

Figure 6.2: FESEM images of as–grown and Au nanoparticles decorated vertically aligned ZnO nanowires: (a) single as–grown ZnO nanowire; (b and c) Side view and top view of the same nanowire after the Au nanoparticles decoration on the surface of the nanowire. Presence of Au nanoparticles is clearly visible on the side surface and top surface of the ZnO nanowire (marked by white arrow).

To confirm further, TEM imaging was performed on the heterostructures. Figure **6.3** shows the TEM image of the Au_60s sample, which shows that NPs are uniformly distributed over the NW surface. It also revealed that NPs density is more at the top of the NW, which is consistent with the FESEM images. The insets show the selected region in magnified scale and corresponding SAED pattern, which clearly shows that Au NPs are attached on the NW surface with sizes in range of 3–6 nm. From the high resolution lattice fringe image, the lattice spacing of ZnO NW is found to be 0.51 nm,

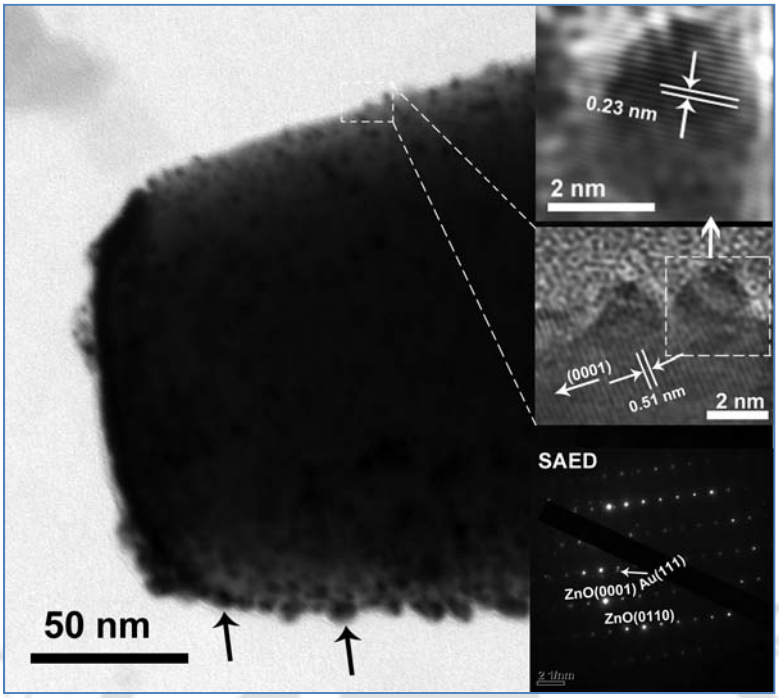

Figure 6.3: TEM image of the Au nanoparticles decorated ZnO nanowire heterostructure (sample:Au_60s). Insets show the selected region in magnified scale and corresponding SAED pattern. Both the high resolution TEM image and SAED pattern confirm the decoration of ultra small diameter Au nanoparticles on the surface of ZnO nanowire.

which indicates that the NW are single crystalline and growth direction is along (0001). The lattice spacing calculated from the lattice fringe image of the NPs matches with the (111) plane of Au crystal. The SAED pattern shows the diffraction spots corresponding to the Au(111) plane along with the diffraction spots of ZnO. The SAED pattern further confirmed the crystallinity of the ZnO NWs and presence Au NPs. Therefore, FESEM and TEM imaging confirmed the fabrication of ZnO/Au NW heterostructures.

To study further about the structures and orientation of the as–grown NWs and heterostructures, XRD patterns are recorded using Mo x–ray gun and the results are shown in Fig. **6.4**. All the patterns show one intense peak corresponding to the (002) plane and a weak peak corresponding to the (103) plane of hexagonal structure. The XRD analyses show that the NWs are single crystalline and oriented along the *c*–axis of hexagonal structure. After the NPs decoration, intensity of the XRD peak reduces while the Au NPs related XRD peak corresponding to Au(111) plane increases with higher coverage of Au NPs.

6.1.1.3. UV–Vis Absorption Studies

Figure **6.5(a)** shows the UV–Vis specular (angle of incidence 45°) reflectance spectra of

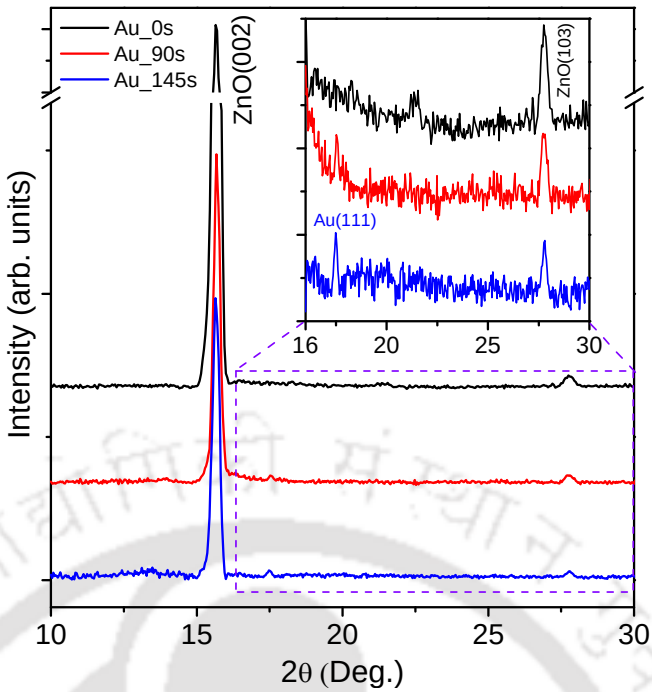

Figure 6.4: XRD patterns of the as–grown and Au nanoparticles decorated ZnO nanowire heterostructures. Strong ZnO(002) peaks reflect the higher crystallinity of the nanowires. In the inset, weak peak related to Au (111) plane can be visible for nanowires with higher Au coverage. Here the Mo (λ=0.7093Å) x-ray gun was used for measurement.

the as–grown and Au_30s sample. Very low percentage of reflectance in the UV region indicates a high absorption in this region. Other samples show similar spectra with low reflectance in the UV region. The absorption spectra were calculated from the specular reflectance spectra of all the samples according to the method described in the Chapter–2. The UV–Vis absorption spectra [Fig. **6.5(b)**] of the as–grown and ZnO/Au heterostructures show a high absorption in the UV region with a distinct peak at 367 nm corresponding to the band–to–band absorption. The observed weak absorption component in the green region is due to the absorption by the defect states present on the surface of the NWs. The intensity of absorption in the UV region as well as the green region gradually increases with the increase of Au NPs coverage. The inset of Fig. **6.5(b)** shows the directly measured absorption spectrum of the 2 nm thick Au film deposited on a quartz substrate. This spectrum shows a strong surface plasmon (SP) related band at ~550 nm along with the broad absorption in the UV–Violet region due to interband transition.[245] In a metallic material, a continuous spectrum of available states has been formed by overlapping of valence and conduction bands. However, some inner levels do not split enough to overlap with these bands, so the system may exhibit interband transitions similar to those in semiconductors. And the interband transitions are more

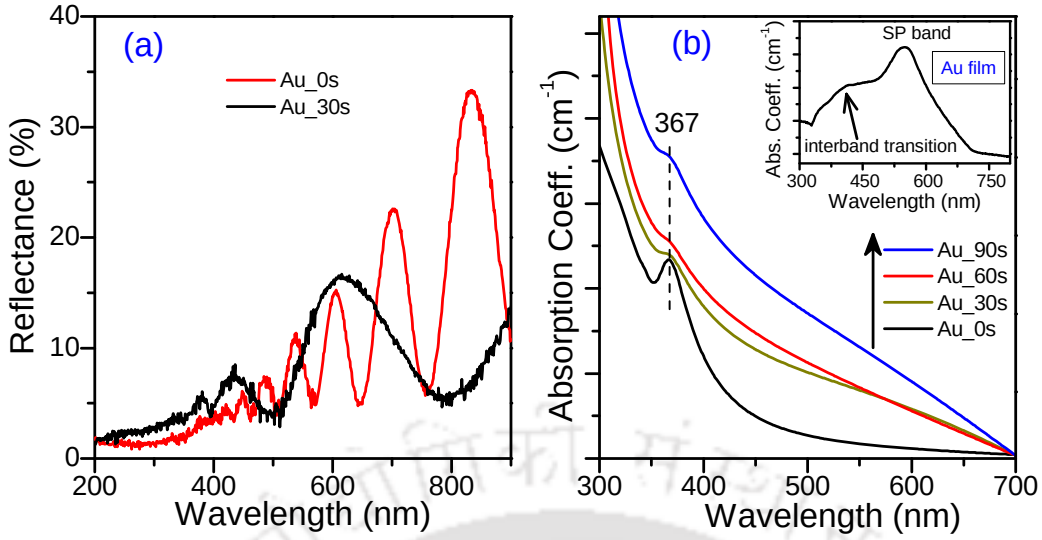

Figure 6.5: (a) UV–Vis specular reflectance spectra of the Au_0s and Au_30s samples. (b) Absorption spectra of the Au_0s and ZnO/Au nanowire heterostructures with different deposition time of Au nanoparticles. The spectra are derived from the specular reflectance spectra. Inset shows the absorption spectrum of the 2 nm thick Au film deposited on a quartz substrate.

prominent in metal NPs due to limited number of atoms. Therefore, we believe that the obtained enhanced absorption after the Au decoration is due to the combined effect of ZnO and Au NPs absorption. Therefore, it is expected that the obtained high absorption in the ZnO/Au heterostructures will result in enhanced PC as well as UV PL peak intensity. Note that, decoration of metal NPs affects the surface defects by modifying the surface of the ZnO NWs, which can also enhance the PC and UV PL intensity.

6.1.1.4. Photocurrent and Photoresponse Studies

Figure **6.6(a)** shows the dark current–voltage (I–V) characteristics of the as–grown NWs, Au_90s and Au_145s samples. The I–V characteristics show nearly linear behaviours with current in the range of nA. After the Au NPs decoration, the dark current is reduced to 8.6 nA from 11.5 nA at 3V bias for the Au_90s sample and it reduces further with higher Au coverage. The decrement of current is more prominent in the lower bias range and at higher bias voltage it reached a value close to the dark current of as–grown NWs, which is clearly visible from the log–log plot shown in the inset of Fig. **6.6(a)**. Details of the changes in dark current with Au NPs coverage are mentioned in table **6.2**.

The decrement in dark current in ZnO/Au heterostructures can be explained from the band structure alignment at the interface between the metal NPs and ZnO. It is known

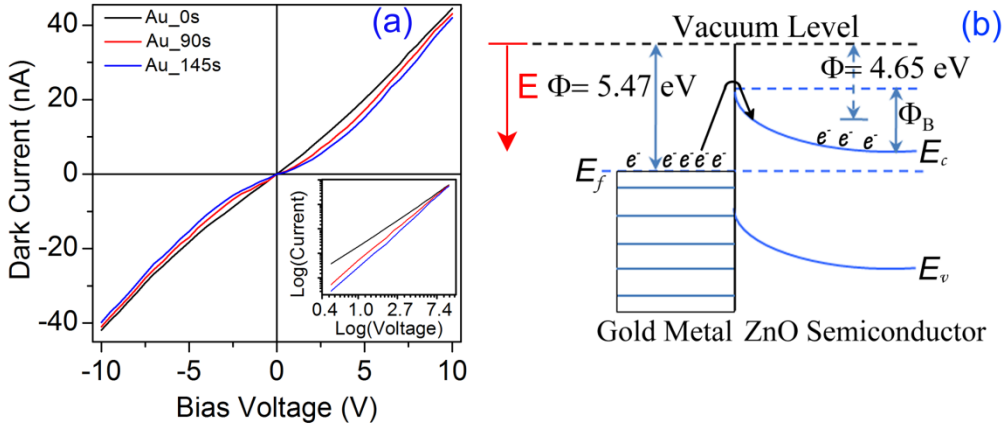

Figure 6.6: (a) Dark I–V characteristics of the ZnO/Au nanowire heterostructures with different deposition time of Au. Inset of (a) shows the I–V curves in log–log scale. (b) Schematic of the energy band diagrams with band alignment for ZnO/Au nanowire heterostructures.

that when a metal is brought in contact with semiconductor, it induces band bending due to the equilibrium of Fermi level.[246] Depending on the difference in the work–functions of metal and semiconductor, two types of contacts have been formed at the metal semiconductor interface. Since the work–function of ZnO (4.65 eV)[244] is smaller than the Au (5.47 eV),[243] an upward band bending is expected and a Schottky type contacts will be formed at the interface region [see Fig. **6.6(b)**]. As a result, no electron will transfer from Au to the conduction band of ZnO. However, at a lower bias voltage a few electrons can pass from ZnO to the Al electrode, giving a very low dark current. At higher bias voltage, which is greater than the Schottky barrier height, all the electrons can flow to external circuit giving almost equal dark current as for the case of as–grown NWs.

Table 6.2: Photocurrent and photoresponse parameters of the as–grown and ZnO/Au heterostructures.

Sample Name	Dark Current (nA)	Photoc--urrent (μA)	Photosensitivity	PC Growth time constants (s)		PC Decay time constants (s)	
				τ_1	τ_2	τ_3	τ_4
Au_0s	11.5	4.7	414	17.3	218.8	19.3	316.0
Au_90s	8.6	25.3	2937	2.4	79.1	13.4	272.5
Au_145s	7.0	15.1	2160	2.5	54.0	13.9	179.0

As the dark current of the ZnO/Au heterostructures is lower than the as–grown ZnO NWs, it is expected that the PC would be lower than the as–grown case. However, we obtained enhanced PC under the UV excitation. To study the origin of the enhanced PC from the ZnO/Au heterostructures, we carefully measured the wavelength dependence of PC at a bias of 3V under the excitation wavelength in the range 300–700 nm. The measured PC spectra of the ZnO/Au heterostructures are shown in Fig. **6.7**, along with that of the as–grown ZnO NWs. The PC spectra of the as–grown NWs show a strong peak in the UV region at 369 nm and a broad peak in the green region. The observed strong peak at 369 nm in the PC spectra is due to the band–edge absorption followed by generation of photocarriers (electron–hole pair).[35,189] The other peak in the visible region is due to the generation of carriers from the defect states.[155] For the Au_90s sample, the magnitude of the PC peak in the UV as well as in the visible region is significantly enhanced. The maximum PC obtained from Au_90s NWs is 25.3 µA, leading to a very high photosensitivity value of 2.9k. Compared to the photosensitivity of the as–grown NWs (414), seven–fold enhancement in photosensitivity is obtained. The improvement in the broad photocurrent peak from the ZnO/Au heterostructures in the visible region is due to the Au NPs absorption related carrier transfer to the conduction band of ZnO. The obtained PC spectra are consistent with the absorption spectra of the corresponding samples. With further increase of Au NPs coverage the maximum PC decreased to 15.1 µA for Au_145s sample.

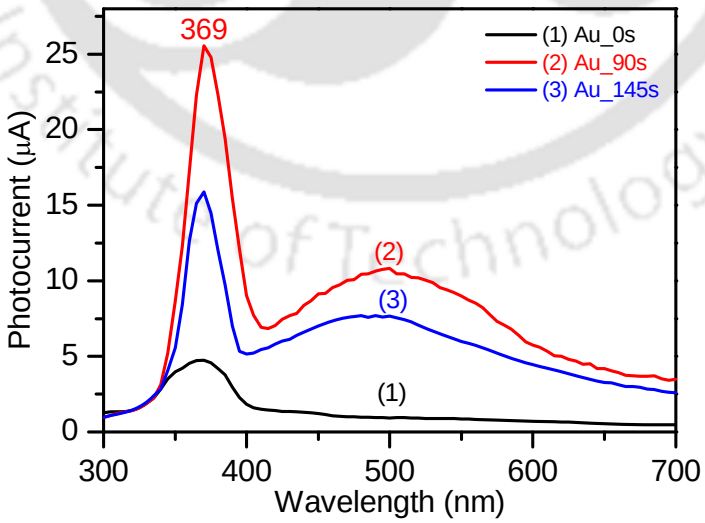

Figure 6.7: Photocurrent spectra of the ZnO/Au nanowire heterostructures with different deposition time of Au.

The obtained improvement in the PC spectra from ZnO/Au heterostructures can be explained from the absorption spectra and the energy band diagram. In case of ZnO NWs grown from vapor deposition method, the green emission (~ 500 nm) is well known and it is generally regarded to be related to the oxygen vacancy related surface defect.[117,118] In case of ZnO/Au heterostructures, with respect to the vacuum level, the energy level of green emission related defect states (5.43 eV) and Fermi level of Au (5.47 eV) is very close to each other.[243] Therefore, the electrons from this defect states can transfer to the Fermi level of Au, which increases the electron density at the Fermi level of Au. The Au NPs are excited by incident light in the UV–violet region due to interband transition and in the green region due to the surface plasmon resonance (SP band)[245], as seen from the absorption spectra of Au NPs. Subsequently, the excited energetic electrons stay in higher energy states, and these are so active that they can escape from the surface of the NPs and transfer to the conduction band of ZnO. The schematic diagram of surface plasmon assisted electrons transfer from Au NPs to ZnO NWs is shown in Fig. **6.8**. Under external bias, these electrons along with photogenerated electrons due to band–edge absorption of ZnO contribute to the current conduction process. Earlier, Lin *et al.*[247] explained the electrons transfer process from Au to the conduction band of ZnO to account for the enhancement of UV PL intensity from the Au NPs decorated ZnO NRs. In the present case, we believe that the enhanced photocurrent in the UV as well as visible region is due to the increase in electron density in the conduction band of ZnO by ZnO band–edge absorption and electron transport via Au NPs. For the Au_145s sample, NPs grew larger and form a continuous film instead of NPs. Therefore, a significant decrement in the absorption magnitude by Au NPs is expected. Because, the interband

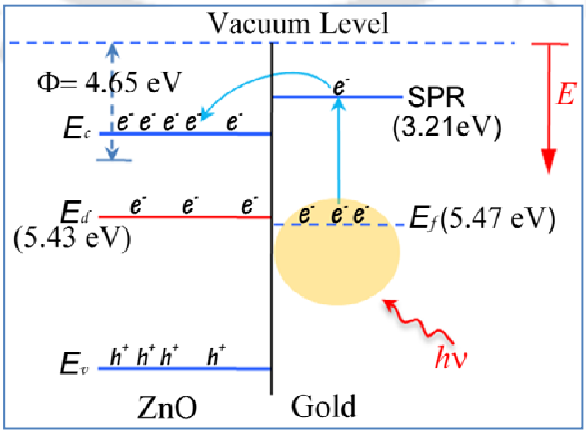

Figure 6.8: Schematics of the surface plasmon assisted electrons transfer from Au NPs to the ZnO NWs.

transition as well as surface plasmon resonance are prominent in the smaller diameter NPs due to limited number of atoms. This explains the reduction of PC with high Au coverage i.e. 145s sputtering of Au.

To study further the effect Au NPs decoration on the photoresponse, we performed the photocurrent growth and decay measurement of the as–grown and ZnO/Au heterostructures under the UV light (wavelength 365 nm) pulse in ON and OFF conditions and the results are shown in Figure **6.9**. The individual growth and decay time constants are calculated from a bi–exponential fitting, as described in the Chapter–5. The obtained photoresponse parameters are tabulated in Table **6.2**. The photoresponse time for the as–grown NWs is very slow due to the presence of intrinsic defects/trap centres.

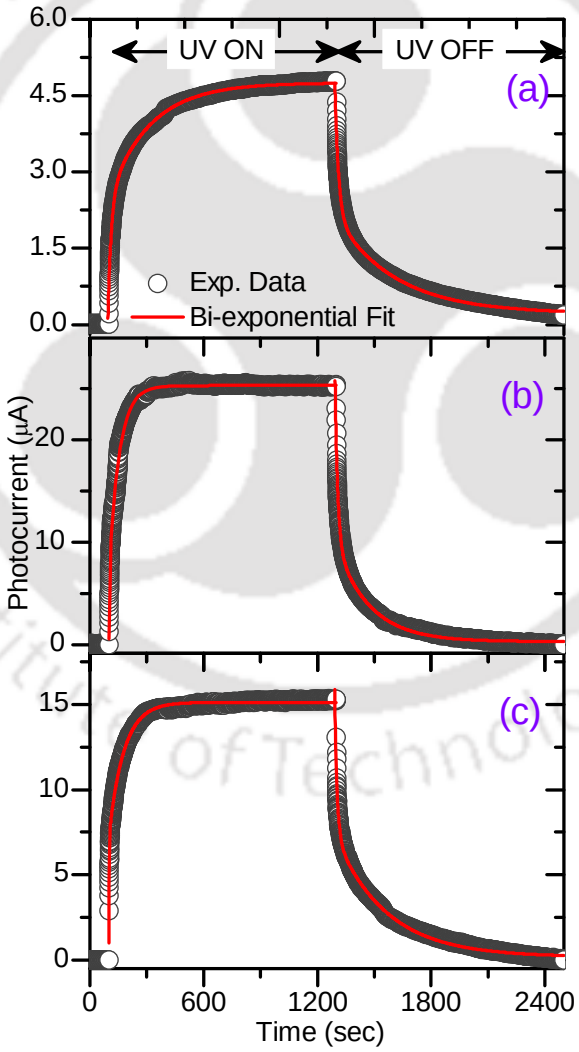

Figure 6.9: Photoresponse behaviour of the: (a) as–grown, (b and c) ZnO/Au nanowire heterostructures with 90 and 145s deposition of Au nanoparticles, measured at a bias voltage of 3 V and under the illumination of 365 nm UV light. Red lines are the bi–exponential growth and bi–exponential decay fitting to the corresponding experimental data points.

The calculated time constants are 17.3 and 218.8s for the PC growth, 19.3 and 316.0s for the PC decay, respectively. For Au_90s heterostructures, the first growth and decay time constants are drastically reduced to 2.4s and 13.4s, respectively, which do not changes with further Au NPs coverage. Whereas, the time constant related to the oxygen absorption in case of PC growth as well as decay is gradually decreased with increase in Au coverage. In a recent work, Park *et al.*[180] showed that rough surface morphology in the NWs introduces traps, which fasten the photoresponse process. In their case, they prepared the rough surface morphology in the ZnO NWs by isopropyl alcohol treatment for few days. In the present case, the decoration of Au NPs induces rough surface morphology with large number of ZnO/Au interfaces and surface of the ZnO NWs becomes modified. We believe that this modified surface facilitates to increase the adsorption and desorption process, resulting in faster photoresponse. From the studies in the ZnO/Au heterostructures, we argued that the nature of contacts formed between Au NPs and ZnO NWs interplay on the enhancement of photocurrent and UV PL.

6.1.1.5. Photoluminescence Studies

The room temperature PL spectra of the as–grown and ZnO/Au heterostructures are shown in Fig. **6.10(a–d)**. As–grown NWs exhibit NBE UV emission at 379 nm and a broad green emission band. The green emission band constitute of two bands, one centred at 490 nm (1st green emission) and other at 545 nm (2nd green emission). After the Au NPs decoration, the UV peak intensity is drastically enhanced and green emission peaks are significantly reduced. The intensity of the UV peak gradually increases with the Au NPs coverage up to Au_90s and then suddenly decreases with higher gold coverage. Here a fourteenth–fold enhancement in the UV peak intensity is obtained from the Au_90s sample as compared to the pristine NWs. In the present case, the obtained enhancement factor is significantly high. Similar improvement in the UV emission and subsequent quenching of green emission from the Au NPs decorated ZnO nanostructures have been reported earlier.[248,249] And the observed enhancement is attributed to the interaction between the spontaneous recombination in ZnO and surface plasmons arising from metal NPs interfaces. The changes in enhancement factor of various peaks from ZnO/Au heterostructures with Au NPs deposition time are shown in Fig. **6.10(e and f)**. Enhancement factor of both the UV emission and UV to first green emission gradually increases up to Au_90s and then decreased. Whereas, the 1st and 2nd green emissions is

drastically dropped for Au_30s sample and then it slowly decreases with further Au NPs coverage.

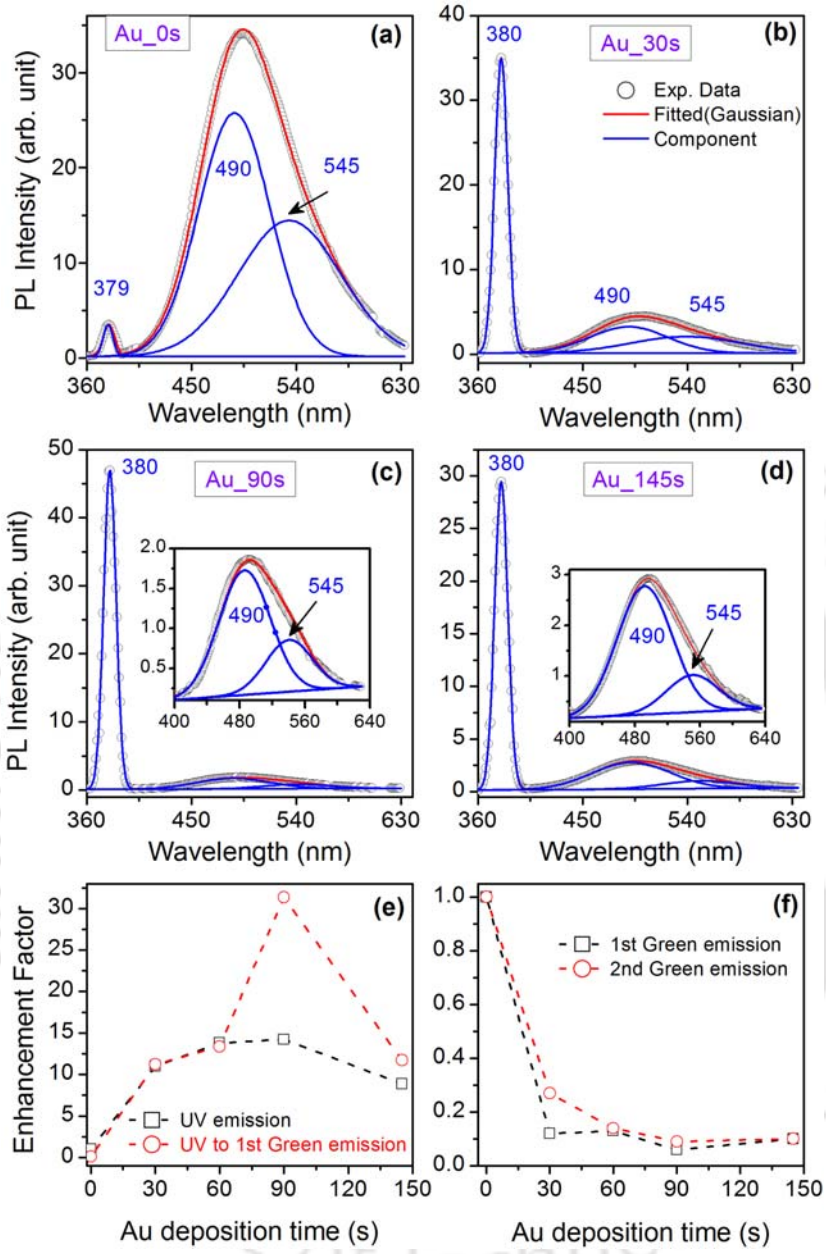

Figure 6.10: The room temperature PL spectra of the: (a) Au_0s, (b) Au_30s, (c) Au_90s, and (d) Au_145s nanowires. Insets show the corresponding PL spectra in magnified scale. (e and f) Variations of enhancement factors of UV and green emissions with different deposition time of Au nanoparticles.

The enhanced PL from the ZnO/Au heterostructures can be explained from the energy band diagram mentioned before to explain the enhanced PC spectra. In case of ZnO/Au heterostructures, when it is excited with 325 nm laser light ZnO will absorb the light and will emits in UV and green region. As explained before, the defect level (5.43 eV) and Fermi level of Au (5.47 eV) is very close to each other.[243] Therefore, the electrons from

this defect states can transfer to the Fermi level of Au, which increases the electron density at the Fermi level of Au. From the absorption spectra it is clear that due to the surface plasmon resonance Au absorbs the green emission from ZnO and get excited. After resonance, energetic electrons on the surface of the NPs will moves to the SP band, which have energy higher than the conduction band of ZnO. These active electrons can easily moves to the conduction band of ZnO, which facilitate the radiative recombination process between electrons in the conduction band and holes in the valance band of ZnO. This mechanism explains the enhancement in the UV PL and decrement in the green emission intensities in ZnO/Au heterostructures. It is also likely that the coupling between ZnO exciton and Au SP is possible which may lead to the PL enhancement.[112]

To study further about changes on the green emission, we measured PL decay dynamics of the 490 nm band. The PL decay profile of the as–grown and ZnO/Au heterostructures are shown in Fig. **6.11**. The individual decay time constants are calculated from the bi–exponential fitting to the experimental data points as explained in Chapter–4. It is found that both the decay time constants gradually decrease with increase in Au NPs coverage, which is shown in Fig. **6.11(f)**. The observed faster decay is due to the combined effects of recombination through defect states and absorption by Au NPs, since the Au SP band lies in this region. Therefore, the PL decay profiles of the ZnO/Au heterostructures further confirmed the absorption of green emission by Au NPs.

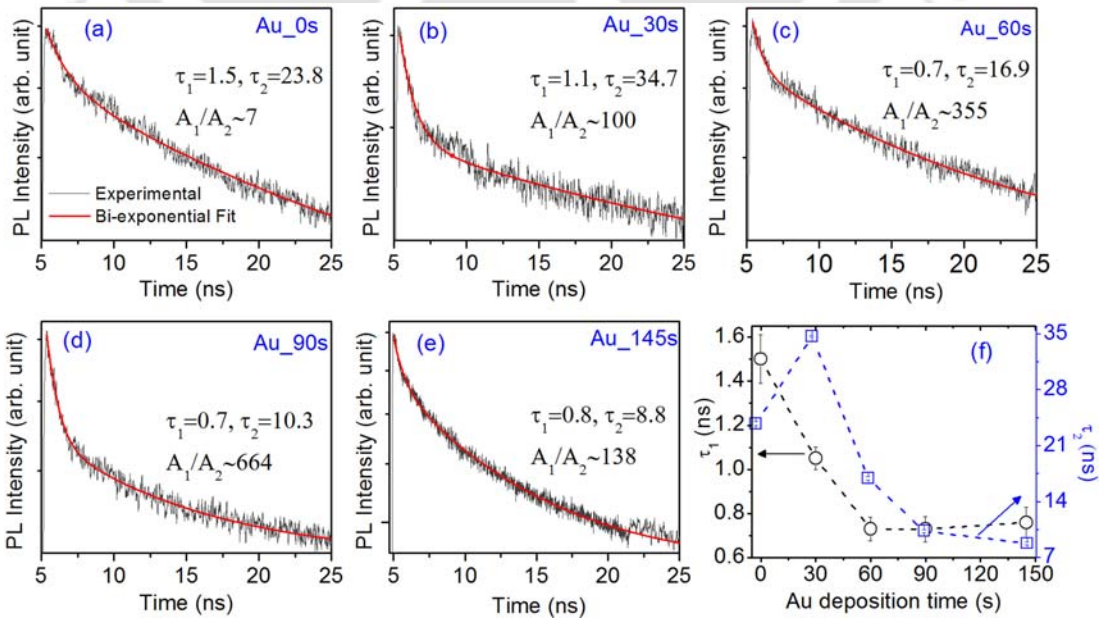

Figure 6.11: Green PL decay profile of the: (a) Au_0s, (b) Au_30s, (c) Au_60s, (d) Au_90s and (e) Au_145s nanowire heterostructures. (f) Variations of decay time constants of green emissions with different deposition time of Au nanoparticles.

6.1.2. ZnO/Ti Nanowire Heterostructure

From the photoresponse and PL studies of the ZnO/Au heterostructures, we argued that the nature of contact formed between Au NPs and ZnO interplay on the enhancement of the PC and UV PL. For better understanding of the process involved, we choose a metal with low work function, Ti for the fabrication of heterostructures and investigated the PL and Photoresponse properties.

6.1.2.1. Fabrication of the Heterostructure

For the fabrication of the ZnO/Ti heterostructures, Ti NPs were deposited on the surface of the NWs for different time duration and the samples are named according to the deposition time. For as–grown and Ti deposited for 60, 145 and 290 sec samples are named as Ti_0s, Ti_60s, Ti_145s, and Ti_290s, respectively. The approximate thicknesses are 2, 5 and 10 nm for Ti_60s, Ti_145s, and Ti_290s, respectively. The details of the sputtering parameters and approximate thicknesses of the metal layers are mentioned in the Table **6.3**.

Table 6.3: The sputtering details of Au NPs for the fabrication of ZnO/Ti heterostructures.

Sample Name	DC Bias (kV)	DC Current (mA)	Deposition Time (s)	Approx. Thickness (nm)
Ti_60s	1	5	60	2
Ti_145s	1	5	145	5
Ti_290s	1	5	290	10

6.1.2.2. Photocurrent and Photoresponse Studies

Ti NPs decorated NWs show a dramatic increment in the dark current as compared to the as–grown NWs, as shown in Fig. **6.12(a)**. The dark current gradually increases with increase in Ti NPs coverage. Detail of the change in dark current with Ti is mentioned in Table **6.4**. The increase in dark current in ZnO/Ti heterostructures can be explained from the band structure alignment at the interface between the metal and ZnO. In ZnO/Ti heterostructures, due to the lower work–function of Ti (4.26 eV)[243] an Ohmic contact is formed with downward band bending, which is shown schematically in Fig. **6.12(b)**. In this case, more number of electrons can easily transfer from Ti to the conduction band of ZnO at the interface. Then under the external bias, these electrons

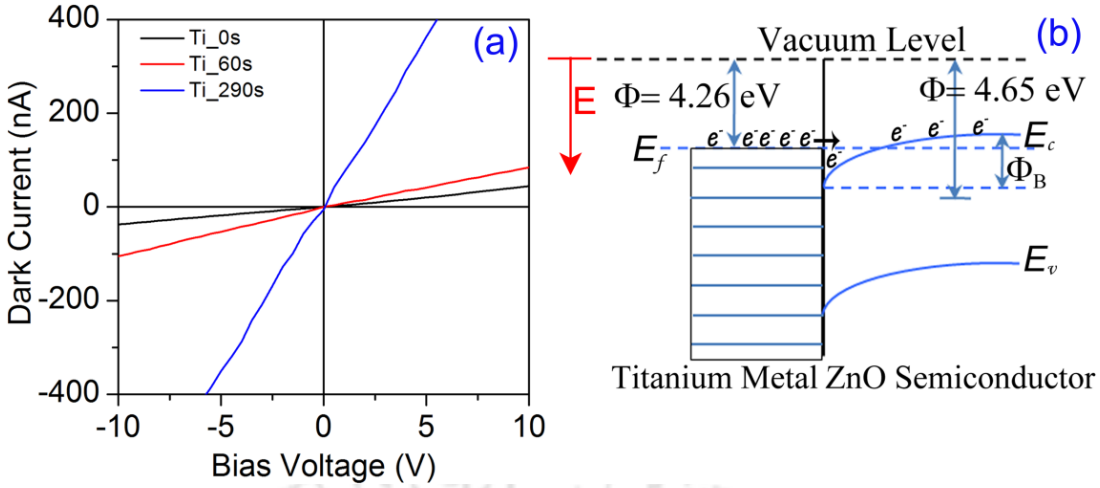

Figure 6.12: (a) Dark I–V characteristics of the ZnO/Ti nanowire heterostructures with different deposition time of Ti nanoparticles. (b) Schematic of the energy band diagrams with band alignment for ZnO/Ti NWs heterostructure.

will contribute to the current conduction process resulting in a higher dark current. As the thickness of the Ti layer increased, more number of electrons can flow from Ti to the ZnO causing gradual increase of dark current with increase in Ti coverage. Therefore, the band bending at metal–ZnO interface can explain the observed changes in the dark current satisfactorily.

Table 6.4: Photocurrent and photoresponse parameters of the as–grown and ZnO/Ti nanowire heterostructures.

Sample Name	Dark Current (nA)	Photoc--urrent (μA)	Photosensitivity	PC Growth time constants (s)		PC Decay time constants (s)	
				τ_1	τ_2	τ_3	τ_4
Ti_0s	11.5	4.72	414	17.3	218.8	19.3	316.0
Ti_60s	25.4	9.33	367	4.71	53.0	9.1	65.0
Ti_290s	211.0	65.50	310	1.4	43.9	4.7	219.5

The measured PC spectra for the ZnO/Ti heterostructures are shown in Fig. **6.13**, along with that of the as–grown ZnO NWs. For the ZnO/Ti NWs, the PC gradually increases with increase in Ti NPs coverage. The PC in the UV region dramatically enhanced, while in the visible region it increases slightly with higher Ti coverage. The Ti_290s sample gives a PC of 65.5 μA for the excitation at 369 nm. Although the obtained PC from ZnO/Ti heterostructures are quite high, but due to higher dark current the photosensitivity values are relatively low. In the ZnO/Ti heterostructures, due to the

formation of Ohmic contact, a large numbers of electrons transfer from Ti to conduction band of ZnO and it increases the electron density. When the sample is excited with UV light it gives a very high PC. With the higher thickness of Ti coating, more numbers of Ti NPs are attached on the surface of the ZnO NWs, which increases the electron density in the conduction band of ZnO. As a result, PC increases with the increase in Ti coverage.

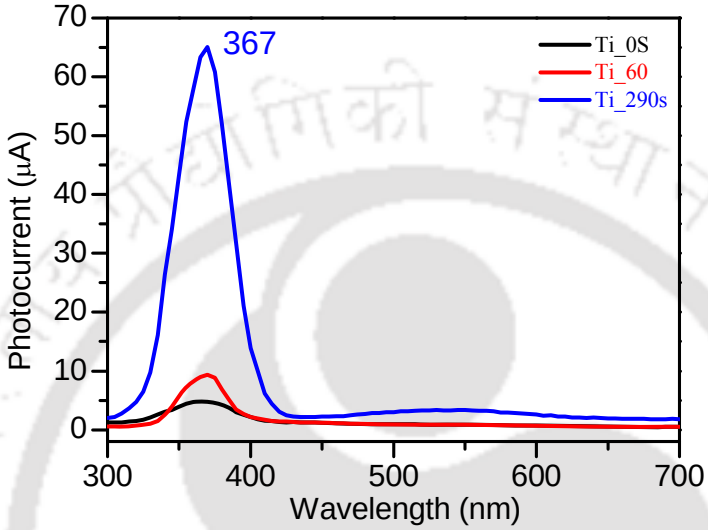

Figure 6.13: Photocurrent spectra of the ZnO/Ti nanowire heterostructures with different deposition time of Ti nanoparticles.

In order to study the effect of Ti NPs decoration on the photoresponse, we measured the photocurrent growth and decay under the excitation at 365 nm, which is shown in Fig. **6.14**. In this case, we also observed faster photoresponse time. The growth time constants are significantly reduced and show a gradual decrement with the increase in Ti coverage. The Ti_290s sample shows fastest photoresponse with growth and decay time constants of 1.4, 43.9s and 4.7, 219.5s, respectively. These data demonstrate a significant improvement in the photoresponse process in heterostructures.

6.1.2.3. Photoluminescence Studies

As compared to the pristine ZnO NWs, the room temperature PL spectra of the ZnO/Ti heterostructures show enhancement in the UV as well as green emissions intensities, as shown in Fig. **6.15(a–d)**. The change in enhancement factors for various PL peaks with the Ti deposition time is shown in Fig. **6.15(e and f)**. In this case, enhancement factors of UV, 1st green, 2nd green emission and ratio of UV to 1st green emission gradually increase with the increase in Ti NPs deposition time. The obtained PL spectra of the

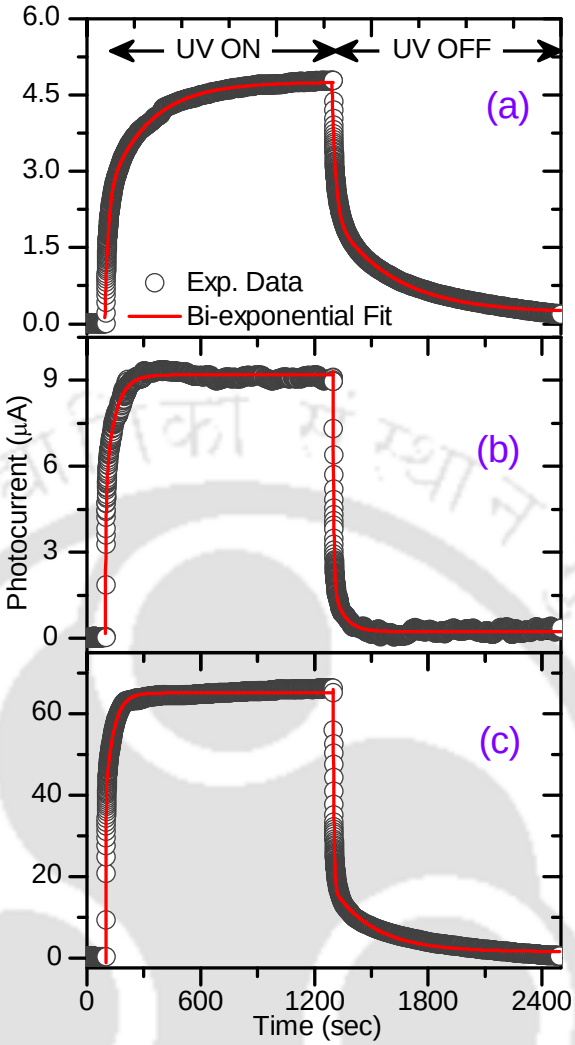

Figure 6.14: Photoresponse behaviour of the: (a) Ti_0s, (b) Ti_60s and (c) Ti_290s nanowire heterostructures, measured at a bias voltage of 3 V and under the illumination of 365 nm UV light.

ZnO/Ti heterostructures are consistent with the corresponding PC spectra. The observed enhancement on the ZnO/Ti heterostructures is similar to the previous work by Liao *et al.*.[250] They prepared Ti doped ZnO NWs by Ti plasma immersion ion implantation method and shown that UV PL intensity as well as the transport properties could be tuned by energy controlled Ti plasma immersion ion implantation.

The observed changes in the PL spectra from the ZnO/Ti heterostructures can be explained as follows. Due to the formation of Ohmic type contacts at the interface, ZnO/Ti heterostructures will facilitate the electrons transferring process from Ti to ZnO and electrons accumulation on the interface will increase substantially. Therefore, even if the photon generated electron–hole pairs are separated at the interface, the radiative recombination probability of electrons on the conduction band and in the defect energy

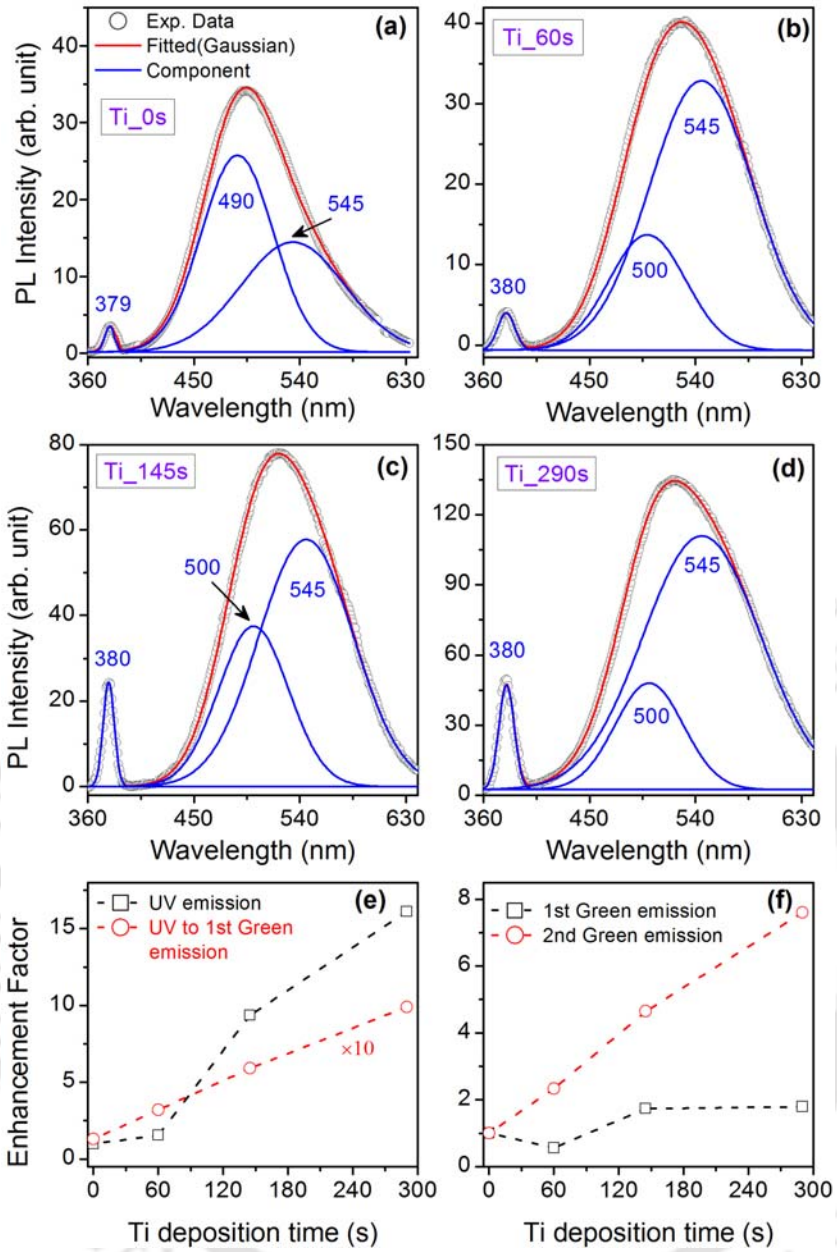

Figure 6.15: The room temperature PL spectra of the: (a) Ti_0s, (b) Ti_60s, (c) Ti_145s, and (d) Ti_290s NWs. Insets show the corresponding PL spectra in magnified scale. (e and f) Variations of enhancement factors of UV and green emissions with different deposition time of Ti nanoparticles.

band with holes in the valence band will increase dramatically due to replenishment of electrons from Ti. As a result, both the UV and green emissions intensities increase with Ti coverage. The low temperature PL data of the polymer coated ZnO NWs measured by Liu *et al.*[108] and Zn coated ZnO NWs measured by Fang *et al.*[115] showed a significant improvement in the intensity of donar bound exciton (DX)/surface exciton (SX) related emission. Since these emissions are associated with the excitons trapped on the surface, means after coating number of excitons and thus exciton related recombination increases.

The PL decay profile of the green emission of ZnO/Ti heterostructures was studied further. The decay rate is measured at 500 nm, which is shown in Fig. **6.16**. The calculation of individual decay time constants reveals no significant changes in the recombination time with Ti decoration. Therefore, Ti NPs decoration on the ZnO NWs does not affect the decay mechanism of the green emission.

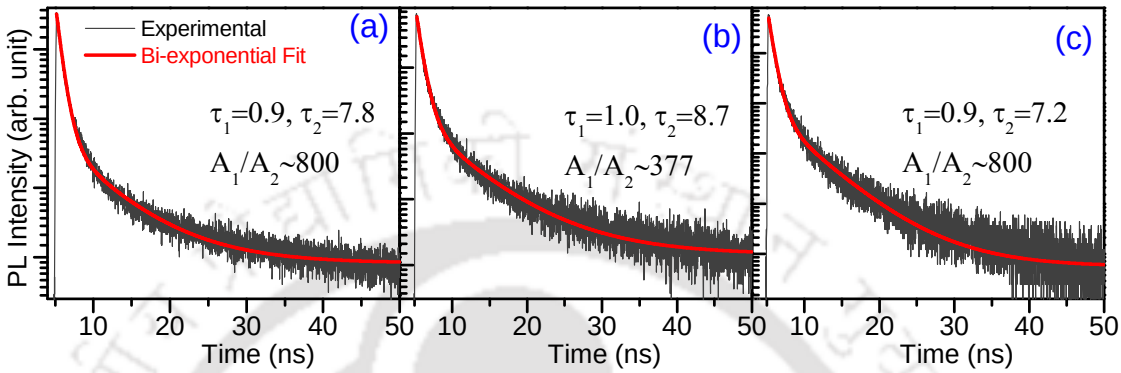

Figure 6.16: Green PL decay profile of the: (a) Ti_0s, (b) Ti_60s and (c) Ti_290s nanowire heterostructures.

6.2. Au decorated Al doped ZnO Nanowire Heterostructure

The above described heterostructures are able to give very high photosensitivity, however it fails to show ultrafast photoresponse, which is one of the essential requirements for the real time applications of ZnO NWs based UV photodetectors. Here we have adopted an effective new approach to improve the photoresponse and reset times as well as the photosensitivity of ZnO NWs. We have shown that a substantially improved (ultrafast) photoresponse and reset time, and enhanced photosensitivity could be obtained by the combined effects of Al doping and Au NPs decoration on the surface of the ZnO NWs network.

6.2.1. Fabrication of the Heterostructure

3% doped Al:ZnO NWs sample was used for the decoration of ultra small Au NPs on the surface of the NWs by sputter deposition process. Al doping was achieved by ball milling of the source powder followed by the VLS growth, as discussed in Chapter–3. The Au sputtering was done at 1kV DC voltage for 180 sec, which results in an estimated 25 Å thick Au layer on the NWs. From the studies on ZnO/Au heterostructures, it is found that this thickness is optimum for the maximum improvement in the PC in the ZnO NWs.

6.2.2. Photocurrent and Photoresponse Studies

The dark current–voltage characteristic of the Au NPs deposited Al:ZnO NWs is shown in Fig. **6.17**. Compared to the dark current of the 3% Al:ZnO NWs (110 nA), the Au/Al:ZnO NWs shows a reduction in the dark current (70 nA). The observed change in the dark current is due to the upward band bending at the interface between Au and ZnO. The upward energy band bending occurs at the interface due to the differences in work function of ZnO (4.65 eV) and Au (5.47 eV), as explained in details in the section **6.1.1.4**.

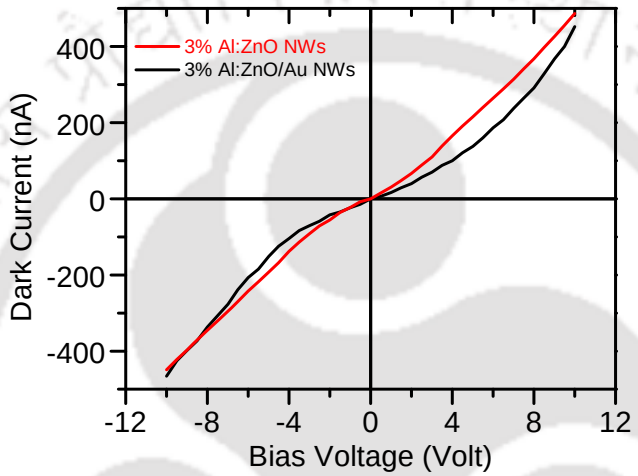

Figure 6.17: Dark current–voltage characteristic of the 3% Al:ZnO nanowires after the Au nanoparticles decoration.

The photoresponse of the Al:ZnO NWs measured under the excitation of 365 nm UV light is shown in Fig. **6.18**. The Al:ZnO/Au NWs shows a maximum PC of 21.0μA, leading to a photosensitivity of 300. Therefore, the heterostructure shows a significant improvement in the UV photosensitivity with an enhancement factor of six with respect to 3% Al:ZnO NWs. The changes in the PC and photoresponse parameters are tabulated in Table **6.5**. For comparison, the results of the 3% doped Al:ZnO NWs are also tabulated. At the same time, the photoresponse and reset times are also significantly reduced, which results in an ultra fast photodetection. The obtained photoresponse and reset times are 0.10 and 0.11s, respectively. After the Au NPs decoration, the photoresponse and reset times are about one order of magnitude faster, which is very significant. Therefore, the Au NPs decorated Al:ZnO NWs are found to be most appropriate for the fabrication of ultra fast UV photodetectors.

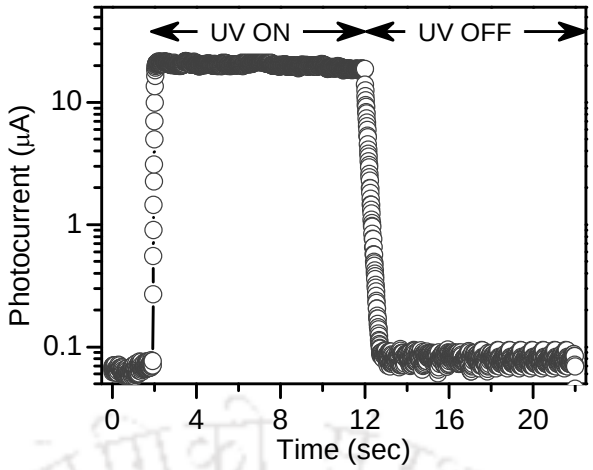

Figure 6.18: Photoresponse of the 3% Al:ZnO nanowires after the surface decoration with Au nanoparticles.

Table 6.5: Photocurrent, photoresponse and photoluminescence parameters of the Al:ZnO/Au nanowire heterostructure.

ZnO NWs	Dark current (nA)	Photoc--urrent (μA)	Photo sensiti vity	PC Response time (s)	PC Reset time (s)	PL Enhancement Factor	
						UV peak	UV-to-494 peak
3%Al:ZnO	110	5.2	47	0.90	1.10	1	0.94
Al:ZnO/Au	70	21.0	300	0.10	0.11	4	7.5

The improvement in the photoresponse and photosensitivity for the Al:ZnO/Au NWs can be explained as follows. In the Al:ZnO/Au NWs, the decoration of Au NPs induces rough surface morphology resulting in interfacial states between Au and ZnO. These rough surface induced traps can capture the carriers (photogenerated) resulting in an ultrafast photoresponse and reset times. The enhancement in photosensitivity in the Al:ZnO/Au NWs could be explained on the basis of interband transition and surface plasmon assisted interfacial electrons transfer to the conduction band of ZnO. From the absorption study of the Au NPs [Fig. **6.5**], it is known that the electrons in the Fermi level of Au NPs are excited by incident light in the UV–violet region due to interband transition and in the green region due to the surface plasmon resonance. [245] In the present case, when the Al:ZnO/Au NWs were illuminated with UV light, the excited energetic electrons in the Au NPs can escape from the surface of the NPs and transfer to the conduction band of ZnO through the interface. Under external bias, these electrons along with photogenerated electrons (due to band edge absorption of ZnO) contributed to the

current conduction process, resulting in the enhanced photocurrent. Therefore, we believe that the enhanced photocurrent in the present case is due to the increase in electron density in the conduction band of ZnO by band edge absorption of ZnO and plasmon assisted interfacial electron transport from Au NPs.

6.2.3. Photoluminescence Studies

The PL spectrum of the Al:ZnO/Au NWs is shown in Fig. **6.19**. The UV peak intensity is dramatically enhanced and green emission peak is significantly reduced in the doped heterostructure. Here a four–fold enhancement in the UV peak intensity is obtained from the Al:ZnO//Au NWs, while the 1st green emission intensity reduced to half and the 2nd green emission intensity is one third of its initial value. Compared to the as–grown 3% Al:ZnO case, the UV peak is enhanced by a factor of four, while the UV–to–green emission ratio shows more than seven times improvement. The observed improvement in the PL spectrum is due to the surface plasmon assisted enhanced radiative recombination in the Al:ZnO heterostructures.

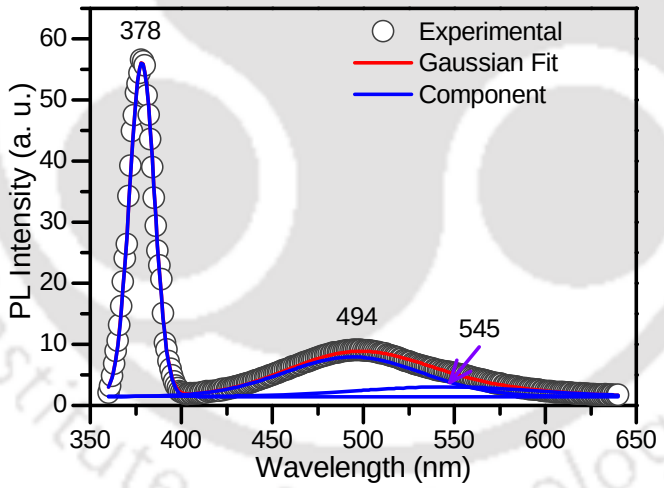

Figure 6.19: PL spectrum of the 3% Al doped nanowires after the decoration with Au nanoparticles.

6.3. Inorganic/Organic Type Nanowire Heterostructures

Another type of NW heterostructures was fabricated using highly UV sensitive organic materials. Two inorganic/organic type heterostructures were fabricated, one with anthracene and the other with CuPc. As these organic materials are highly UV sensitive organic semiconductor, it can influence to enhance the photosensitivity of the ZnO/anthracene system. At the same time, the surface of the ZnO NWs becomes

modified, which will affects the oxygen adsorption and desorption process. Therefore, using inorganic/organic heterostructure approach, fabrication of ultrafast photodetectors could be possible.

6.3.1. ZnO/Anthracene Nanowire Heterostructure

Anthracene is an organic semiconductor with wide bandgap. The crystal structure of the anthracene is monoclinic with large inter–planar spacing (d_{001} =9.14 Å) and have a long range coherency with each (001) plane.[251] Due to the lowest surface energy of (001) face, anthracene crystal grown by a periodic layer–by–layer growth process along (001) plane.[252] Efficient organic light emitting diodes (OLEDs) was fabricated by using thin films of anthracene derivatives by Huang *et al.*[253] and Zhu *et al.*.[254] There is also report on the use of anthracene based organic dye for the dye–sensitized solar cells.[255] However, there are a few reports on the fabrication of nanoscale heterostructures with anthracene. Chen *et al.*[256] used anthracene functionalization to the ruthenium NPs and studied the PL and electron conductivity. In another work, Das *et al.*[257] prepared an organic capped ZnO NPs composite using anthracene derivative and studied the photoinduced quenching properties. As the photoresponse is strongly influenced by surface capping, therefore it would be interesting to study the photoresponse behaviour of the anthracene capped ZnO NWs. However, there is no study on the effect of surface modification of the ZnO NWs by anthracene on the photodetection and photoresponse behaviour of the ZnO NWs. Therefore, we fabricated ZnO/anthracene NWs heterostructure by capping with the anthracene and investigated the effect of surface modification with anthracene on the PC, photoresponse and PL properties.

6.3.1.1. Fabrication of the Heterostructure

ZnO/anthracene heterostructure was fabricated by dip coating of the NWs in the anthracene solution in ethanol solvent with concentration of 3mM for 30 min. After removing the NWs from the anthracene solution, it was dried in air and then heated at 150°C for 15 min to remove the solvent and water moister. The schematic diagram of the inorganic/organic type ZnO/anthracene heterostructure is shown in Fig. **6.20**.

6.3.1.2. Morphology and Structural Characterization

Figure **6.21(a)** shows the typical TEM image of single ZnO NW with diameter 65 nm.

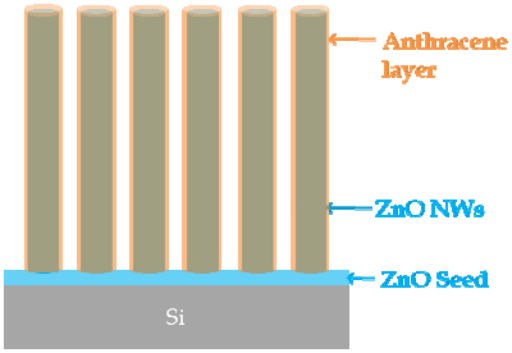

Figure 6.20: Schematic diagram of the growth of ZnO/anthracene NW heterostructure.

Figure **6.21(b)** shows the high–resolution lattice image of the top end of the ZnO NWs. From the high resolution lattice fringe image, the lattice spacing of ZnO NW is found to be 0.26 nm, which indicates the NWs are single crystalline and growth direction is along <002>. The high resolution TEM image of the ZnO/anthracene system is shown in Fig. **6.21(c)** and it shows the presence of thin anthracene layer over the ZnO NW. With anthracene capping, the NWs look slightly thicker due to the coverage of anthracene layer. The average thickness of the anthracene layer is found to be 15 nm.

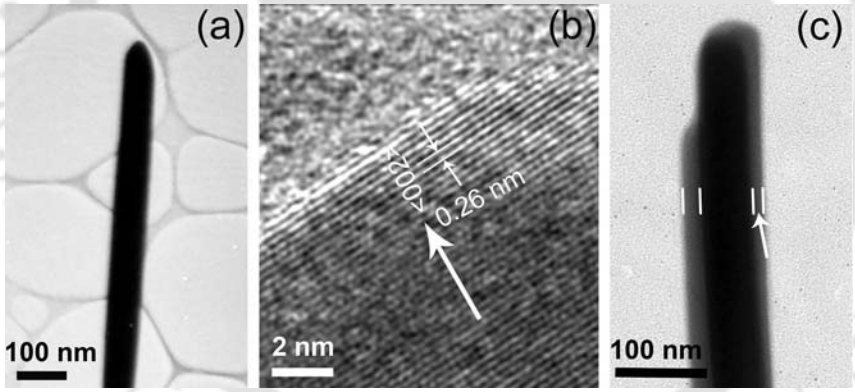

Figure 6.21: (a) TEM image of the as–grown single nanowire. (b) The high resolution lattice fringes of the above nanowire, solid arrow shows the growth direction. (c) Magnified TEM image of the ZnO/anthracene heterostructure, which clearly shows the presence of thin anthracene layer over the ZnO nanowire (region marked by white line).

To study further about the crystal structure of the ZnO NWs, x–ray diffraction measurements were made on the as–grown NWs and ZnO/anthracene heterostructure, and the results are shown in Fig. **6.22**. The intense peak corresponding to the (002) plane of hexagonal structure confirms the single crystalline nature and orientation of the NWs is along the *c*–axis. After the anthracene capping, the intensity of the XRD peaks was reduced due to the coverage of the anthracene layer. Although the outer anthracene layer is crystalline (monoclinic) however, no peak is observed in the XRD pattern. Because of

the large inter–planar spacing (d_{001} =9.14 Å), the intense peak comes below 10° of 2θ, where the sensitivity of the XRD detector is very weak.

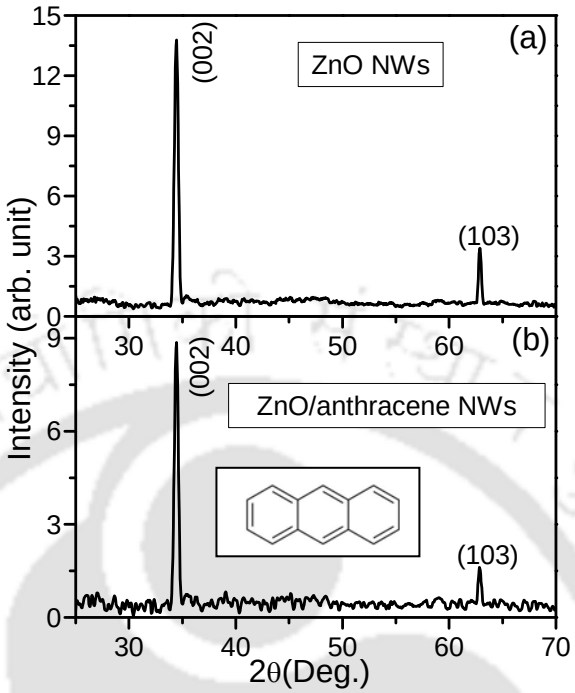

Figure 6.22: XRD patterns of the: (a) as–grown ZnO nanowires and (b) ZnO/anthracene nanowires heterostructure, respectively. Inset in (b) shows the molecular structure of anthracene.

The presence of anthracene layer on the surface of the NWs is further confirmed by FTIR reflectance measurements, as shown in Fig. **6.23**. The NWs shows only the peaks related to the bending and stretching modes of Zn–O, which are clearly shown in the inset of Fig. **6.23**. On the other hand, the ZnO/anthracene heterostructure shows peaks related to the bending and stretching modes of hexagon ring and C–H bonds of anthracene, along with the bending and stretching modes of Zn–O. The observed reflectance bands at 473 and 532 cm^{-1} correspond to the Zn–O bending mode and 580 cm^{-1} corresponds to Zn–O stretching vibration mode of nanocrystalline ZnO.[258] The peak at 520 cm^{-1} is the signature of the skeletal bending (out of plane) mode of the anthracene hexagon ring.[252] The bands observed at 810 and 1275 cm^{-1} are due to the aromatic C–H bending modes. The skeletal vibration of the anthracene hexagon ring could be assigned to the peaks at 1620 cm^{-1}. The characteristic and strong peak at 3100 cm^{-1} is due to the aromatic C–H stretching vibration. Therefore the FTIR analysis further confirmed the presence of anthracene layer over the ZnO NWs surface. It is also

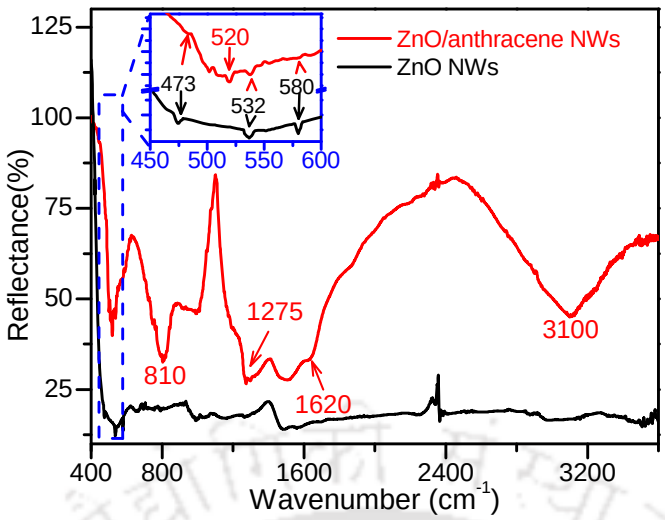

Figure 6.23: FTIR reflectance spectra of the ZnO nanowire and ZnO/anthracene nanowires heterostructure. Inset shows the spectra of low frequency region at a magnified scale.

observed that the unheated ZnO/anthracene heterostructure shows the presence of water moister on the surface. However, after oven heating the water moister is fully removed and does not attach again. It has been recognized that the as–grown ZnO NWs contains oxygen vacancy states on the surface, which can occur in both singly or doubly ionized states, V_0^+ or V_0^{++}. The anthracene molecules are most likely attached on the surface of the NWs at V_0^+ or V_0^{++} sites by metal–ligand interfacial bonding interaction. This is supported by previous reports on surface functionalization of ruthenium and ZnO NPs with the anthracene derivatives.[256,257]

6.3.1.3. Photoluminescence Studies

The room temperature PL spectra of the NWs and ZnO/anthracene NWs heterostructure are shown in Fig. **6.24(a–b)**. As–grown NWs exhibit weak NBE UV emission at 378 nm and a broad green emission band. Gaussian multi–peak fitting shows the existence of two green emission bands, one at 497 nm (1st green emission) and another at 548 nm (2nd green emission). The ZnO/anthracene heterostructure shows significant enhancement in the UV peak intensity, while the intensity of the green emission peaks are reduced. After the anthracene capping, the intensity of the UV emission is enhanced by a factor of three, while the green emission intensity is reduced to half of the value of the as–grown case. The ratio of UV–to–1st green emission intensities also shows a major improvement by a factor of seven. The observed enhancement in the UV emission is likely to be caused by the high absorption by anthracene in this region and reduction in the green emission is

believed to be due to the surface modification by anthracene. To understand the obtained enhancement in the UV PL intensity, we need to know about the corresponding absorption and emission behaviours of the anthracene. The measured excitation and emission spectra for the anthracene powder are shown in Fig. **6.24(c)**. The emission spectrum show strong emission in the UV–blue region with sharp peaks at 383 and 410 nm. To understand the absorption behaviour of the anthracene, excitation scan was monitored for the emission at 410 nm. The excitation spectrum show sharp absorption peaks at 350 and 370 nm. The first one is corresponding to the emission at 383 nm and later one for the emission at 410 nm. Therefore, in the ZnO/anthracene heterostructure when the system is excited with the 325 nm laser, both the ZnO and anthracene layers are excited and it creates electron–hole pairs. It is known that the highest occupied molecular orbital (HOMO) and lowest unoccupied molecular orbital (LUMO) in the anthracene molecule are positioned at –5.6 eV and –2.25 eV[253], i. e., LUMO is situated above the conduction band of ZnO (electron affinity ~4.65 eV). The excitation spectrum

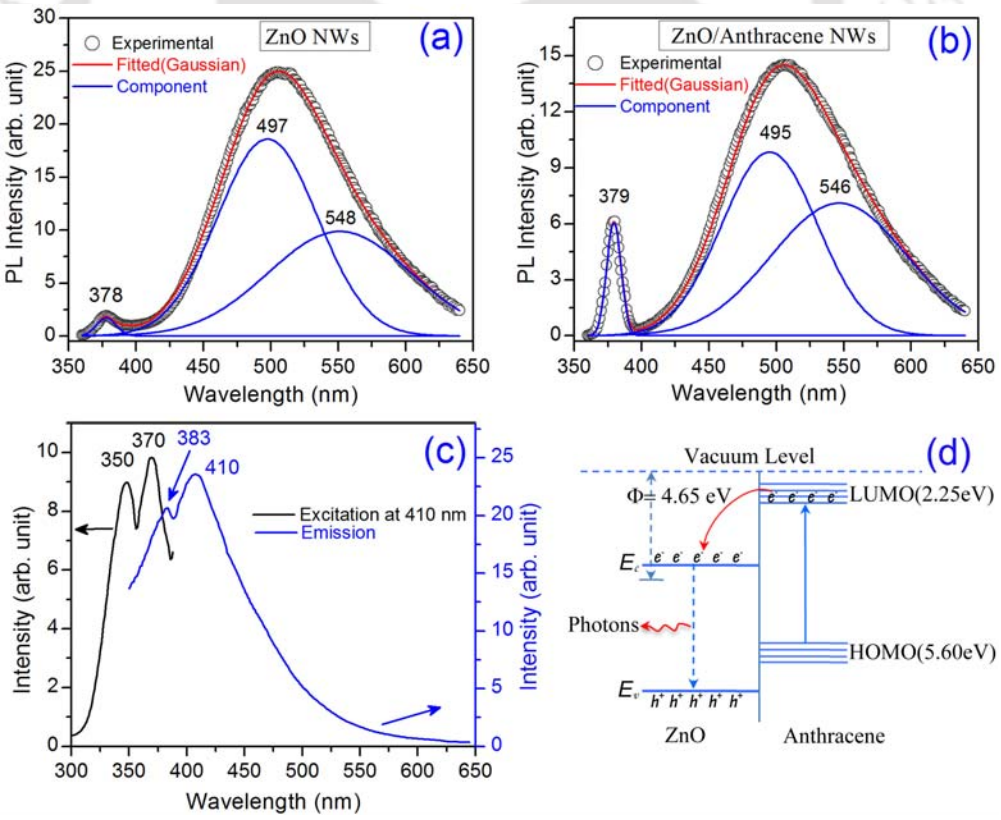

Figure 6.24: Room temperature PL spectra of the: (a) ZnO nanowires and (b) ZnO/anthracene nanowires heterostructure. (c) Excitation and emission spectra of the anthracene powder. Excitation scan was performed for the emission at 410 nm. (d) Schematic of the energy band diagram of the ZnO/anthracene heterostructure and possible interfacial electron transfer mechanism.

of the anthracene is in agreement with the positions of HOMO and LUMO. Therefore, these photoexcited electrons in the LUMO states can easily transfer to the conduction band of ZnO through interfacial interaction, and this is schematically shown in the Fig. **6.24(d)**. This process will lead to the accumulation of more charge carriers at the conduction band, which will boost the electron–hole recombination probability. Simultaneously, few of the electrons at the LUMO states recombine with the holes in the HOMO states resulting in enhancement of UV PL intensity. However, due to the transfer of most of the electrons and very thin layer of the anthracene, this emission does not have strong effects on the enhanced UV PL of the ZnO/anthracene heterostructure. As explained before, the anthracene molecules are likely to be attached to the surface of the NWs at the oxygen vacancy sites, which significantly reduced the oxygen vacancy states of ZnO NWs. This process results in the decrement in the green emissions in the ZnO/anthracene system. On the other hand, the transfer of photoexcited electrons from the LUMO in anthracene to the conduction band of ZnO could be the strongest possible source for the enhanced UV PL intensity.

To get more insight in to the capping effect on the green emission by surface modification, we measured the PL decay dynamics of the 1st green emission under the excitation of 375 nm pulsed laser. The decay profile of the bare ZnO NWs and ZnO/anthracene heterostructure are shown in Fig. **6.25**. Both the decay curves show bi–exponential decay dynamics corresponding to the components of 1st and 2nd green emissions. Therefore, PL decay confirmed the presence of two components in the broad

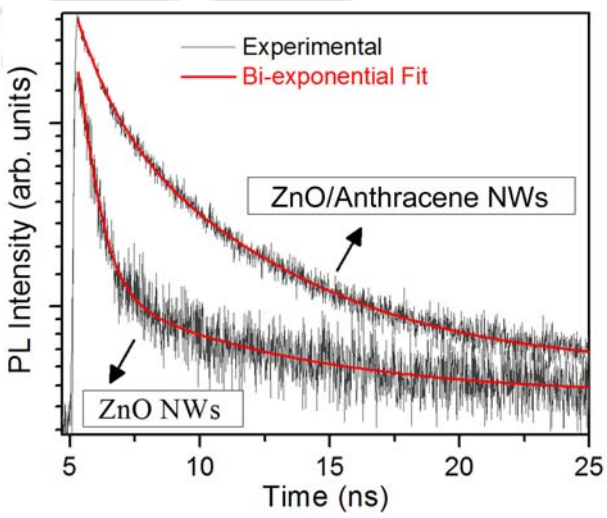

Figure 6.25: PL decay profile of the first green emission (~500 nm) of the ZnO nanowires and (b) ZnO/anthracene nanowires heterostructure, measured under the excitation of 375 nm pulsed laser source.

green emission. The calculated decay life times are 0.7 and 7.6 ns for the as–grown ZnO NWs and 1.2 and 5.6 ns for the ZnO/anthracene system, respectively. The PL decay rates become relatively slow after the anthracene treatment because of the covering of the vacancy defect states by anthracene. A reduction in the defect density essentially increases the lifetime of the carriers. Therefore, the anthracene capping slows down the decay rate of green emission peak, which supports the fact that anthracene molecules is attached at the oxygen vacancy sites of the ZnO NWs. This is consistent with the results of the RTA treated ZnO nanostructures (discussed in Chapter–4), where we observed slowing down of the green PL decay behaviour from the structurally improved ZnO NWs with reduced defect density.

6.3.1.4. Photocurrent and Photoresponse Studies

Figure **6.26(a)** shows the dark I–V characteristics of the NWs and ZnO/anthracene NW heterostructure. The I–V characteristics show nearly linear behaviour with current in the range of nA. After the heterostructure formation, the dark current is increased to 12 nA from 6.0 nA at 3V bias. The wavelength dependence of PC at a bias of 3V in the range 300–650 nm is shown in Figure **6.26(b)**. The PC spectra of the as–grown NWs show a strong peak in the UV region at 369 nm and a very weak broad peak in the green (shown as inset). For the ZnO/anthracene system, the intensity of the PC peak in the UV region is significantly enhanced. The calculated PC and photoresponse parameters are tabulated in the Table **6.6**. The maximum PC is enhanced to 48.2 μA from 4.0 μA, which is for the as–grown NWs. Photosensitivity value is also increased to 4000, leading to the six–fold enhancement, as compared to the bare NWs. Very high photosensitivity and low dark current are the basic requirements for efficient photodetection. Therefore, the ZnO/anthracene system is very sensitive in the UV region makes it an important and effective candidate for the efficient photodetector.

The enhancement in the dark current as well as in the PC in the heterostructure can be explained as follows. Due to the presence of intrinsic oxygen vacancy defects on the surface of the uncapped ZnO NWs, in dark condition oxygen molecules are attached on the above defect states by adsorption process and trapped two free electrons.[21,152] This process results in decrement in conductivity by forming a depletion layer near the surface, resulting in a very low dark current. After anthracene capping, as the anthracene molecules are possibly attached at the oxygen vacancy sites with the carbon

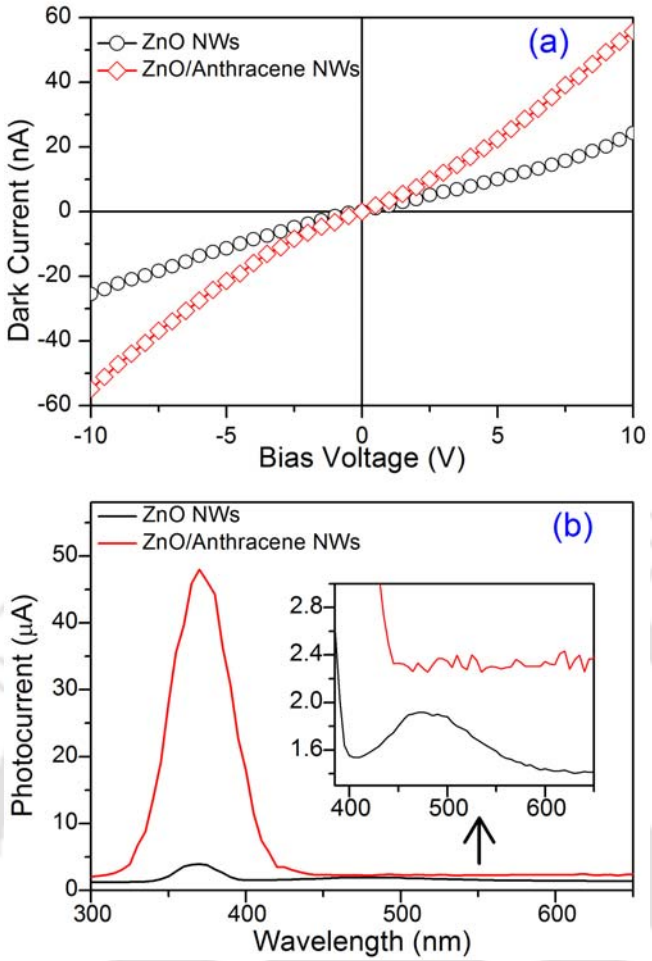

Figure 6.26: (a) Dark current–voltage characteristics and (b) wavelength dependent photocurrent of the ZnO nanowires and ZnO/anthracene nanowires heterostructure, respectively. Inset in (b) shows the specific region in magnified scale.

atom in the centre ring of anthracene, it would trap only one electron from ZnO to stabilize the vacant defect. This accounts for the somewhat higher dark current from the ZnO/anthracene NWs heterostructure. Under the UV irradiation, electron–hole pairs are generated that increase the PC and oxygen molecules are released by photodesorption process. In the case of ZnO/anthracene NWs heterostructure, both the ZnO and

Table 6.6: Photocurrent, photoresponse and photoluminescence parameters of the ZnO/anthracene nanowires heterostructure.

Sample	Dark current (nA)	Photocu--rrent (μA)	Photose--nsitivity	PC Response time (s)	PC Reset time (s)	PL Enhancement Factor	
						$I_{UV}/I_{UV(pristine)}$	I_{UV}/I_{495nm}
ZnO NWs	6	4.0	668	7.3	63.3	1.0	0.09
ZnO/anthracene	12	48.2	4000	1.5	1.6	3.5	0.61

anthracene layers generate electron–hole pairs. Then the electrons at the LUMO states of anthracene transfer to the conduction band of ZnO. Under external bias, these electrons along with the photogenerated electrons due to band edge absorption of ZnO contributed to the current conduction process, resulting in enhanced PC.

The photoresponse behaviour of the ZnO NWs and ZnO/anthracene NW heterostructure, measured at 360 nm are shown in Fig. **6.27**. The ZnO/anthracene NWs heterostructure shows very fast response with response and reset times of 1.5 and 1.6s, respectively. In contrast, the uncapped NWs have response and reset time about 7.2 and 63.2s, respectively. As expected the photoresponse time for the uncapped NWs is very slow due to the presence of intrinsic defects/trap centres. Therefore, ZnO/anthracene NWs heterostructure shows five times faster response and about forty times faster reset time, which is significant for the real time photodetection application. Figure **6.27(c)** shows the photoresponse of the ZnO/anthracene NWs under periodic UV illumination. The maximum photocurrent in one cycle is same as that of any other cycle. Second and third

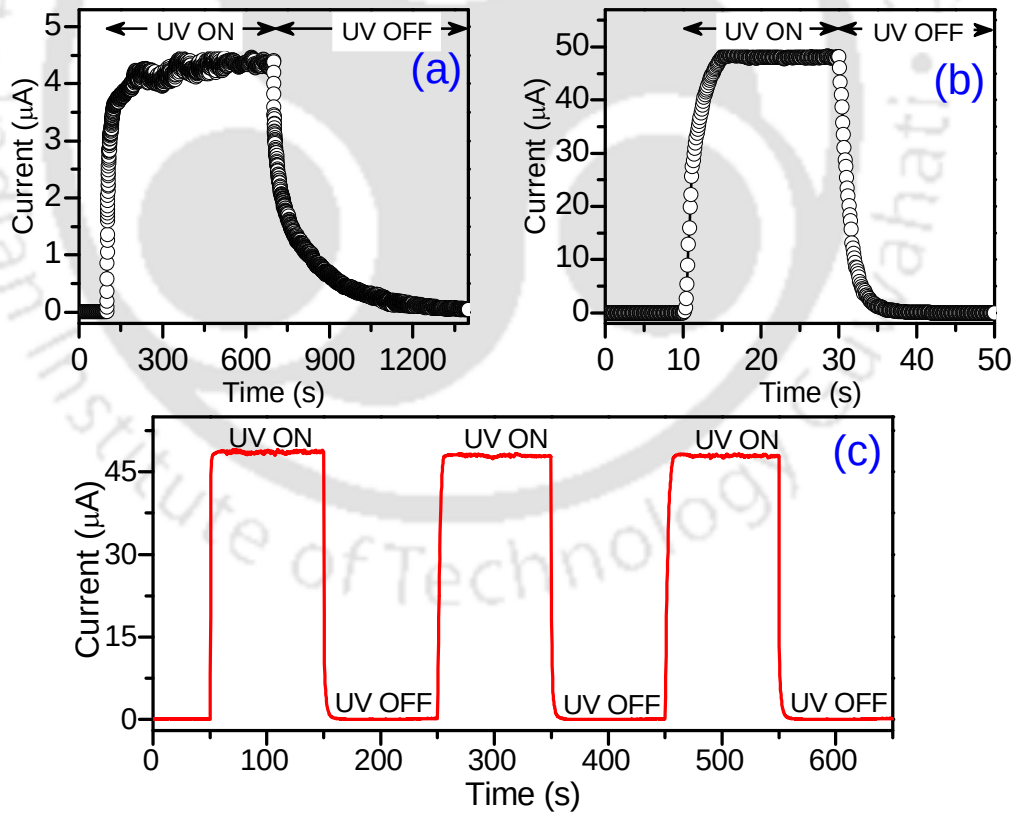

Figure 6.27: photoresponse behaviour (at 360 nm) of the: (a) ZnO nanowires and (b) ZnO/anthracene nanowires heterostructure, respectively, measured at a bias voltage of 3 V. (c) Photoresponse of the above heterostructures under the pulse (200s) UV light illumination of same wavelength.

cycles of photocurrent growth and decay show exactly the replica of first cycle, indicating a fast and reproducible PC response, which is important for the real time application in photodetctors. It is known that, anthracene molecule photodimerizes under the UV exposure. The obtained reproducible fast response from the heterostructure indicates that this photodimerization does not affect on the photoresponse behaviour. However, this dimer can be reverted to anthracene by UV irradiation below 300 nm. To study the influence of environment on the performance of the ZnO/anthracene heterostructure, we measured the PC in different environmental condition (different humidity and O_2 pressure). It is found that there is no notable change in the photoresponse behaviour as the effect of humidity or O_2 pressure.

In general, it is known that the rates of O_2 adsorption and photodesorption processes primarily control the photoresponse time. The chemisorbed O_2 molecules trapped the free electrons available on the surface of the NWs, which results in the formation of a depletion layer, resulting in a upward band bending and leading to a barrier height for electrical conduction.[152,189] During the UV illumination, the photoexcited holes are generated and trapped by the adsorbed O_2^- through the surface electron–hole recombination, while the photoexcited unpaired electrons significantly increase the conductivity. The photocurrent gradually increases with time until desorption and readsorption of O_2 reach an equilibrium state. At the end of the UV illumination, the hole density is much lower than electron density in the NW. Although holes recombine quickly with electrons upon turning off the UV light, there are still a lot of electrons left in the NWs. With the surface readsorption of O_2, the current comes to the initial value very slowly. In the present case, due to the anthracene covering on the surface of the ZnO NWs, defect states are considerably passivated/ reduced. As a result, band bending in the NW is also reduced, which results in a less effective charge separation. The ZnO/anthracene NWs show comparatively higher dark current, which supports the reduction of band bending in the NW. This is similar to the case when the surface of the NWs is covered with water moister.[153] Now, electrons and holes can easily recombine, leading to a shorter carrier life time. During the interfacial charge transfer from anthracene to ZnO, it is believed that sufficient amount of holes are also transfer to the valence band of ZnO. Therefore, at the end of UV illumination, sufficient amount of electrons and holes are available in the NW. During decay, the electrons and holes are

recombining in fast way due to the shorter carrier life time. This process results in a much faster photoresponse, compared to the case of uncapped ZnO NWs.

6.3.2. ZnO/CuPc Nanowire Heterostructure

In the search of suitable external material for the heterostructure fabrication here we consider another organic semiconductor, copper phthalocyanine (CuPc). ZnO/CuPc heterostructure was fabricated and investigated the effect of CuPc layer deposition on the surface of the ZnO NWs on the photoresponse and PL properties. The most commonly observed crystal phases of CuPc are α and β polymorphs. For the CuPc thin film, α phase is stable up to the substrate temperature of 200°C and above it changes to β phase.[259] The structure of α phase is known to be an orthorhombic crystal having unit cell dimensions: a = 25.92 Å, b = 3.79 Å, and c = 23.92 Å. The structure of β phase is a monoclinic crystal with the following unit cell dimensions: a = 14.68 Å, b = 4.98 Å and c = 19.6 Å. CuPc has been widely studied because of its important applications in hybrid organic solar cells and multilayer based organic light emitting diodes.[260,261] Earlier, thin film *p–n* Junctions based on ZnO and CuPc were fabricated and the junction parameters and rectifying behaviour were studied.[262,263] Recently, Liu *et al.*[264] fabricated ZnO/CuPc NWs heterostructure by dip coating technique and studied the photovoltaic property by measuring surface photovoltage.

6.3.2.1. Fabrication of the Heterostructure

An aqueous chemically grown vertically aligned ZnO NWs array is used for the fabrication of ZnO/CuPc heterostructure. Ultra thin layer of CuPc was deposited on the surface of the ZnO NWs for 2 min at a sublimation temperature of 375°C by thermal evaporation process at a very low flux of CuPc vapor. The deposition was carried out at chamber pressure of 1×10^{-5} mbar.

6.3.2.2. FTIR Reflectance Study

The presence of CuPc layer on the surface of the NWs is confirmed by FTIR reflectance measurements, as shown in Fig. **6.28**. The uncapped NWs shows only the peaks related to the bending and stretching modes of Zn–O. On the other hand, the ZnO/CuPc heterostructure shows peaks related to the bending and stretching modes of CuPc molecule and C–N bonds, along with the bending and stretching modes of Zn–O. The

observed reflectance bands at 467 and 544 cm^{-1} correspond to the Zn–O bending modes and 521 and 585 cm^{-1} corresponds to Zn–O stretching vibration modes of nanocrystalline ZnO.[258] The peak at 748 cm^{-1} is the signature of ring deformation of CuPc molecule.[265] The peaks at 897 and 1287 cm^{-1} correspond to bending and stretching modes of C–N bond, respectively. The phthalocyanine skeletal vibration related peaks are observed at 1092 and 1119 cm^{-1}. The peaks at 1390 and 1609 cm^{-1} are related to the stretching of aromatic phenol ring and benzene ring, respectively. The peak at 1504 is due to the stretching of pyrrol group. Therefore the FTIR analysis confirmed the presence of anthracene layer over the ZnO NWs surface. In this case, the CuPc molecules are possibly attached at the defect sites on the surface of the NWs by electrostatic interaction.

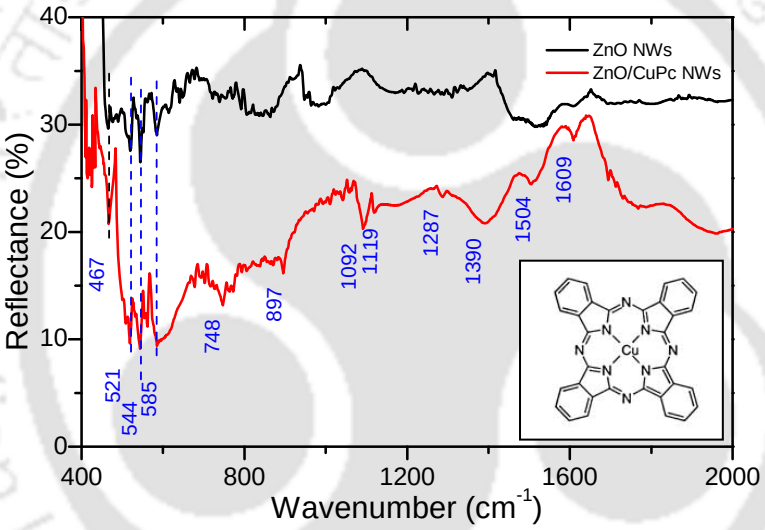

Figure 6.28: FTIR reflectance spectra of the ZnO nanowire and ZnO/CuPc nanowires heterostructure. Inset shows the molecular structure of CuPc.

6.3.2.3. Photoluminescence Studies

The room temperature PL spectra of the ZnO NWs and ZnO/CuPc NWs heterostructure are shown in Fig. **6.29(a–b)**. ZnO NWs exhibits NBE UV emission at 379 nm and a broad visible emission band in the blue–green region. Gaussian multi–peak fitting shows the existence of two emission bands, one at blue region and another at green region. The first one is centred at 436 nm and second one is at 520 nm. The observed NBE emission is due to free excitonic recombination while the blue and green emissions are due to the presence of interstitial zinc[117] and single ionized oxygen vacancy,[122] respectively. The strong blue peak indicates the formation of dense interstitial zinc states in the as–grown

ZnO NWs. It is known that in aqueous chemical method the zinc nitrate provides Zn^{2+} ions whereas the H_2O supply the OH^- ions required for the oxidation of Zn^{+2} ions. Due to the comparatively faster rate of hydrolysis of zinc nitrate than the H_2O, formation of high density of interstitial zinc in the as–grown NWs is expected. After the CuPc deposition, the UV peak intensity is dramatically enhanced, while the intensity of blue and green emissions are considerably reduced. The UV PL intensity is enhanced by a factor of seven whereas the green emissions intensity is almost half, compared to the case of uncapped NWs. The intensity of the blue emission is slightly reduced. The observed

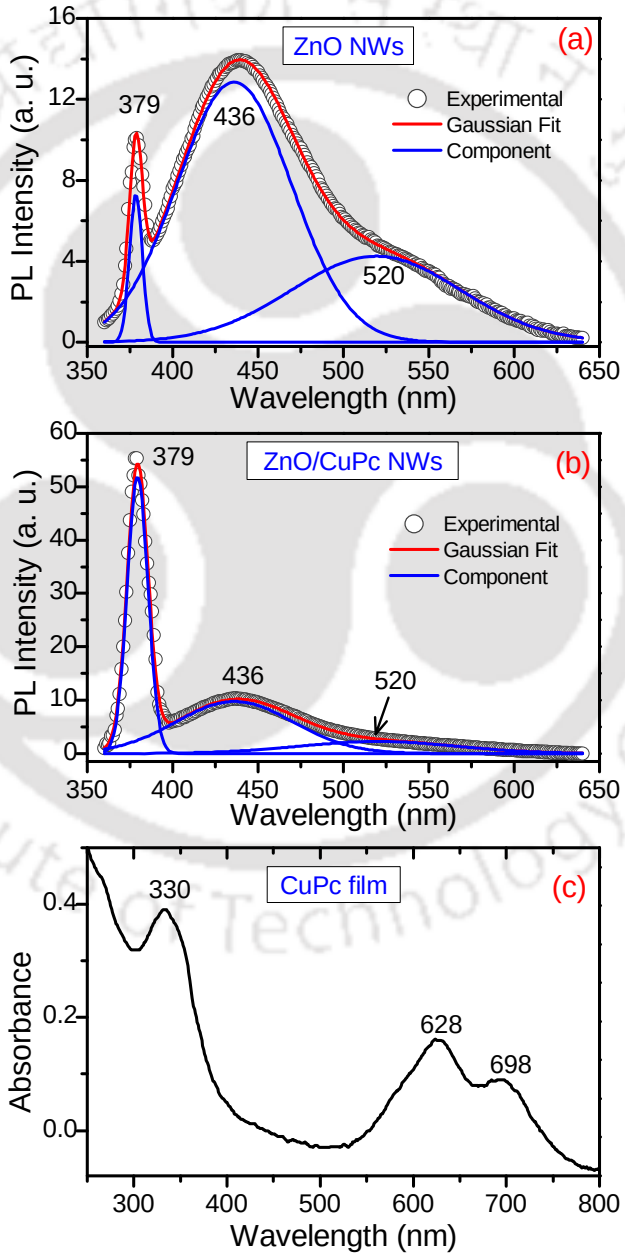

Figure 6.29: Room temperature PL spectra of the: (a) ZnO NWs and (b) ZnO/CuPc NWs. (c) Absorption spectra of the CuPc thin film grown on the quartz substrate.

enhancement in the UV emission is likely to be due to the high absorption by CuPc in this region and reduction in the green emission is believed to be due to the surface modification by CuPc.

In order to understand the observed improvement in the PL spectra, we studied the absorption behaviour of the CuPc thin film, which is shown in Fig. **6.29(c)**. The absorption spectrum shows a strong peak in the UV region with centre at 330 nm, which is known as B band. The B band originates from the π to π* orbital transition.[266] The doublet peaks in the visible region are known as Q band. The higher energy peak (628 nm) is connected with first π–π* transition on the phthalocyanine macrocycle, while the lower energy peak (698 nm) has been variously attributed to the vibrational interval[267] or excitonic transition.[268] The obtained enhancement in the PL spectra from the ZnO/CuPc heterostructure can be explained as follows. When the ZnO/CuPc system is excited with the 325 nm laser, both the ZnO and CuPc layers are excited and excitons are created. It is known that the HOMO level in the CuPc molecule is positioned at -5.1 eV. Therefore, the electrons associated with the B band transition have energy higher than the conduction band of ZnO (electron affinity ~4.65 eV). Then, these photoexcited electrons are injected to the conduction band of ZnO through the ZnO/CuPc interface. This process will lead to the accumulation of more charge carriers at the conduction band, which will boost the electron–hole recombination probability. As explained before, the CuPc molecules are likely to attach to the surface of the NWs at the oxygen vacancy sites, which significantly reduced the oxygen vacancy states of ZnO NWs. This process results in the decrement in the blue–green emissions in the ZnO/CuPc heterostructure.

6.3.2.4. Photocurrent and Photoresponse Studies

Figure **6.30(a)** shows the dark I–V characteristics of the ZnO NWs and ZnO/CuPc system. The I–V characteristics show nearly a linear behaviour with current in range of nA. After the CuPc capping, the dark current is increased to 8.3 nA from 2.8 nA at 3V bias. I–V curve of the heterostructure deviates from the linear behaviour, due to the formation of the ZnO/CuPc interface. The PC spectra [**Fig. 6.30(b–c)**] of the uncapped NWs show a strong peak in the UV region at 369 nm and two relatively weak broad peaks in the blue–green region. For the ZnO/CuPc system, the intensity of the PC peak in the UV region is significantly enhanced. The calculated PC and photoresponse parameters are tabulated in the Table **6.7**. The maximum PC is increased to 19.8 μA

from 3.8 μA of the uncapped case. Photosensitivity value is also increased to ~2385, leading to enhancement of nearly two. Therefore, the ZnO/CuPc system is very sensitive in the UV region which makes it an important and effective candidate for the efficient photodetector.

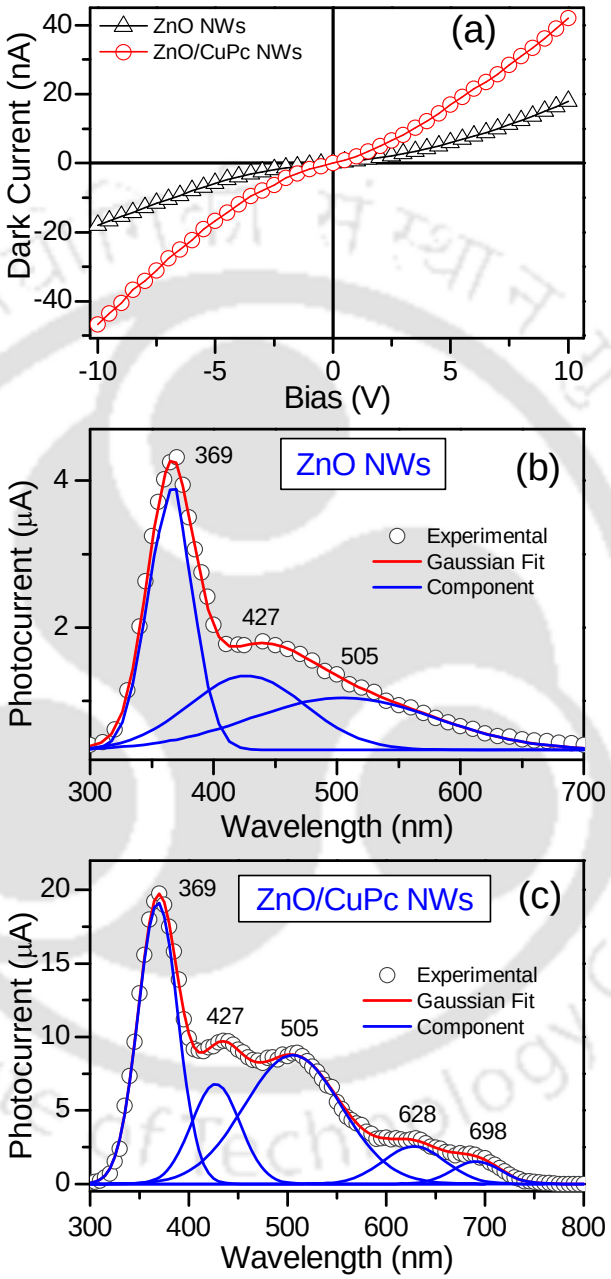

Figure 6.30: (a) Dark current–voltage characteristics of the ZnO nanowires and ZnO/CuPc nanowires heterostructure. (b and c) Wavelength dependent photocurrent of the ZnO nanowires and ZnO/CuPc nanowires heterostructure, respectively. The photocurrent measured at as bias of 3 V.

The photoresponse behaviour of the ZnO/CuPc heterostructure is shown in Fig. **6.31**. It shows that during PC growth, PC initially grows very fast, then slowly increases with

time and finally saturates. Similarly, during the decay process PC initially decreases very rapidly and then slowly reaches the dark current value. The individual growth and decay

Table 6.7: Photocurrent, photoresponse and photoluminescence parameters of the ZnO/CuPc nanowires heterostructure.

Sample Name	Dark Current (nA)	Photoc--urrent (μA)	Photosens--itivity	PC Growth time constants (s)		PC Decay time constants (s)	
				τ_1	τ_2	τ_3	τ_4
ZnO NWs	2.8	3.8	1357	7.4	52.0	7.4	180.4
ZnO/CuPc heterostructure	8.3	19.8	2385	5.4	44.1	5.4	92.2

time constants are calculated from the bi–exponential fitting to the experimental data points as explained before. The calculated time constants are 7.4 and 52.0s for PC growth, 7.4 and 180.4s for PC decay, respectively. For the ZnO/CuPc, the first component of growth and decay time constants are reduced to 5.4s from 7.4s for that of the bare NWs. Similarly the second component (growth and decay time constants) are decreased to 44.1s and 92.2s, respectively. Therefore, the overall growth and decay time constants are reduced implying that the photoresponse is considerably faster in the ZnO/CuPc heterostructure.

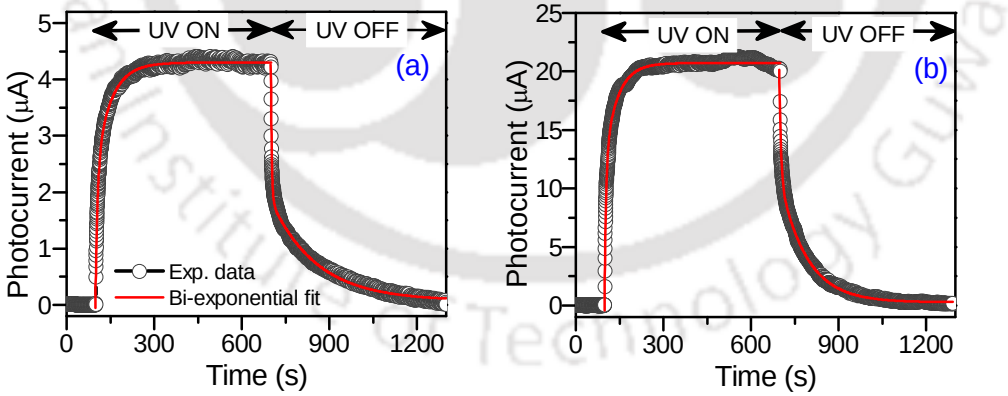

Figure 6.31: (a and b) The photoresponse behaviour of the ZnO nanowires and ZnO/CuPc nanowires heterostructure, respectively. The photocurrent measured at as bias of 3 V under the excitation of 365 nm.

Improved PC and photoresponse behaviours for the ZnO/CuPc system can be explained as follows. Under the UV irradiation, the ZnO and CuPc layer generate electron–hole pairs. Then the electrons in the excited states of CuPc transfer to the conduction band of ZnO, as discussed before to explain the enhancement of UV PL intensity. Under external

bias, these electrons along with the photogenerated electrons from ZnO contribute to the current conduction process, resulting in the enhanced PC. Due to the CuPc covering on the surface of the ZnO NWs, defect states are considerably passivated/ reduced. As a result, band bending in the NW is also considerably reduced, which results in a less effective charge separation. The ZnO/CuPc heterostructure shows comparatively higher dark current, which supports the small reduction of band bending in the NW. Now, electrons holes recombination time could considerably improve. This process results in a comparatively faster photoresponse, as compared to the case of as–grown ZnO NWs.

6.4. Summary

We fabricated several new types of ZnO NWs heterostructures for efficient UV photodetection and faster photoresponse. The PL and photoresponse behaviours of these heterostructures are studied systematically. These heterostructures show major improvement in the photosensitivity and ultra fast photoresponse as compared to the bare ZnO NWs. The possible mechanism for the improvement in photodetection behaviour from each of the heterostructure is explained systematically. Our studies establish that the ZnO NWs heterostructures are indeed excellent candidates for UV photodetectors with very high sensitivity and faster response for real time photosensing applications. The important findings of this chapter are summarized below.

1. Varieties of new types of ZnO NWs heterostructures (semiconductor/metal and semiconductor/semiconductor) were fabricated and characterized for the efficient photodetection.
2. The UV PL intensity and photocurrent are improved by several orders of magnitude by fabricating heterostructures with suitable materials.
3. In case of metal NPs decorated ZnO NWs heterostructure, nature of contacts formed between metal NPs and ZnO play a major role on the enhancement of photocurrent and faster photoresponse time.
4. A very high photosensitivity (4000) and faster photoresponse (1.5 s) could be obtained when the surface of the NWs is modified with UV sensitive organic semiconductor like anthracene and CuPc.
5. Ultra fast photoresponse (100 ms) and high photosensitivity (300) could be obtained from Al doped ZnO NWs decorated with Au NPs with optimum sizes.

6. The Au NPs decorated Al doped ZnO NWs and ZnO/anthracene NWs heterostructures are suitable for real time photosensing applications.

Chapter 7
Summary and Conclusions

This chapter presents the summary and important conclusions of the present thesis work to highlight the new findings on the controlled growth and optoelectronic properties of ZnO NWs and NRs arrays for their application as UV photodetectors. Scopes for further works related to the thesis work are presented at the end of the chapter.

7.1. Summary and Conclusions

In this dissertation, I have described about the controlled growth of well–aligned ZnO NWs and NRs array and fabrication of NW heterostructures for the application of efficient photodetectors. A systematic study is performed on the effects of several growth parameters to achieve control over the shape, size and orientation of the NWs/NRs. A new growth strategy has been adopted for the growth of vertically aligned ZnO NWs and NRs arrays. Use of ZnO NWs heterostructure approach for the efficient UV photodetector is explored in details. Using the heterostructure approach, we have achieved very high photosensitivity and ultrafast photoresponse from the ZnO NWs. The origin of this improvement from these heterostructures is studied systematically and explained through suitable models.

The major contributions of the present thesis work are summarized below.

A. Critical Growth Parameters for the Controlled Grwth

Effects of several critical growth parameters for the well–aligned growth of ZnO NWs and NRs have been studied systematically. We have shown that ZnO seed layer or Au catalyst layer individually failed to produce well–aligned ZnO NWs/NRs. In contrast, the combined effects of ZnO seed layer and Au catalyst layer strongly favor the growth of

well-aligned ZnO NWs and NRs arrays on Si substrate. From this study, we concluded that the ZnO seed layer and Au layer together act as a nucleation site and the Au catalyst layer transfer the orientation of the seed layer to the NWs/NRs, resulting in well–aligned vertical growth of ZnO NWs/NRs. The growth temperature and thickness of the seed layer primarily control the diameter of the NWs/NRs. Next, a simple technique for the synthesis of the high quality Al doped ZnO NWs with varying doping concentration by TVD method has been demonstrated.

Shape evolution of the ZnO nanostructure is observed with the change in growth conditions, where ZnO NWs undergo a shape evolution to nanoribbons and then to NRs. The shape evolution is observed only when the ZnO nano powder is used as the source material instead of the conventional bulk ZnO powder. From the detailed studies, it is concluded that Zn vapor pressure, supersaturation rate, growth temperature and ultrathin catalyst layer are the key factors controlling the shape evolution.

B. Improved Optoelectronic Properties by RTA Treatment

We have demonstrated that a post–growth fast processing technique, rapid thermal annealing (RTA) is an effective and a simple way to achieve higher photosensitivity and faster photoresponse along with an enhanced UV PL intensity in the ZnO NWs/NRs, as a result of structural improvement. The band–edge UV emission intensity is enhanced by 3–5 times, while the green emission is significantly reduced after RTA treatment. The UV photosensitivity value shows a five–fold enhancement. RTA is shown to improve the structural quality of the NWs and NRs by releasing the built–in stress and partially removing the structural and surface defects.

C. ZnO Nanowire Heterostructures for Efficient UV Photodetection

As the photosensitivity and photoresponse of the pristine ZnO NWs are quite low, it is not suitable for application in the efficient photodetection. Here we utilized the ZnO NWs heterostructures approach for the efficient UV photodetection. Two types of heterostructures were fabricated; one with decorating the surface of the NWs with ultra small metal (Au and Ti) nanoparticles (NPs) and other one is inorganic/organic type heterostructures with anthracene and copper phthalocyanine (CuPc). These heterostructures show significant improvement in the photodetection properties as well as the UV PL intensity. From the heterostructures, a large enhancement of 5–7 times in the photosensitivity and ultra fast response with photoresponse and reset times about 100

ms are obtained. ZnO/anthracene system shows high photosensitivity (4000) and faster response (1.5 s). On the other hand, Au NPs decorated Al:ZnO NWs shows ultra fast response (100 ms) however, the photosensitivity is low. To understand the origin of this improvement, we studied the absorption and PL emission, and the mechanism of enhancement is explained on the basis of high absorption by the external materials and interfacial charge transfer process. From the studies on metal nanoparticles decorated heterostructures, it is concluded that the nature of contacts formed between metal nanoparticles and ZnO strongly influence the enhancement of photocurrent and faster photoresponse as well as the enhancement of UV PL intensity. The results demonstrate that Au NPs decorated Al doped ZnO NWs and anthracene capped ZnO NWs heterostructures are highly suitable candidates for the real time photosensing applications.

Therefore, our studies establishes that the ZnO NWs heterostructures are indeed excellent candidates for efficient UV photodetectors with very high sensitivity and faster response for real time photosensing applications. The understanding about the obtained improvement from the heterostructures will help to design and fabricate commercial ZnO NWs heterostructure based efficient UV photodetectors. Compared to the conventional "*pick and place*" method for the photodetection property studies, our technique enable an easy and low cost process with improved photodetection behaviour. Our approaches show comparable/significant improvement over other approaches reported in the literature for the ZnO NWs based photodetectors.

7.2. Scopes for Further Works

In the present work, we demonstrated the growth of well–aligned high quality ZnO NWs and NRs arrays over large area by controlling several critical growth parameters and fabrication of ZnO NWs based heterostructures for efficient UV photodetection. We are able to achieve high quality well–aligned NWs and high improvement in the photodetection properties of the ZnO NWs based heterostructures. The present work can be extended in several ways as follows;

1. The present study has shown a route for the well–aligned growth of the ZnO NWs/NRs on the Si(100) substrate. For future work, this technique can be applied to grow the NWs on the plastic substrate for the fabrication of the flexible electronic devices using ZnO NWs/NRs. This will require a relatively low temperature growth.

2. Polarized PL studies on the ZnO NW heterostructures could be performed for better understanding and related application of the NWs based Laser and LEDs.

3. Fabricated ZnO NWs based heterostructures show good prospects for the applications in UV photodetectors with very high sensitivity and ultrafast response. However, low cost integration of these devices in to the chip is the present barrier. Therefore, in future this work can be focus on the low cost integration of NWs heterostructure and packaging, and finding of new architecture/heterostructure materials for further improvement in the photoresponse behaviour.

4. *In situ* fabrication of this type of ZnO NWs based heterostructures could be attempted. This fabrication process will enable a smooth formation of interface between the ZnO NWs and the external material, which will boost the easy transfer of charge carriers to the host materials.

5. The present understanding could be utilized for the fabrication of multifunction detectors for the next–generation sensing applications. There will be several channels for sensing and each channel will contain array of NWs with selective property. The response of the multifunctional detector may be multi–light, multi–gas sensing and specific functional groups sensing.

6. In addition, these heterostructures could be utilized for the efficient energy production by fabrication of dye sensitized solar cells.

7. Since the heterostructures show very intense PL, it is expected that heterostructures will show strong UV lasing action, which could be attempted.

8. *p*–type doping in the ZnO NWs/NRs could be tried for the fabrication of *p–n* junction based photodetectors.

9. Al doped ZnO NWs with Au NPs coating shows ultrafast photoresponse at a cost of loosing the photosensitivity to some extent. Simultaneous improvement of photosensitivity and photoresponse from such heterostructures need to be achieved by a suitable technique.

References

1. D. Brenner, S. Lyshevski, G. Iafrate, and W. A. Goddard, eds., *Handbook of nanoscience, engineering and technology,* CRC Press, Boca Raton, USA, (2002).
2. T. Takagahara and K. Takeda, "Theory of the quantum confinement effect on excitons in quantum dots of indirect–gap materials", *Phys. Rev. B* **46**, 15578–81 (1992).
3. H. Yu, J. Li, R. A. Loomis, L.-W. Wang, and W. E. Buhro, "Two–versus three–dimensional quantum confinement in indium phosphide wires and dots", *Nat. Mater.* **2**, 517–20 (2003).
4. E. Comini, C. Baratto, G. Faglia, M. Ferroni, A. Vomiero, and G. Sberveglieri, "Quasi–one dimensional metal oxide semiconductors: Preparation, characterization and application as chemical sensors", *Prog. Mater. Sci.* **54**, 1–67 (2009).
5. A. Wei, L. Pan, and W. Huang, "Recent progress in the ZnO nanostructure–based sensors", *Mater. Sci. Eng. B* **176**, 1409–21 (2011).
6. T. V. Duncan, "Applications of nanotechnology in food packaging and food safety: Barrier materials, antimicrobials and sensors", *J. Coll. Interface Sci.* **363**, 1–24 (2011).
7. T. Zhai, L. Li, X. Wang, X. Fang, Y. Bando, and D. Golberg, "Recent developments in one–dimensional inorganic nanostructures for photodetectors", *Adv. Funct. Mater.* **20**, 4233–48 (2010).
8. E. Monroy, F. Omnes, and F. Calle, "Wide–bandgap semiconductor ultraviolet photodetectors", *Semicond. Sci. Technol.* **18**, R33–R51 (2003).
9. X. S. Fang, Y. Bando, U. K. Gautam, T. Y. Zhai, H. B. Zeng, and X. J. Xu, "ZnO and ZnS nanostructures: ultraviolet–light emitters, lasers and sensors", *Crit. Rev. Solid State Mat. Sci.* **34**, 190–223 (2009).
10. Y. Li, F. Qian, J. Xiang, and C. M. Lieber, "Nanowire electronic and optoelectronic devices", *Mater. Today* **9**, 18–27 (2006).
11. Z. L. Wang, ed., *Nanowires and nanobelts: materials, properties and devices,* Kluwer Academic Pub., Boston, USA, (2003), Vol. 1&2.
12. K. D. Sattler, ed., *Handbook of nanophysics: Nanotubes and nanowires,* CRC Press, Boca Raton, USA, (2011), Vol. 4.

13. C. N. R. Rao, F. L. Deepak, G. Gundiah, and A. Govindaraj, "Inorganic nanowires", *Prog. Solid State Chem.* **31**, 5–147 (2003).

14. W. Lu and C. M. Lieber, "Semiconductor nanowires", *J. Phys. D: Appl. Phys.* **39**, R387–R406 (2006).

15. L. C. L. Y. Voon, Y. Zhang, B. Lassen, M. Willatzen, Q. Xiong, and P. C. Eklund, "Electronic Properties of Semiconductor Nanowires", *J. Nanosci. Nanotechnol.* **8**, 1–26 (2008).

16. S. C. Lyu, Y. Zhang, H. Ruh, H. J. Lee, H. W. Shim, E. K. Suh, and C. S. Lee, "Low temperature growth and photoluminescence of well–aligned zinc oxide nanowires", *Chem. Phys. Lett.* **363**, 134–38 (2002).

17. H. Zhou, J. Fallert, J. Sartor, R. J. Dietz, C. Klingshirn, H. Kalt, D. Weissenberger, D. Gerthsen, H. Zeng, and W. Cai, "Ordered n–type ZnO nanorod arrays", *Appl. Phys. Lett.* **92**, 132112 (2008).

18. J. H. He, P. H. Chang, and K. T. Tsai, "Electrical and optoelectronic characterization of a ZnO nanowires contacted by focused–ion–beam–deposited by Pt", *Nanotechnol.* **20**, 135701 (2009).

19. M. Sakurai, Y. G. Wang, T. Uemura, and M. Aono, "Electrical properties of individual ZnO nanowires", *Nanotechnol.* **20**, 155203 (2009).

20. H. Kind, H. Q. Yan, B. Messer, M. Law, and P. D. Yang, "Nanowire ultraviolet photodetectors and optical switche", *Adv. Mater.* **14**, 158–60 (2002).

21. C. Soci, A. Zhang, B. Xiang, S. A. Dayeh, D. P. R. Aplin, J. Park, X. Y. Bao, Y. H. Lo, and D. Wang, "ZnO nanowire UV photodetectors with high internal gain", *Nano Lett.* **7**, 1003–09 (2007).

22. Z. L. Wang and J. Song, "Piezoelectric nanogenerators based on Zinc Oxide nanowire arrays", *Science* **312**, 242–46 (2006).

23. J. Song, X. Wang, J. Liu, H. Liu, Y. Li, and Z. L. Wang, "Piezoelectric potential output from ZnO nanowire functionalized with p–type oligomer", *Nano Lett.* **8**, 203–07 (2008).

24. H. Y. Yang, S. P. Lau, S. F. Yu, and A. P. Abiyas, "High temperature random lasing in ZnO Nanoneedles", *Phys. Rev. Lett.* **89**, 011103 (2006).

25. M. H. Huang, S. Mao, H. Feick, H. Yan, Y. Wu, H. Kind, E. Weber, R. Russo, and P. Yang, "Room–temperature ultraviolet nanowire nanolasers", *Science* **292**, 1897–99 (2001).

26. N. H. Alvi, M. Riaz, G. Tzamalis, O. Nur, and M. Willander, "Fabrication and characterization of high–brightness light emitting diodes based on n–ZnO nanorods grown by a low–temperature chemical method on p-4H-SiC and p-GaN", *Semicond. Sci. Technol.* **25**, 065004 (2010).

27. J. Liu, Y. H. Ahn, J.-Y. Park, K. H. Koh, and S. Lee, "Hybrid light–emitting diodes based on flexible sheets of mass–produced ZnO nanowires", *Nanotechnol.* **20**, 445203 (2009).

28. M. Law, L. E. Green, J. C. Jhonson, R. Saykally, and P. Yang, "Nanowire dye–sensitized solar cells", *Nat. Mater* **4**, 455–95 (2005).

29. M. Law, L. E. Greene, A. Radenovic, T. Kuykendall, J. Liphardt, and P. Yang, "ZnO–Al_2O_3 and ZnO–TiO_2 core–shell nanowire dye–sensitized solar cells", *J. Phys. Chem. B* **110**, 22652–63 (2006).

30. A. Wei, X. W. Sun, J. X. Wang, Y. Lei, X. P. Cai, C. M. Li, Z. L. Dong, and W. Huang, "Enzymatic glucose biosensor based on ZnO nanorod array grown by hydrothermal decomposition", *Appl. Phys. Lett.* **89**, 123902 (2006).

31. N. Kumar, A. Dorfman, and J.-i. Hahm, "Ultrasensitive DNA sequence detection using nanoscale ZnO sensor arrays", *Nanotechnol.* **17**, 2875–81 (2006).

32. W. Martienssen, "Semiconductors," in *Handbook of condensed matter and materials data*, W. Martienssen and H. Warlimont, eds. Springer, Berlin, Germany, 575–691 (2005).

33. N. Fujimura, T. Nishihara, S. Goto, J. Xu, and T. Ito, "Control of preferred orientation for ZnO_x films: control of self–texture", *J. Cryst. Growth* **130**, 269–79 (1993).

34. Y. Wei, W. Wu, R. Guo, D. Yuan, S. Das, and Z. L. Wang, "Wafer–scale high–throughput ordered growth of vertically aligned ZnO nanowire arrays", *Nano Lett.* **10**, 3414–19 (2010).

35. S. E. Ahn, J. S. Lee, H. Kim, S. Kim, B. K. Kang, K. H. Kim, and G. T. Kim, "Photoresponse of sol–gel–synthesized ZnO nanorods", *Appl. Phys. Lett.* **84**, 5022–24 (2004).

36. H. Chang, Z. Sun, K. Y. Ho, X. Tao, F. Yan, W. M. Kwok, and Z. Zheng, "A highly sensitive ultraviolet sensor based on a facile in situ solution–grown ZnO nanorod/graphene heterostructure", *Nanoscale* **3**, 258–64 (2011).

37. C. Ye, X. Fang, Y. Hao, X. Teng, and L. Zhang, "Zinc Oxide nanostructures: morphology derivation and evolution", *J. Phys. Chem. B* **109**, 19758–65 (2005).

38. S. Mandal, A. Dhar, and S. K. Ray, "Growth and photoluminescence characteristics of ZnO tripods", *J. Appl. Phys.* **105**, 033513 (2009).

39. Z. L. Wang, "Zinc oxide nanostructures: growth, properties and applications", *J. Phys.: Condens. Matter* **16**, R829–R58 (2004).

40. C. Li, G. Fang, J. Li, L. Ai, B. Dong, and X. Zhao, "Effect of seed layer on structural properties of ZnO nanorod arays grown by vapor–phase transport", *J. Phys. Chem. C* **112**, 990–95 (2008).

41. S. A. Fortuna and X. Li, "Metal–catalyzed semiconductor nanowires: a review on the control of growth direction", *Semicond. Sci. Technol.* **25**, 024005 (2010).

42. M. H. Huang, Y. Wu, H. Feick, N. Tran, E. Weber, and P. Yang 13, "Catalytic growth of Zinc Oxidenanowires by vapor transport", *Adv. Mater.* **13**, 113–16 (2001).

43. B. D. Yao, Y. F. Chan, and N. Wang, "Formation of ZnO nanostructures by a simple way of thermal evaporation", *Appl. Phys. Lett.* **81**, 757–59 (2002).

44. H. Yuan and Y. Zhang, "Preparation of well–aligned ZnO whiskers on glass substrate by atmospheric MOCVD. ", *J. Cryst. Growth* **263**, 119–24 (2004).

45. W. I. Park, D. H. Kim, S. W. Jung, and G. C. Yi, "Metalorganic vapor–phase epitaxial growth of vertically well–aligned ZnO nanorods", *Appl. Phys. Lett.* **80**, 4232–34 (2002).

46. D. C. Kim, B. H. Kong, and H. K. Cho, "Synthesis and growth mechanism of catalyst free ZnO nanorods with enhanced aspect ratio by high flow additional carrier gas at low temperature", *J. Phys. D: Appl. Phys.* **42**, 065406 (2009).

47. Y. W. Heo, V. Varadarajan, M. Kaufman, K. Kim, D. P. Norton, F. Ren, and P. H. Fleming, "Site–specific growth of ZnO nanorods using catalysis–driven molecular–beam epitaxy", *Appl. Phys. Lett.* **81**, 3046–48 (2002).

48. M. Breedon, C. Rix, and K. Kalantar-zadeh, "Seeded growth of ZnO nanorods from NaOH solutions", *Mater. Lett.* **63**, 249–51 (2009).

49. M. A. Verges, A. Mifsud, and C. J. Serna, "Formation of rodlike zinc–oxide microcrystals in homogeneous solutions.", *J. Chem. Soc., Faraday Trans.* **86**, 959–63 (1990).

50. Y. Tak and K. Yong, "Controlled growth of well–aligned ZnO nanorod array using a novel solution method", *J. Phys. Chem. B* **109**, 19263–69 (2005).

51. C. Pacholski, A. Kornowski, and H. Weller, "Self–assembly of ZnO: from nanodots to nanorods", *Angew. Chem. Int. Ed.* **41**, 1188–91 (2002).

52. J. Song and S. Lim, "Effect of seed layer on the growth of ZnO nanorods", *J. Phys. Chem. C* **111**, 596–600 (2007).

53. J. J. Wu, H. I. Wen, C. H. Tseng, and S. C. Liu, "Well–aligned ZnO nanorods via hydrogen treatment of ZnO films", *Adv. Funct. Mater. Lett.* **14**, 806–10 (2004).

54. R. S. Wagner and W. C. Ellis, "Vapor–liquid–solid mechanism of single crystal growth", *Appl. Phys. Lett.* **4**, 89–90 (1964).

55. E. I. Givargizov, "Fundamental aspects of VLS growth", *J. Cryst. Growth* **31**, 20–30 (1975).

56. Y. Wu and P. Yang, "Germanium nanowire growth via simple vapor transport", *Chem. Mater.* **12**, 605–07 (2000).

57. Y. J. Zhang, Q. Zhang, N. L. Wang, Y. J. Yan, H. H. Zhou, and J. Zhu, "Synthesis of thin Si whiskers (nanowires) using $SiCl_4$", *J. Cryst. Growth & Design* **226**, 185–91 (2001).

58. Y. Wu and P. Yang, "Direct observation of vapor–liquid–solid nanowire growth", *J. Am. Chem. Soc.* **123**, 165–66 (2001).

59. M. S. Gudiksen and C. M. Lieber, "Diameter–selective synthesis of semiconductor nanowires", *J. Am. Chem. Soc.* **122**, 8801–02 (2000).

60. Y. Wu, H. Yan, M. Huang, B. Messer, J. H. Song, and P. Yang, " Inorganic semiconductor nanowires: rational growth, assembly, and novel properties", *Chem. Eur. J.* **8**, 1260–68 (2002).

61. X. Duan and C. M. Lieber, "General synthesis of compound semiconductor nanowires", *Adv. Mater.* **12**, 298–302 (2000).

62. Z. W. Pan, Z. R. Dai, and Z. L. Wang, "Nanobelts of semiconducting oxides", *Science* **291**, 1947–49 (2001).

63. P. X. Gao, Y. Ding, and Z. L. Wang, "Crystallographic–orientation aligned ZnO nanorods grown by tin catalyst", *Nano Lett.* **3**, 1315–20 (2003).

64. C. C. Chen, C. C. Yeh, C. H. Chen, M. Y. Y. MY, and H. L. Liu, "Catalytic growth and characterization of gallium nitride nanowires", *J. Am. Chem. Soc.* **123**, 2791–98 (2001).

65. Y. Wang, L. Zhang, C. Liang, G. Wang, and X. Peng, "Catalytic growth and photoluminescence properties of semiconductor single–crystal ZnS nanowires", *Chem. Phys. Lett. A* **357**, 314–18 (2002).

66. Y. Wu and P. Yang, "Watching GaN Nanowires Grow", *Nano Lett.* **3**, 867–69 (2003).

67. M. S. Gudiksen, J. Wang, and C. M. Liebe, "Synthetic control of the diameter and length of single crystal semiconductor nanowires", *J. Phys. Chem. B* **105**, 4062–64 (2001).

68. Y. C. Kong, D. P. Yu, B. Zhang, W. Fang, and S. Q. Feng, "Ultraviolet–emitting ZnO nanowires synthesized by a physical vapor deposition approach", *Appl. Phys. Lett.* **78**, 407–09 (2001).

69. D. Banerjee, J. Y. Lao, D. Z. Wang, J. Y. Huang, Z. F. Ren, D. Steeves, B. Kimball, and M. Sennett, "Large–quantity free–standing ZnO nanowires", *Appl. Phys. Lett.* **83**, 2061–63 (2003).

70. J. H. He, J. H. Hsu, C. W. Wang, H. N. Lin, L. J. Chen, and Z. L. Wang, "Pattern and feature designed growth of ZnO nanowire arrays for vertical devices", *J. Phys. Chem. B* **110**, 50–53 (2006).

71. J. Y. Li, X. L. Chen, H. Li, M. He, and Z. Y. Qiao, "Fabrication of Zinc Oxide Nanorods", *J. Cryst. Growth* **233**, 5–7 (2001).

72. H. J. Yuan, S. S. Xie, D. F. Liu, X. Q. Yan, Z. P. Zhou, L. J. Ci, J. X. Wang, Y. Gao, L. Song, L. F. Liu, W. Y. Zhou, and G. Wang, "Characterization of zinc oxide crystal nanowires grown by thermal evaporation of ZnS powders", *Chem. Phys. Lett.* **371**, 337–41 (2003).

73. L. Khomenkova, P. Ferna´ndez, and J. Piqueras, "ZnO nanostructured microspheres and elongated structures grown by thermal treatment of ZnS powder", *Cryst. Growth & Design* **7**, 836–39 (2007).

74. C. Li, G. Fang, F. Su, G. Li, X. Wu, and X. Zhao, "Synthesis and photoluminescence properties of vertically aligned ZnO nanorod–nanowall junction arrays on a ZnO–coated silicon substrate", *Nanotechnol.* **17**, 3740 (2006).

75. S. Li, X. Zhang, B. Yan, and T. Yu, "Growth mechanism and diameter control of well–aligned small–diameter ZnO nanowire arrays synthesized by a catalyst–free thermal evaporation method", *Nanotechnol.* **20**, 495604 (2009).

76. L. E. Greene, M. Law, D. H. Tan, M. Montano, J. Goldberger, G. Somorjai, and P. Yang, "General route to vertical ZnO nanowire arrays using textured ZnO seeds", *Nano Lett.* **5**, 1231–36 (2005).

77. L. Feng, A. Liu, M. Liu, Y. Ma, J. Wei, and B. Man, "Synthesis, characterization and optical properties of flower–like ZnO nanorods by non–catalytic thermal evaporation", *J. Alloys Comp.* **492**, 427–32 (2010).

78. Y. Kajikawa, "Texture development of non–epitaxial polycrystalline ZnO films", *J. Cryst. Growth* **289**, 387 (2006).

79. J.-I. Hong, J. Bae, Z. L. Wang, and R. L. Snyder, "Room–temperature, texture–controlled growth of ZnO thin films and their application for growing aligned ZnO nanowire arrays", *Nanotechnol.* **20**, 085609 (2009).

80. T. Yanagitani and M. Kiuchi, "Control of in–plane and out–of–plane texture in shear mode piezoelectric ZnO films by ion–beam irradiation", *J. Appl. Phys.* **102**, 044115 (2007).

81. S. R. Hejazi and H. R. M. Hosseini, "A diffusion–controlled kinetic model for growth of Au–catalyzed ZnO nanorods: Theory and experiment", *J. Cryst. Growth* **309**, 70–75 (2007).

82. M. Kirkham, X. Wang, Z. L. Wang, and R. L. Snyder, "Solid Au nanoparticles as a catalyst for growing aligned ZnO nanowires: A new understanding of the vapour–liquid–solid process", *Nanotechnol.* **18**, 365304 (2007).

83. S. Y. Li, C. Y. Lee, and T. Y. Tseng, "Copper–catalyzed ZnO nanowires on silicon (100) grown by vapor–liquid–solid process", *J. Cryst. Growth* **247**, 357–62 (2003).

84. S. C. Lyu, Y. Zhang, and C. J. Lee, "Low–temperature growth of ZnO Nanowire array by a simple physical vapor–deposition method", *Chem. Mater.* **15**, 3294–99 (2003).

85. W.-Y. Wu, M.-T. Chen, and J.-M. Ting, "Growth and characterizations of ZnO nanorod/film structures on copper coated Si substrates", *Thin Solid Films* **518**, 1549–52 (2009).

86. C. J. Lee, T. J. Lee, S. C. Lyu, Y. Zhang, H. Ruh, and H. J. Lee, "Field emission from well–aligned zinc oxide nanowire grown at low temperature", *Appl. Phys. Lett.* **81**, 3648–50 (2002).

87. S. J. Pearton, D. P. Norton, K. Ip, Y. W. Heo, and T. Steiner, "Recent progress in processing and properties of ZnO", *Prog. Mater. Sci.* **50**, 293–340 (2005).

88. S. Xu, N. Adiga, S. Ba, T. Dasgupta, C. F. J. Wu, and Z. L. Wang, "Optimizing and improving the growth quality of ZnO nanowire arrays guided by statistical design of experiments", *ACS Nano* **3**, 1803–12 (2009).

89. Z. Guo, C. Andreazza-Vignolle, P. Andreazza, T. Sauvage, D. X. Zhao, Y. C. Liu, B.Yao, D. Z. Shen, and X. W. Fan, "Tuning the growth of ZnO nanowires", *Physica B* **406**, 2200–05 (2011).

90. D. S. Boyle, K. Govender, and P. O'Brien, "Novel low temperature solution deposition of perpendicularly orientated rods of ZnO: Substrate effects and evidence of the importance of counter–ions in the control of crystallite growth", *Chem. Commun.* 80–81 (2002).

91. L. Vayssieres, "Growth of arrayed nanorods and nanowires of ZnO from aqueous solutions", *Adv. Mater.* **15**, 464–66 (2003).

92. L. E. Greene, B. D. Yuhas, M. Law, D. Zitoun, and P. Yang, "Solution–Grown Zinc Oxide Nanowires", *Inorg. Chem.* **45**, 7535–43 (2006).

93. J. Qiu, X. Li, F. Zhuge, X. Gan, X. Gao, W. He, S.-J. Park, H.-K. Kim, and Y.-H. Hwang, "Solution–derived 40 μm vertically aligned ZnO nanowire arrays as photoelectrodes in dye–sensitized solar cells ", *Nanotechnol.* **21**, 195602 (2010).

94. H. E. Unalan, P. Hiralal, N. Rupesinghe, S. Dalal, W. I. Milne, and G. A. J. Amaratunga, "Rapid synthesis of aligned zinc oxide nanowires", *Nanotechnol.* **19**, 255608 (2008).

95. M. C. P. Wang and B. D. Gates, "Directed assembly of nanowires", *Mater. Today* **12**, 34–43 (2009).

96. K. Heo, E. Cho, J. E. Yang, M. H. Kim, M. Lee, B. Y. Lee, S. G. Kwon, M. S. Lee, M. H. Jo, H. J. Choi, T. Hyeon, and S. Hong, "Large–scale assembly of silicon nanowire network–based devices using conventional microfabrication facilities", *Nano Lett.* **8**, 4523–27 (2008).

97. J. Chai and J. M. Buriak, "Using cylindrical domains of block copolymers to selfassemble and align metallic nanowires", *ACS Nano* **2**, 489–501 (2008).

98. C. M. Hangarter and N. V. Myung, "Magnetic alignment of nanowires", *Chem. Mater.* **17**, 1320–24 (2005).

99. S. Xu, Y. Wei, M. Kirkham, J. Liu, W. Mai, D. Davidovic, R. L. Snyder, and Z. L. Wang, "Patterned growth of vertically aligned ZnO nanowire arrays on inorganic Substrates at low temperature without catalyst", *J. Am. Chem. Soc.* **130**, 14958–59 (2008).

100. T. Martensson, P. Carlberg, M. Borgstrom, L. Montelius, W. Seifert, and S. L., "Nanowire arrays defined by nanoimprint lithography", *Nano Lett.* **4**, 699–702 (2004).

101. M. T. Bjo¨rk, B. J. Ohlsson, T. Sass, A. I. Persson, C. Thelander, M. H. Magnusson, K. Deppert, L. R. Wallenberg, and L. Samuelson, "One–dimensional heterostructures in semiconductor nanowhiskers", *Appl. Phys. Lett.* **80**, 1058–60 (2002).

102. M. S. Gudiksen, U. J. Lauhon, J. Wang, D. C. Smith, and C. M. Lieber, " Growth of nanowire superlattice structures for nanoscale photonics and electronics", *Nature* **415**, 617–20 (2002).

103. Y. Wu, R.Fan, and P. Yang, "Block–by block growth of single–crystalline Si/Si-Ge superlattice nanowires", *Nano Lett.* **2**, 83–86 (2002).

104. B. Pradhan, S. K. Batabyal, and A. J. Pal, "Rectifying junction in a single ZnO vertical nanowire", *Appl. Phys. Lett.* **89**, 233109 (2006).

105. A. Bera and D. Basak, "Effect of surface capping with poly(vinyl alcohol) on the photocarrier relaxation of ZnO nanowires", *ACS Appl. Mater. Interface* **1**, 2066–70 (2009).

106. J. Liu, J. Park, K. H. Park, Y. Ahn, J. Y. Park, K. H. Koh, and S. Lee, "Enhanced photoconduction of free–standing ZnO nanowire films by L–lysine treatment", *Nanotechnol.* **21**, 485504 (2010).

107. A. Bera and D. Basak, "Photoluminescence and photoconductivity of ZnS–coated ZnO nanowires", *ACS. Appl. Mater. Interface* **2**, 408–12 (2010).

108. K. W. Liu, R. Chen, G. Z. Xing, T. Wu, and H. D. Sun, "Photoluminescence characteristics of high quality ZnO nanowires and its enhancement by polymer covering", *Appl. Phys. Lett.* **96**, 023111 (2010).

109. C. Cheng, T.-L. Wang, L. Feng, W. Li, K. M. Ho, M. M. T. Loy, K. K. Fung, and N. Wang, "Vertically aligned ZnO/amorphous-Si core–shell heterostructured nanowire arrays", *Nanotechnol.* **21**, 475703 (2010).

110. H.-D. Um, S. A. Moiz, K.-T. Park, J.-Y. Jung, S.-W. Jee, C. H. Ahn, D. C. Kim, H. K. Cho, D.-W. Kim, and J.-H. Lee, "Highly selective spectral response with enhanced responsivity of n-ZnO/p-Si radial heterojunction nanowire photodiodes ", *Appl. Phys. Lett.* **98**, (2011).

111. H. Y. Lin, C. L. Cheng, Y. Y. Chou, L. L. Huang, Y. F. Chen, and K. T. Tsen, "Enhancement of band gap emission stimulated by defect loss", *Opt. Express* **16**, 2372–79 (2006).

112. C. W. Cheng, E. J. Sie, B. Liu, C. H. A. Huan, T. C. Sum, H. D. Sun, and H. J. Fan, "Surface plasmon enhanced band edge luminescence of ZnO nanorods by capping Au nanoparticles", *Appl. Phys. Lett.* **96**, 071107 (2010).

113. C.-A. Lin, D.-S. Tsai, C.-Y. Chen, and J.-H. He, "Significant enhancement of yellow–green light emission of ZnO nanorod arrays using Ag island films", *Nanoscale* **3**, 1195–99 (2011).

114. S. Dhara and P. K. Giri, "On the origin of enhanced photoconduction and photoluminescence from Au and Ti nanoparticles decorated ZnO nanowire heterostructures", *J. Appl. Phys.* **110**, 124317 (2011).

115. Y. J. Fang, J. Sha, Z. L. Wang, Y. T. Wan, W. W. Xia, and Y. W. Wang, "Behind the change of the photoluminescence property of metal–coated ZnO nanowire arrays", *Appl. Phys. Lett.* **98**, 033103 (2011).

116. J. S. Reparaz, F. Güell, M. R. Wagner, A. Hoffmann, A. Cornet, and J. R. Morante, "Size–dependent recombination dynamics in ZnO nanowires", *Appl. Phys. Lett.* **96**, 053105 (2010).

117. B. Lin, Z. Fu, and Y. Jia, "Green luminescent center in undoped zinc oxide films deposited on silicon substrates", *Appl. Phys. Lett.* **79**, 943–45 (2001).

118. A. B. Djuriˇsi´c, Y. H. Leung, K. H. Tam, Y. F. Hsu, L. Ding, W. K. Ge, Y. C. Zhong, K. S. Wong, W. K. Chan, H. L. Tam, K. W. Cheah, W. M. Kwok, and D. L. Phillips, "Defect emissions in ZnO nanostructures", *Nanotechnol.* **18**, 095702 (2007).

119. J. Liu, S. Lee, Y. H. Ahn, J.-Y. Park, and K. H. Koh, "Tailoring the visible photoluminescence of mass–produced ZnO nanowires", *J. Phys. D: Appl. Phys.* **42**, 095401 (2009).

120. A. F. Kohan, G. Ceder, D. Morgan, and C. G. V. d. Walle, "First–principles study of native point defects in ZnO", *Phys. Rev. B* **61**, 15019 (2000).

121. A. Janotti and C. G. V. d. Walle, "Native point defects in ZnO", *Phys. Rev. B* **76**, 165202 (2007).

122. K. Vanheusden, W. L. Warren, C. H. Seager, D. R. Tallant, J. A. Voigt, and B. E. Gnade, "Mechanisms behind green photoluminescence in ZnO phosphor powders", *J. Appl. Phys.* **79**, 7983–90 (1996).

123. A. Janotti and C. G. Van de Walle, "New insights into the role of native point defects in ZnO", *J. Cryst. Growth* **287**, 58–65 (2006).

124. Z.-M. Liao, H.-Z. Zhang, Y.-B. Zhou, J. Xua, J.-M. Zhang, and D.-P. Yua, "Surface effects on photoluminescence of single ZnO nanowires", *Phys. Lett. A* **372**, 4505–09 (2008).

125. L. E. Greene, M. Law, J. Goldberger, F. Kim, J. C. Johnson, Y. Zhang, R. J. Saykally, and P. Yang, "Low–temperature wafer–scale production of ZnO nanowire arrays", *Angew. Chem., Int. Ed.* **42**, 3031–34 (2003).

126. G.-Y. Huang, C.-Y. Wang, and J.-T. Wang, "First–principles study of diffusion of oxygen vacancies and interstitials in ZnO", *J. Phys.: Condens. Matter* **21**, 195403 (2009).

127. Y. Ding and Z. L. Wang, "Structures of planar defects in ZnO nanobelts and nanowires", *Micron* **40**, 335–42 (2009).

128. S. Bethke, H. Pan, and B. Wessels, "Luminescence of heteroepitaxial zinc oxide", *Appl. Phys. Lett.* **52**, 138–40 (1988).

129. C.-H. Hsu and D.-H. Chen, "Synthesis and conductivity enhancement of Al–doped ZnO nanorod array thin films ", *Nanotechnol.* **21**, 285603 (2010).

130. C. Xu, M. Kim, J. Chun, and D. Kim, "Growth of Ga–doped ZnO nanowires by two–step vapor phase method ", *Appl. Phys. Lett.* **86**, 133107 (2005).

131. H. J. Fan, B. Fuhrmann, R. Scholz, C. Himcinschi, A. Berger, H. Leipner, A. Dadgar, A. Krost, S. Christiansen, U. Gösele, and M. Zacharias, "Vapour–transport–deposition growth of ZnO nanostructures: switch between c–axial wires and a–axial belts by indium doping", *Nanotechnol.* **17**, S231 (2006).

132. P. Nguyen, H. T. Ng, J. Kong, A. M. Cassell, R. Quinn, and J. Li, "Epitaxial directional growth of indium–doped tin oxide nanowire arrays", *Nano Lett.* **3**, 925–28 (2003).

133. J. Jie, G. Wang, X. Han, Q. Yu, Y. Liao, G. Li, and J. G. Hou, "Indium–doped zinc oxide nanobelts", *Chem. Phys. Lett* **387**, 466–70 (2004).

134. J. Y. Lao, J. G. Wen, and Z. F. Ren, "Hierarchical ZnO nanostructures", *Nano Lett.* **2**, 1287–91 (2002).

135. P.-Y. Yang, J.-L. Wang, P.-C. Chiu, J.-C. Chou, C.-W. Chen, H.-H. Li, and H.-C. Cheng, "PH sensing characteristics of extended–gate field–effect transistor based on Al–doped ZnO nanostructures hydrothermally synthesized at low temperatures", *IEEE Electron Device Lett.* **32**, 1603–05 (2011).

136. J. Goldberge, D. J. Sirbuly, M. Law, and P. Yang, "ZnO Nanowire Transistors", *J. Phys. Chem. B* **109**, 9–14 (2005).

137. Y. W. Heo, D. P. Norton, L. C. Tien, Y. Kwon, B. S. Kang, F. Ren, S. J. Pearton, and J. R. LaRoche, "ZnO nanowire growth and devices", *Mater. Sci. Eng. R* **47**, 1–47 (2004).

138. H. T. Ng, J. Han, T. Yamada, P. Nguyen, Y. P. Chen, and M. Meyyappan, "Single crystal nanowire vertical surround–gate field–effect transistor", *Nano Lett.* **4**, 1247–52 (2004).

139. M. S. Hammer, C. Deibel, J. Pflaum, and V. Dyakonov, "Effect of doping of zinc oxide on the hole mobility of poly(3–hexylthiophene) in hybrid transistors", *Org. Electron.* **11**, 1569–77 (2010).

140. H.-W. Ra, D. H. Choi, S. H. Kim, and Y.-H. Im, "Formation and characterization of ZnO/a-C core–shell nanowires", *J. Phys. Chem. C* **113**, 3512–16 (2009).

141. X. Fang, J. Li, D. Zhao, D. Shen, B. Li, and X. Wang, "Phosphorus–doped p–type ZnO nanorods and ZnO nanorod p−n homojunction LED fabricated by hydrothermal method", *J. Phys. Chem. C* **113**, 21208–12 (2009).

142. J.-Y. Zhang, P.-J. Li, H. Sun, X. Shen, T.-S. Deng, K.-T. Zhu, Q.-F. Zhang, and J.-L. Wua, "Ultraviolet electroluminescence from controlled arsenic–doped ZnO nanowire homojunctions", *Appl. Phys. Lett.* **93**, 021116 (2008).

143. X. Zhang, M. Lu, Y. Zhang, L. Chen, and Z. L. Wang, "Fabrication of a high–brightness blue–light–emitting diode using a ZnO–nanowire array grown on p–GaN thin film", *Adv. Mater.* **21**, 2767–70 (2009).

144. J. Bao, M. A. Zimmler, F. Capasso, X. Wang, and Z. F. Ren, "Broadband ZnO single–nanowire light–emitting diode", *Nano Lett.* **6**, 1719–22 (2006).

145. A. El-Shaer, A. Dev, J.-P. Richters, S. R. Waldvogel, J. Waltermann, W. Schade, and T. Voss, "Hybrid LEDs based on ZnO–nanowire arrays", *Phys. Stat. Sol. (b)* **247**, 1564–67 (2010).

146. R. Konenkamp, R. C. Word, and M.Godinez, "Ultraviolet electroluminescence from ZnO/polymer heterojunction light–emitting diodes", *Nano Lett.* **5**, 2005–08 (2005).

147. H. Yan, R. He, J. Johnson, M. Law, R. J. Saykally, and P. Yang, "Dendrite Nanowire Ultraviolet Laser Array", *J. Am. Chem. Soc.* **125**, 4728–29 (2003).

148. J. C. Johnson, H. Yan, R. D. Schaller, L. H. Haber, R. J. Saykally, and P. Yang, "Single Nanowire Laser", *J. Phys. Chem. B* **105**, 11387–90 (2001).

149. R. Q. Guo, J. Nishimura, M. Matsumoto, M. Higashihata, D. Nakamura, J. Suehiro, and T. Okada, "Aligned growth of ZnO nanowires and lasing in single ZnO nanowire optical cavities", *Appl. Phys. B* **90**, 539–42 (2008).

150. K. S. Leschkies, R. Divakar, J. Basu, E. E. Pommer, J. E. Boercker, C. B. Carter, U. R. Kortshagen, D. J. Norris, and E. S. Aydil, "Photosensitization of ZnO nanowires with CdSe quantum dots for photovoltaic devices", *Nano Lett.* **7**, 1793–98 (2007).

151. N. O. V. Plank, H. J. Snaith, C. Ducati, J. S. Bendall, L. S. Mende, and M. E. Welland, "A simple low temperature synthesis route for ZnO–MgO core–shell nanowires", *Nanotechnol.* **19**, 465603 (2008).

152. Q. H. Li, T. Gao, Y. G. Wang, and T. H. Wang, "Adsorption and desorption of oxygen probed from ZnO nanowire films by photocurrent measurements", *Appl. Phys. Lett.* **86**, 123117 (2005).

153. Y. Li, F. D. Valle, M. Simonnet, I. Yamada, and J. J. Delaunaya, "Competitive surface effects of oxygen and water on UV photoresponse of ZnO nanowires", *Appl. Phys. Lett.* **94**, 023110 (2009).

154. A. Bera and D. Basak, "Carrier relaxation through two–electron process during photoconduction in highly UV sensitive quasi–one–dimensional ZnO nanowires", *Appl. Phys. Lett.* **93**, 053102 (2008).

155. A. Bera and D. Basak, "Role of defects in the anomalous photoconductivity in ZnO nanowires", *Appl. Phys. Lett.* **94**, 163119 (2009).

156. Q. H. Li, Q. Wan, Y. X. Liang, and T. H. Wang, "Electronic transport through individual ZnO nanowires", *Appl. Phys. Lett.* **84**, 4556–58 (2004).

157. J. Y. Park, Y. S. Yun, Y. S. Hong, H. Oh, J.-J. Kim, and S. S. Kima, "Synthesis, electrical and photoresponse properties of vertically well–aligned and epitaxial ZnO nanorods on GaN–buffered sapphire substrates", *Appl. Phys. Lett.* **87**, 123108 (2005).

158. C. L. Hsu, S. J. Chang, Y. R. Lin, P. C. Li, T. S. Lin, S. Y. Tsai, T. H. Lu, and I. C. Chen, "Ultraviolet photodetectors with low temperature synthesized vertical ZnO nanowires.", *Chem. Phys. Lett.* **416**, 75–78 (2005).

159. J. B. K. Law and J. T. L. Thong, "Simple fabrication of a ZnO nanowire photodetector with a fast photoresponse time", *Appl. Phys. Lett.* **88**, 133114 (2006).

160. Z. Y. Fan, D. Dutta, C. J. Chien, H. Y. Chen, E. C. Brown, P. C. Chang, and J. G. Lu, "Electrical and photoconductive properties of vertical ZnO nanowires in high density arrays", *Appl. Phys. Lett.* **89**, 213110 (2006).

161. J. D. Prades, R. Jimenez-Diaz, F. Hernandez-Ramirez, L. Fernandez-Romero, T. Andreu, A. Cirera, A. Romano-Rodriguez, A. Cornet, J. R. Morante, S. Barth, and S. Mathur, "Towards a systematic understanding of photodetectors based on individual metal oxide nanowires", *J. Phys. Chem. C* **112**, 14639–44 (2008).

162. J. P. Cheng, Y. J. Zhang, and R. Y. Guo, "ZnO microtube ultraviolet detectors", *J. Cryst. Growth* **310**, 57–61 (2008).

163. D. Park and K. Yong, "Photoconductivity of vertically aligned ZnO nanoneedle array", *J. Vac. Sci. Technol. B* **26**, 1933–36 (2008).

164. L. Peng, J. L. Zhai, D. J. Wang, P. Wang, Y. Zhang, S. Pang, and T. F. Xie, "Anomalous photoconductivity of cobalt–doped zinc oxide nanobelts in air", *Chem. Phys. Lett.* **456**, 231–35 (2008).

165. Y. B. Li, F. D. Valle, M. Simonnet, I. Yamada, and J. J. Delaunay, "High–performance UV detector made of ultra–long ZnO bridging nanowires", *Nanotechnol.* **20**, 045501 (2009).

166. C. C. Lin, W. H. Lin, and Y. Y. Li, "Synthesis of ZnO nanowires and their applications as an ultraviolet photodetector", *J. Nanosci. Nanotechnol.* **9**, 2813–19 (2009).

167. N. Chantarat, Y. W. Chen, S. Y. Chen, and C. C. Lin, "Enhanced UV photoresponse in nitrogen plasma ZnO nanotubes", *Nanotechnol.* **20**, 395201 (2009).

168. A. Manekkathodi, M. Y. Lu, C. W. Wang, and L. J. Chen, "Direct growth of aligned zinc oxide nanorods on paper substrates for low–cost flexible electronics", *Adv. Mater.* **22**, 4059–63 (2010).

169. C. C. Huang, B. D. Pelatt, and J. F. Conley, "Directed integration of ZnO nanobridge sensors using photolithographically patterned carbonized photoresist", *Nanotechnol.* **21**, 195307 (2010).

170. Y. W. Ra, K. S. Choi, J. H. Kim, Y. B. Hahn, and Y. H. Im, "Fabrication of ZnO nanowires using nanoscale spacer lithography for gas sensors", *Small* **4**, 1105–09 (2008).

171. L. Li, H. Q. Yang, H. Zhao, J. Yu, J. H. Ma, L. J. An, and X. W. Wang, "Hydrothermal synthesis and gas sensing properties of single–crystalline ultralong ZnO nanowires", *Appl. Phys. A* **98**, 635–41 (2010).

172. N. Zhang, K. Yu, Q. Li, Z. Q. Zhu, and Q. Wan, "Room–temperature high–sensitivity H_2S gas sensor based on dendritic ZnO nanostructures with macroscale in appearance", *J. Appl. Phys.* **103**, 104305 (2008).

173. P. R. Solanki, A. Kaushik, A. A. Ansari, G. Sumana, and B. D. Malhotra, "Zinc oxide–chitosan nanobiocomposite for urea sensor", *Appl. Phys. Lett.* **93**, 163903 (2008).

174. X. D. Bai, P. X. Gao, Z. L. Wang, and E. G. Wang, "Dual–mode mechanical resonance of individual ZnO nanobelts", *Appl. Phys. Lett.* **82**, 4806–08 (2003).

175. G. Zheng, F. Patolsky, Y. Cui, W. U. Wang, and C. M. Lieber, "Multiplexed electrical detection of cancer markers with nanowire sensor arrays", *Nat. Biotechnol.* **23**, 1294–301 (2005).

176. B. P. Timko, T. Cohen–Karni, Q. Qing, B. Tian, and C. M. Lieber, "Design and implementation of functional nanoelectronic interfaces with biomolecules, cells and tissue using nanowire device arrays", *IEEE Trans. Nanotechnol.* **9**, 269–80 (2010).

177. S. Xu, Y. Qin, C. Xu, Y. Wei, R. Yang, and Z. L. Wang, "Self–powered nanowire devices ", *Nat. Nanotechnol.* **5**, 366–73 (2010).

178. L. Luo, Y. F. Zhang, S. S. Mao, and L. W. Lin, "Fabrication and characterization of ZnO nanowires based UV photodiodes", *Sens. Actuators A, Phys.* **127**, 201–06 (2006).

179. L. Vj, J. Oh, A. P. Nayak, A. M. Katzenmeyer, K. H. Gilchrist, S. Grego, N. P. Kobayashi, S.-Y. Wang, A. A. Talin, N. K. Dhar, and M. S. Islam, "A perspective on nanowire photodetectors: currentStatus, future challenges, and opportunities", *IEEE J. Selected Top. Quantum Electron.* **17**, 1002–32 (2011).

180. W. Park, G. Jo, W. K. Hong, J. Yoon, M. Choe, S. Lee, Y. Ji, G. Kim, Y. H. Kahng, K. Lee, D. Wang, and T. Lee, "Enhancement in the photodetection of ZnO nanowires by introducing surface–roughness–induced traps", *Nanotechnol.* **22**, 205204 (2011).

181. A. Bera and D. Basak, "Pd–nanoparticle–decorated ZnO nanowires: ultraviolet photosensitivity and photoluminescence properties", *Nanotechnol.* **22**, 265501 (2011).

182. J. Zhou, Y. D. Gu, Y. F. Hu, W. J. Mai, P. H. Yeh, G. Bao, A. K. Sood, D. L. Polla, and Z. L. Wang, "Gigantic enhancement in response and reset time of ZnO UV nanosensor by utilizing Schottky contact and surface functionalization", *Appl. Phys. Lett.* **94**, 191103 (2009).

183. D. C. Kim, B. O. Jung, J. H. Lee, H. K. Cho, J. Y. Lee, and J. H. Lee, "Dramatically enhanced ultraviolet photosensing mechanism in a n-ZnO nanowires/i-MgO/n-Si structure with highly dense nanowires and ultrathin MgO layers", *Nanotechnol.* **22**, 265506 (2011).

184. K.-P. Kim, D. Chang, S. K. Lim, S.-K. Lee, H.-K. Lyu, and D.-K. Hwang, "Effect of TiO_2 Nanoparticle Modification on Ultraviolet Photodetection Properties of Al-Doped ZnO Nanowire Network", *J. J. Appl. Phys.* **50**, 06GF07 (2011).

185. J. S. Lee, M. S. Islam, and S. Kim, "Photoresponses of ZnO nanobridge devices fabricated using a single–step thermal evaporation method", *Sens. Actuators B, Chem.* **126**, 73–77 (2007).

186. X. G. Zheng, Q. S. Li, W. Hu, D. Chen, N. Zhang, M. J. Shi, J. J. Wang, and L. C. Zhang, "Photoconductive properties of ZnO thin films grown by pulsed laser deposition.", *J. Lumines.* **122–123**, 198–201 (2007).

187. Q. Yang, Xin Guo, W. Wang, Y. Zhang, S. Xu, D. H. Lien, and Z. L. Wang, "Enhancing sensitivity of a single ZnO micro-/nanowire photodetector by piezo–phototronic effect", *ACS Nano* **4**, 6285–91 (2010).

188. J. Chang, C. K. Najeeb, J.-H. Lee, M. Lee, and J.-H. Kim, "High–performance photoresponse from single–walled carbon nanotube–zinc oxide heterojunctions", *J. Phys. D: Appl. Phys.* **44**, 095101 (2011).

189. S. Dhara and P. K. Giri, "Enhanced UV photosensitivity from rapid thermal annealed vertically aligned ZnO nanowires", *Nanoscale Res. Lett.* **6**, 504 (2011).

190. S. Dhara and P. K. Giri, "ZnO/anthracene based nanowires heterostructure: photoresponse and photoluminescence studies ", *J. Appl. Phys.* **111,** 044320 (2012).

191. J. H. He, Y. H. Lin, M. E. Mcconney, V. V. Tsukruk, and Z. L. Wang, "Enhancing UV photoconductivity of ZnO nanobelt by polyacrylonitrile functionalization", *J. Appl. Phys.* **102**, 084303 (2007).

192. C. S. Lao, M.-C. Park, Q. Kuang, Y. Deng, A. K. Sood, D. L. Polla, and Z. L. Wang, "Giant enhancement in UV response of ZnO nanobelts by polymer surface–functionalization", *J. Am. Chem. Soc.* **129**, 12096–97 (2007).

193. P. J. Li, Z. M. Liao, X. Z. Zhang, X. J. Zhang, H. C. Zhu, J. Y. Gao, K. Laurent, Y. L. Wang, N. Wang, and D. P. Yu, "Electrical and photoresponse properties of an

intramolecular p-n homojunction in single phosphorus–doped ZnO nanowires", *Nano Lett.* **9**, 2513–18 (2009).

194. D. Lin, H. Wu, W. Zhang, H. Li, and W. Pan, "Enhanced UV photoresponse from heterostructured Ag–ZnO nanowires", *Appl. Phys. Lett.* **94**, 172103 (2009).

195. S. Dhara and P. K. Giri, "Improved fast photoresponse from Al doped ZnO nanowires network decorated with Au nanoparticles", *Chem. Phys. Lett.* 541, 39–43 (2012).

196. H. Y. Park, S. C. Nam, Y. C. Lim, K. G. Choi, K. C. Lee, G. B. Park, J. B. Kim, H. P. Kim, and S. B. Cho 52, "$LiCoO_2$ thin film cathode fabrication by rapid thermal annealing for micro power sources", *Electrochimica Acta* **52**, 2062–67 (2007).

197. S. Xu, Y. Shen, Y. Ding, and Z. L. Wang, "Growth and transfer of monolithic horizontal ZnO nanowire superstructures onto flexible substrates", *Adv. Funct. Mater.* **20**, 1493–95 (2010).

198. S. Xu and Z. L. Wang, "One–dimensional ZnO nanostructures: solution growth and functional properties", *Nano Res.* **4**, 1013–98 (2011).

199. D. K. Schroder, *Semiconductor material and device characterization,* 3rd ed., Wiley–Interscience, New Jersey, USA, (2006).

200. B. D. Cullity and S. R. Stock, *Elements of x–ray diffraction,* 3rd ed., Prentic Hall, New Jersey, USA, (2001).

201. "The International Centre for Diffraction Data", retrieved www.isdd.com.

202. Y. Wu, X.-H. Zhang, F. Xu, L.-S. Zheng, and J. Kang, "A hierarchical lattice structure and formation mechanism of ZnO nano–tetrapods", *Nanotechnol.* **20**, 325709 (2009).

203. Ü. Özgür, Y. I. Alivov, A. T. C. Liu, M. A. Reshchikov, S. Doğan, V. Avrutin, S.-J. Cho, and H. Morkoçd, "A comprehensive review of ZnO materials and devices", *J. Appl. Phys.* **98**, 041301 (2005).

204. M. S. Dresselhaus, Y.-M. Lin, O. Rabin, M. R. Black, J. Kong, and G. Dresselhaus, "Nanowires," in *Springer handbook of nanotechnology,* 2nd ed., B. Bhushan, ed. Springer, Berlin, Germany, 113–53 (2007).

205. Rusli and G. A. Amaratunga, "Determination of the optical constants and thickness of thin films on slightly absorbing substrates", *J. Appl. Optics* **34**, 7914–24 (1995).

206. R. Swanepoel, "Determination of the thickness and optical constants of amorphous silicon", *J. Phys. E: Sci. Instrum.* **16**, 1214–22 (1983).

207. E. D. Palik, ed., *Handbook of Optical Constants of Solids,* Academic Press, New York, USA, (1998), Vol. 3.

208. G. D. Gilliland, "Photoluminescence spectroscopy of crystalline semiconductors", *Mat. Sci. Eng. R* **18**, 99–400 (1997).

209. C. R. Brundle, J. Charles A. Evans, and S. Wihon, eds., *Encyclopedia of material characterization: surfaces, interfaces, thin films,* Butterworth–Heinemann, Stoneham, USA, (1992).

210. J. B. Cui, C. P. Daghlian, U. J. Gibson, R. Pusche, P. Geithner, and L. Ley, "Low–temperature growth and field emission of ZnO nanowire arrays", *J. Appl. Phys.* **97**, 44315 (2005).

211. D. Zhao, C. Andreazza, P. Andreazza, J. Ma, Y. Liu, and D. Shen, "Buffer layer effect on ZnO nanorods growth alignment", *Chem. Phys. Lett.* **408**, 335–38 (2005).

212. S. Dhara and P. K. Giri, "Ti nanoparticles decorated ZnO nanowires heterostructure: photocurrent and photoluminescence properties", J. Exp. NanoSci. (2012, In Press).

213. C. S. Hsiao, C. H. Peng, S. Y. Chen, and S. C. Liou, "Tunable growth of ZnO nanorods synthesized in aqueous solutions at low temperatures", *J. Vac. Sci. Technol. B* **24**, 288–91 (2006).

214. P. K. Giri, S. Dhara, and R. Chakraborty, "Effect of ZnO seed layer on the catalytic growth of vertically aligned ZnO nanorod arrays", *Mater. Chem. Phys.* **122**, 18–22 (2010).

215. S. Dhara and P. K. Giri, "Effect of ZnO nanopowder source and growth temperature on the shape evolution of one–dimensional ZnO nanostructures", *Int. J. Nanosci.* **10**, 833–37 (2011).

216. W. D. Yu, X. M. Li, X. D. Gao, P. S. Qiu, W. X. Cheng, and A. L. Ding, "Effect of zinc sources on the morphology of ZnO nanostructures and their photoluminescence properties", *Appl. Phys. A* **79**, 453–56 (2004).

217. V. Ruth and J. P. Hirth, "Kinetics of diffusion–controlled whisker growth", *J. Chem. Phys.* **41**, 3139–49 (1964).

218. C. Y. Nam, D. Tham, and J. E. Fischer, "Effect of the polar surface on GaN nanostructure morphology and growth orientation", *Appl. Phys. Lett.* **85**, 5676–78 (2004).

219. B. Cordero, V. Gómez, A. E. Platero–Prats, M. Revés, J. Echeverría, E. Cremades, F. Barragán, and S. Alvarez, "Covalent radii revisited", *Dalton Trans.* **21**, 2832–38 (2008).

220. C. P. Dietrich, M. Lange, F. J. Klüpfel, H. v. Wenckstern, R. Schmidt–Grund, and M. Grundmann, "Strain distribution in bent ZnO microwires", *Appl. Phys. Lett.* **98**, 031105 (2011).

221. S. Dhara and P. K. Giri, "Size–dependent visible absorption and fast photoluminescence decay dynamics from freestanding strained silicon nanocrystals", *Nanoscale Res. Lett.* **6**, 320 (2011).

222. I. D. Wolf, "Stress measurements in Si microelectronics devices using Raman spectroscopy", *J. Raman Spectrosc.* **30**, 877–83 (1999).

223. T. Gruber, G. M. Prinz, C. Kirchner, R. Kling, F. Reuss, W. Limmer, and A. Waag, "Influences of biaxial strains on the vibrational and exciton energies in ZnO", *J. Appl. Phys.* **96**, 289–93 (2004).

224. H.-W. Suh, G.-Y. Kim, Y.-S. Jung, W.-K. Choi, and D. Byun, "Growth and properties of ZnO nanoblade and nanoflower prepared by ultrasonic pyrolysis", *J. Appl. Phys.* **97**, 044305 (2005).

225. Y.-C. Cheng, "Effects of post–deposition rapid thermal annealing on aluminum–doped ZnO thin films grown by atomic layer deposition", *Appl. Surf. Sci.* **258**, 604– 07 (2011).

226. J. W. Leem, Y. M. Song, Y. T. Lee, and J. S. Yu, "Antireflective properties of AZO subwavelength gratings patterned by holographic lithography", *Appl. Phys. B* **99**, 695–700 (2010).

227. G.-N. He, S.-T. Wu, J. Li, B. Huang, and Q.-H. Wu, "Influence of ph value on the structures and optical properties of ZnO nanocrystalline synthesized with a solution process", *Funct. Mater. Lett.* **3**, 107–10 (2010).

228. R. Chakraborty, S. Dhara, and P. K. Giri, "Effect of rapid thermal annealing on microstructure and optical properties of ZnO nanorods", *Int. J. Nanosci.* **10**, 65–68 (2011).

229. A. V. Dijken, E. A. Meulenkamp, D. Vanmaekelbergh, and A. Meijerink, "The kinetics of the radiative and nonradiative processes in nanocrystalline ZnO particles upon photoexcitation", *J. Phys. Chem. B* **104**, 1715–23 (2000).

230. J. V. Foreman, J. Li, H. Peng, S. Choi, H. O. Everitt, and J. Liu, "Time–resolved investigation of bright visible wavelength luminescence from sulfur–doped ZnO nanowires and micropowders", *Nano Lett.* **6**, 1126–30 (2010).

231. S. A. Studenikin and M. Cocivera, "Time–resolved luminescence and photoconductivity of polycrystalline ZnO film", *J. Appl. Phys.* **91**, 5060–65 (2002).

232. J. H. Huang, C. Y. Chen, Y. F. Lai, Y. Shih, Y. C. Lin, J. H. He, and C. P. Liu, "Large–area oblique–aligned ZnO nanowires through a continuously bent columnar buffer: growth, microstructure, and antireflection", *Cryst. Growth & Design* **10**, 3297–301 (2010).

233. S. Dhara and P. K. Giri, "Rapid thermal annealing induced enhanced band–edge emission from ZnO nanowires, nanoribbons and nanorods", *Funct. Mater. Lett.* **4**, 25–29 (2011).

234. Q. P. Wang, D. H. Zhang, Z. Y. Xue, and X. T. Hao, "Violet luminescence emitted from ZnO films deposited on Si substrate by RF magnetron sputtering", *Appl. Surf. Sci.* **201**, 123–28 (2002).

235. E. Burstein, "Anomalous optical absorption limit in InSb", *Phys, Rev.* **93**, 632 (1954).

236. T. S. Moss, "Theinterpretation of the properties of indium antimonide", *Proc. Phys. Soc. (London)* **B76**, 775 (1954).

237. A. Rose, "Space charge limited currents in solids", *Phys. Rev.* **97**, 1538–44 (1955).

238. H. Y. Peng, G. P. Li, J. Y. Ye, Z. P. Wei, Z. Zhang, D. D. Wang, G. Z. Xing, and T. Wu, "Electrode dependence of resistive switching in Mn–doped ZnO: Filamentary versus interfacial mechanisms", *Appl. Phys. Lett.* **96**, 192113 (2010).

239. T. Harada, I. Ohkubo, K. Tsubouchi, H. Kumigashira, T. Ohnishi, M. Lippmaa, Y. Matsumoto, H. Koinuma, and M. Oshima, "Trap–controlled space–charge–limited current mechanism in resistance switching at Al/$Pr_{0.7}Ca_{0.3}MnO_3$ interface", *Appl. Phys. Lett.* **92**, 22113 (2008).

240. H. K. Yadav, K. Sreenivas, and V. Gupta, "Study of metal/ZnO based thin film ultraviolet photodetectors: The effect of induced charges on the dynamics of photoconductivity relaxation", *J. Appl. Phys.* **107**, 044507 (2010).

241. Y. Feng, W. Hou, X. Zhang, P. Lv, Y. Li, and W. Feng, "Highly sensitive reversible light–driven switches using electrospun porous aluminum–doped zinc oxide nanofibers", *J. Phys. Chem. C* **115**, 3956–61 (2011).

242. D. Lin, H. Wu, and W. Pan, "Photoswitches and memories assembled by electrospinning aluminum–doped zinc oxide single nanowires", *Adv. Mater.* **19**, 3968–72. (2007).

243. D. R. Lide, *CRC Handbook of chemistry and physics,* CRC press, Boca Raton, USA, (2009).

244. C. A. Aguilar, R. Haight, A. Mavrokefalos, B. A. Korgel, and S. Chen, "Probing electronic properties of molecular engineered zinc oxide nanowires with photoelectron spectroscopy", *ACS. Nano* **3**, 3057–62 (2009).

245. M. A. Garcia, "Surface plasmons in metallic nanoparticles: fundamentals and applications", *J. Phys. D: Appl. Phys.* **44**, 283001 (2011).

246. S. A. Dayeh, C. Soci, P. K. L. Yu, E. T. Yu, and D. Wang, "Influence of surface states on the extraction of transport parameters from InAs nanowire field effect transistors", *Appl. Phys. Lett.* **90**, 162112 (2007).

247. H. Y. Lin, C. L. Cheng, Y. Y. Chou, L. L. Huang, Y. F. Chen, and K. T. Tsen, "Enhancement of band gap emission stimulated by defect loss", *Opt. Exp.* **16**, 2372–79 (2006).

248. T. Chen, G. Z. Xing, Z. Zhang, H. Y. Chen, and T. Wu, "Tailoring the photoluminescence of ZnO nanowires using Au nanoparticles", *Nanotechnol.* **19**, 435711 (2008).

249. K. W. Liu, B. Liu, S. J. Wang, Z. P. Wei, T. Wu, C. X. Cong, Z. X. Shen, X. W. Sun, and H. D. Sun, "Influence of thin metal nanolayers on the photodetective properties of ZnO thin films", *J. Appl. Phys.* **106**, 083110 (2009).

250. L. Liao, Z. Zhang, Y. Yang, B. Yan, H. T. Cao, L. L. Chen, G. P. Li, T. Wu, Z. X. Shen, B. K. Tay, T. Yu, and X. W. Sun, "Tunable transport properties of n–type ZnO nanowires by Ti plasma immersion ion implantation", *J. Appl. Phys.* **104**, 076104 (2008).

251. C. P. Brock and J. D. Dunity, "Temperature dependence of thermal motion in crystalline anthracene", *Acta Crysta.* **B46**, 795–806 (1990).

252. P. Zhang, J. Deng, X. Zeng, Z. Liu, Y. Qiu, H. Zhong, Y. Fan, J. Huang, J. Zhang, and K. Xub, "Growth mechanism of large–size anthracene single crystal sgrown by a solution technique", *J. Cryst. Growth* **311**, 4708–13 (2009).

253. H. Huang, Q. Fu, S. Zhuang, G. Mu, L. Wang, J. Chen, D. Ma, and C. Yang, "Solution–processable 1,3,5-tri(9-anthracene)-benzene cored propeller–shaped materials with high T_g for blue organic light–emitting diodes", *Org. Electron.* **12**, 1716–23 (2011).

254. M. Zhu, T. Ye, C.-G. Li, X. Cao, C. Zhong, D. Ma, J. Qin, and C. Yang, "Efficient solution–processed nondoped deep–blue organic light–emitting diodes based on fluorene–bridged anthracene derivatives appended with charge transport moieties", *J. Phys. Chem. C* **115**, 17965–72 (2011).

255. K. R. J. Thomas, P. Singh, A. Bahetia, Y.-C. Hsu, K.-C. Ho, and J. T. s. Lin, "Electro–optical properties of new anthracene based organic dyes for dye–sensitized solar cells", *Dyes and Pigments* **91**, 33–43 (2011).

256. W. Chen, S. Pradhan, and S. Chen, "Photoluminescence and conductivity studies of anthracene–functionlized ruthenium nanoparticles", *Nanoscale* **3**, 2294–300 (2011).

257. R. K. Das, S. Bhat, S. Banerjee, C. Aymonier, A. Loppinet–Serani, P. Terech, U. Maitra, G. Raffy, J.-P. Desvergne, and A. D. Guerzo, "Self–assembled composite nano–materials exploiting a thermo reversible n–acene fibrillar scaffold and organic–capped ZnO nanoparticles ", *J. Mater. Chem.* **21**, 2740–50 (2011).

258. M. Andres-Verges, A. Mifsud, and C. J. Serna, "Formation of rod–like zinc oxide microcrystals in homogeneous solutions", *J. Chem. Soc., Faraday Trans.* **86**, 959–63 (1990).

259. S. Karan and B. Mallik, "Templating effects and optical characterization of copper (II) phthalocyanine nanocrystallites thin film: nanoparticles, nanoflowers, nanocabbages, and nanoribbons", *J. Phys. Chem. C* **111**, 7352–65 (2007).

260. G. D. Sharma, R. Kumar, S. K. Sharma, and M. S. Roy, "Charge generation and photovoltaic properties of hybrid solar cells based on ZnO and copper phthalocyanines (CuPc)", *Sol. Energy Mater. Sol. Cells* **90**, 933–46 (2006).

261. S. A. V. Slyke, C. H. Chen, and C. W. Tang, "Organic electroluminescent devices with improved stability", *Appl. Phys. Lett.* **69**, 2160 (1996).

262. R. K. Gupta, F. Yakuphanoglu, K. Ghosh, and P. K. Kahol, "Fabrication and characterization of p–n junctions based on ZnO and CuPc", *Microelectronic Eng.* **88**, 3067–69 (2011).

263. W. Guo, Y. Yang, J. Qi, and Y. Zhang, "Room temperature negative differential resistance based on a single ZnO nanowire/CuPc nanofilm hybrid heterojunction", *Appl. Phys. Lett.* **97**, 263118 (2010).

264. Y. Liu, A. Liu, W. Liu, Y. Sang, Z. Hu, and D. Kang, "Photovoltaic properties of the copper–phthalocyanine and ZnO nanorod array system affected by ethanol", *Appl. Surf. Sci.* **257**, 2176–79 (2011).

265. R. Prabakaran, E. Fortunato, R. Martins, and I. Ferreira, "Fabrication and characterization of hybrid solar cells based on copper phthalocyanine/porous silicon", *J. NonCryst. Solids* **354**, 2892–96 (2008).

266. J. Mack and M. J. Stillman, "Transition assignments in the ultraviolet−visible absorption and magnetic circular dichroism spectra of phthalocyanines", *J. Inorg. Chem.* **40**, 812–14 (2001).

267. S. Senthilarasu, R. Sathyamoorthy, S. Lalitha, A. Subbarayan, and K. Natarajan, "Thermally evaporated ZnPc thin films—band gap dependence on thickness", *Sol. Energy Mater. Sol. Cells* **82**, 179–86 (2004).

268. H. Laurs and G. Heiland, "Electrical and optical properties of phthalocyanine films", *Thin Solid Films* **149**, 129–42 (1987).